Volume 3, Issue I

April 2026
ISSN: 3021-9795/Print
ISSN: 3059-9628/Online

# POKHARA ENGINEERING COLLEGE JOURNAL (PECJ)

*Applied Sciences and Engineering Insights*

"A double-blind, peer-reviewed, open-access journal indexed in NepJOL, dedicated to advancing knowledge and research dissemination."

**Pokhara Engineering College (PEC)**
Phirke, Pokhara-8, Kaski, Nepal
PO Box: 540, Tel: 977-61-581209/578530
E-mail: info@pec.edu.np.
www.pec.edu.np

Published By:

**Research Management Cell (RMC)**

**Pokhara Engineering College**



**Special Thanks to:**

Pokhara Engineering College

## ABOUT THE JOURNAL

### Focus and Scope

Pokhara Engineering College Journal (PECJ) is a scientific journal published by Pokhara Engineering College (PEC). PECJ covers a broad spectrum of applied sciences and engineering topics.

Our aim is to be a high-quality, multi-disciplinary journal publishing the results of basic and applied research. We place emphasis on the quality of all published papers. The journal should also bridge basic research in natural sciences and applied research in all technical disciplines.

We support the innovative research results published by young scientists or doctoral fellows and the high-quality papers by researchers from the international scientific community.

**Peer Review Process**

The Editorial Board assesses all papers, and accepted papers are reviewed by at least two independent reviewers in **a double-blind review process.**

**The review process is usually completed within four months.**

**Open Access Policy**

PEC Journal is an Open Access journal, meaning that all content is freely available to the user or his/her institution without charge. Users are allowed to read, download, copy, distribute, print, search, or link to the full texts of the articles in this journal without asking prior permission from the publisher or the author.

Article submission or **processing charge** (APC, publication fee) is not required from authors - publishing in PECJ is **free.**

**Periodicity**

Annually.

# TABLE OF CONTENTS

Asst. Prof. Dr. Bidur Devkota
Assistant Professor, Gandaki College of Engineering & Science (im.bidur@gmail.com )
Asst. Prof. Er. Deepak Thapa
Assistant Professor Western Regional Campus, T.U(deepakthapa@wrc.edu.np)

Asst. Prof. Dr. Durga Bastakoti
Assistant Professor, Institute of Engineering, Tribhuvan University (durgabastakoti@gmail.com )

Asst. Prof. Dr. Prakash Devkota
Assistant Professor, Oxford Engineering College (prakash.devkota567@gmail.com)

Asst. Prof. Dr. Sujan Tripathi
Assistant Professor, Institute of Engineering, Tribhuvan university(sujantripathi@ioe.edu.np)

Asst. Prof. Dr. Abhishek Ghimire
Research Associate, University of Western Australia (abhi.ghimire45@gmail.com)

Asst. Prof. Dr. Arjun Baniya
Assistant Professor, Pokhara Engineering College (arjunbaniya36@yahoo.com)

Asst. Prof. Er. Yam Bahadur Thapa
Assistant Professor, Pokhara Engineering College(viceprincipal@pec.edu.np)

Asst. Prof. Er. Bikash Baral
Assistant Professor, Pokhara Engineering College (bikash_baral@hotmail.com)

Asst. Prof. Er. Suraj Basanta Tulachan
Assistant Professor, Pokhara Engineering College(hod.cmp@pec.edu.np)

Asst. Prof. Er. Bimal Bhandari
Assistant Professor, Pokhara Engineering College(hod.civil@pec.edu.np)

Er. Prabin Kumar Shrestha
Assistant Professor, Pokhara Engineering College (eca@pec.edu.np )

Asst. Prof. Ar. Roshni Subedi
Assistant Professor, Pokhara Engineering College(pec.roshani@gmail.com)

Asst. Prof. Er. Saroj Giri
Assistant Professor, Gandaki University (girisaroj061@gmail.com )

Asst. Prof. Ar. Luna Thapa
Assistant Professor, Institute of Engineering, Tribhuvan university (lunathapa88@gmail.com)

Pokhara Engineering College Journal (PECJ)
*Applied Sciences and Engineering Insights*

ISSN: 3021-9795 (Print) / 3059-9628 (Online)
(Volume-3, Issue- I)

# Comparative Study of Behaviour of Buildings using NBC 105:2020 and IS 1893:2016 based on Horizontal Irregularities

Suchana Rijal[1*], Pujan Tharu[2], Sanskar Shrestha[3], Saurav Poudel[4], Krishna Ghimire[5]

[1,2,3,4] *Department of Civil Engineering Pokhara Engineering College, Pokhara, Nepal*

[5] *Assistant Professor, Department of Civil Engineering, Pokhara Engineering College, Pokhara, Nepal*

*Corresponding email: krishnaghimire040@gmail.com



*Received:15- January-2026; Revised: 10- February-2026; Accepted: 08- March-2026*
*DOI: https://doi.org/10.3126/pecj.v3i1.93517*

**Abstract**

Seismic performance of structures is highly influenced by building configuration and the design code adopted. Irregular buildings, especially those with L-, C- and E-shaped plans, are known to exhibit complex dynamic behavior compared to regular-shaped structures. This study focuses on evaluating the seismic response of such irregular configurations using two widely adopted design standards: NBC 105:2020 (Nepal) and IS 1893:2016 (India). A comparative analysis was conducted through equivalent static method using ETABS software, assessing key parameters such as lateral displacement, inter-storey drift, and torsional irregularity. Four different building models—regular, L-shaped, C-shaped, and E-shaped—were analyzed under identical loading, material, and geometric conditions. The results revealed that irregular buildings consistently exhibited higher lateral displacement and drift, particularly at the re-entrant corners where stress concentrations were most severe. Among the codes, NBC 105:2020 produced notably higher drift values in all configurations compared to IS 1893:2016, indicating a more conservative approach. Torsional irregularities were also more pronounced in L- and C-shaped buildings under NBC, due to its stricter consideration of eccentricity and mass irregularity. Overall, the study highlights the critical impact of both structural configuration and seismic code selection on the response of buildings. It is concluded that while NBC 105:2020 provides a higher margin of safety, especially for irregular buildings, careful consideration of building geometry during the design phase remains essential for seismic resilience. The findings underscore the need for enhanced code-specific design provisions for irregular structures in high-seismic zones.
**Keywords:** Code comparison, horizontal irregularities, base shear, drift, torsion, displacement

## 1. Introduction

Seismic forces significantly impact the safety and performance of buildings, especially in earthquake-prone countries like Nepal and India. One of the key factors influencing seismic response is horizontal irregularity, which includes non-uniform building shapes in plan such as L-shaped, U-shaped, and E-shaped structures. These irregular configurations cause uneven distribution of stiffness and mass, which results in stress concentrations and enhanced torsional effects during ground motion (Agarwal and Shrikhande, 2010). To address these concerns, national seismic design codes such as NBC 105:2020 in Nepal and IS 1893 (Part 1):2016 in India provide criteria for identifying and analysing horizontal irregularities. Both codes define types of plan irregularities, including torsional irregularity, re-entrant corners, diaphragm discontinuities, and non-parallel lateral force-resisting systems. For torsional irregularity, both codes state that it exists when the maximum storey displacement at one end exceeds 1.5 times the minimum displacement at the other end of the same storey (NBC 105:2020 and IS 1893:2016).

Previous studies highlight that buildings with horizontal irregularities often experience higher seismic demand compared to regular buildings. According to Adhikari et al. (2020), L- and U-shaped buildings show significantly increased lateral displacement and torsional response. Goyal and Choudhury (2019) emphasized that torsional effects are especially critical when such buildings are analysed using simplified methods like the equivalent static approach. Sharma and Khandelwal (2017) found that NBC 105:2020 generally leads to higher base shear and more conservative designs than IS 1893, due to differences in seismic zoning and design assumptions. Despite these observations, limited research has been conducted that directly compares NBC 105:2020 and IS 1893:2016 in the context of horizontally irregular structures under a consistent modelling approach.

Although seismic codes like NBC 105:2020 and IS 1893:2016 discourage the use of horizontally irregular buildings due to their poor seismic performance, such irregular forms are still commonly used in practice for functional or architectural reasons. This mismatch between codal intent and construction practice can compromise structural safety.
Moreover, the two codes differ in their treatment of irregularities, which may lead to variations in design and seismic response. There is limited comparative analysis of how these codes address horizontal irregularities in terms of drift, displacement, and torsion. The main objective of the research is to compare seismic codes NBC 105:2020 and IS 1893:2016 based on horizontal irregularities. This study aims to fill that gap by analysing and comparing the behaviour of irregular buildings under both codes.

The scope of the study encompasses various aspects in functional planning and structural analysis of building with NBC and IS using ETABS. The comparative analysis using NBC and IS will be for the four buildings (5 storey + staircase cover); one is the designed to be building named Regular building and others are the buildings having horizontal irregularities, i.e. L shaped building, C shaped building and E shaped building. The research uses Equivalent Static Method for analysis and it will evaluate how each code handles torsional irregularities. The soil type is considered “soil type D” for NBC and “soil type III” for IS. This research outlines the approach to utilizing different plans, for seismic analysis and comparison (NBC and IS) along with detailed design of an apartment building.
The load cases and load combinations used in the analysis were adopted from IS 1893:2016 and NBC 105:2020, ensuring that the structural evaluation reflects the seismic design provisions, safety requirements, and code-based guidelines specified by both Indian and Nepalese standards for accurate and reliable assessment of critical element forces.

The seismic load combinations were adopted from IS 1893:2016 and NBC 105:2020. As per IS 1893:2016, the structure is designed considering bidirectional seismic effects using combinations such as (ELX ± 0.3 ELY) and (ELY ± 0.3 ELX), where X and Y are orthogonal horizontal directions. These are incorporated into load combinations provided in code to capture critical loading conditions. In contrast, NBC 105:2020 specifies load combinations for both parallel and non-parallel systems likely DL + λLL ± E and other combination as mentioned in code, where the live load factor λ is taken as 0.6 for storage facilities and 0.3 for other occupancies. For non-parallel systems, directional combinations such as (EX ± 0.3EY) and (0.3EX ± EY) are considered, ensuring realistic representation of seismic action in both principal directions.

## 2. Materials and Methodology

### 2.1 Building configuration

For comparison, an identical structural model is adopted for all seismic codes, and the important characteristics of the building are presented in the table below. The study was conducted on four different building configurations—regular, L-shaped, C-shaped, and E-shaped—where each model was subjected to the same loading conditions, material properties, and geometric parameters. This consistent approach ensures that the comparison of structural responses is purely based on the effect of building shape and plan irregularity.

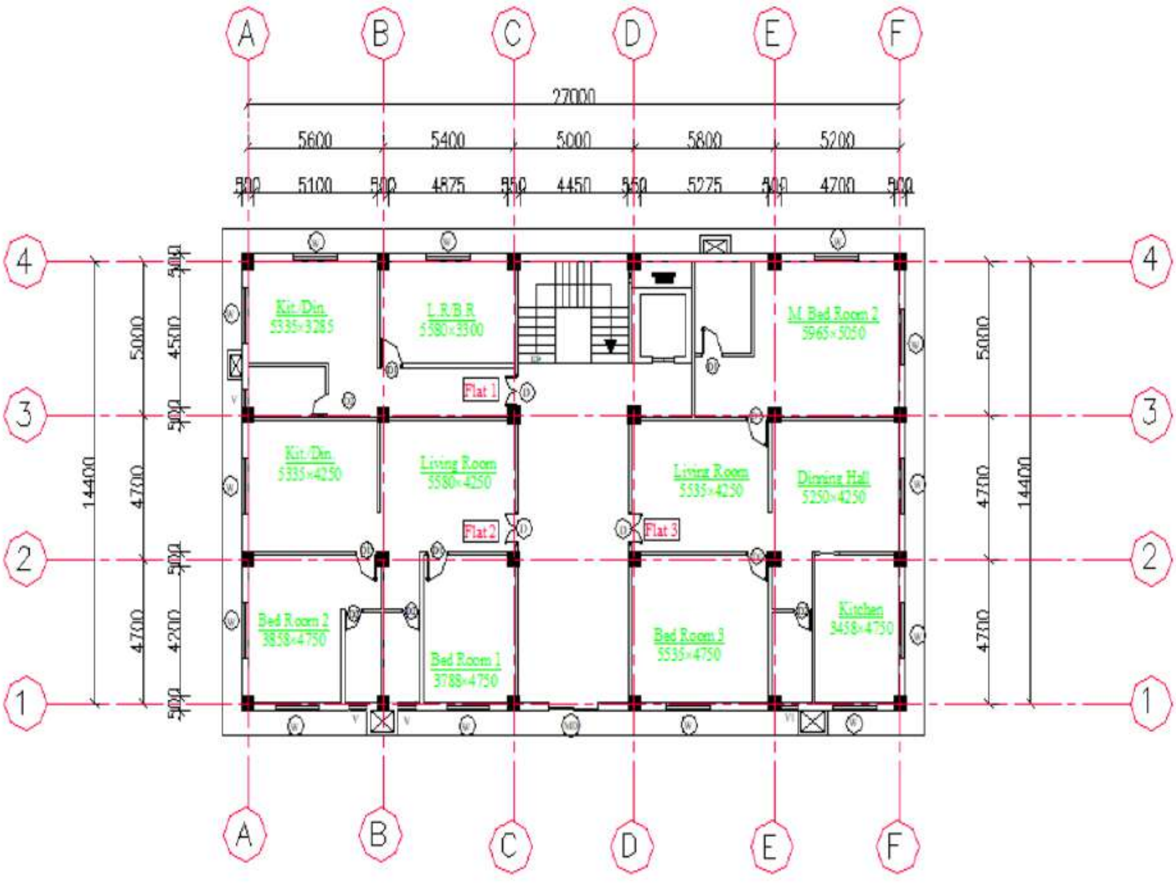


**Figure 1:** Architectural Drawing of Ground Floor.

**Table 1:** Description of Building (NBC 206:2015, Architectural Design Requirements).

| Parameters | Details |
|---|---|
| Types of Building | Apartment Building |
| Category of Building | Mid-Rise Building |
| Structural System | RCC Frame Structures; SMRF |
| Number of Story | 5 (G + 4 + Staircase Cover) |
| No. of Bays in X Direction | 5 nos. of Bays |
| No. of Bays in Y Direction | 3 nos. of Bays |
| Plint Area | 429.93 Sq m |
| Floor Height | 3.0 m |
| Size of Building | Length = 27000 mm, Breadth = 14400 mm |
| Grade of Concrete | M25 for Beam, Column and M20 for Slab |
| Grade of Steel | Fe 500 |

### 2.2 Material

**Table 2:** Parameters used for the design of models (IS 456:2000, Indian Standard Code of Practice for Plain and Reinforced Cement Concrete)

| Description | Section/Constant | Units |
|---|---|---|
| Parameters | Data | Unit |
| Column size | 500X500 | mm X mm |
| Main Beam size | 300X500 | mm X mm |
| Slab thickness | 125 | mm |
| Shear wall | 200 | mm |
| Specific weight of concrete | 25 | $KN/m^3$ |
| Unit weight of Brick | 19.0 | $KN/m^3$ |
| Modulus of elasticity of concrete | 25000 | MPa |

### 2.3 Modelling of Buildings

Modelling is done using ETABS 2000 Vs. 24.0, using the finite element model of a building. Modelling is done as per the architectural drawing, and the changes are made later as per the structural requirements. Special attention is given while modelling the building in ETABS as a very small and unnecessary section may cause the failure of the whole structure which is undesirable.

The structure is a mid-rise apartment building with RCC frame construction using a Special Moment Resisting Frame (SMRF) system. It has a total of 5 stories (Ground + 4 floors + staircase cover). The building layout consists of 5 bays along the X direction and 3 bays along the Y direction. The building was modeled and analyzed using the Equivalent Static Method according to both Nepal (NBC 105:2020) and Indian (IS 1893:2016) seismic codes. After the initial analysis of the regular building, additional building configurations—C-shaped, E-shaped, and L-shaped plans—were created to study the effects of plan irregularity on seismic response. The analysis is done following Equivalent static method (ESM)

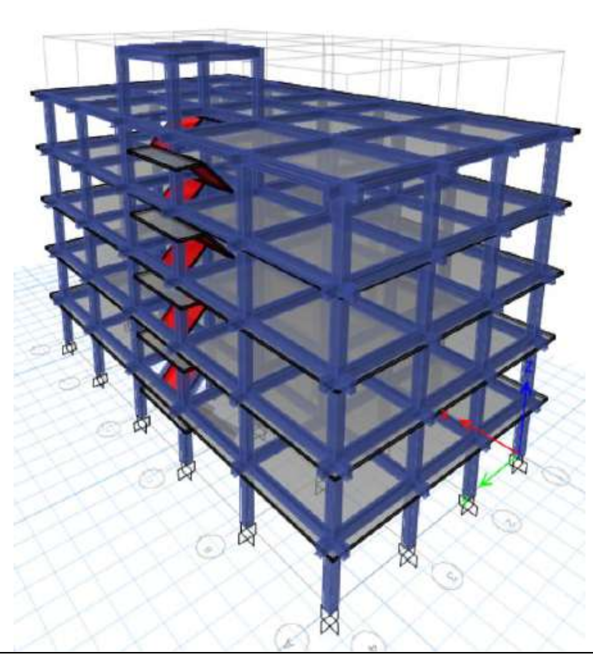

**Figure 2 a**: Regular Shape Building

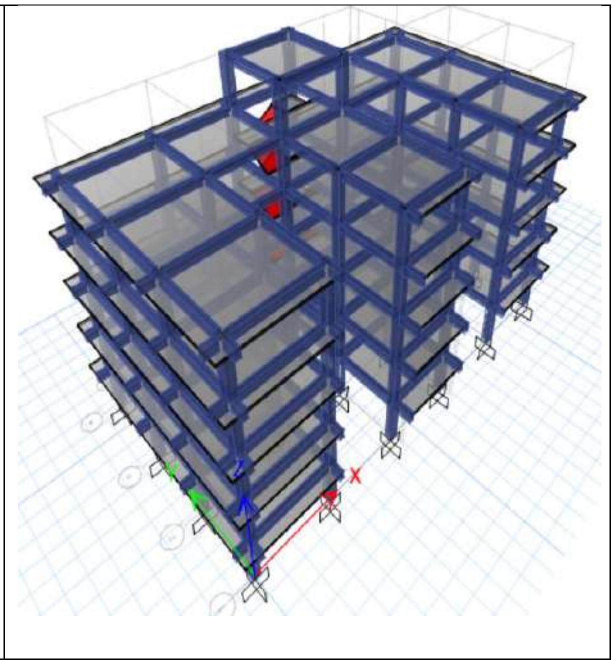

**Figure 2 b:** E Shape Building

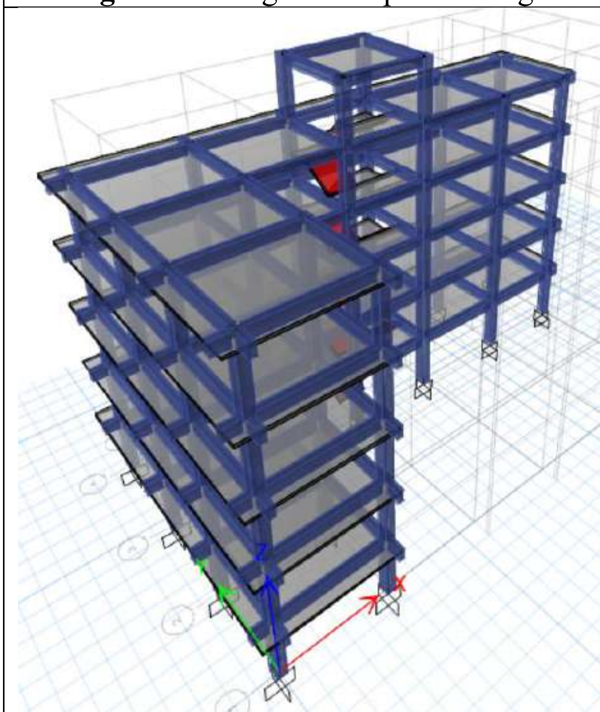

**Figure 2 c:** L Shape Building

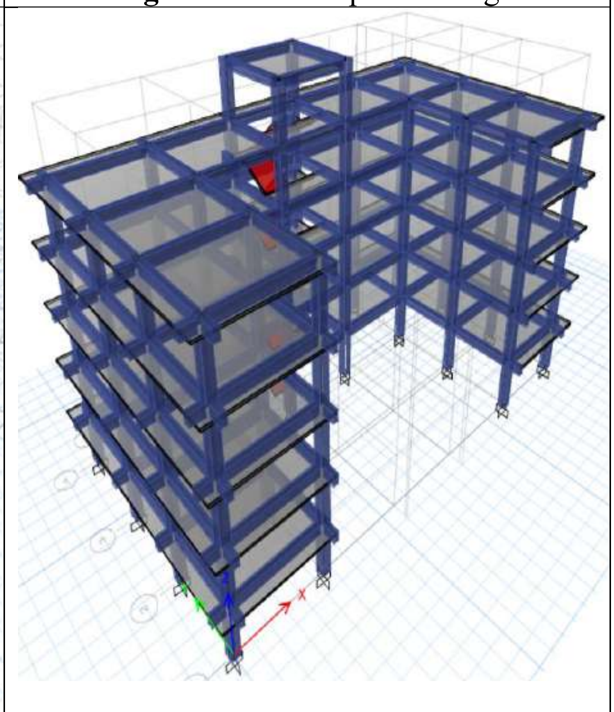

**Figure 2 d:** C Shape Building

**Figure 2**: Different sides Extrude view of building from ETABS.

**2.4 Seismic coefficient calculation:**

Using NBC 105:2020, The base shear coefficient will be determined separately for ultimate limit state and serviceability limit state from the figure 4.

$Cd(T1) = (C(T1))/((R\mu)(\Omega u))$ (1)

$Cd(T1) = (Cs(T1))/\Omega s$ (2)

Where, Cd(T1) = Elastic Site Spectra for Ultimate Limit State

Cs (T1)) = Elastic Site Spectra for Serviceability Limit State

Rμ= Ductility Factor

Ωu = Over strength Factor for Ultimate Limit State

Ωs = Over strength Factor for Serviceability Limit State

The horizontal seismic base shear at the base of the structure in the direction is calculated as:

V =Cd(T1).W

Where, Cd(T1) = Horizontal base shear coefficient

The Elastic site spectra for horizontal loading shall be as given by

C (T) =Ch(T) Z I (3)

where, Ch(T) = Spectral Shape factor

According to IS 1893:2016 (Part 1), the base shear coefficient is determined based on various factors such as the seismic zone, importance of the structure, and the structural system's response.

The base shear is calculated using the formula:

$V_B$=Ah.W

where, $V_B$ = Total base shear (in KN)

Ah = Horizontal seismic coefficient

W= Seismic weight of the structure (in KN)

$$Ah = \frac{Z.I.Sa}{2.R.g} \quad (4)$$

Z = Zone Factor

I = Importance Factor

R = Response Reduction Factor

Sa/g = Average Response Acceleration

g = Acceleration due to gravity

**Table 3:** According to IS 875 (Part 1): 1987 and IS 875 (Part 2): 1987 Indian Standard Code of Practice for Design Loads

| Parameters | Dead Load | Units |
|---|---|---|
| External Brick wall Without Opening | 13.25 | KN/m |
| External Brick wall 25% Opening | 9.95 | KN/m |
| Partition Brick wall Without Opening | 8.75 | KN/m |
| Partition Brick wall With Opening | 6.5 | KN/m |
| Dead load of Floor finish for Roof | 0.75 | $KN/m^2$ |

| | | |
|---|---|---|
| Dead load of Floor finish with Granite | 1.50 | $KN/m^2$ |
| Dead load of Floor finish with Tile | 1.25 | $KN/m^2$ |
| Balcony and staircase, | 4 | $KN/m^2$ |
| Kitchen and Hall | 3 | $KN/m^2$ |
| Toilet and Bathroom | 2 | $KN/m^2$ |
| Roof accessible | 1.5 | $KN/m^2$ |
| Roof not accessible | 0.75 | $KN/m^2$ |

## 3. Results and Discussion

A study is performed in apartment RC Building of different configuration through different edition of National Building Code (NBC) from Nepal, and Indian Standard Code (IS) from India. The Results are interpreted in terms of base shear, displacement, torsion, drift, lateral forces.

**Base Shear comparison bar chart is Shown below:**

**Table 4**: Base Shear along X- Direction

| Building | NBC SLS (KN) | NBC ULS (KN) | IS (KN) |
|---|---|---|---|
| Regular | 2716.52 | 2842.28 | 2245.14 |
| L- Shape | 1561.09 | 1633.28 | 1361.97 |
| U- Shape | 2042.76 | 2137.34 | 1712.82 |
| E- Shape | 2274.32 | 2379.622 | 1927.02 |

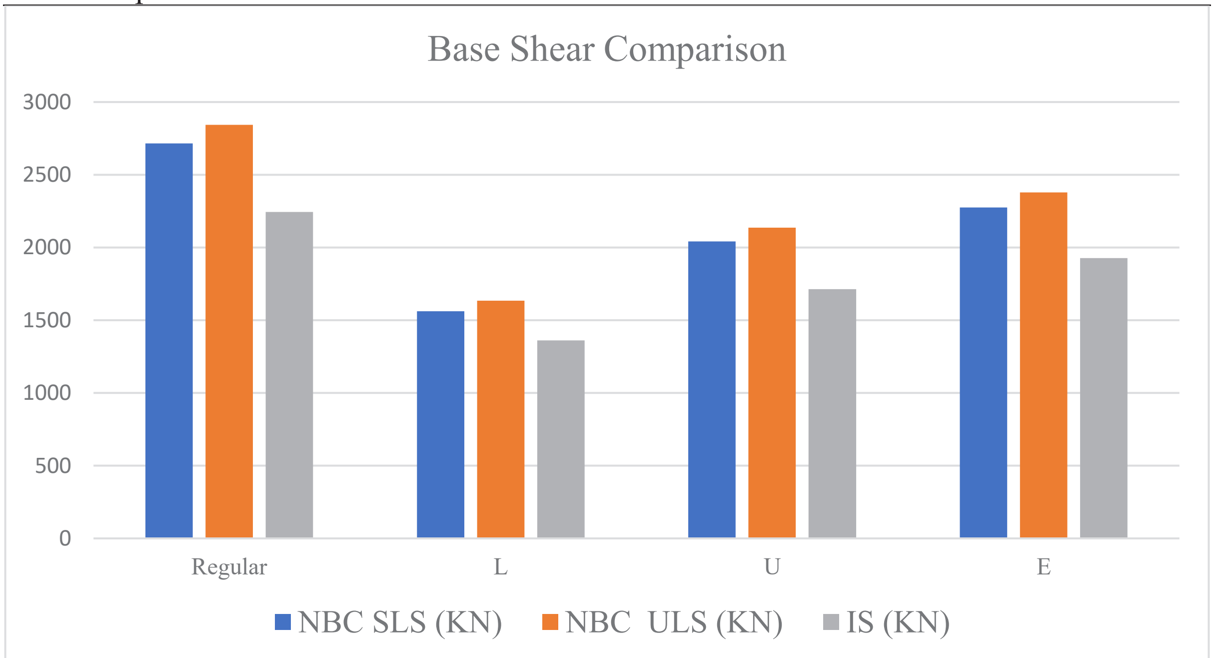


**Figure 3**: Base Shear in EQX Direction

The comparison of base shear values indicates that the NBC (National Building Code) produces higher base shear values for all building configurations compared to the Indian Code. The Regular-shaped building shows the highest difference, where the NBC value is 26.5% greater. Similarly, the L-shaped, C-shaped, and E-shaped buildings show increases of 19.92%, 24.78%, and 23.48%, respectively. This suggests that the NBC provisions result in more conservative base shear estimates, leading to potentially safer structural designs for different building plan irregularities than IS Code.

**The story displacement are compared and presented below:**

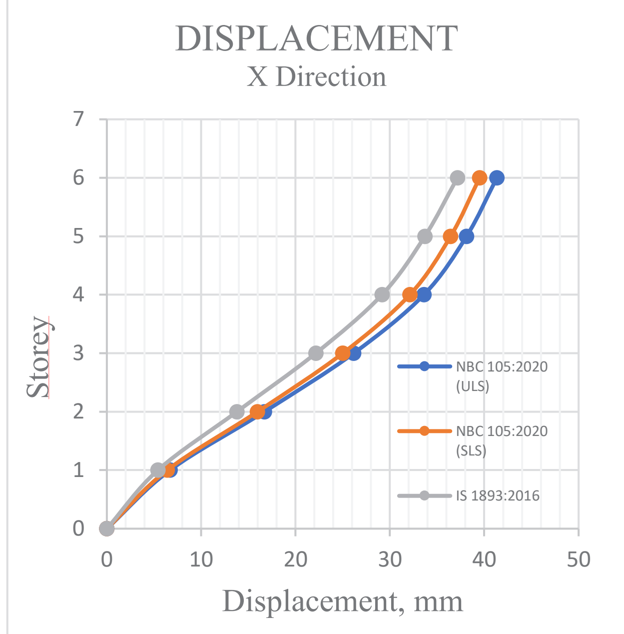


**Figure 4:** Displacement in X-Direction of Regular Building

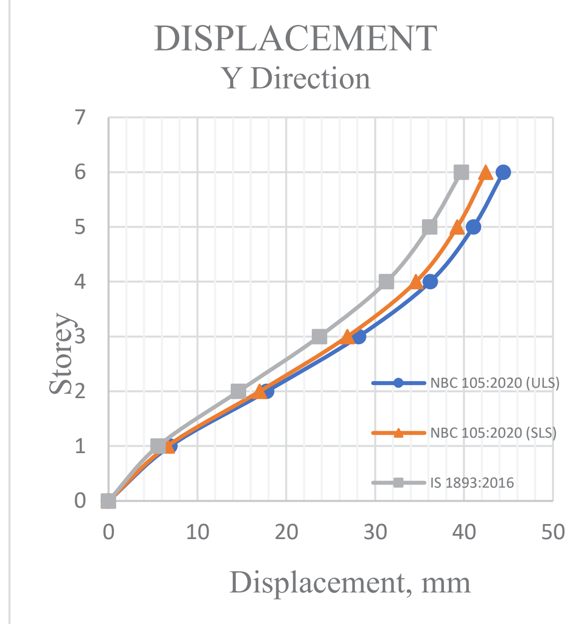


**Figure 5:** Displacement in X-Direction of Regular Building

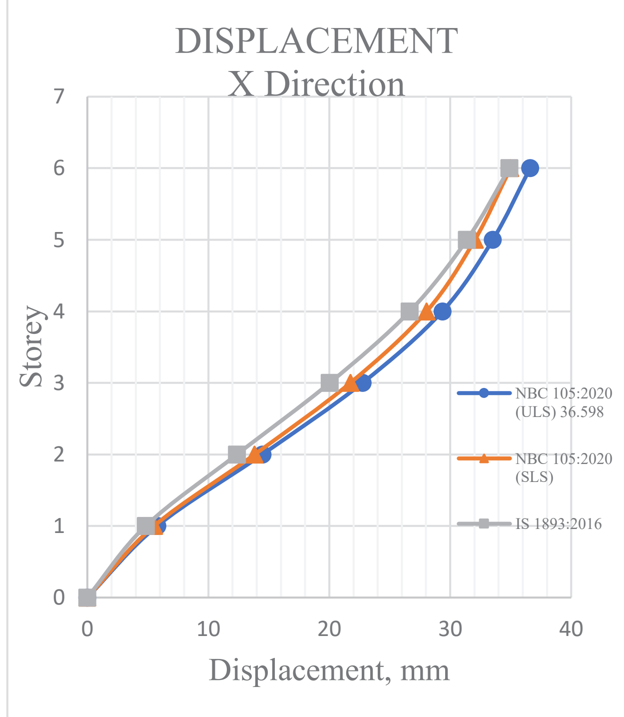


**Figure 6:** Displacement in X-Direction of L-shaped Building

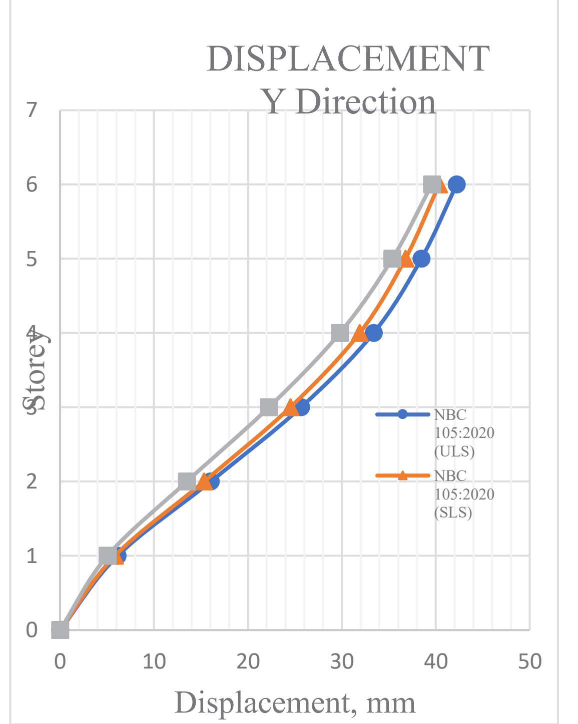


**Figure 7:** Displacement in Y-Direction of L- shaped Building

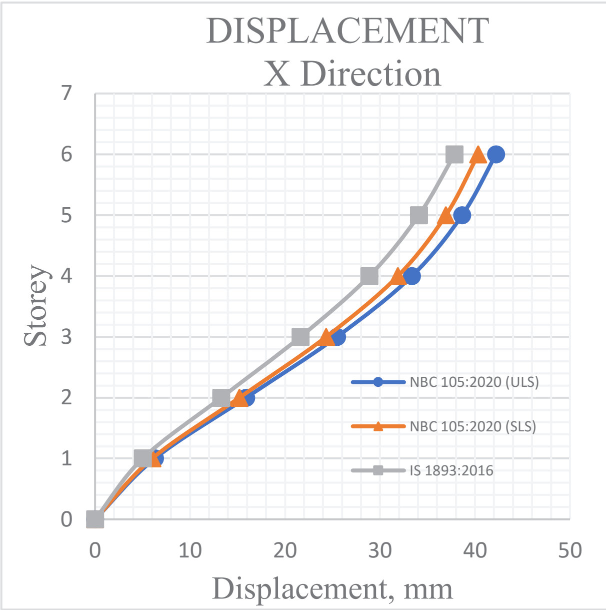


**Figure 8:** Displacement in X-Direction of C-shaped Building

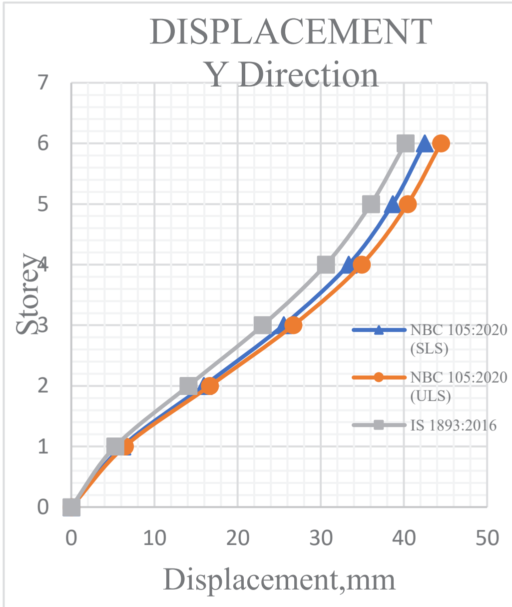


**Figure 9:** Displacement in Y-Direction of C- shaped Building

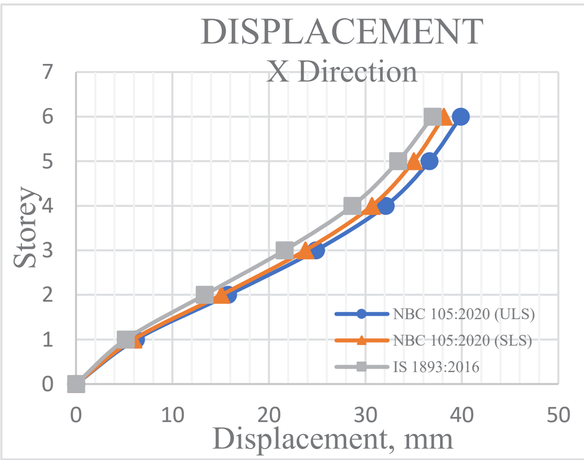


**Figure 10:** Displacement in X-Direction of E-shaped Building

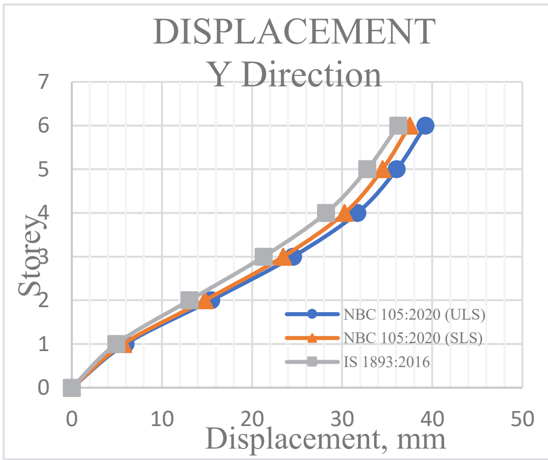


**Figure 11:** Displacement in Y-Direction of E- shaped Building

The comparison of results in both X and Y directions shows that the values obtained using NBC provisions are higher for all building configurations. In the X direction, the Regular and C-shaped buildings show the highest increase of 21%, followed by the E-shaped building (15%) and the L-shaped building (10%). Similarly, in the Y direction, the Regular building again shows the highest increase (12%), while the L-shaped building shows the lowest difference (7%). The C-shaped and E-shaped buildings show increases of 11% and 8%, respectively. Overall, the results indicate that NBC tends to produce higher response values compared to the other code, suggesting a more conservative design approach for different building configurations and directions.

**The story drift graphs are compared and demonstrated:**

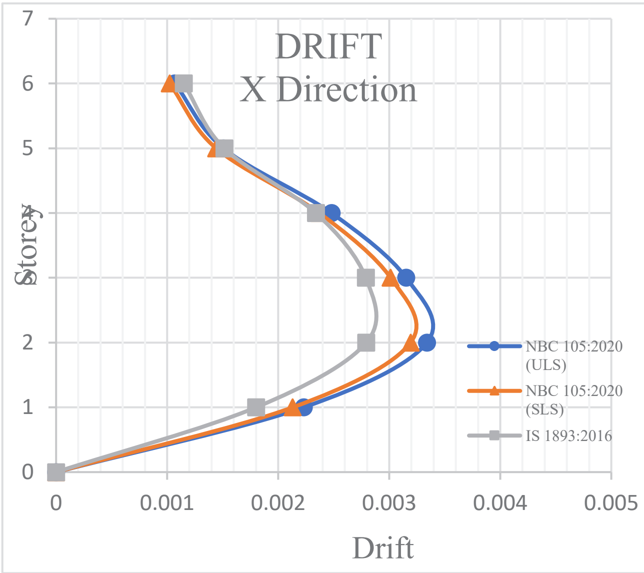


**Figure 12:** Inter Story Drift in X- Direction of Regular Building

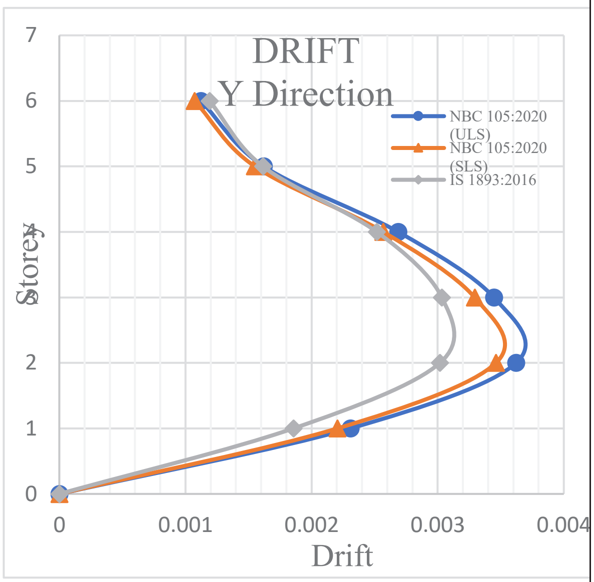


**Figure 13:** Inter Story Drift in X- Direction of Regular Building

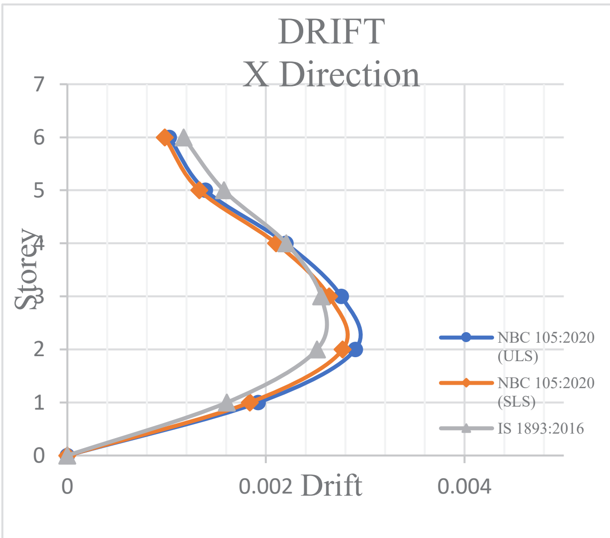


**Figure 14:** Inter Story Drift in X- Direction of L- Shaped Building

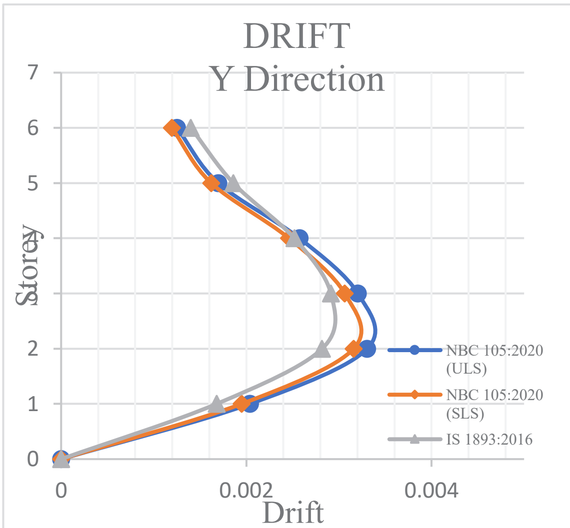


**Figure 15:** Inter Story Drift in X- Direction of L- Shaped Building

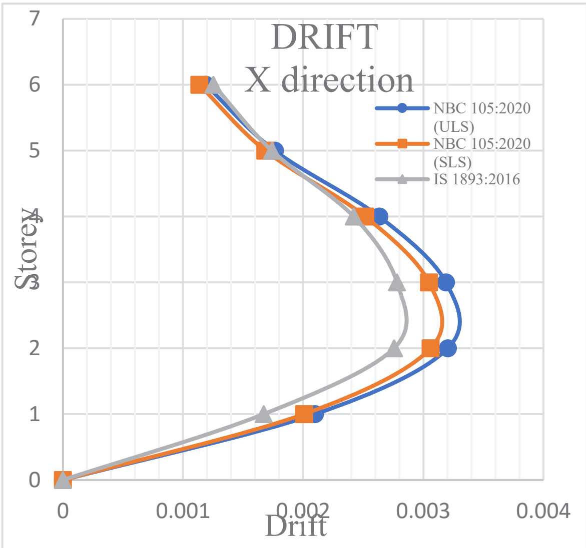


**Figure 16:** Inter Story Drift in X- Direction of C- Shaped Building

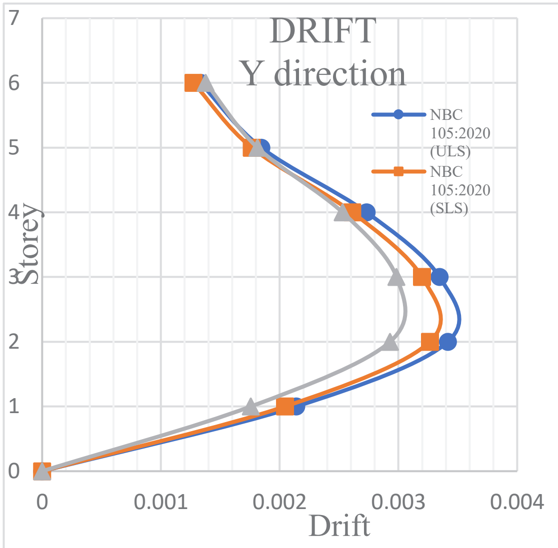


**Figure 17:** Inter Story Drift in X- Direction of C- Shaped Building

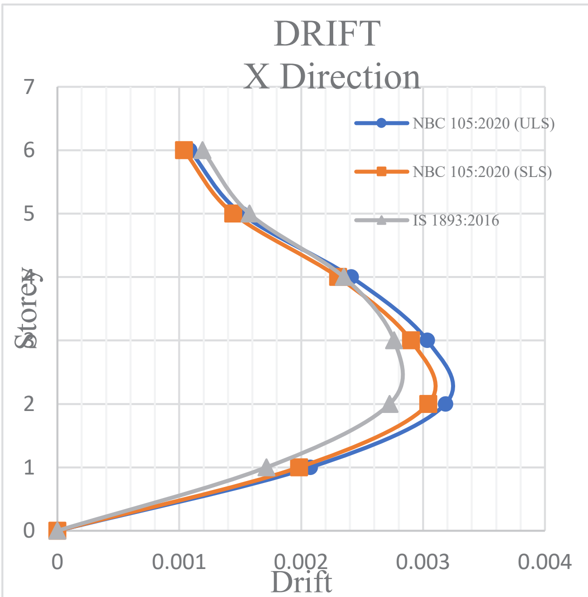


**Figure 18:** Inter Story Drift in X- Direction of E- Shaped Building

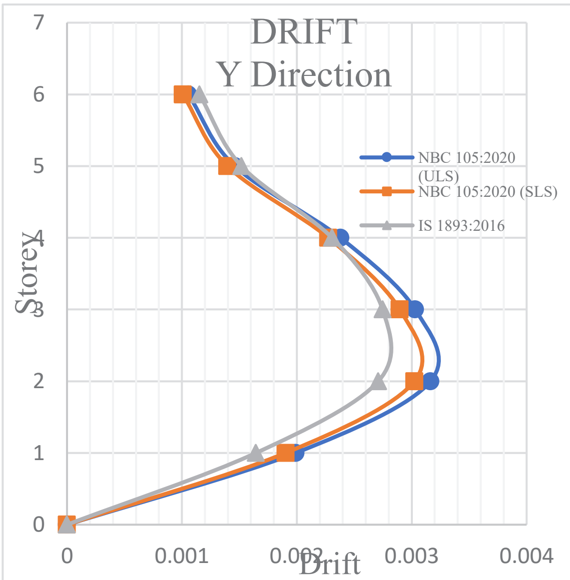


**Figure 19:** Inter Story Drift in X- Direction of E- Shaped Building

The comparison of storey drift at the 2nd storey shows that the values obtained from NBC are higher than IS code for all building configurations in both directions. In the X-direction, the Regular building shows drift higher in NBC by 18%, while the L-shaped building shows an increase of 15%. Similarly, the C-shaped and E-shaped buildings show higher drift values in NBC by 16% each. In the Y-direction, the Regular building again shows the highest difference where NBC gives 19% higher drift than IS code. The L-shaped building shows 16% higher drift, and the C-shaped and E-shaped buildings also show 16% higher drift compared to IS code. From the above comparison, it is clear that NBC consistently produces higher maximum storey drift values than IS code, with differences ranging from 15% to 19% in the X-direction and 16% to 19% in the Y-direction for both regular and irregular building configurations.

**The torsion graphs are compared and illustrated as:**

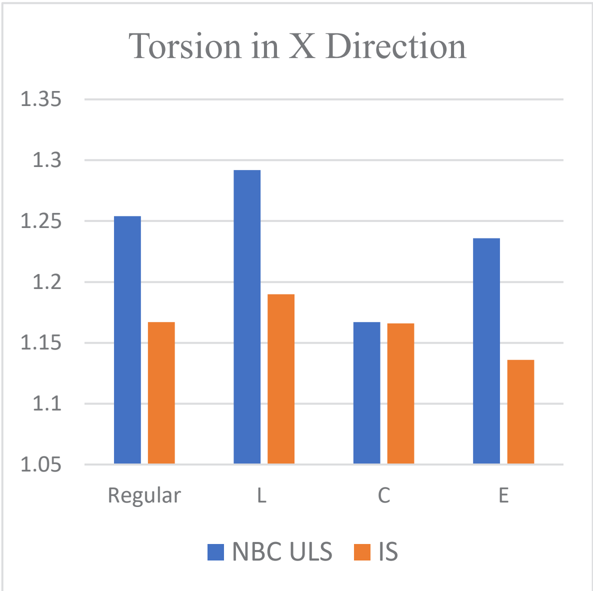


**Figure 20:** Maximum torsion in EQX

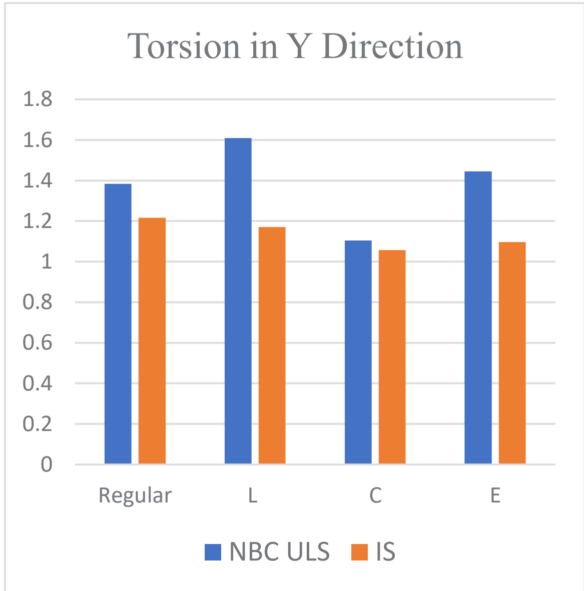


**Figure 21:** Maximum torsion in EQY

**Table 5**: Torsion comparison in X direction

| Buildings | Remarks (Torsion in X Direction) |
|---|---|
| Regular | Higher in NBC by 8% |
| L | Higher in NBC by 9% |
| C | Higher in NBC by 1% |
| E | Higher in NBC by 9% |

**Table 6**: Torsion comparison in Y direction

| Buildings | Remarks (Torsion in Y Direction) |
|---|---|
| Regular | Higher in NBC by 13% |
| L | Higher in NBC by 32% |
| C | Higher in NBC by 5% |
| E | Higher in NBC by 28% |

The NBC code predicts higher torsional response in irregular building shapes such as L, C, and E configurations compared to the IS code. This increased torsional effect is mainly due to the stricter eccentricity provisions specified in NBC, which consider greater accidental eccentricity in the analysis. Furthermore, the lower Response Reduction Factor (R) adopted in NBC results in higher design seismic forces, which consequently increases the torsional response of the structure.

The Comparison Graph of Maximum Percentage of reinforcement in Column

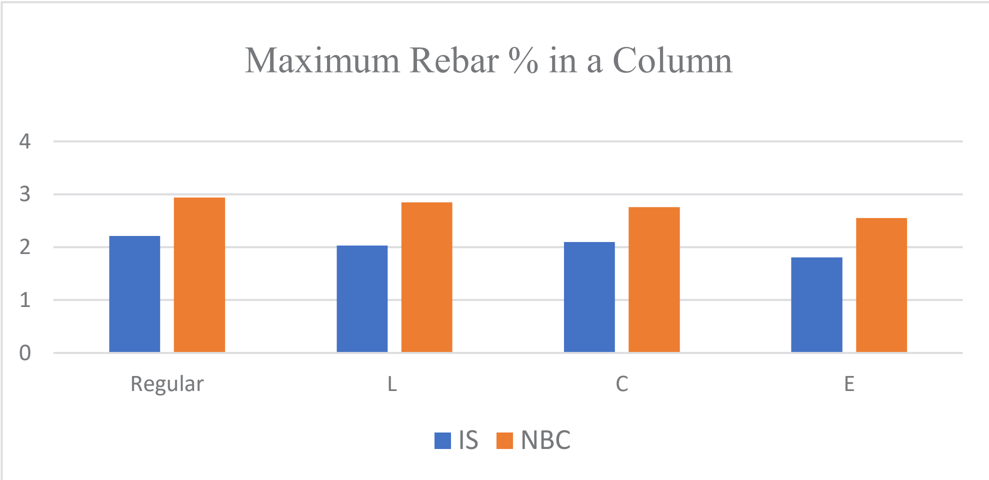


**Figure 22:** maximum percentage of reinforcement in column

NBC requires up to 20% higher reinforcement than the IS code, which increases construction cost but ensures a safer and more earthquake-resistant structural design.

Discussions:

This research compares the seismic performance of buildings using two codes: NBC 105:2020 and IS 1893:2016. Both codes have different rules for handling horizontal irregularities like L, U and C shaped buildings. These irregular shapes affect how buildings behave during earthquakes. The discussion focusses on how the results differ between two codes in terms of drift, displacement and torsion. The seismic responses of irregular buildings vary under NBC 105:2020 and IS 1893:2016 due to differences in key parameters such as seismic zoning factor, response reduction factor, importance factor, and base shear calculation method.

1. NBC 105:2020 uses Peak Ground Acceleration (PGA) values derived from Probabilistic Seismic Hazard Analysis (PSHA), which results in higher seismic demand in regions with greater seismic risk. In contrast, IS 1893:2016 uses a zone factor (Z) based primarily on historical seismic data, which may lead to comparatively lower seismic design forces. As a result, NBC generally produces higher base shear, displacement, and storey drift values compared to IS code, leading to a more conservative seismic design approach.

2. In NBC, the Response Reduction Factor (R) for Special Moment Resisting Frame (SMRF) is taken as 4.0, whereas in IS 1893:2016, the value of R for SMRF is 5.0. A higher value of R reduces the design seismic force, as it assumes greater capacity of the structure to undergo inelastic deformation during earthquakes. Due to the higher R value in IS, the design seismic forces are generally lower, which may lead to lighter and more flexible structural members. In contrast, the lower R value in NBC results in higher design forces, leading to stronger and relatively stiffer structural members with lower ductility demand, and less emphasis on ductile

detailing. The elastic properties like Young's modulus remain unchanged, but the structural behaviour shifts between elastic and inelastic depending on R.

3. The NBC 105:2020 considers 30% of live load for seismic weight under the category live load for other purposes, which applies to our building type. IS 1893:2016 considers 25% of live load for seismic weight when the live load is less than or equal to 3 KN/m², which also the case for our structure. A higher seismic weight leads to a higher base shear. As a result, the NBC generally predicts greater seismic forces, making the design safer but more conservative compared to the IS. This difference, though small (only 5%), can influence member sizing, reinforcement, and overall cost.

4. For torsional Criteria NBC uses stricter limits for allowable torsion ratio (Dmax/Davg > 1.5) to define irregularity. IS allows a slightly more relaxed criterion. In the range 1.5-2.0, (a) the building configuration shall be be revised to ensure that the natural period of the fundamental torsional mode of oscillation shall be smaller than those of the first two translational modes along each of the principal plan directions, and then (b) three-dimensional dynamic analysis method shall be adopted and more than 2.0, the building configuration shall be revised. As a result, IS flags torsional irregularity more aggressively, while NBC gives a more realistic response based on true building geometry. So, it requires heavier design in IS; NBC allows more efficient design but only if torsion is within limits.

5. Regarding eccentricity NBC considers a fixed accidental eccentricity of ±0.1b (10% of building width perpendicular to seismic force direction). It doesn't include or amplify the static eccentricity (actual offset between centre of mass and centre of rigidity). IS considers design eccentricity= 1.5× static eccentricity ±0.05b. it accounts for both actual torsional irregularity and accidental uncertainty. IS is more conservative, leading to higher torsional moments and safer design, especially for irregular buildings. NBC may underestimate torsion, which could lead to less safe design in buildings with significant asymmetry.

**4. Conclusions**

The reasons why these differences matter are stated as:

- Base Shear directly influences the total lateral force; higher base shear causes higher drift and displacement.

- The comparison of base shear values indicates that the NBC (National Building Code) produces higher base shear values for all building configurations compared to the Indian Code, leading to potentially safer structural designs but less economic.
- The Base shear of Regular-shaped building shows the highest difference, where the NBC value is 26.5% greater. Similarly, the L-shaped, C-shaped, and E-shaped buildings show increases of 19.92%, 24.78%, and 23.48%, respectively.
- Overall, NBC 105:2020, requires a higher percentage of longitudinal rebar than IS 1893: 2016 in structural members.

- Torsion becomes critical in irregular buildings where mass and stiffness are not symmetrically distributed; stricter torsion checks in NBC mean it catches irregular behavior earlier.
- The NBC code assumes a 10% accidental eccentricity compared to 5% in the IS code, resulting in higher torsional forces in structural design.
- The comparison of results in both X and Y directions shows that the values obtained using NBC provisions are higher for all building configurations. In the X direction, the Regular and C-shaped buildings show the highest increase of 21%, followed by the E-shaped building (15%) and the L-shaped building (10%).
- Drift affects structural safety and serviceability and NBC tends to produce higher drift values than IS code due to higher input forces, with differences ranging from 15% to 19% in the X-direction and 16% to 19% in the Y-direction for both regular and irregular building configurations.

**References**

•Agarwal, P. K., & Shrikhande, M. (2008). Earthquake resistant design of structures (5. Pr). Prentice-Hall of India Pvt. Ltd.

•Adhikari, R. and Poudel, M., 2023. Comparative study on seismic performance of RC buildings using IS 1893:2016 and NBC 105:2020.

•Banjara, R., Thapa, D., Katuwal, T. and Adhikari, S., 2023. Seismic behaviour of buildings as per NBC 105:1994, NBC 105:2020 and IS 1893:2016. 10th IOE Graduate Conference

•Department of Urban Development and Building Construction, 2020. NBC 105:2020 Nepal National Building Code for Seismic Design of Buildings in Nepal: Commentary. Kathmandu: DUDBC.

•Department of Urban Development and Building Construction, 2015. NBC 206:2015 Architectural Design Requirements. Kathmandu: DUDBC.

•Dhital, S.and Rathore, Y., 2022. Torsional irregularities in mass-variant RC frames under IS and NBC codes. International Journal of Structural Research, 6(3), pp.118-127.

•Duggal, S. K. (2007). Earthquake Resistant Design of Structures, Oxford University Press.

•Hampshire, S., Santos, D.C., and Giarlelis, C., 2018. Comparative study of some seismic codes for building design regarding criteria for non-linear methods of analysis. 16th Edition Earthquake Engineering, Federal University of Rio de Janeiro, June 21.

•Gyawcha, A., Karki, P. and Neupane, M., 2024. Seismic response comparison of G+8 RC building using IS 1893:2002, NBC 105:1994 and NBC 105:2020. Nepal Journal of Civil Engineering, 9(1), pp.22–31.

•IS 456:2000, Indian Standard Code of Practice for Plain and Reinforced Cement Concrete, 4th revision, Bureau of Indian Standards, New Delhi.

- IS 875 (Part 1): 1987, Indian Standard Code of Practice for Design Loads (Other than Earthquake) for Buildings and Structures - Part 1: Dead Loads, Bureau of Indian Standards, New Delhi.

- IS 875 (Part 2): 1987, Indian Standard Code of Practice for Design Loads (Other than Earthquake) for Buildings and Structures - Part 2: Imposed Loads, Bureau of Indian Standards, New Delhi.

- IS 13920:2016, Indian Standard Code of Practice for Ductile Detailing of Reinforced Concrete Structures Subjected to Seismic Forces, Bureau of Indian Standards, New Delhi.

- IS 1893 (Part 1): 2016, Criteria for Earthquake Resistant Design of Structures - Part 1: General Provisions and Buildings, 6th revision, Bureau of Indian Standards, New Delhi.

- Ghimire, K. and Ranabhat Sudip, A comparative study of middle rise apartment building with different seismic codes, Pokhara Engineering College Journal (PECJ) Applied Sciences and Engineering Insights ISSN: 3021-9795 (Print) / 3059-9628 (Online) (Volume-2, Issue II)

- Ghimire, K. and Chaulagain, H., 2021. Influence of structural irregularities on seismic performance of RC frame buildings. *Journal of Engineering Issues and Solutions*, 44, pp.71-88.

- NBC 105:2020, Nepal National Building Code for Seismic Design of Buildings in Nepal: Commentary, Department of Urban Development and Building Construction.

- NBC 206:2015, Architectural Design Requirements, Department of Urban Development and Building Construction, Kathmandu.

- Pandit, K., 2023. High-rise RC building performance on various soil types using IS 1893 and NBC 105:2020. In: Proceedings of the 9th National Earthquake Engineering Conference. Kathmandu, Nepal.

- Pokharel, S., Shrestha, B. and Thapa, D., 2023. Response spectrum analysis of low-rise RC buildings under IS 1893:2016 and NBC 105:2020. Structural Engineering Review, 11(2), pp.55–64

- Punmia, B. C., Jain, A. K., & Jain, A. K. (2019). Limit State Design of Reinforced Concrete, Laxmi Publications Pvt. Ltd.

- Subramanian, N. (2013). Design of reinforced concrete structures, Oxford University

- SP 16 – 1980, Design Aids for Reinforced Concrete To IS: 456-L 978, Bureau of Indian Standards, New Delhi.

- SP 22 – 1982, Explanations on IS: 1893-1975 Criteria for Earthquake Resistant Design of Structures, Third Revision, Bureau of Indian Standards, New Delhi.

- SP 34(S & T) – 1987, Handbook on Concrete Reinforcement and Detailing, Bureau of Indian Standards, New Delhi.

Pokhara Engineering College Journal (PECJ)
*Applied Sciences and Engineering Insights*

ISSN: 3021-9795 (Print) / 3059-9628 (Online)
(Volume-3, Issue- I)

# Dynamics of Air Pollution and its Dispersion in a Topographically Constrained Urban Area: A Case Study of Kathmandu Valley

Rajib Pokhrel[1*]

[1] *School of Engineering, Faculty of Science and Technology, Pokhara University, Nepal*

**Corresponding email: rajibp@pu.edu.np*



*Received:10- February-2026; Revised: 28- February-2026; Accepted: 20- March-2026*
*DOI: https://doi.org/10.3126/pecj.v3i1.93523*

## Abstract

Kathmandu, one of the world's prominent cultural and touristic cities, has undergone rapid urbanization over recent decades, creating substantial challenges for environmental quality management amid accelerating population growth and infrastructure development. This study examines the meteorological characteristics, ambient air quality, and pollutant dispersion mechanisms in the Kathmandu Valley through an integrated analysis of primary observations, secondary datasets, and numerical simulations. Meteorological and air quality data from multiple monitoring stations indicate strong seasonal variability, with daily mean temperatures ranging from approximately 10 °C to 24 °C. Higher wind speeds (~6 m/s) prevail in spring and summer, while calm winds dominate autumn and winter, accounting for more than 50% of observations. Particulate matter concentrations frequently exceed guideline levels, with PM10 surpassing 100 µg/m³ and PM2.5 reaching up to 80 µg/m³, particularly during winter, when pollution levels are more than twice those observed in spring and autumn. Monsoonal rainfall significantly suppresses particulate concentrations during summer. Source characterization highlights the predominance of soil-based dust, which accounts for over 60% of non-ionic components and approximately 25% of PM10, alongside a relatively high black carbon fraction (~17%). Numerical simulations reveal a pronounced diurnal mountain–valley breeze system, with mountain breezes dominating at night and valley breezes prevailing during the day. Stronger north–south airflow governs pollutant transport, causing emissions from the northern and central Valley to disperse widely, while pollutants originating from southern and southeastern sources exhibit limited penetration into the urban core.

**Keywords:** *Meteorology; Mountain/Valley Breeze; Air Pollution; Dispersion Model, UHI*

## 1. Introduction

Kathmandu Valley comprises three administrative districts and covers an area of 933.73 km², accommodating approximately 3 million inhabitants according to the Central Bureau of Statistics (CBS, 2021). Over the past three decades, the Valley has experienced rapid population growth, extensive spatial expansion, and intense urban densification. Collectively, the three districts of Kathmandu Valley exhibit an average population density of approximately 97 persons per km²; however, Kathmandu Metropolitan City alone records an exceptionally high density of about 13,225 persons per km². The annual population growth rate in the Valley exceeded 4.5%, significantly surpassing the national average growth rate of approximately 2.5% during the same period (Central Bureau of Statistics, Nepal, 2001). This accelerated urbanization has posed substantial challenges to environmental management, particularly in maintaining air quality and overall environmental health. According to reports by the World Health Organization (WHO), Kathmandu Valley is among the most polluted urban areas in Asia, with persistently high levels of air pollution arising from road dust, vehicular emissions, brick kilns, and other airborne particulate sources throughout the year.


(a) Geographic location of Nepal (b) Top view of Kathmandu Valley

**Figure 1:** The geographic location of the Kathmandu Valley in Nepal.

The air quality of the Valley was improved in 2003, and it was aggravated again in 2005. There was a slight improvement in air quality in 2006, but it has been steadily worsening since 2007 (Chaudhari, 2010). Dust particles, oxides of nitrogen (NOx), carbon monoxide (CO), sulfur oxides (SOx), Hydrocarbons (HCs), benzenes, etc., are the major pollutants in the valley air (Panday et al., 2009). The increased exposure to PM10 is associated with various adverse health effects, such as respiratory diseases, cardiovascular mortality, morbidity, and probably malignant lung diseases (Goldberg et al., 2006; Chang et al., 2005; Kan et al., 2003; Donaldson et al., 2001). Fine particulate matter is mostly generated from vehicle emissions, and the secondary pollution aggravates the atmospheric visibility by scattering or absorbing the visible light (Pokhrel et al., 2011, and Pokhrel et al., 2021). Similarly, the gaseous pollutants in the air cause severe physical environmental and health effects (Panday et al., 2009). In addition, the inversion height is below the surrounding mountains, and it plays a role like a lid for the Valley air, mostly in the winter season when the air pollution is accumulated in the confined boundary, and the air quality is aggravated further (Pudasainee et al., 2010; Sapkota, 2002; Sharma, 1997).

A large number of vehicles, brick kiln factories, concrete gridding factories, etc., are the major sources of air pollution in the Kathmandu valley. The brick kiln industry is one of the major air pollution sources, where brick is one of the major construction materials in the valley and its neighboring areas (Pokhrel and Lee, 2014). The total production of 350 million bricks was the major single source of sulfur dioxide and suspended particulate matter in the valley. It contributes over 60% of emissions and is responsible for the 31% of TSP (Total Suspended Particle) and 28 % of PM10 (Tuladhar et al., 2002; World Bank, 1997; Shrestha et al., 1996). Although it has a significant contribution to the valley air pollution, there is a lack of emission inventory data from each stage of brick production. Moreover, large numbers of construction works have been running around the valley area, which has also become one of the major emission sources.

(a) Satdobato – 30 Nov. 2016 (b) Road side dust at Chakrapath (C) Stack Emission

**Figure 2:** Air pollution situation and major sources in the Valley

## 2. Air Dispersion Model

Modeling technique is an essential tool for atmospheric environmental studies together with observational data. Models are divided into two types: physical and mathematical. The physical model is a small-scale, laboratory representation of the phenomena, and the mathematical model is the set of analytical/numerical algorithms addressing the physical and numerical aspects of the problems. Based on the quantitative and qualitative studies, the mathematical models are categorized into deterministic and statistical models. The deterministic models are based on fundamental mathematical descriptions of atmospheric processes, whereas the statistical models are based on semi-empirical statistical relations among available data and measurements.

For calculating the specific value of output based on certain input data, deterministic models are used. The statistical models are generally used to forecast or estimate the values by using statistical functions and the measurement values. In the case of atmospheric environmental studies, a large number of meteorological models and air pollution diffusion/dispersion models have been developed using different mathematical models. Various analytical models have been introduced to calculate the exact analytical solutions using mathematical formulas and observational data. In addition, the mathematical models can be numerical models, where the approximate numerical solutions are attained using numerical integration techniques. With the introduction of computer applications for scientific studies, numerical simulations based on mathematical models have been widely introduced since the 1970s. Later, the simulations are updated and the results are validated with observational data. Then the numerical simulation methods have been one of the most popular techniques for environmental forecasting, air pollution estimation, environmental impact assessment studies, etc. since few decades.

**2.1. Gaussian approach**

In 1991, the American Meteorological Society (AMS) and the U.S. Environmental Protection Agency (EPA) initiated a formal collaboration with the designed goal of introducing current planetary boundary layer (PBL) concepts into regulatory dispersion models. A working group (AMS/EPA Regulatory Model Improvement Committee, AERMIC) comprised of AMS and EPA scientists was organized for the collaborative effort. In most air quality applications, one is concerned with dispersion in the PBL, the turbulent air layer close to the earth's surface is controlled by the surface heating and friction and the overlying stratification. The PBL typically ranges from a few hundred meters in depth during nighttime to 1 – 2 km during daytime. Major developments in understanding the PBL began in the 1970's through numerical modeling, field observations, and laboratory simulations (Wyngaard, 1988). For the convective boundary layer (CBL), a milestone was Deardorff's (1972) numerical simulations, which revealed the CBL's vertical structure and important turbulence scales. Major insights into dispersion followed from laboratory experiments, numerical simulations, and field observations are described in Briggs (1988), Lamb (1982), and Weil (1988a).

In February 1991, the U.S. EPA, in conjunction with the AMS, held a workshop for state and EPA regional meteorologists on the parameterization of PBL turbulence and the state-of-the-art dispersion modeling. One of the outcomes of the workshop was the formation of AERMIC, and the major purpose of the AERMIC activity was to build upon the earlier model developments and to provide a state-of-the-art dispersion model for regulatory applications.

The early efforts of the AERMIC group were described by Weil (1992). The new model developed by AERMIC was aimed at short-range dispersion from stationary industrial sources, the same scenario handled by the EPA Industrial Source Complex Model, ISC3 (U.S. Environmental Protection Agency 1995). In addition, AERMIC selected the EPA's ISC3 Model for a major overhaul and the AERMIC's objective was to develop a complete replacement for ISC3 by (1) adopting ISC3's input/output computer architecture; (2) updating, where practical, antiquated ISC3 model algorithms with newly developed or current state-of-the-art modeling techniques; and (3) insuring that the source and atmospheric processes presently modeled by ISC3 will continue to be handled by the AERMIC Model (AERMOD) (EPA, 2002).

AERMOD currently contains new or improved algorithms for (1) dispersion in both the convective and stable boundary layers; (2) plume rise and buoyancy ; (3) plume penetration into elevated inversions; (4) computation of vertical profiles of wind, turbulence, and temperature; (5) the urban nighttime boundary layer; (6) the treatment of receptors on all types of terrain from the surface up to and above the plume height; (7) the treatment of building wake effects; (8) an improved approach for characterizing the fundamental boundary layer parameters; and (9) the treatment of plume meander (EPA, 2002).

AERMOD is a steady-state plume model. In a stable boundary layer (SBL), it assumes the concentration distribution to be Gaussian in both the vertical and horizontal. In the convective boundary layer (CBL), the horizontal distribution is also assumed to be Gaussian, but the vertical distribution is described with a bi-Gaussian probability density function (pdf). This behavior of the concentration distribution in the CBL was demonstrated by Willis and Deardorff (1981) and Briggs (1993). Additionally, in the CBL, AERMOD treats "plume lofting", whereby a portion of plume mass, released from a buoyancy source, rises to and remains near the top of the boundary layer before becoming mixed into the CBL.

**2.2. Lagrangian approach**

A2C (Atmospheric to Computational fluid dynamics) flow and A2C t&d (transport &diffusion) are the updated versions of HOTMAC and RAPTAD, respectively. The basic equations of HOTMAC for mean wind, temperature, mixing ratio of water vapor, and turbulence are similar to those used by Yamada (1981, 1985). It has the addition of nested grid capability and the effect of shadows produced by terrain. The terrain vertical coordinate system is used in this model in order to increase the accuracy in the treatment of surface boundary conditions.

$$z^* = \overline{H}\frac{z - z_g}{H - z_g} \qquad (1)$$

Where z* and z are the transformed and Cartesian vertical coordinates, respectively; zg is ground elevation; the material surface top of the model in the z* coordinate; and H, the corresponding height in the z - coordinate. The governing equations following the coordinate transformation are explained in Yamada 1978, 1981, Yamada et al., 1988, Yamada, 1999 and 2003. Puff concentration distributions are assumed in different forms, and one of the simplest ways is to assume a Gaussian distribution where variances are determined as the time integration of the velocity variances encountered over the history of the puff. The concentration level at a given time and place is calculated as the sum of the concentrations from each puff (Yamada, 1999). Concentration C at (X, Y, Z) is computed by using equation (2).

$$C(X,Y,Z) = \frac{Q\Delta t}{(2\pi)^{3/2}}\sum_{k=1}^{N}\frac{1}{\sigma_{xk}\sigma_{yk}\sigma_{zk}}\exp\left[-\frac{1}{2}\frac{(x_k - X)^2}{\sigma_{xk}^2}\right]\times\exp\left[-\frac{1}{2}\frac{(y_k - Y)^2}{\sigma_{yk}^2}\right]$$
$$\times\left\{\exp\left[-\frac{1}{2}\frac{(y_k - Y)^2}{\sigma_{yk}^2}\right] + \exp\left[-\frac{1}{2}\frac{(z_k + Z - 2z_g)^2}{\sigma_{zk}^2}\right]\right\} \qquad (2)$$

Where $(x_k, y_k, z_k)$ is the location of the $k^{\text{th}}$ puff, $\sigma_{xk}$, $\sigma_{yk}$ and $\sigma_{zk}$ are the standard deviations of a Gaussian distribution, and $z_g$ is the ground elevation. A brief description of the RAPTAD model was reported in detail by Yamada et al. (1988) and Yamada (1998, 1999). The concept has already been introduced for analyzing the air flow dynamics in Pokhara Valley (Pokhrel, 2025), which shows that this algorithm can be useful for further study in the Kathmandu Valley too.

## 3. Methodology

### 3.1. Study site

Kathmandu, located between 27º37’30” N and 27º45’0” N Latitude and 85º15’0” E and 85º22’30” E Longitude, is about 1500 m above sea level and covers about 340 km$^2$. The cross-section of the Kathmandu valley is about 20 km north-to-south and 30 km east-to-west. Kathmandu valley has a bowl-like shape surrounded by four major mountains, namely Shivapuri, Phulchowki, Nagarjun, and Chandragiri at an elevation of approximately 1400 m from its base.

Four distinct seasons, viz. spring, summer, autumn, and winter, are observed in the Kathmandu valley. During the course of study, the temperature of the valley varied from 5°C to 32°C, and dry air with low temperature was frequently observed during the winter season, whereas high humidity (more than 90%) and hot weather were observed in the summer season.


**Figure 3:** Study domain covering the central, residential/agricultural area and the surrounding high hills.

### 3.2. Research framework

The local climate of the Kathmandu valley is typical, as it is surrounded by the high hills. Most of the urban land is covered with built-up area and fine sandy soil, which can easily be blown by the wind, covering the top of the land surface. Air pollution, especially particulate matter (PM) dispersion pattern from the point/area source in the valley, has been studied. Meteorological data were collected from the Department of Hydrology and Meteorology. Surface topography and landuse data of 30" resolution were retrieved from USGS data. Major data and tools used in this study are summarized in the Figure 4.

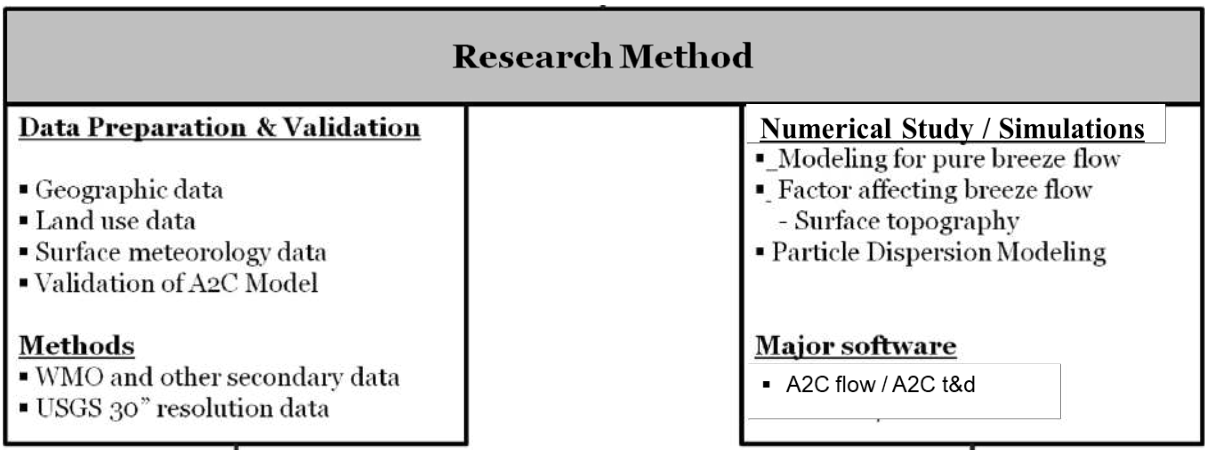


**Figure 5:** Summary of the research methods.

### 3.3. Data collection

Meteorological data were obtained from established monitoring stations located at Tribhuvan International Airport (TIA) and Babarmahal, Kathmandu. As the TIA station records wind speed only and lacks wind direction measurements, wind data from the Babarmahal station were utilized to characterize airflow patterns through the construction of wind rose diagrams. Ambient air quality data, specifically PM10 and PM2.5 concentrations, were collected from a network of existing monitoring stations, including Ratnapark, Phora Durbar (U.S. Embassy), Pulchowk, Bhaisipati, U.S. Embassy (Kathmandu), Shankapark, and Birendra School (Bhaktapur). Hourly averaged data spanning an entire year were compiled to examine both monthly and seasonal variations in air quality across the Kathmandu Valley. In addition, supplementary information from published secondary sources was consulted to define model boundary conditions and to support the interpretation of meteorological and air quality characteristics of the Valley. High-resolution topographic and land-use datasets (USGS 30”) were employed as input for numerical modeling. Airflow dynamics and pollutant dispersion were simulated using a Lagrangian modeling framework (A2C Flow/t&d).

### 3.4 Air flow dynamics and dispersion modeling

Kathmandu Valley, characterized by its enclosed, basin-like topography, experiences persistently elevated levels of air pollution, with particularly high concentrations of particulate matter (PM) in the ambient atmosphere throughout the year. A comprehensive understanding of pollutant types, emission sources, and dispersion processes constitutes a fundamental prerequisite for the development of effective air quality management strategies. Previous studies have identified mobile sources, notably vehicular emissions; point sources, including brick kilns, cement and grinding industries, and commercial establishments; and area sources, such as forest fires and agricultural activities in surrounding regions, as the dominant contributors to air pollution in the Valley. Local meteorological conditions, especially airflow dynamics governed by valley - mountain circulation, play a critical role in the transport, accumulation, and dispersion of atmospheric pollutants within the study area. To simulate local airflow patterns and pollutant (puff) dispersion within the modeling domain, this study employs the Atmospheric to Computational Fluid Dynamics (A2C) Flow model coupled with the A2C Transport and Diffusion (A2C t&d) framework. Pollutants are treated as non-reactive primary species, and atmospheric chemical transformation processes occurring during transport and diffusion are not considered in this mesoscale simulation.

The modeling domain (84°35" E, 27°03" N to 86°10" E, 28°12" N) was set using the USGS 30" resolution topographic and land use data. It covers Kathmandu valley and its nearby mountains, as in Figure 5. The outer domain covers 150 km × 129 km with a grid resolution of 3 km, the interim domain covers 75 km × 75 km with a grid resolution of 1.5 km, and the innermost domain 33 km × 33 km with a grid resolution of 500 m.

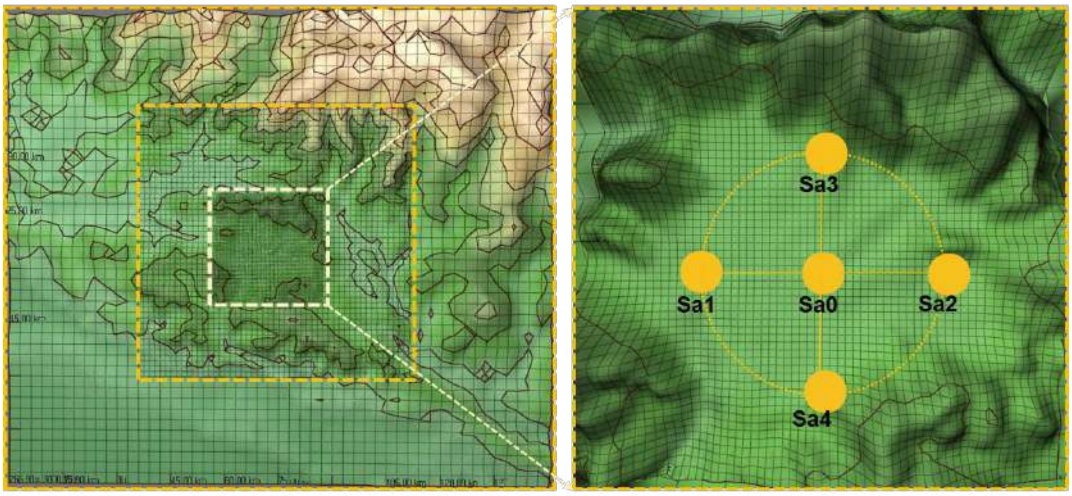


**Figure 5:** Modeling the domain in the inner grid shows the core Kathmandu Valley and its surroundings, respectively.

Modeling cases were designed by considering the local meteorological conditions, avoiding the external driving effect, such as the monsoon. 60-70 % of annual rainfalls occur during the monsoon season when external wind (monsoon wind) dominates the local wind. Modeling cases are designed at (a) Spring season – Pre-monsoon period, and (b) With the modification of landuse change for analyzing the UHI effects. Corresponding meteorological information has been used for setting the initial and boundary conditions.

### 3.4.1. Air flow dynamics and dispersion modeling – case study of spring season

The modeling period selected included mid-spring, i.e., April (Julian day 105 - 111), before the monsoon season when the effect of external wind is minimum in the study region. The potential temperature (298 K) and reference pressure (1013 mb) were referred based on the meteorology data monitored at the airport, and the inversion height (700 m) was referred from the literature (Regmi et al., 2003). The initial wind speed (0 m/s) was set by considering the pure breeze and the rest of the parameters were set as default suggested in the manual (HOTMAC® and RAPTAD® 7.8; Yamada Science & Art Corporation). In addition, the puff sources (Sa0, Sa1, Sa2, Sa3 and Sa4) were set at the center, east, west, north and south part of the internal modeling domain (in the Kathmandu Valley) where Sa0 is located in-between Ratnapark and Dillibazaar (27.709N, 85.326E), Sa1 is located in Tahachal near to Chakrapath (27.702N, 85.282E), Sa2 is located at Bhaktapur area (27.6643N, 85.4460E), Sa3 is located at north part of the Valley (27.7469N, 85.335E) near to Narayan Gopal Chowk and Sa4 is located near to Sunakothi Lalitpur (27.632N, 85.3227E) as in the Figure 5. Elevation of all the puff sources was set 10 m above the surface, and the puff emission option was set continuous with the emission rate of 1 g/s. Moreover, the nudging option was set active to minimize the effect of initial and boundary conditions, and the earth rotation was set active by considering the solar angle and the gravity effect on air flow.


**Figure 6:** Geographic position of puff sources in Google Map.

3.4.2. Impact of landuse change on local breeze flow

With the urbanization, the landuse pattern of the Kathmandu Valley has been changing rapidly. The fertile irrigated cropped land has been changed to a built-up area where the surface characteristics, such as roughness coefficient, albedo, soil moisture, surface specific heat capacity, anthropogenic heat, etc., may be changed. The variation of surface characteristics may change the air flow and air dispersion characteristics of the valley; therefore three cases were simulated in the study by considering irrigated crop landuse, mixed landuse and urban landuse. The surface characteristics were set based on the value suggested from the manual, based on USGS data, and the innermost domain covering the valley basin only. Further simulation was carried out by setting the boundary condition to the same as in the case study of the spring season.

**Table 1:** Parameters affecting the local air flow.

| S.N. | Landuse Type | Anthropogenic Heat ($W/m^2$) | Specific Heat (J/kgK) | Surface Albedo |
|---|---|---|---|---|
| 1 | USGS landuse (mixed) | 0 -50 | 800 – 4186 | 0.03 – 0.3 |
| 2 | Irrigated farm land | 0 | 3650 | 0.2 |
| 3 | Urban land | 50 | 879 | 0.15 |

*Source: USGS landuse data for Kathmandu Valley. The index values vary with the change of landuse type.*

Numerous studies were carried out to study the Urban Heat Island (UHI) in different parts of the world, where waste heat from the facilities plays an important role in the formation of UHI. The amount of additional anthropogenic heat in the landside proportionally increases with the rate of urbanization. There might exist a difference in thermal properties, especially in the landside before and after the period of urbanization. Moreover, thermodynamic properties (heating and cooling properties) are dependent on the specific heat capacity of the material. The landuse and land surface material vary with the level of urbanization and the trend of adopting the construction material. Therefore, the specific heat capacity and the surface moisture of the land surface are also modified as per the data mentioned in the table. The albedo of typical materials for the visible light range from 0.9 for fresh snow to 0.04 for charcoal. The albedo for an ideal black body reaches to zero. The albedo for most of the land area ranges from 0.1 to 0.4. According to the USGS landuse data, the albedo for irrigated farming land and urban land are 0.2 and 0.15, respectively.

## 4. Results and Discussion

### 4.1. Meteorology of the Kathmandu Valley

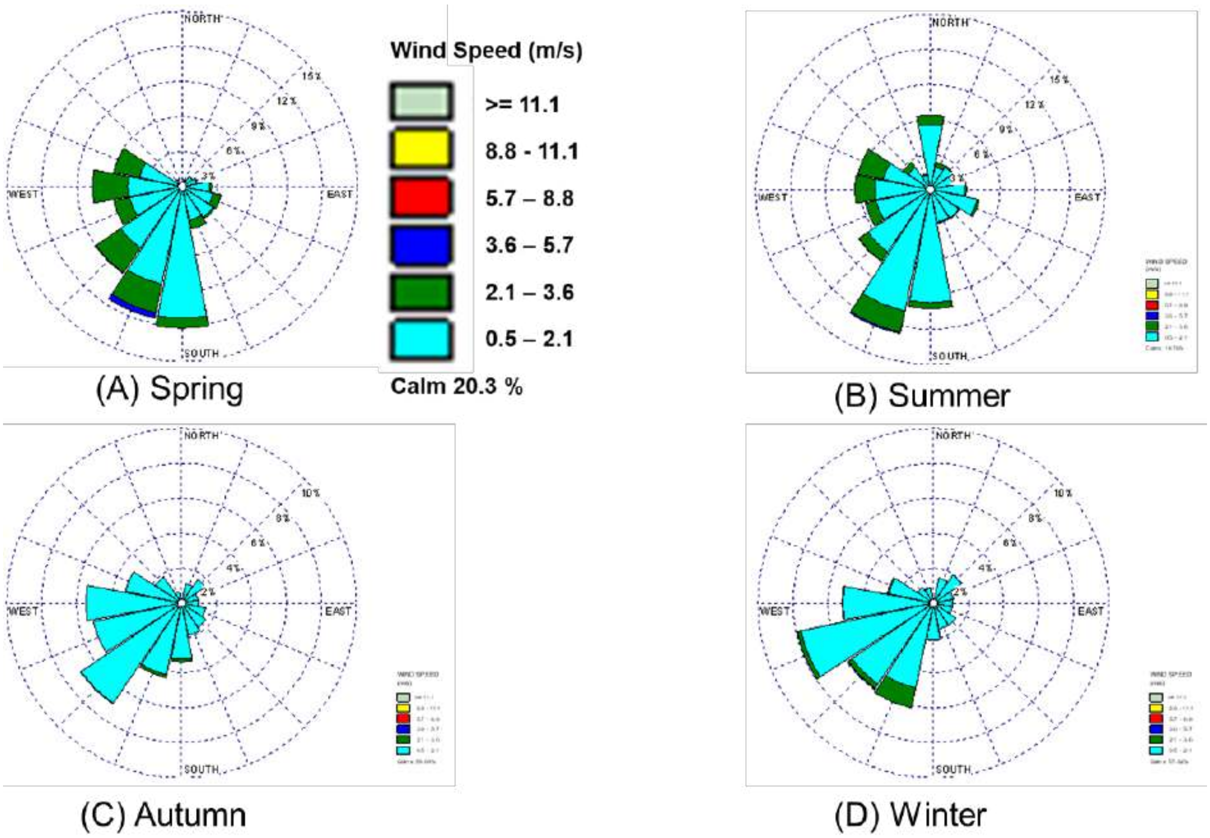


**Figure 7:** Windrose for the seasonal variation of wind speed and direction.

There are four distinct seasons in Kathmandu valley where the daily mean temperature varies from 10°C to 24°C. The highest temperature was recorded in the end of May to mid-June, and the lowest temperature was recorded in the month of January. Generally, the temperature of the valley varies from 2°C to 29°C, where winter is moderately cold and the rest of the seasons are cool. Approximately 1500 mm of rainfall has been recorded in the valley, where around 70% rain falls in the three months of the summer season, although there is a slight variation in each year. Moderately strong wind speeds (approximately 6 m/s) occur during the spring and summer seasons. Mostly, calm and moderately calm winds (wind speed of 0.5 m/s to 2.1 m/s) are evidenced during the autumn and winter, as shown in Figure 7. The lower temperature in the valley caused the formation of temperature inversion at the surface level, where the calm wind speed catalyzed the temperature inversion and caused accumulation of pollutants in a confined region.

### 4.2 Air quality of the Kathmandu Valley

Particulate matters such as PM10 and PM2.5, which have been monitored at Ratnapark, US-Embassy (Phora Durbar), Pulchowk, Bhaisipati, US-Embassy (Kathmandu), Shankhapark and Birendra School (Bhaktapur) were collected and analyzed to identify the monthly and seasonal variation of PM in the Kathmandu Valley, as in Figure 8. Due to the technical errors, there was PM10 data missing in the spring season, although the PM2.5 was recorded continuously. The data shows that the air pollution level was more than two times higher in the winter season (December, January, and February) than the spring season (March, April, and May) and the autumn season (September, October, and November). Moreover, the concentration of particulate matter was very low (both PM10 and PM2.5 were less than 20 μg/m$^3$) as in Figure 8. There was more than 70% rainfall in the summer season only. The frequent rain may wash out the dust from the atmosphere as well as wash out the re-suspended dust from the surface.

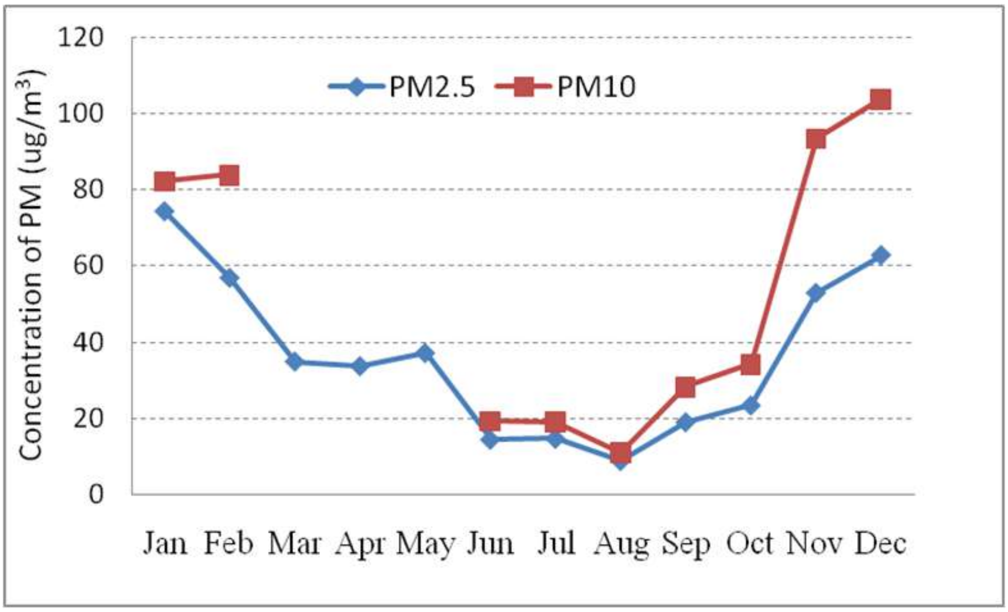


**Figure 8:** Monthly variation of the particulate matter in the Kathmandu Valley for the year 2018-2020.

### 4.3 Air flow/dispersion modeling

4.3.1.A Case study of the spring season

Mesoscale air flow/air dispersion modeling was carried out for the study area. Local air flow is generally produced due to the differential heating and cooling effect on the Earth's surface. In the Mountain / Valley area, a thermal circulation often develops due to the diurnal heating and cooling of the mountain slopes. Solar radiation warms the Mountain slopes or Valley walls, which in turn warms the air in contact with it; the heated air (being less dense than the air at the same elevation above the Valley floor) rises as an upslope wind and is called the valley wind. Due to the outgoing radiation during the night, the mountain slopes cool more quickly than the Valley floor. The air in contact with the slopes and up to a certain depth generally cools through conduction and turbulent mixing. This cooler air flows down the slope and is called a slope or a mountain wind (Arya, 1999). The Valley wind is particularly strong in the south-facing slopes; however, the Valley is surrounded by high mountains, with most of the Mountain slopes facing the midday Sun, therefore, a significant amount of Mountain and Valley winds are developed. The surface elevation in the domain varied widely; it ranged from 78 m to 6688 m (maximum surface elevation above sea level). The internal modeling domain covered the Kathmandu Valley with a base elevation of approximately 1350 m from sea level; whereas, the surrounding mountains were approximately 2825 m (Nagarjun) from sea level.

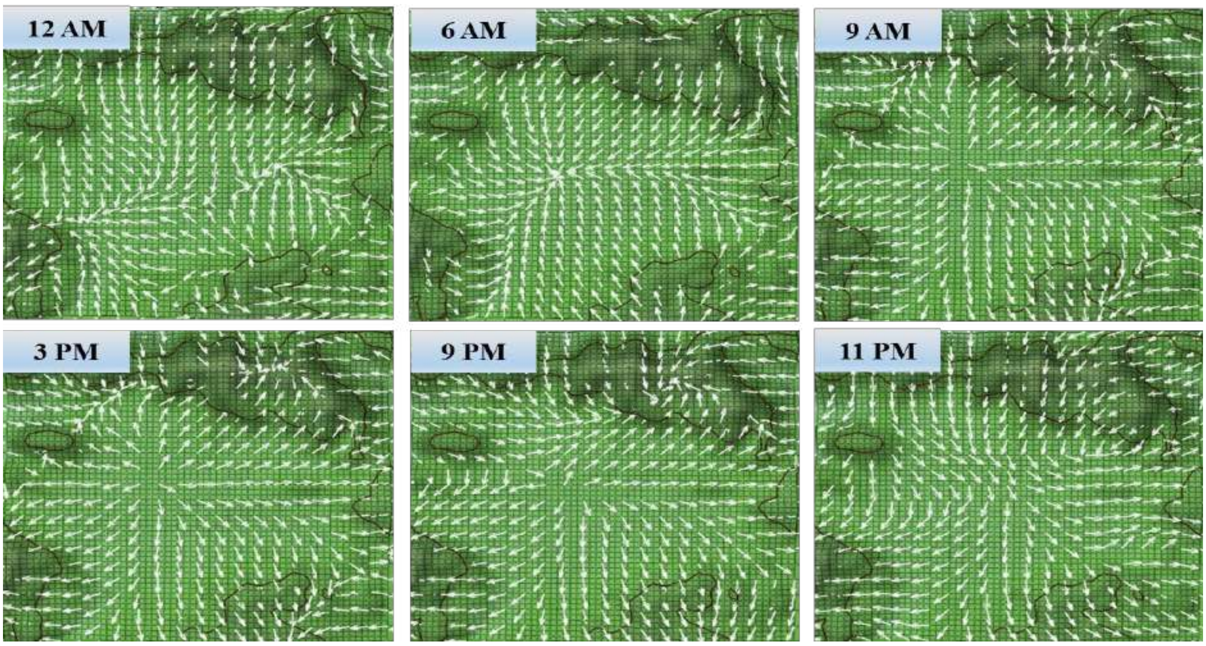


**Figure 9:** Wind flow vectors 10 m above the surface in the study domain at 12 AM, 6 AM, 9 AM, 3 PM, 9 PM and 11 PM.

Figure 9 shows the diurnal variation of the air flow vectors at different time intervals. Most of the Valley area was covered by the urban structure, and the mountain area was covered with the forest. After sunset, the mountain slopes released heat faster than the Valley surface, wherein the urbanization pattern and land-use type/material affect it and consequently influence on the airflow. Figure 9; 12 AM, 6 AM, and 11 PM show the breeze flow towards the Valley (Mountain breeze), while Figure 12; 9 AM, 3 PM, and 9 PM show the breeze flow towards the mountain slopes (Valley breeze). The momentum of the breeze and its direction varied with time and geographical location. It is known that the intensity of solar radiation as well as the surface emissivity is time-dependent; however, surface elevation, land-use parameters, meteorological parameters, etc., vary with location.

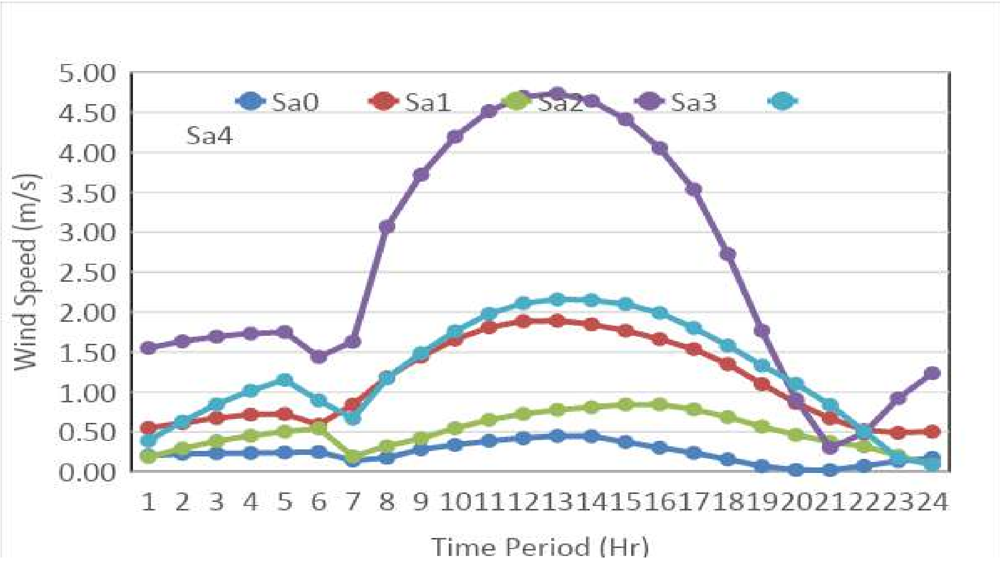


**Figure 10:** Diurnal variation of Mountain/Valley breeze at different sampling points; here the symbols represent as Sa0 (Ratnapark), Sa1 (Tahachal near to Ringroad), Sa2 (Bhaktapur), Sa3 (Near to Narayan Gopal Chowk) and Sa4 (Sunakothi, Lalitpur).

Figure 10 shows the diurnal variation of breeze flow for the monitoring points Sa0, Sa1, Sa2, Sa3, and Sa4. The momentum of the Valley breeze (up to 4.5 m/s) was more than double that of the mountain breeze (up to 1.8 m/s). Although the breeze momentum varies at different locations. With the decline of solar radiation in the evening, the breeze momentum reduced; it reached a calm condition around 9 PM. This could be referred to as a transition period. As the air pressure at the Valley surface became lower than the Mountain slopes, at around 11 PM, the Mountain breeze was generated; this Mountain breeze continued till 7 AM during the simulation period. The Mountain breeze gained maximum momentum just before sunrise, and it reached a transition stage between 7 and 8 AM. Due to the higher solar intensity, mountain slopes generally heat faster, and this in turn generates a significantly strong Valley breeze. Valley breeze gained maximum momentum at around 1 ~ 2 PM. The process repeats until the external air force or adverse climatic change does not occur.

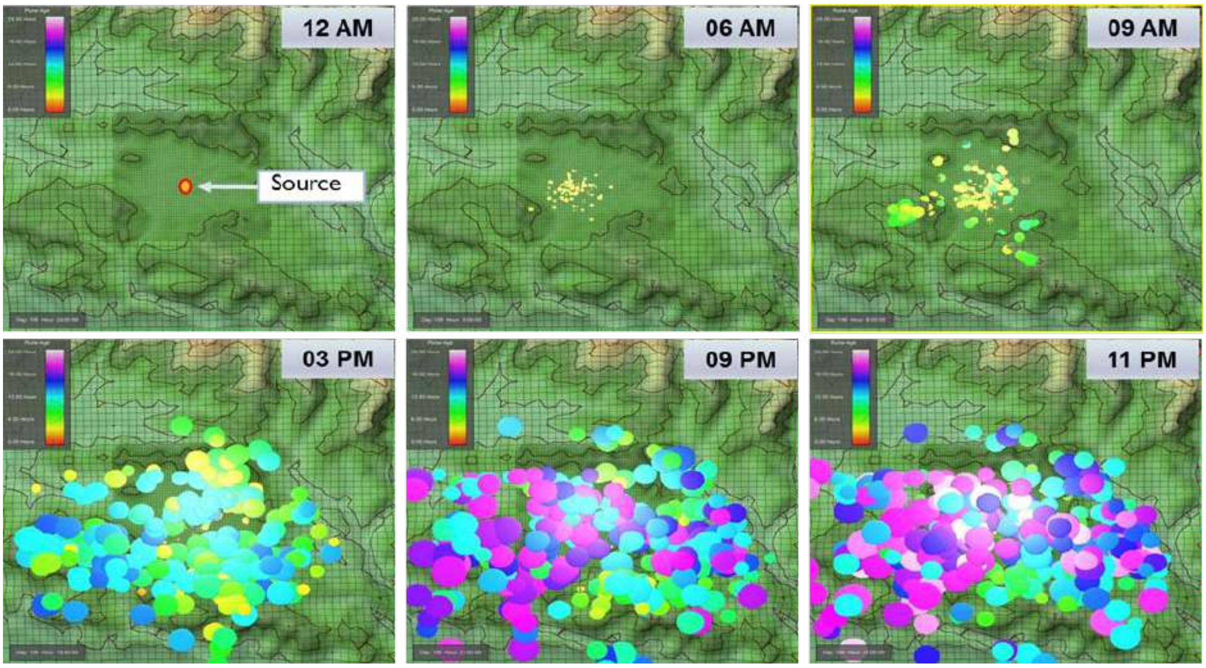


**Figure 11:** Puff dispersion mechanism from the point source in the Valley, wherein the puff source is at the central part of the Valley.

Puffs were emitted continuously from the point sources located at the central, eastern, southern, and northern parts of the Valley with a constant emission rate. Transport and dispersion mechanisms of the puffs from the point sources at different locations varied with the local air flow mechanism. The puffs emitted from the center of the Valley (southern part of KMC) disperse throughout the Valley; however, from midnight to early morning, the major portion of the puffs skewed towards the south-west direction, following the local air flow pattern as in Figure 11. The puffs emitted from the eastern part of the Valley were transported and dispersed in the eastern and south-eastern part of the Valley and its nearby mountain area (as in Figure 12). Similarly, the puffs emitted from the southern part of the Valley dispersed in the southern and south-eastern part of the Valley and its vicinity (as in Figure 13). Moreover, the puffs generated in the northern part of Metropolitan City were transported towards the valley area in the late night to the early morning, and it transported towards the uphill side in the daytime (as in Figure 14). The pollution transport and dispersion pattern in the Valley was affected by the local air flow characteristics. The smog generated in the eastern part of the mountainous area (touristic region) could be affected by the pollution transported from the central part and the eastern part of the Kathmandu Valley.

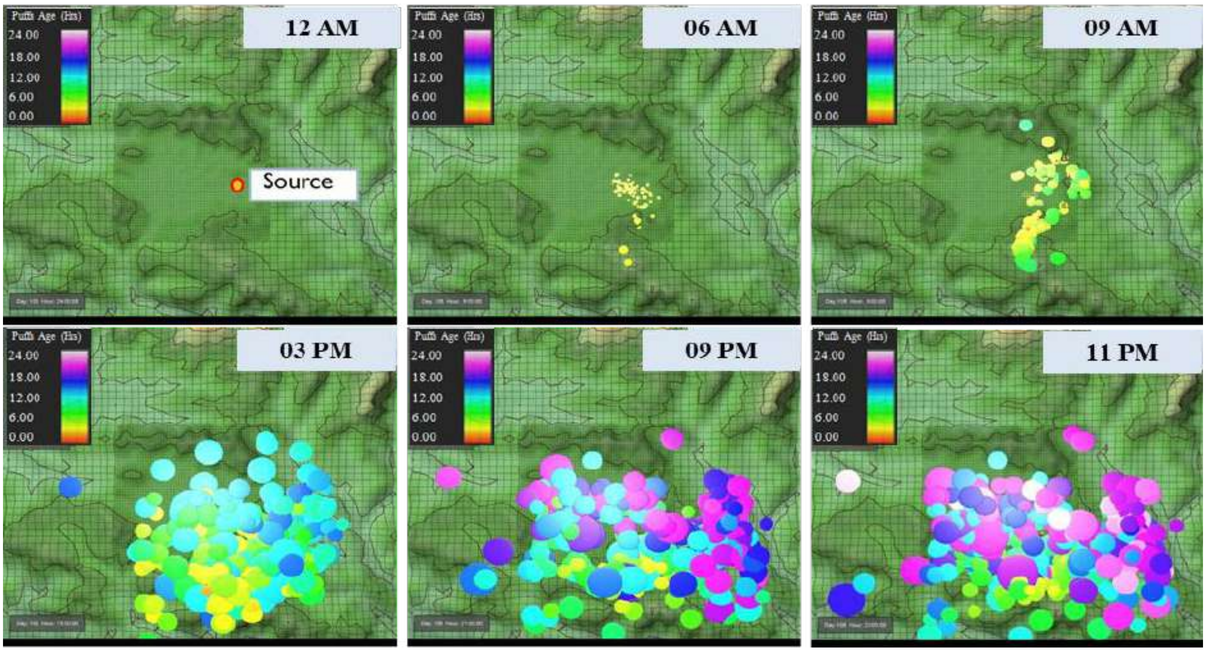


**Figure 12:** Puff dispersion mechanism from the point source, wherein the puff source is at the eastern part of the Valley.

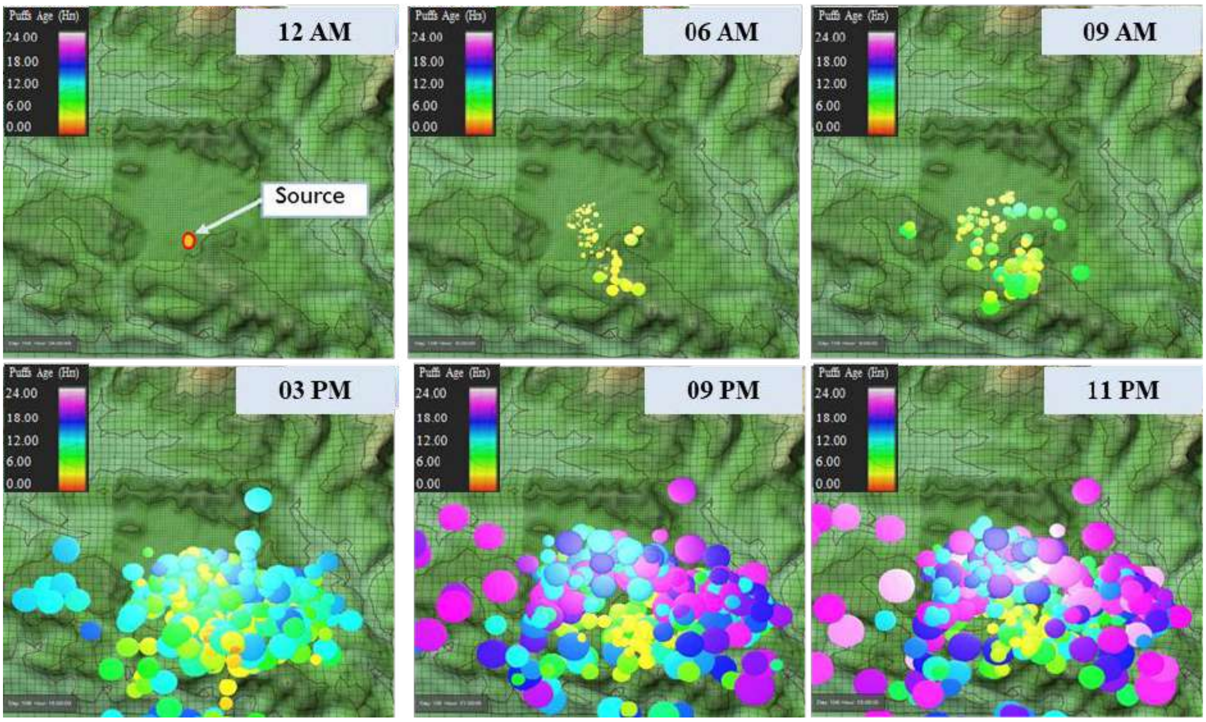


**Figure 13:** Puff dispersion mechanism from the point source, wherein the puff source is at the southern part of the Valley.

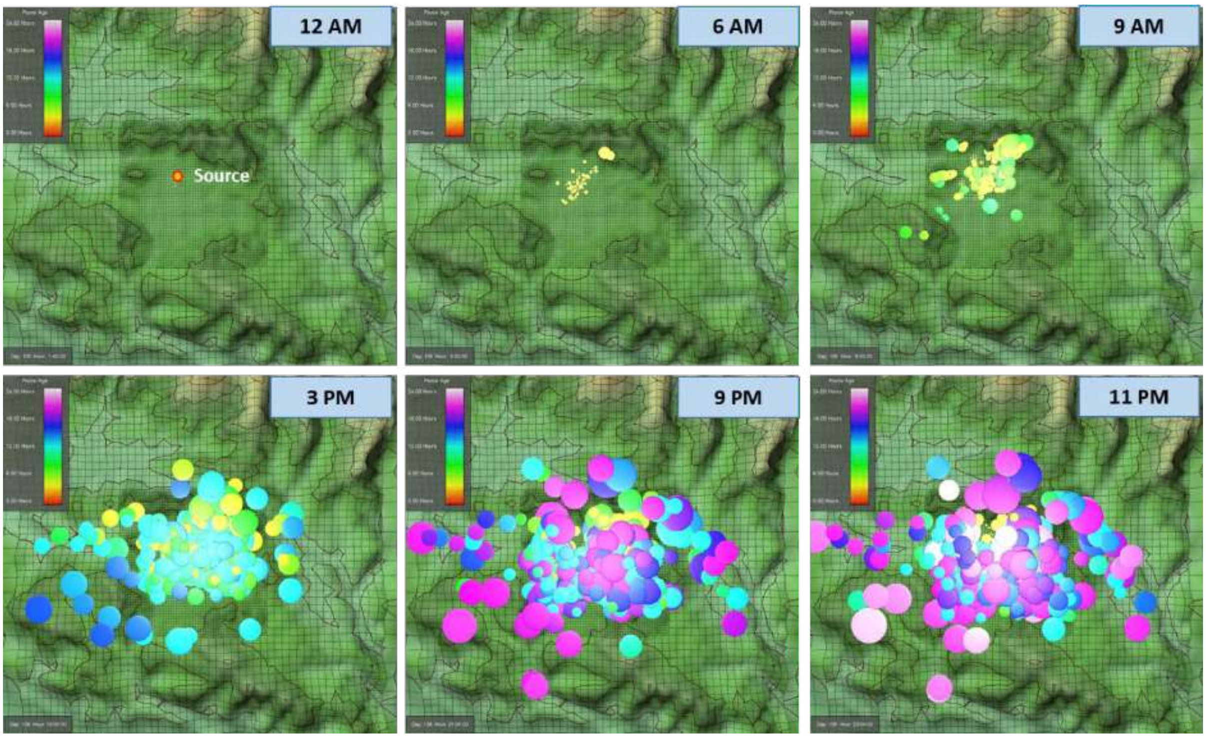


**Figure 14:** Puff dispersion mechanism from the point source in the Valley wherein the puff source is at the northern part of the Valley.

In the figure, the red color represents the younger puff and the white color represents the aged puff. As the puffs become older, the puff's size gradually expands and color also transforms towards white, as in Figures 11 – 14. The majority of the puffs in the surface area of the Valley mostly follow the breeze path. The aged puff dispersed at higher altitudes and wider areas where the breeze impact was least. Moreover, a large number of puffs capped the Valley top. This was because, as shown in Figure 11, the puff source was at the central part of the Valley, where most of the puffs were dispersed in the Valley area. This shows that understanding the air flow characteristics and air flow corridor could be helpful for managing the air quality of the Kathmandu Valley. This study also suggests that the north-to-south air flow is common in the study area; moreover, the air flow corridors are at the southern, south-eastern part of the Valley.

4.3.2 Impact of landuse change on breeze flow

Even if the solar incoming radiation is constant in nearby areas, the temperature of the Earth's surface differs significantly from place to place due to the different landuses and characteristics i.e., anthropogenic heat, specific heat capacity, albedo, etc., of the objects covering the land surface. After the sunset, the mountainous surface releases heat faster than the valley basin;

therefore, the temperature of the mountain slope becomes lower than the valley basin from late evening to the early morning. After the sunrise, the air flow phenomenon becomes reversed. When the irrigated crop land changes to the urban land, the surface characteristics such as soil moisture, specific heat capacities, albedo, anthropogenic heat emission, etc., also change. It consequently affects local wind characteristics. Figure 15 shows the breeze flow at different sampling locations when the valley land surface is covered with irrigated crop land, and Figure 16 shows the breeze flow pattern when the valley land surface changes to urban land. The results show that the local breeze becomes stronger during the day and weaker during the night when the irrigated crop land changes to the urban land.

In other words, there is a chance of the development of an urban heat island in the downtown area that increases the temperature of the urban area, which can be distinctly observed at nighttime. Major and densely urbanized cities such as Tokyo, Seoul, Taipei, etc. have already experienced the heat island effects. The daily average wind speeds at different sampling points do not vary significantly with the change of landuse pattern as in Figure 17.

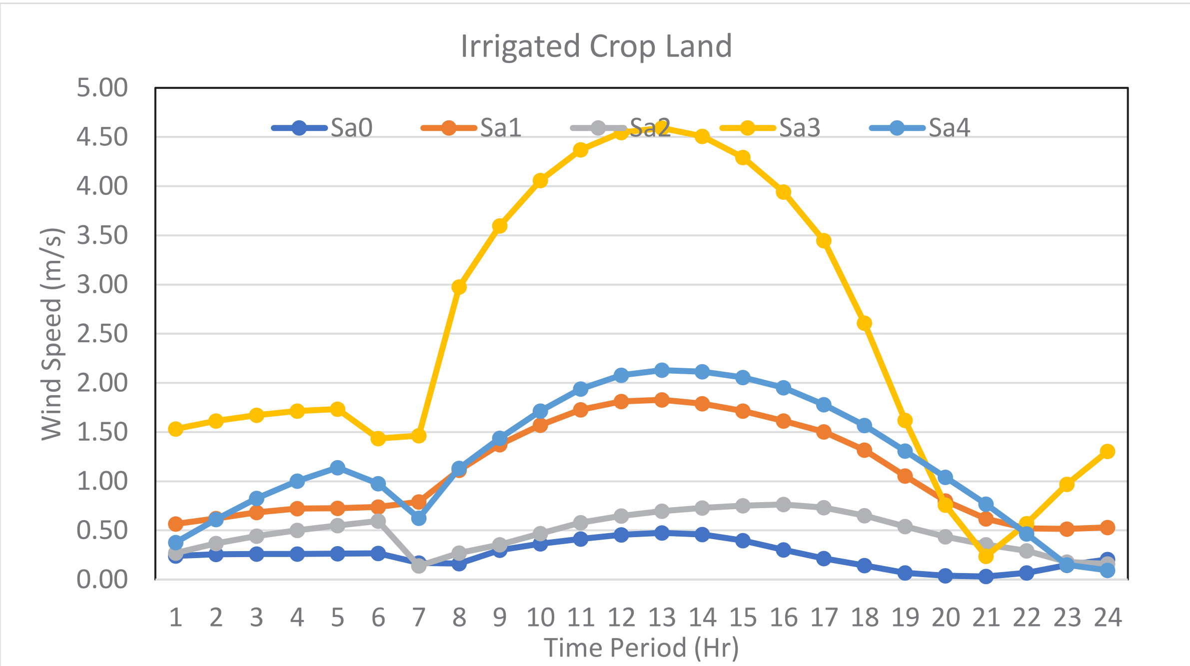


**Figure 15:** Diurnal variation of wind speed (Irrigated crop land).

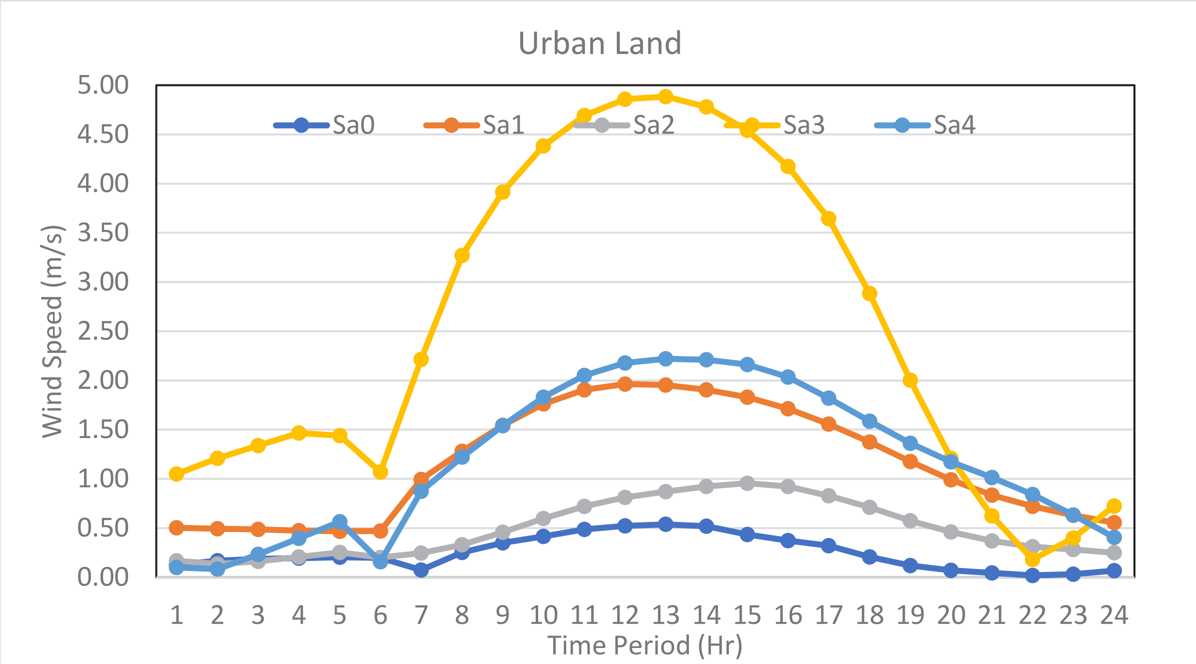


**Figure 16:** Diurnal variation of wind speed (Urban landuse).

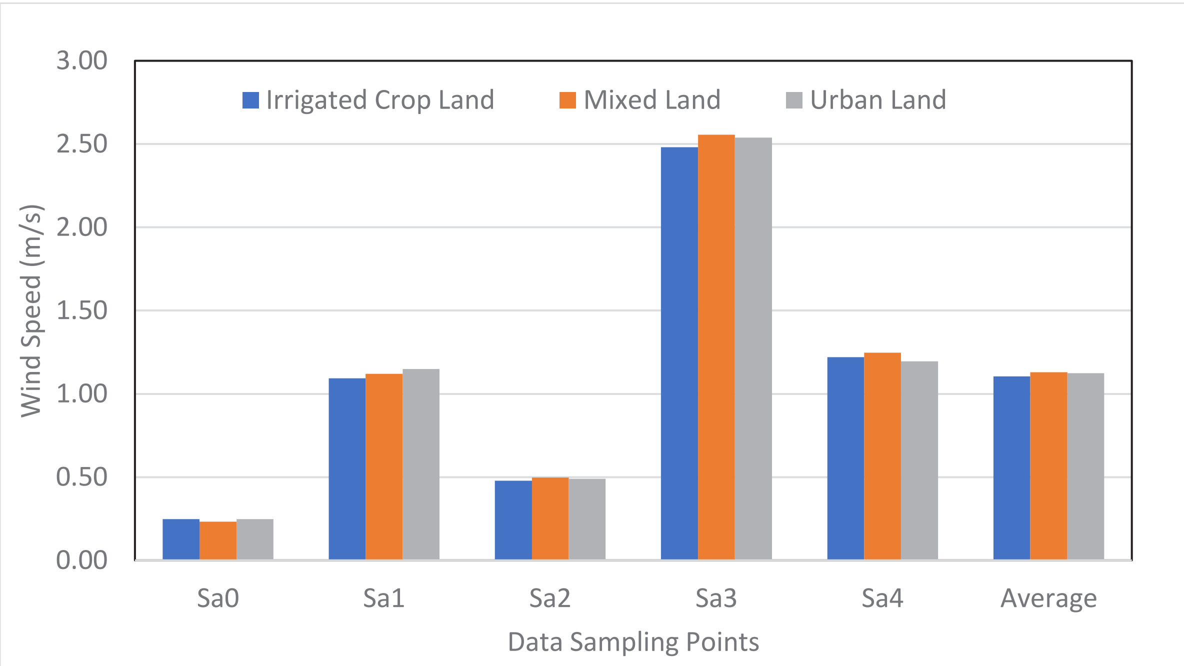


**Figure 17:** Comparison of average wind speed for different cases at various sampling locations.

## 5. Conclusion and Recommendation

Air quality management in the Kathmandu Valley remains an exceptionally complex and pressing challenge, shaped by the interplay of diverse emission sources, valley-specific topography, meteorological conditions, and transboundary influences. This study demonstrates that soil-based dust and combustion-derived pollutants are the dominant contributors to ambient air pollution, largely originating from construction and demolition activities, agricultural practices, and vehicular movement on unpaved or poorly maintained roads. The dispersion modeling results reveal that calm wind conditions prevailing in the central valley inhibit pollutant transport, leading to prolonged accumulation of emissions near their sources and a sustained deterioration of air quality. In contrast, emissions generated in the southern and southeastern sectors exert comparatively limited influence on the overall pollution burden, suggesting spatial variability in pollution impacts. These findings underscore the necessity of coordinated and integrated air quality management across Kathmandu Metropolitan City (KMC) and its neighboring municipalities, as isolated interventions are unlikely to yield meaningful or lasting improvements.

The study further highlights the critical importance of spatial planning, source decentralization, and technology transition in mitigating air pollution in the Valley. Strategic relocation of pollution-intensive development projects toward climatically favorable zones, decentralization of emission sources away from the core urban area, and a rapid shift from fossil-fuel-based public transport to electric mobility emerge as key long-term solutions. Complementary measures—including urban greening, preservation of agricultural land, promotion of pervious surfaces, and incorporation of air pollution hazards into multi-hazard risk-sensitive land-use planning—are essential for addressing both air quality degradation and associated urban heat island effects. Moreover, strict regulation of construction and demolition activities, improved road design and maintenance, reliable vehicle emission testing with enforceable penalties, and public awareness programs targeting open waste burning and forest fires are indispensable policy priorities. Collectively, these integrated and evidence-based interventions provide a robust framework for policymakers to advance sustainable urban development while progressively improving air quality in the Kathmandu Valley.

**Acknowledgements**

This work was partially supported by the Mayor's Research Fellowship 2020, Kathmandu Metropolitan City. The author would like to acknowledge Prof. Dr. Ram Kumar Sharma and all the CPC members. The author would like to acknowledge the Asian Institute for Environmental Research and Energy for providing the simulation software. Paraphrasing and language correction were done using OpenAI.

**References**


- Chang, C.C., Tsai, S.S., Ho, S.C., Yang, C.Y. (2005) Air pollution and hospital admissions for cardiovascular diseases in Taipei. Taiwan, Environmental Research 98, 114-119.
- Copper, C.D., Alley, F.C. (2002) Air Pollution Control: A design approach. Waveland Press Inc., USA.
- Donaldson, K., MacNee, W. (2001) Potential mechanism of adverse pulmonary and cardiovascular effects of particulate air pollution (PM10). International Journal of Hygienic and Environmental Health 203, 411-415.
- ENPHO (2001) Status of brick kiln in Kathmandu valley. Environment and public health organization (ENPHO), Kathmandu.
- Goldberg, M.S., Burnett, R.T., Yale, J.F., Valois, M.F., Brook, J.R. (2006) Association between ambient air pollution and daily mortality among persons with diabetes and cardiovascular disease. Environmental Research 100, 255-267.
- Kan, H., Chen, C. (2003) Air pollution and daily mortality in Shanghai: a time-series study. Archives of Environmental Health 58, 360-367.
- KVAQMP (2076) Kathmandu Valley Air Quality Management Action Plan 2076.
- Panday, A.K., Prinn, R.G. (2009a), Diurnal cycle of air pollution in the Kathmandu Valley, Nepal: Observations. Journal of Geophysical Research 114, D09305.
- Panday, A.K., Prinn, R.G., Schar, C. (2009b) Diurnal cycle of air pollution in the Kathmandu Valley, Nepal: 2.Modeling results. Journal of Geophysical Research 114, D21308, doi:10.1029/2008JD009808.
- Pandey, A. (2006) The diurnal cycle of air pollution in the Kathmandu Valley, Nepal. Ph.D. thesis, Massachuetts Institute of Technology, US.
- Pokhrel, R. & Lee, H. (2014) Integrated Environment Impact Assessment of Brick Kiln using Environmental Performance Scores. Asian J. Atmos. Environ 8, 15–24. https://doi.org/10.5572/ajae.2014.8.1.015
- Pokhrel, R. (2025) Study of air pollution and its dispersion pattern in Pokhara Valley. Pokhara Engineering College Journal 2 (1), 11 – 22. DOI: 10.3126/pecj.v2i1.76827
- Pokhrel, R., Lee, H. (2011) Algorithm development of visibility monitoring using digital image analysis. Asian Journal of Atmospheric Environment 5-1, 8-20. DOI: 10.5572/ajae.2011.5.1.008

- Pokhrel, R., Lee, H., Sharma, R.K. et al. (2021) Aerosol Dispersion Over a High Altitude Region: a Case Study of Kathmandu, Nepal. Water Air Soil Pollut 232, 80. https://doi.org/10.1007/s11270-021-05007-4
- Pudasainee, D., Sapkota, B., Bhatnagar, A., Kim, S.H., Seo, Y.C. (2010) Influence of weekdays, weekends and bandhas on surface ozone in Kathmandu valley. Atmospheric Research, 95, pp. 150-156.
- Regmi, R.P., Kitada, T., Kurata G. (2003) Numerical simulation of late wintertime local flows in Kathmandu Valley, Nepal:implication for air pollution transport. Journal of Applied Meteorology 42, 389-403.
- Sapkota, B., Dhaubadel, R. (2002) Atmospheric turbidity over Kathmandu Valley. Atmospheric Environment 36, 1249-1257.
- Sharma, C.K. (1997) Urban air quality of Kathmandu Valley “Kingdom of Nepal”. Atmospheric Environment 31, 2877-2883.
- Shrestha, R.M., Malla, S. (1996) Air pollution from energy use in developing country city - the case study of Kathmandu valley, Nepal. Clean Air Initiative (http://cleanairinitiative.org/portal/system/files/articles-58928_resource_1.pdf).
- World Bank (1997) URBAIR - Urban air quality management strategy in Asia: Kathmandu valley report, New York, USA

# Pokhara Engineering College Journal (PECJ)

*Applied Sciences and Engineering Insights*

ISSN: 3021-9795 (Print) / 3059-9628 (Online)

(Volume-3, Issue I)


## A Study on Soil Cement Bricks with Addition of Thatch


Sanjaya Lamichhane[1*],Arjun Baniya[2]

[1] *Department of Civil Engineering Pokhara Engineering College, Pokhara, Nepal*

[2] *Associate Professor, Department of Civil Engineering, Pokhara Engineering College, Pokhara, Nepal*

**Corresponding email:* ersanzaylc@gmail.com





*Received:12- January-2026; Revised:03-February-2026; Accepted: 04-March-2026*
*DOI: https://doi.org/10.3126/pecj.v3i1.93530*



**Abstract**

This study investigates the effects of thatch content on the characteristics of soil-cement bricks, offering valuable insights into thatch's potential application as an alternative to binder. Compressive strength, water absorption and cost analysis are the three primary research areas. The favorable effect of thatch as a binder on brick strength is demonstrated by the results, which indicate a considerable increase in compressive strength as thatch content rises in the 0-1% range. According to the Nepal National Building Code (NBC 109: 1994), hand-made bricks may absorb up to 25% of the total weight, but the average water absorption for all percentage mixes is still 23% overall, indicating the possibility of improved water resistance. A cost study further validates the economic viability of the soil-cement bricks, with production costs ranging from NRs 13 to 14, suggesting potential profitability for manufacturers. Collectively, our findings show the feasibility and advantages of use thatch as an alternative binder in the production of soil-cement bricks, offering the construction industry a cost-effective and sustainable choice.



**Keywords:** Soil- cement bricks, thatch, compressive strength, water absorption, cost


## 1. Introduction

Traditional rise residential construction often relies on clay bricks, which have been used as a building material since ancient times. Interestingly 30% of the population still resides in structures made from these bricks. This enduring popularity is due, to their simplicity, affordability, insulation for heat and sound, practicality and long lifespan(Al-Ajmi *et al.*, 2016). Moreover, clay can be returned to the earth without harming the environment. However, the conventional method of manufacturing bricks involves energy kiln firing processes that result in harmful pollutants being released into the atmosphere(Quezon *et al.*, 2017). In years there has been a growing demand for eco sustainable brick making techniques. One such alternative technique involves using a mixture of soil, cement, sand and thatch without any burning involved. The resulting bricks produced through this method are not of quality but also durable and environmentally friendly. Cement and sand act as binding agents while red soil provides the clay content for brick production. Additionally, incorporating materials, like thatch, straw or rice husk as reinforcement enhances the integrity of these bricks. Mud bricks, made from fibers like straw, have been strengthened since ancient times for their tensile strength and compressive strength. Fibers prevent deformation, protect surfaces, and improve elasticity. As fibers increase, their distribution becomes random, enhancing tensile strength and adaptability(Binici, Aksogan and Shah, 2005). Compressed earth blocks, also known as compressed soil blocks, are building materials made from damp soil compressed at high pressure. It uses local resources, consumes less energy, emits fewer greenhouse gases, and offers better thermal insulation. However, its strength and mechanical properties are not widely used('Final Report On The Study on Characteristics of Compressed Stabilized Earth Blocks ( CSEB ) using Chemical Stabilizer', no date).They are energy-efficient, environmentally friendly, and safe, making them a crucial component in reducing global energy consumption. These blocks can be stabilized with Portland cement, making them a popular choice for construction. Compressed Stabilized Earth Blocks (CSEB) offer benefits like local resource use, reduced transportation costs, high-quality housing accessibility, and local economic activity. They require less skilled labor, have good strength, insulation, and thermal properties, and produce low energy and carbon emission(BhaskaranPP and MohanKP, no date). Earth's short lifespan due to weak compressive strength is a disadvantage. Stabilization can improve soil's strength, dimensional stability, and durability for construction. To make bricks we mix red soil, cement, sand and thatch together. Press the mixture into brick shaped molds. Afterwards we let the bricks dry naturally in the sun of using a kiln. This process significantly reduces energy consumption and harmful emissions.

In order to meet Pokhara's housing needs and develop its infrastructure, brick production is essential. However, the traditional brick-making method, which involves burning, uses a lot of energy, contributes to air pollution, and raises environmental issues. To achieve sustainable and environmentally friendly construction methods, it is urgently necessary to fix the ratios of red soil, cement, sand, and thatch for low-cost brick production in Pokhara without the use of burning techniques. This research aims to identify the proper ratios of red soil, cement, sand, and thatch for low-cost brick production in Pokhara without burning. This will ensure the production of low-cost bricks that adhere to quality and strength standards. The Specific objectives of this research is to examine the physical properties and cost of soil cement bricks with addition of thatch.

(Binici, Aksogan and Shah, 2005)Investigated the mechanical characteristics of fibrous waste materials using stabilizers. The greatest increase in compressive strength was provided by plastic fibers (19% over straw and 36% over fabric made of polystyrene). The suggested combination complied with the minimum compressive strength standards of the Turkish Standard and ASTM. The results show promise for using waste materials in buildings. (Patowary *et al.*, 2015)The goal of the study was to identify the best soil for making CSSBs, or compressed stabilized sand bricks. The engineering features of CSSBs, such as compressive strength, durability, and water absorption, were studied in various stabilized materials, such as cement, coir, lime, fly ash, and chemicals. According to the study, stabilizing soil up to a certain amount improves its technical characteristics, producing a finished product that is more durable than conventional burnt clay brick. Although Black Cotton Soil did not meet the requirements for water absorption, it was discovered to have a favorable density index for the production of CSSB. The soil showed potential as a CSSB-appropriate material because its compressive strength was higher than that of a typical brick. (Jangid and Darade, 2017)The eco-friendly and non-burned CSEBs were the subject of the researchers' research. As a result, during manufacture, no hazardous gases are produced. This paper displays the test results for the soil that was used to produce CSEB. In the laboratory, highly compressed unburnt blocks with various compositions and varying ratios of sand (70%) to clay (20%) and stabilizers like cement (10%) had a compressive strength of 3.11 N/mm2, compared to standard fired brick's 3.984 N/mm2. However, these blocks are more cost-effective because they don't require burning. (Dawood *et al.*, 2021)In this project, clay was combined with natural fibers, sand, and cement to make eco-friendly, unfired bricks. The intention was to lessen shrinkage-related cracking and boost the brick's tensile strength. The resulting bricks, mortar, and masonry were tested for compressive and flexural strengths, and the behavior of unfired and fired clay brick prisms was compared. The results show that the maximum compressive strength for unfired masonry prisms was created by a mixture of clay, coarse sand, and straw, while the highest flexural strength for bricks was produced by a mixture of clay and sawdust. The compressive strength of the brick and mortar was also used to create a formula for determining the compressive strength of unfired brick masonry. Overall, the study sheds light on the potential of eco-friendly and non-fired bricks as a sustainable building material. (Muhammad Sajid Rehman, Masrur Momen, 2018) offers a thorough investigation into the compressive strength of several compressed stabilized earth block kinds. Nine different types of mixtures were used to prepare 101 compressed earth block specimens. As a soil stabilizer, cement was employed in each of them. Using universal testing equipment, prepared mixes were compressed under a 20-ton load. The goal was to examine the impacts of admixture addition and the water-cement ratio. A test of compressive strength was conducted after 7, 28, 60, and 90 days. For several sample types, the compressive strength test findings weren't what was anticipated; they revealed a drop in compressive strength 28- or 60-days following sample preparation. (Salah and Din, 2020)Earth is a popular building material in impoverished nations, but its receptivity to water can negatively impact its strength. Cement, lime, fly ash, and other stabilizers are used to make earthen constructions weather-resistant. This study aimed to determine the 28-day compressive strength of a locally accessible cement-based soil stabilizer reinforced with bale straw. The soil sample from Zangali, Khyber Pakhtoon Khwa, was stabilized using 10% cement and 1% straw bale. The cement content was maintained at 10% in all samples. Exams showed that using 10% stabilizer and 1% straw bale resulted in a decline in compressive strength, while adding additional straw bale increased it. ('Final Report On The Study on Characteristics of Compressed Stabilized Earth Blocks ( CSEB ) using Chemical Stabilizer', no date)This study investigated the structural features of compressed stabilized earth block (CSEB) masonry by performing compressive and shears strength tests on soil samples from five distinct locations. The compressive strength of CSEB brickwork in cement mortar was found to be satisfactory and promising on all sites. The compressive and shear strengths of masonry were heavily impacted by the mortar and CSEB component strengths. The study sheds light on the structural properties of CSEB masonry as well as soil variations in various areas, which can aid in the creation of sustainable and cost-effective housing options. Nawalparasi has the highest 28-day compressive strength of 16.71 N/mm2 and the highest CSEB masonry compressive strength of 4 N/mm2. Surya Binyak had a shear strength of 1.16 N/mm2, whereas Chovar had a maximum compressive strength of 4.15 N/mm2. These results show how useful CSEB may be as a sustainable building.

This study does have limitations; that is, mixing of varying percentages of red soil, cement, sand, thatch where bricks were tested not more than 28 days strength which did not involve efflorescence test, Durability test, weathering test

## 2. Materials and Methods

### 2.1 Material

The material used in this study include locally available red soil, cement, sand, thatch and water.

#### 2.1.1 Red Soil

Locally Available red soil which is rich in iron oxide was extracted from pokhara metropolitan city at a depth of 30 cm, crushed and dried in sun. Its properties, including particle size distribution, plasticity, and mineral composition, affect workability and strength. The tests done for red soil are given below('Field Tests on Soil To Determine Suitability of Soil for Brick', 2022);Sedimentation Test, moisture content (IS:2720 (Part 2)-1973, 1973),Liquid Limit (IS: 2720 (part 5):1985, 1985),Plastic Limit, Particle size distribution (IS : 2720 (Part 4 - 1985), 1985), textural classification of soils (Any *et al.*, no date)

#### 2.1.2 Cement

Standard OPC cement of 43 and 53 grade is used for all type of mixes. The physical properties of the cement at room temperature $27^0$c used are given in. The test performed for the cement were fineness test, consistency test, setting time test accordance to (IS: 1727, 2013).

### 2.1.3 Sand

Sand is a fine aggregate that is often added to the mixture of red soil and cement to improve the overall quality of the bricks. Sand helps reduce shrinkage during the drying process and enhances the workability of the mixture. It also contributes to better compaction and minimizes cracking as the bricks cure. The addition of sand helps achieves a smoother and more uniform texture on the brick's surface. There are different methods for testing the quality of sand at the construction site for the manufacture of unburnt bricks. Among various tests, we conducted a silt content test (IS 2386- Part III, 1963) and Bulking of Sand (IS 2386- Part III, 1963).

### 2.1.4 Thatch

Thatch is a natural material used in unburned bricks, enhancing structural integrity, reducing cracking and increasing durability by binding and strengthening the mixture. It is typically made from dried plant fibers like straw, reeds, grasses, or palm leaves. Firstly, we collected thatch from the study area. After collection, it is cleaned, chopped, and sun-dried for two days. The Size of thatch varies from 10mm to 20mm and the width from 2mm to 5mm.

### 2.1.5 Water

Normal water available is used in this experiment.

## 2.2 Preparation of Specimens

### 2.2.1 Material Selection and Proportions:

Soil mix design is the process of determining the proper ratios of soil, cement, sand and thatch for unburnt Bricks to produce desired strength in constructions. Soil Mix = Soil: Cement: Sand: Thatch can be used to describe the design of a Soil mix. Based on previous studies, we determine the proper mix proportions, which numerous procedures, mathematics, and laboratory testing. The specific ratios may vary depending on factors such as type of soil, use of brick and location condition.

### 2.2.2 Mixing the Dry Ingredients:

Consulting with brick manufacturers, contractors, engineers, clients, geologists etc. we found dry weight of fried brick approximately ranging from 2.8kg-3.2kg. On basis of traditional manufacturing process of fried bricks, approximate weight is taken base for producing unburnt bricks.Red soil is first extracted at a depth of 30 cm, devoid of any organic materials, debris, or large stones. The soil is then left outside to dry in the sun, removing any moisture or other impurities. Then soil passing from IS sieve 1.18mm is considered for manufacturing. Fine sand (Passing from IS sieve 1.18mm) from neighbouring rivers will be gathered. Ordinary Portland Cement from nearby market was collected. Add chopped or shredded thatch that has been sun-dried. Use the trial-and-error method to mix the proportions in a specific ratio. Gradually add water to the mixture while continuously mixing. Start with a moderate amount of water and adjust as needed to achieve the desired workability and consistency. The different mixtures are placed in brick mould as per Nepal National Building Code on required sizes given on table below(Mahal and Kathmandu, 2070). During a process, the mould is compacted (either manually or mechanically) to eliminate air pockets and ensure proper shape. In this experiment the mixture is placed under universal testing machine (UTM). A compressive load of 25kN is applied at uniform rate. After it has been compacted, it is extracted out from UTM and covering them with plastic to stop them from drying out too quickly. The bricks should next be air-dried for 7 to 14 days exposed to direct sunshine. Test the physical properties of brick.

**Figure 1:** Sample weighting and Hand mixing

**Fig 2:** Mould Design **Fig 3:** Calculating percentage of samples

**Figure 4:** Placement of mixture in mould

### 2.2.3 Mixing Design

The mixing process was carried out on an iron plate with a trowel and shovel. The materials used in the mixing process were weighted using a high-precision electronic measuring balance. The weight of materials to be added is obtained from the trial-and-error method. By taking different samples from various brick factories such as Machhapuchre Brick factory,Jamune Bhanjyang.tanahu, Gorkha chyangling bricks, Gorkha district, ) Pokhareli brick factory,Jamune Bhanjyang,tanahu, Pokhara Eco Red Bricks, Polyang, Kaski (PERP). The weight of more than 50 samples before burning from the different factories was found to be in the range of 2.5kg-2.9kg. Taking reference to this data, we tried to take a minimum range of weight due to including ingredients such as red soil, cement, sand, and thatch in our product. The proportion of red soil, Cement, Sand, Thatch, and Water is tabulated below on basis of previous literature reviews. Based on our observation the total weight of soil was 2.5kg per sample. our product consisted (85%, 80%, and 75%) of red soil, 10% cement, various percentages of Sand given in design mix and (0%, 0.25%, 0.50%, 0.75%, 1%) thatch, where cement, sand, thatch, and water ratio were identified on basis of red soil percentage.

**Figure 5:** Placing mould in UTM

**Table 1:** Mix Design (Group A)

| S.N | Soil | Cement | Sand | Thatch | Water | Remarks |
|---|---|---|---|---|---|---|
| 1. | 75 % | 10% | 15% | 0% | 28% | A1 |
| 2. | 75 % | 10% | 14.75% | 0.25% | 28% | A2 |
| 3. | 75 % | 10% | 14.50% | 0.50% | 28% | A3 |
| 4. | 75 % | 10% | 14.25% | 0.75% | 28% | A4 |
| 5. | 75 % | 10% | 14% | 1.00% | 28% | A5 |

**Table 2:** Mix Design (Group B)

| S.N | Soil | Cement | Sand | Thatch | Water | Remarks |
|---|---|---|---|---|---|---|
| 1. | 80 % | 10% | 10% | 0% | 28% | B1 |
| 2. | 80 % | 10% | 9.75% | 0.25% | 28% | B2 |
| 3. | 80 % | 10% | 9.50% | 0.50% | 28% | B3 |

| | | | | | | |
|---|---|---|---|---|---|---|
| 4. | 80 % | 10% | 9.25% | 0.75% | 28% | B4 |
| 5. | 80 % | 10% | 9% | 1.00% | 28% | B5 |

**Table 3:** Mix Design (Group C)

| S.N | Soil | Cement | Sand | Thatch | Water | Remarks |
|---|---|---|---|---|---|---|
| 1. | 85 % | 10% | 5% | 0% | 28% | C1 |
| 2. | 85 % | 10% | 4.75% | 0.25% | 28% | C2 |
| 3. | 85 % | 10% | 4.50% | 0.50% | 28% | C3 |
| 4. | 85 % | 10% | 4.25% | 0.75% | 28% | C4 |
| 5. | 85 % | 10% | 4.00% | 1.00% | 28% | C5 |

### 2.3 Test on Physical properties.

The physical properties of bricks are essential factors that determine their suitability for various construction applications. These properties play a crucial role in ensuring the strength, durability, and overall performance of brick structures. Here are some important physical properties of bricks.

#### 2.3.1 Shape and Size Test

In this test a specimen brick should be closely inspected. It should be of standard size (Mahal and Kathmandu, 2070)and its shape should be truly rectangular with sharp edges. The standard brick size of 230 x 115 x 57 mm with 10 mm thick horizontal and vertical mortar joints is preferable. Tolerances of -10 mm on length, -5 mm on width and ±3 mm on thickness shall be acceptable for the purpose of thick walls according to NBC 205:MRT RCC without masonry infill.

#### 2.3.2 Hardness Test

This test is conducted by making a scratch on brick surface with the help of finger nail. If no impression is left on the surface; the brick is treated to be sufficiently hard

#### 2.3.3 Water Absorption Test.

For ordinary burnt clay bricks, there are two procedures to measure the water absorption percentage by mass as per the five-hour boiling water test and the 24-hour immersion cold water test. These are each mentioned below(of Indian Standards, no date).

## 3. Results and Discussions.

This research aims to create sustainable, environmentally friendly earth bricks for construction and disaster reconstruction. It examines the effectiveness of red soil with cement, sand, and thatch. The soil identification test determines the appropriateness of creating compressed earth bricks. The behaviour of soil stabilized with cement is studied using different ratios of red soil, sand, and thatch to know the Physical characteristics of stabilized earthen bricks. This page presents test specimen images and compares the physical characteristics of stabilized soil bricks. Based on these tests and field observations, construction guidelines for stabilized bricks are suggested for low-cost housing in Pokhara along with graphs and charts for visual representation.

### 3.1 Sedimentation Test.

After collecting soil samples, we determine the proportion of clay, silt, and sand in terms of percentage which is tabulated below:

**Table 4:** Observation Table of Sedimentation Test

| Description | Unit | Container No. | | |
|---|---|---|---|---|
| | | 1 | 2 | 3 |
| Height of Clay (H1) | mm | 23.33 | 15 | 22 |
| Height of Silt (H2) | mm | 7.66 | 10 | 12 |
| Height of Sand (H3) | mm | 49.01 | 53 | 56 |
| Height of Soil (H) | mm | 80.00 | 78 | 90 |
| Percentage of Clay | % | 29.16 | 19.23 | 24.44 |
| Percentage of Silt | % | 9.58 | 12.82 | 13.33 |
| Percentage of Sand | % | 61.26 | 67.97 | 62.22 |

### 3.2 Atterbgs limit of soil sample

For the classification of soil Atterberg limit test was performed. Moisture content, Plastic limit test, Liquid limit, and Plasticity Index test were performed. These tests are performed using an air-dried powder soil sample. After testing several times, the moisture content, plastic limit, liquid limit, and plasticity index of the soil sample were found to be 17.60%, 34.42%, 28.93% and 16.81% respectively.

### 3.3 Textural Classification of Soil

From sedimentation tests, the percentage of clay, silt, and sand were found to be 30%, 10%, and 60%. These values are located on the triangular chart of the textural soil classification system. The soil samples were sandy loam which was suitable for making bricks

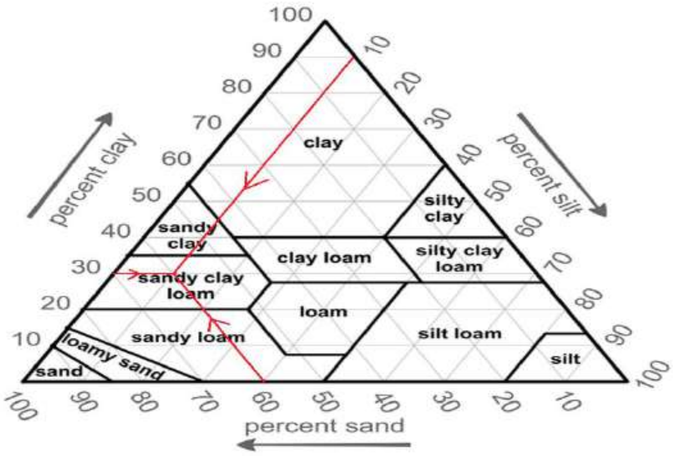


**Figure 6:** Textural Classification of Soil

### 3.4 Particle size distribution system.

As the soil is basically sandy loam-type soil, sieve analysis was performed to determine the properties of soil samples. The soil samples taken were oven dried which was sieved using listed sieve sizes.

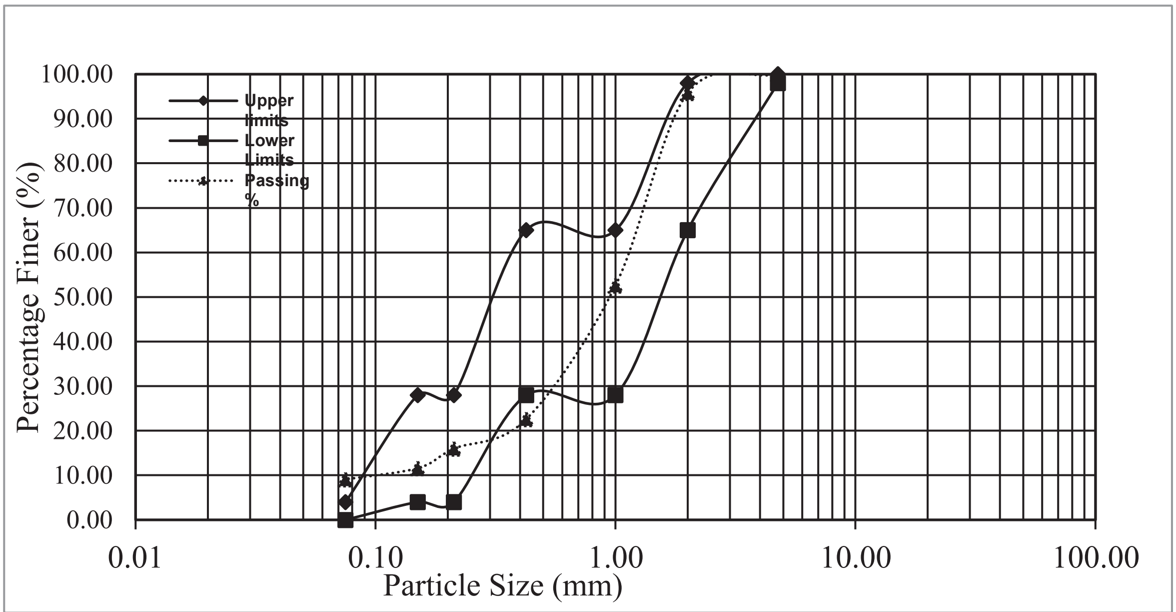


Percentage of Gravel =>4.75 mm, Percentage of coarse Sand = 4.75mm -2.00 mm, Percentage of medium Sand = 2.00 mm – 0.425mm, Percentage of Fine Sand =0.425 mm – 0.075 mm, Percentage of Silt-Clay fraction = <0.075mm

### 3.5 Cement Test

The quantity of cement that was used for making bricks were tested and result obtained was 32 percent consistency, 3 percent fineness, 135 minutes initial setting time and 387 minutes final setting time.

### 3.6 Silt content test.

The silt content present in sand were tested according to relevant code where three samples were taken and clay lumps on sand was found to be 13.12 percent on sand.

### 3.7 Bulking of sand.

The Bulking of sand was tested according to relevant code where three samples was placed in beaker and average was found to be 54.46 percent.

### 3.8 Shape and size test of brick

The manufactured brick was closely inspected which was rectangular with sharp edges whose standard size was measured and tabulated below.

**Table 5:** Observation Table for shape and size test (Group A)

| Brick Class | A1 | A2 | A3 | A4 | A5 | Standard Size (as per NBC) |
|---|---|---|---|---|---|---|
| Length | 230 | 230 | 230 | 230 | 230 | 230 |
| Breadth | 115 | 115 | 115 | 115 | 115 | 115 |
| Height | 57 | 55 | 65 | 60 | 55 | 57 |

**Table 6:** Observation Table for shape and size test (Group B)

| Brick Class | B1 | B2 | B3 | B4 | B5 | Standard Size (as per NBC) |
|---|---|---|---|---|---|---|
| Length | 230 | 230 | 230 | 230 | 230 | 230 |
| Breadth | 115 | 115 | 115 | 115 | 115 | 115 |
| Height | 57 | 55 | 65 | 60 | 55 | 57 |

**Table 7:** Observation Table for shape and size test (Group C)

| Brick Class | C1 | C2 | C3 | C4 | C5 | Standard Size (as per NBC) |
|---|---|---|---|---|---|---|
| Length | 230 | 230 | 230 | 230 | 230 | 230 |
| Breadth | 115 | 115 | 115 | 115 | 115 | 115 |
| Height | 57 | 55 | 65 | 60 | 55 | 57 |

*Note: All size is in mm


**Figure 7:** Sample of brick

### 3.9 Hardness test

The manufactured brick was tested for hardness and no scratched or impression was left on the surface Which treats brick as sufficiently hard.

### 3.10 Water Absorption Test

If the water absorption capacity of a brick is more its strength will be comparably low for first class brick, the water absorption capacity should not be more than 20% by weight. However, a brick shall not absorb more water than 15 % of its weight after 24 hours of soaking in water at normal temperatures. However, hand-made bricks may have water absorption up to 25 % of their weight according to Nepal national Building code NBC 109: 1994. A triplicate brick samples of each group were tested for water absorption where water absorption varies with percent of thatch on different mixes presented in graph below: The figure below shows that changing percentage of soil (75,80,85) % on different thatch ratios varies water absorption and average tested value was found to be 23 percentages as required to mentioned code.

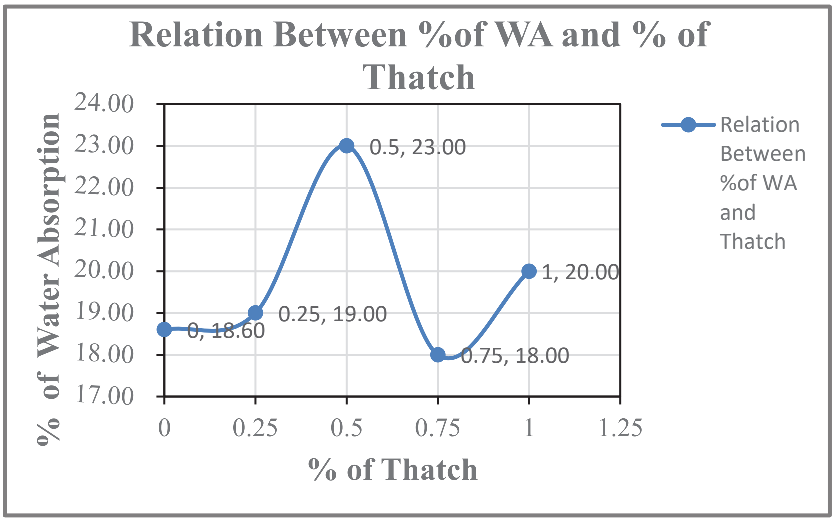


| % Of Thatch | % Of WA |
|---|---|
| 0 | 18.6 |
| 0.25 | 19 |
| 0.50 | 23 |
| 0.75 | 18 |
| 1 | 20 |

**Figure 8:** Soil (75) and Thatch (0, 0.25, 0.50, 0.75) **Percentage**

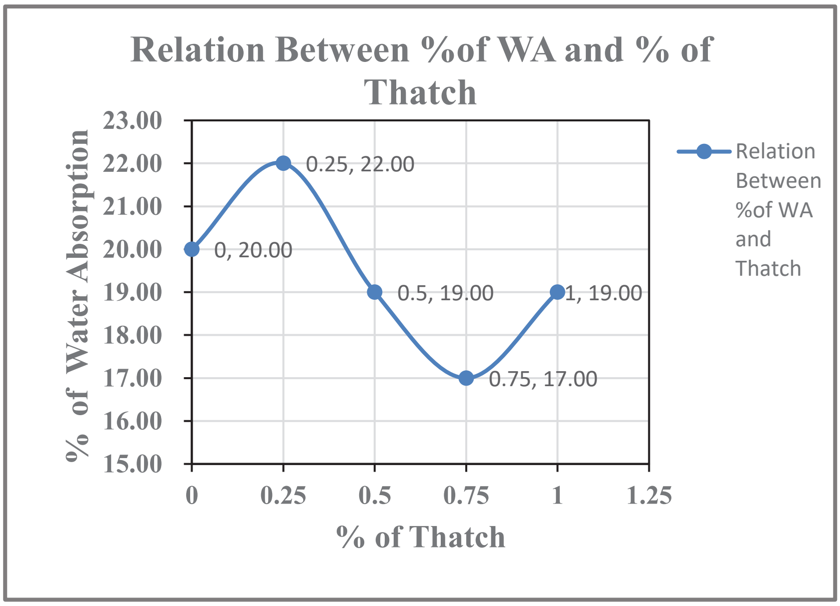


| % Of Thatch | % Of WA |
|---|---|
| 0 | 20 |
| 0.25 | 22 |
| 0.50 | 19 |
| 0.75 | 17 |
| 1 | 19 |

**Figure 9:** Soil (80) and Thatch (0, 0.25, 0.50, 0.75 and 1) Percentage

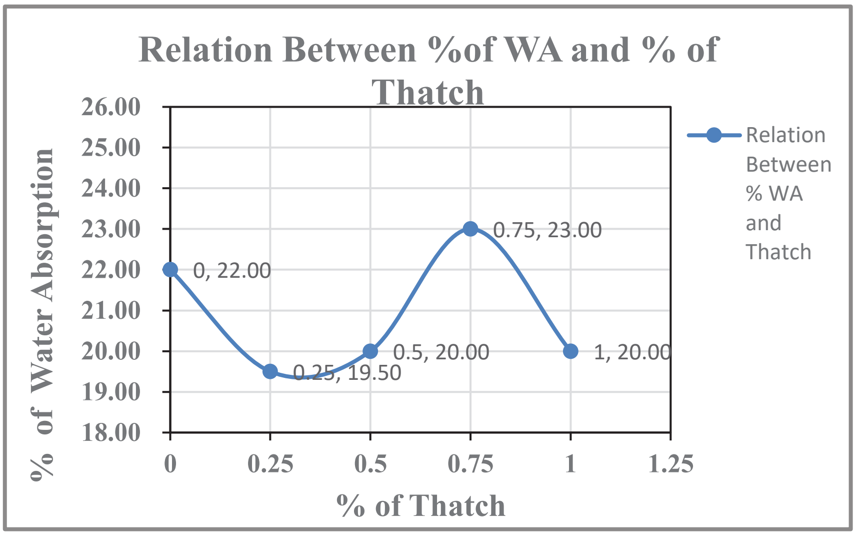


| % Of Thatch | % Of WA |
|---|---|
| 0 | 22 |
| 0.25 | 19.5 |
| 0.50 | 20 |
| 0.75 | 23 |
| 1 | 20 |

**Figure 10:** Soil (85) and Thatch (0, 0.25, 0.50, 0.75 and 1) Percentage

**4. Compressive Strength Test**

Compressive strength is the ability of a material to resist compressive loading. It is an important property of brick, as bricks are often used in load-bearing structures. It's an important factor to consider when choosing bricks for a project. The required compressive strength of the bricks will depend on the type of structure being built and the load that the bricks will be subjected to. Different brick samples of each group were tested for compressive strength which is presented in the graph below.

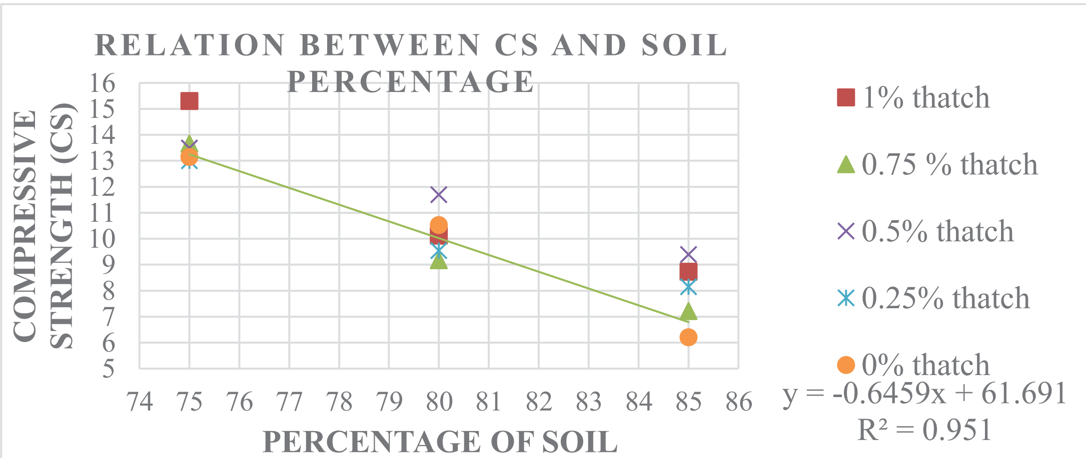


**Figure 11:** Relation between CS and Soil Percentage


**Figure 12:** Compressive strength Test

From figure 5, as a percentage of soil decreases and sand changes with respect with constant cement and water ratio relative to changes in thatch ratio increases compressive strength. All range of tested values on various percentage of soil with addition of thatch from zero to one percentage show a non-significant relation on various samples.

## 5. Cost Analysis

Another element that we considered is cost analysis, since manufacturers are always concerned with profit. Here, we examined the cost for typical unburnt bricks, so that we could get a clear number of how much each brick costs. The rate analysis of soil cement bricks are done according to different manuals and codes('KASKI-DISTRICT-RATES-2080-81.pdf', no date). The following table presents the rate analysis of brick manufacturing process(Darshan Shrestha, 2012) of 1000 brick per day production.

**Table 8:** Rate analysis for unburnt bricks with 75% soil

| S. N | MATERIAL | QUANTITY | UNIT | RATE | AMOUNT |
|---|---|---|---|---|---|
| **A.** | **Material** | | | | |
| 1 | Red Soil | 1.31 | cum | 614.00 | 805.88 |
| 2 | Cement (OPC) | 3.78 | bag | 697.50 | 2636.55 |
| 3 | Sand | 0.20 | cum | 2425.50 | 477.52 |
| 4 | Thatch | 1 | Mutha | 234.28 | 234.28 |
| 5 | water charge | 367.5 | lit | 0.25 | 91.88 |
| | | **Sub Total (A)** | | | **4246.10** |
| **B.** | **Labour charge** | | | | |
| 6 | Skilled | 3 | M/day | 1214 | 3642.00 |
| 7 | Unskilled | 5 | M/day | 852 | 4260.00 |
| | | **Sub Total (B)** | | | **7902.00** |
| **C.** | **Equipment/ Miscellaneous** | **Per year** | | **Total Cost** | **Cost/Day** |
| 8 | Investment Cost (Interest on fixed deposit) | 12 | % | 308000 | 101.26 |
| 9 | Equipment Depreciation (Press Lifespan) | 19.6 | % | 1000000 | 536.99 |
| 10 | Building Depreciation (Site duration) | 50 | % | 50000 | 68.49 |
| 11 | Maintenance cost (Press lifespan) | per lifespan | | 8500 | 23.29 |
| 12 | Miscellaneous (5%of sum of A& B) | 5 | % | 12148.10 | 607.41 |
| | | **Sub Total (C)** | | | **1337.43** |
| | | **Grand Total (A+B+C)** | | | **13485.53** |
| | | **Cost of unit Brick (NRs)** | | | **13.49** |

**Table 9:** Rate analysis for unburnt bricks with 80% soil

| S. N | MATERIAL | QUANTITY | UNIT | RATE | AMOUNT |
|---|---|---|---|---|---|
| **A.** | **Material** | | | | |
| 1 | Red Soil | 1.40 | cum | 614.00 | 859.60 |
| 2 | Cement (OPC) | 4.03 | bag | 697.50 | 2812.32 |
| 3 | Sand | 0.14 | cum | 2425.50 | 339.57 |
| 4 | Thatch | 1 | Mutha | 234.28 | 234.28 |
| 5 | water charge | 392 | lit | 0.25 | 98.00 |
| | | **Sub Total (A)** | | | **4343.77** |
| **B.** | **Labour charge** | | | | |
| 6 | Skilled | 3 | M/day | 1214 | 3642.00 |
| 7 | Unskilled | 5 | M/day | 852 | 4260.00 |
| | | **Sub Total (B)** | | | **7902.00** |
| **C.** | **Equipment/ Miscellaneous** | **Per year** | | **Total Cost** | **Cost/Day** |
| 8 | Investment Cost (Interest on fixed deposit) | 12 | % | 308000 | 101.26 |
| 9 | Equipment Depreciation (Press Lifespan) | 19.6 | % | 1000000 | 536.99 |
| 10 | Building Depreciation (Site duration) | 50 | % | 50000 | 68.49 |
| 11 | Maintenance cost (Press lifespan) | per lifespan | | 8500 | 23.29 |
| 12 | Miscellaneous (5%of sum of A& B) | 5 | % | 12245.77 | 612.29 |
| | | **Sub Total (C)** | | | **1342.32** |
| | | **Grand Total (A+B+C)** | | | **13588.09** |
| | | **Cost of unit Brick (NRs)** | | | **13.59** |

**Table 10:** Rate analysis for unburnt bricks with 85% soil

| S. N | MATERIAL | QUANTITY | UNIT | RATE | AMOUNT |
|---|---|---|---|---|---|
| **A.** | **Material** | | | | |
| 1 | Red Soil | 1.49 | cum | 614.00 | 913.33 |
| 2 | Cement (OPC) | 4.28 | bag | 697.50 | 2988.09 |
| 3 | Sand | 0.07 | cum | 2425.50 | 180.40 |
| 4 | Thatch | 1 | Mutha | 234.28 | 234.28 |
| 5 | water charge | 416.5 | lit | 0.25 | 104.13 |
| | | **Sub Total (A)** | | | **4420.22** |
| **B.** | **Labour charge** | | | | |
| 6 | Skilled | 3 | M/day | 1214 | 3642.00 |
| 7 | Unskilled | 5 | M/day | 852 | 4260.00 |
| | | **Sub Total (B)** | | | **7902.00** |
| **C.** | **Equipment/ Miscellaneous** | Per year | | **Total Cost** | **Cost/Day** |
| 8 | Investment Cost (Interest on fixed deposit) | 12 | % | 308000 | 101.26 |
| 9 | Equipment Depreciation (Press Lifespan) | 19.6 | % | 1000000 | 536.99 |
| 10 | Building Depreciation (Site duration) | 50 | % | 50000 | 68.49 |
| 11 | Maintenance cost (Press lifespan) | per lifespan | | 8500 | 23.29 |
| 12 | Miscellaneous (5%of sum of A& B) | 5 | % | 12322.22 | 616.11 |
| | | **Sub Total (C)** | | | **1346.14** |
| | | **Grand Total (A+B+C)** | | | **13668.35** |
| | | **Cost of unit Brick (NRs)** | | | **13.67** |

## 6. Conclusions

- For 0 to 1% thatch content, the result showed that Compressive strength of soil cement brick increase with increasing thatch content which proves that thatch as an alternative binder influenced brick characteristics.
- For zero to one percent thatch content overall average water absorption for all percentage of mixes in accordance to tested samples were 23% where hand-made bricks may have water absorption up to 25 % of their weight according to Nepal

National Building code NBC 109: 1994.

- As per the cost analysis, soil cement brick was found to be in range of NRs 13 to 14 for the manufacturer and may lead towards profit.

**References**


- Al-Ajmi, F. et al. (2016) 'Strength Behavior of Mud Brick in Building Construction', Open Journal of Civil Engineering, 06(03), pp. 482–494. Available at: https://doi.org/10.4236/ojce.2016.63041
- Any, Sand et al. (no date) 'Activity 31 : Determining a Soil ' s Textural Classification Maine Geological Survey Time : Background :
- BhaskaranPP, B. and MohanKP, M. (no date) 'Study On Compressed Stabilized Earth Blocks By Using Chemicals', IOSR Journal of Applied Geology and Geophysics, 6(3), Available at: https://doi.org/10.9790/0990-0603035156.
- Binici, H., Aksogan, O. and Shah, T. (2005) 'Investigation of fibre reinforced mud brick as a building material', Construction and Building Materials, 19(4), pp. 313–318. Available at: https://doi.org/10.1016/j.conbuildmat.2004.07.013.
- Darshan Shrestha, H. (2012) 'Standard Norms and Specification for CSEB Block'
- Dawood, A.O. et al. (2021) 'Investigation of Compressive Strength of Straw Reinforced Unfired Clay Bricks for Sustainable Building Construction', Civil and Environmental Engineering, 17(1), pp. 150–163. Available at: https://doi.org/10.2478/cee-2021-0016
- 'Field Tests on Soil To Determine Suitability of Soil for Brick' (2022), pp. 1–11
- 'Final Report On The Study on Characteristics of Compressed Stabilized Earth
- ( CSEB ) using Chemical Stabilizer' (no date), pp. 1–34
- Gubasheva, S. (2017) 'Adobe bricks as a building material', pp. 1–50
- IS : 2720 (Part 4 - 1985) (1985) 'Methods of Test for Soils, Part 4: Grain Size Analysis', Bureau of Indian Standards, New Delhi, India., Reaffirmed(2006), pp. 1–38
- IS: 1727 (2013) 'Methods of test for pozzolanic materials', Bureau of Indian

Standards, New Delhi New Delhi, (February), pp. 1–55

- IS: 2720 (part 5):1985 (1985) 'Determination of Liquid limit and Plastic limit of soil', Bureau of Indian Standards, New Delhi, India., Reaffirmed(2006), pp. 1–16.
- IS:2720 (Part 2)-1973 (1973) 'Determination of water content of soil', Bureau of Indian Standards, New Delhi, India., Reaffirmed(2010), pp. 1–17
- IS 2386- Part III (1963) 'Method of Test for aggregate for concrete. Part III- Specific gravity, density, voids, absorption and bulking', Bureau of Indian Standards, New Delhi, p. (Reaffirmed 2002)
- Jangid, S. and Darade, M. (2017) 'Study on Compressed Stabilized Earth Block', International Research Journal of Engineering and Technology [Preprint]. Available at: www.irjet.net
- 'KASKI-DISTRICT-RATES-2080-81.pdf' (no date)
- Mahal, B. and Kathmandu, N. (2070) N E P A L N A T I O N A L B U I L D I N G C O D E READY TO USE GUIDELINE FOR DETAILINGS OF LOW RISE REINFORCED CONCRETE BUILDINGS WITHOUT MASONRY INFILL Government of Nepal Ministry of Urban Development Department of Urban Development and Building Construction
- Mauloud, Y.I. (2007) 'Straw Stabilized Local Clay Bricks', Zanco Journal of Pure and Applied Science, 10(2)
- Muhammad Sajid Rehman, Masrur Momen, A.S. (2018) 'Department of civil engineering bangladesh university of engineering and technology dhaka 1000, bangladesh october, 2018', p. 74
- Nagaraja, A., Shilpa, S. and Hegde, R. (2018) 'Study on Compressed Stabilised Earth Blocks By Using Chemical Admixtures', International Research Journal of Engineering and Technology (IRJET), 5(6), pp. 5–7. Available at: https://doi.org/10.9790/0990-0603035156
- of Indian Standards, B. (no date) IS 3495-1 to 4 (1992): Methods of tests of burnt clay building bricks: Part 1 Determination of compressive strength Part 2 Determination of water absorption Part 3 Determination of efflorescence, Part 4: Determination of warpage

- Patel, M. (2013) '4 Advantages and Disadvantages of CFD
- Patowary, B.N. et al. (2015) 'Study of Compressed Stabilised Earth Block', International Journal of Scientific and Research Publications, 5(6). Available at: www.ijsrp.org
- Profile, S.E.E. (2018) 'USING NATURAL FIBRE A Thesis Submitted by Md . Imran Hossain Student ID .: 0904037 In partial fulfillment of the requirement for the degree of Under the supervision of Professor Dr . Mohammad Shariful Islam Department of Civil Engineering Bangladesh Unive', (September 2015). Available at: https://doi.org/10.13140/RG.2.2.23877.14563
- Quezon, E.T. et al. (2017) Comparative Study on Compressive Strength of Locally Produced Fired Clay Bricks and Stabilized Clay Bricks with Cement and Lime Construction Project Management View project Modeling Labor Productivity using SD-Hybrid Framework View project Comparative Study on Compressive Strength of Locally Produced Fired Clay Bricks and Stabilized Clay Bricks with Cement and Lime. Available at: www.globalscientificjournal.com
- Salah, E. and Din, U. (2020) 'International Journal of Advance Engineering and Research', International Journal of Advance Engineering and Research Development, 6(December 2019), pp. 270–276. Available at: https://doi.org/10.21090/IJAERD.39611
- Soil, C. and Soil, R. (2018) 'A Study on Manufacturing of Bricks using Black', 3(5), pp. 229–235
- Zultiniar et al. (2018) 'Fabricaton of brick without burning process', in IOP Conference Series: Materials Science and Engineering. Institute of Physics Publishing. Available at: https://doi.org/10.1088/1757-899X/345/1/012017

Pokhara Engineering College Journal (PECJ)
*Applied Sciences and Engineering Insights*

ISSN: 3021-9795 (Print) / 3059-9628 (Online)
(Volume-3, Issue I)

# Comparative Evaluation on Parameters of Seismic Codes for the Design of Masonry Structures

Suyog Bhandari[1], Rajendra Aryal[1*]

[1]*School of Engineering, Faculty of Science and Technology, Pokhara University, Nepal*

**Corresponding email: rajendra.aryal@pu.edu.np*



*Received:02- February-2026; Revised: 25- February-2026; Accepted: 18- March-2026*
*DOI : https://doi.org/10.3126/pecj.v3i1.93529*

## Abstract

Structures are made to withstand specific seismic lateral forces that are related to both the structure and the local seismicity along with dead, imposed and other loads. For design of masonry structure, seismic lateral force needs to be evaluated. The seismic design provisions in three building codes, Nepal (NBC105:2020), India (IS1893:2016) and New Zealand (NZS1170.5:2004) in context of design of masonry structure along with their similarities and differences are presented. Code provisions for the design of masonry structures have been elaborated. The codes and their histories are introduced. Then, the distinctions between the basic period, spectral shape factor, elastic site spectra, seismic zone factor, and importance factor for estimating the seismic load are explored in detail. Following the calculation of the seismic force, base shear coefficients and distribution methods over the building's height are compared. Compressive stress and shear stress are computed on the basis of design load combinations mentioned in respective code and comparison has been carried out. Although the three codes have some subtle differences, they have several characteristics that allow for comparison. The fundamental periods computed from the three codes resides within a contracted range of 0.19 to 0.27s, signifying marginal sensitivity of short-period masonry buildings to formulations of empirical period. Spectral shape factors also exhibit minor variation for short-period structures, whereas differences in ductility and response reduction parameters deliberately influence base shear coefficients and causing masonry stress demand. This comparison shows that the base shear coefficient from NZS is 161% higher than IS and 51% higher than NBC. Stresses obtained from NBC and IS based models shows value in similar range while from NZS based model significantly, larger stresses were obtained. This research improves masonry design safety and competence by comparing NBC, IS, and New Zealand seismic codes, enabling engineers to carry out optimal design, retrofitting, and construction practices, lowering earthquake risks.

***Keywords:*** *Code, Comparison, Indian Standard, Masonry, Nepal National Building Code, New Zealand Standard*

## 1. Introduction

Masonry buildings constitute the main residential construction typology in Nepal and resides highly prone to earthquake-induced destruction. The 2015 Gorkha earthquake opened up serious deficiencies in existing buildings, causing severe human and economic losses (Bilham, 2015; Mosleh et al., 2016). Post-earthquake assessments spotlighted deficiencies in construction quality, detailing practice, and code compliance, underlining the chief role of seismic design standards in safeguarding life safety and satisfactory performance (Gautam & Chaulagain, 2016; Waris et al., 2017). In Nepal, seismic design is governed by NBC 105:2020, which substituted NBC 105:1994 to include revised hazard representation and limit-state concepts. However, masonry-specific codes such as NBC 202:2015 (DUDBC, 2015) were formulated under the previous seismic framework, raising affairs regarding parameter compatibility, force estimation uniformity, and alignment with improved ultimate and serviceability limit-state design demand.

Comparative research consistently shows that seismic demand is very sensitive to hazard modelling, spectral shape, ductility assignment, and response reduction factors. McIntosh and Pezeshk (1997) pointed out divergence between strength-based and working stress approaches in U.S. codes, presenting that design philosophy straight influences prescribed force levels. Parallel discrepancies in base shear were conveyed by Khose et al. (2012) and Zhinan and Zhonghai (2012) among ASCE 7, Eurocode 8, IS 1893, and Chinese codes, mainly caused by variations in soil amplification models and least base shear limits. Dogangun and Livaoglu (2006) further revealed significant differences in design spectra across Eurocode 8, UBC, IBC, and Turkish provisions. These studies jointly indicate that code-to-code variability exhibits differences in reliability calibration and hazard representation instead of procedural inconsistencies only.

In the Nepalese situation, Giri et al. (2018) reported that prior NBC provisions generated comparatively lower base shear estimates than Japanese and European standards, elevating the concerns regarding hazard and response factor standardisation. Although probabilistic seismic hazard analyses for areas such as Pokhara Valley have assisted the usual consistency of national hazard factors (Baruwal et al., 2020), the transition to NBC 105:2020 obliges renewed analytical validation. Current comparisons between NBC 105:2020 and IS 1893 (Part 1):2016 identified remarkable differences in base shear, time period, and displacement demand for reinforced concrete buildings (Khatri et al., 2025; Shah et al., 2025). Regional Himalayan comparisons also revealed variability coming from hazard zonation and response modification parameters (Kunwar et al., 2024). However, these investigations primarily focus on reinforced concrete systems in place of load-bearing masonry structures, which comprise the majority of Nepalese buildings stock.

Masonry-centric research exposes additional inconsistencies in seismic parameter treatment. Analytical and experimental studies on unreinforced, confined, and reinforced masonry systems establish noteworthy variation in drift capacity, confinement effectiveness, and nonlinear behaviour modelling (Adhikari et al., 2023; Borah et al., 2023; Chi et al., 2024; Niu, 2025). Experimental categorisation of Nepalese brick masonry specifies material and construction-specific behaviour that may not be wholly represented by generalized code norms (Parajuli et al., 2020). Furthermore, local earthquake-resistant construction practices cover up essential seismic principles, yet remain inadequately incorporated into formal analytical calibration (Dixit et al., 2004). While NZS 1170.5 (New Zealand Standard, 2004) and NZS 4229:2013 (New Zealand Standard, 2013) provide structured hazard and prescriptive masonry guidance, their direct implementation to Nepal is limited due to differences in construction practice, material control, and execution capacity.

The interaction between contemporary seismic hazard parameters and prescriptive masonry guidelines in Nepal remains inadequately examined. NBC 202:2015 (DUDBC, 2015) recommends geometric and detailing limitations intended to guarantee minimum seismic resistance for load-bearing masonry. Although such guidelines enrich constructability and compliance, they are mostly empirical and not clearly validated against systematic performance assessments under NBC 105:2020 demand formulations. Bothara et al. (2018) observed a post-earthquake shift toward cement-based masonry construction in distant rural areas, extra highlighting the need to ensure rationality between evolving construction practice and seismic demand parameters. Despite proof that seismic codes evolve in response to research and post-earthquake lessons to be learnt (McIntosh & Pezeshk, 1997), methodical evaluation of masonry design implications under the updated national code relative to IS and New Zealand standards leftovers limited.

A critical synthesis of the literature finds three principal gaps. First, although comparative assessments exist for reinforced concrete buildings (Khatri et al., 2025; Shah et al., 2025; Kunwar et al., 2024), there is inadequate analytical comparison dedicated explicitly on low-rise masonry structures under NBC 105:2020. Second, variations in hazard factors, spectral shape representation, and response modification parameters across NBC, IS 1893, and New Zealand standards have not been systematically quantified in terms of their impact on masonry base shear and displacement demand. Third, the compatibility between present national seismic parameters and prescriptive masonry guidelines (DUDBC, 2015) has not been analytically confirmed for typical two-storey residential building configurations, despite the signal of masonry vulnerability from past earthquakes (Bilham, 2015; Gautam & Chaulagain, 2016).

An organised comparison of seismic parameters precisely for load-bearing masonry buildings under the updated NBC105:2020 code provision remains limited. Previous studies primarily focus on reinforced concrete structures and do not measure how variations in hazard representation, spectral shape, and response reduction parameters effect seismic demand in masonry structures. Since masonry buildings lead in number of residential building construction in Nepal and they have limited ductility, differences in these parameters may meaningfully affect estimation of base shear, wall stresses, and as a whole structural safety. Therefore, assimilating the significance of these code parameters is indispensable for refining seismic design consistency and reliability.

Therefore, this study accomplishes a comparative evaluation of principal seismic parameters in NBC 105:2020, IS 1893 (Part 1):2016, and appropriate New Zealand standards, containing NZS 1170.5 and NZS 4229, for the design of masonry structures. The objectives are to compute differences in hazard factors, spectral shape, response reduction parameters, and base shear estimation; to evaluate their impacts through elastic analysis of typical low-rise masonry buildings defined in NBC 202:2015 (DUDBC, 2015); and to ascertain the areas where harmonization could boost design consistency and reliability. By critically scrutinising parametric variations and their structural consequences, the study delivers evidence to aid coherent calibration of masonry design provisions in Nepal, contributing to better seismic safety, economic competence, and context-sensitive code development.

## 2. Materials and Methods

The methodological flow chart for the research is as under.

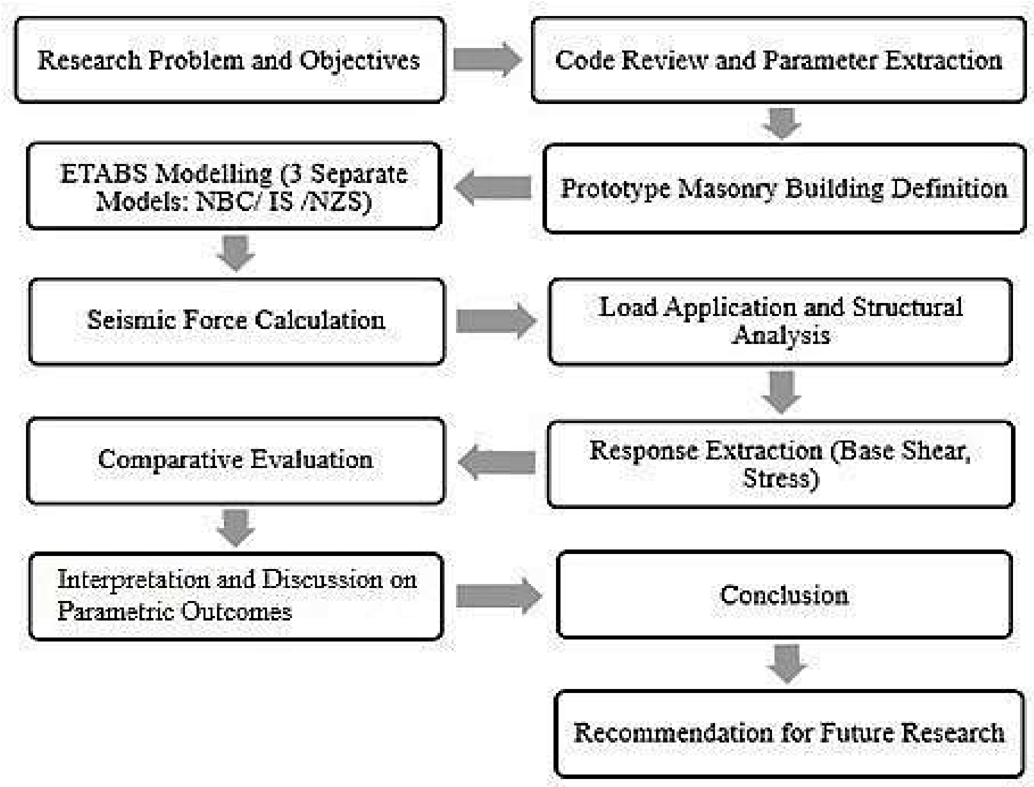


**Figure 1**: Flowchart of methods

This research evaluates seismic demand in two-storey load-bearing masonry buildings signifying common residential construction in Nepal. The study area is Pokhara, corresponding to a seismic zoning factor of 0.3 (PGA) under NBC105:2020. Medium dense soil (N=15 within 50 m depth) was supposed, classified as Soil Type B (NBC), Soil Type II (IS 1893:2016), and Class C (NZS 1170.5:2004). Soil-structure interaction was neglected, and base supports were modelled as fixed for simplification in analysis.

A masonry building Model 1 was first manually analysed applying the equivalent static (seismic coefficient) method to compare base shear coefficients across NBC105:2020, IS 1893 (Part I):2016, and NZS 1170.5:2004. Three numerical models were then developed in ETABS employing finite element method. Slabs and masonry walls were modelled with shell elements, and beams with frame elements. The structural system comprised of two storeys with rigid diaphragm action. Model formations were complied with dimensional limits of NBC 202:2015 (DUDBC, 2015). Building descriptions are concisely presented in Table1, and model dimensions are shown in Table 2. Representative layouts and 3D configurations are shown in Figure 2 to 5.

**Table 1**: Masonry Building Description

| S. N | Masonry Building Description | M1 |
|---|---|---|
| 1 | Plan Area | $26.97m^2$ |
| 2 | X-Y Direction Grid Spacing | 3.5m |
| 3 | Storey Height | 2.5m |
| 4 | Number of Storey | 2 |
| 5 | Slab Thickness | 125mm |
| **Material Specification** | | |
| 1 | Grade of Concrete $M_{20}$ | $f_{ck}$=20N/mm$^2$ |
| 2 | Grade of Mortar | M1 (Cement sand ratio 1:5) |
| 3 | Steel Fe500 | $f_y$=500N/mm$^2$ |
| 4 | Brick Compressive strength | 10N/mm$^2$ |
| 5 | Basic compressive stresses for masonry after 28 days (IS1905-1987) | 0.96N/mm$^2$ |
| 6 | Compressive strength of masonry $f_{m'}$ (IS1893:2016) | =3.37N/mm$^2$ |
| 7 | Young's modulus of brick masonry $E_m$ | 550×3.73=2051.5N/mm$^2$ |
| 8 | Poisson's ratio for brick masonry | 0.3 |
| **Design Loads** | | |
| 1 | Masonry wall | 19kN/m$^3$ |
| 2 | RCC Slab | 25kN/m$^3$ |
| 3 | Floor live load (IS: 875 (Part 2)-1987 Table 1) | 2kN/m$^2$ |
| 4 | Roof Live Load | 1.5kN/m$^2$ |
| 5 | RCC Beam | 25kN/m$^3$ |

**Table 2**: Model dimensions

| Model type | Single bay size | Height of storey (m) |
|---|---|---|
| Model 1 | 3.50 m x 3.50 m | 2.855 |
| Model 2 | 4.73 m x 3.23 m | 3.200 |
| Model 3 | 3.50 m x 3.50 m | 3.200 |

Figures 2 to 5, as shown below, show the representative structural configuration employed for analytical and numerical evaluation. The models signify typical low-rise residential masonry building construction prevalent in Nepal, and were selected to confirm compliance with geometric limitations specified in NBC 202:2015.

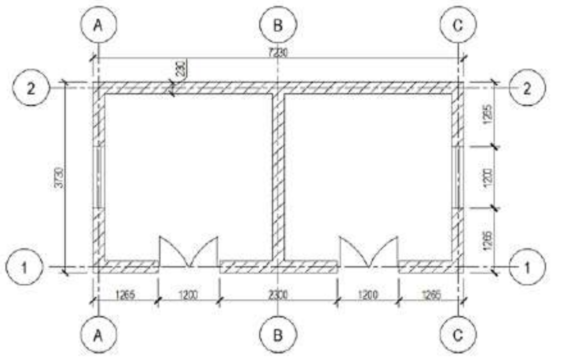


**Figure 2**: Ground floor plan of Model 1 for manual calculation

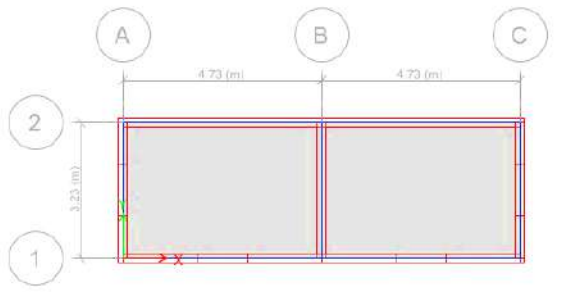


**Figure 3**: Ground floor plan of Model 2

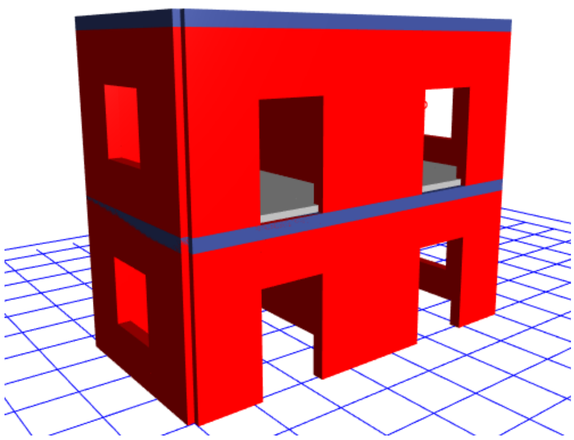

**Figure 4**: 3D Masonry building model (Model 1 )

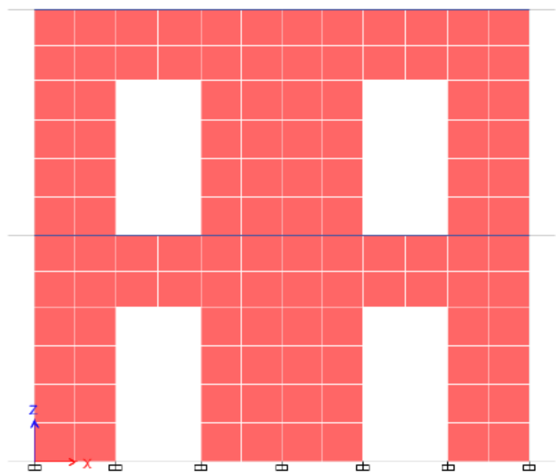


**Figure 5**: Front Elevation View of Model 3

Material properties included $M_{20}$ concrete ($f_{ck}$ = 20 MPa), Fe500 steel ($f_y$ = 500 MPa), brick compressive strength of 10 MPa, and masonry prism strength of 3.37 MPa. Young's modulus of masonry was taken as 2051.5 MPa with Poisson's ratio 0.3. Permissible stresses were adopted from IS 1905:1987. Dead loads were calculated by means of unit weights of 19 kN/m³ for masonry and 25 kN/m³ for RCC, with imposed loads as per IS 875 (Part 2)-1987 and live load factor as per NBC 105:2020 as shown in Table 3 and 4. Seismic weight was evaluated following corresponding codes.

**Table 3**: Imposed load to be considered for calculation of seismic weight as per IS code

| S. N | Imposed Uniformly Distributed Loads kN/m² | Percentage of Imposed Load to be considered |
|---|---|---|
| 1 | Up to and including 3.0 | 25 |
| 2 | Above 3.0 | 50 |

**Table 4**: Live load factor as per NBC 105:2020

| S. N. | Live Load Typology | Factor considered |
|---|---|---|
| 1 | Storage | 0.60 |
| 2 | For Other Purpose | 0.30 |
| 3 | Roof | Nil |

The empirical formula applied to estimate the fundamental period according to individual seismic code are concisely shown below.

- NBC 105:2020 : $T_1 = 1.25\ k_t H^{\frac{3}{4}}$ … [Eq.1] (Cl 5.1.2, 3 NBC 105:2020)

Where, $T_1$ = Approximate fundamental period of vibration, $k_t$ = Structural system co-efficient, $H$ = Height of the building from foundation or from top of a rigid basement.

- IS 1893:2016: $T_a = \frac{0.09h}{\sqrt{d}}$ … [Eq. 2]

Where, $T_a$ = Approximate fundamental natural period of vibration of the building, $h$ = Height of the building in meters, $d$ = Base dimension of the building in meters at the plinth level, measured along the direction of the lateral earthquake force being considered

- NZS 1170.5:2004: $T_1 = 1.25 k_t {h_n}^{0.75}$ … [Eq. 3] (Cl 4.1.2.2 NSZ 1170.5:2020)

Where, $T_1$ = Fundamental natural period of the building (in seconds), $k_t$ = Structural system coefficient, $H$ = Height of the structure (in meters)

The design horizontal seismic coefficients were obtained as follows:

- NBC 105:2020 (ULS): $C_d(T_1) = \frac{C(T_1)}{R\mu \times \Omega u}$ … [Eq. 4]

Where, $C_d(T_1)$ = Horizontal base shear coefficient, $C(T_1)$ = Elastic response spectrum ordinate, $R_\mu$ = Ductility factor, $\Omega_u$= Over-strength factor (for ULS)

- IS 1893:2016: $A_h = \frac{(\frac{Z}{2})(\frac{S_a}{g})}{(\frac{R}{I})}$ … [Eq. 5]

Where, $A_h$ = Design horizontal seismic coefficient, $Z$ = Zone factor, $I$ = Importance factor, $R$ = Response reduction factor, $\frac{S_a}{g}$ = Spectral acceleration coefficient

- NZS 1170.5:2004 (ULS): $C_d(T_1) = \frac{C(T_1)S_p}{K_\mu}$ … [Eq. 6]

Where, $C_d(T_1)$ = Design horizontal seismic action coefficient at the fundamental period, $C(T_1)$ = Elastic site hazard spectrum ordinate at the fundamental period, $T_1$ = Fundamental natural period of vibration of the structure in the direction under consideration, $S_p$= Structural performance factor, $K_\mu$ = Ductility factor modification coefficient

Vertical distribution of storey forces obeyed code-specific formulations. Base shear and storey force patterns were acquired from ETABS and compared with manual results for validation. The consistency of modelling assumptions was established by the agreement between analytical and numerical base shear values.

- NBC 105:2020, NBC 105:1994

$F_i = \frac{W_i {h_i}^k}{\sum_i^n W_i {h_i}^k} \times V$ ... [Eq. 7]

$F_i = \frac{W_i h_i}{\sum W_i h_i} \times V$ ... [Eq. 8]

Where, $F_i$ = Design lateral seismic force at level $i$, $W_i$ = Seismic weight at level i (dead load + appropriate portion of imposed load), $h_i$ = Height of level i measured from the base, $k$ = Exponent related to the fundamental period of the building, $\sum W_i\, h_i^k$ = Summation over all storeys, $V$ = Total design base shear of the building

- IS 1893:2016: $F_i = \frac{W_i {h_i}^2}{\sum_i^n W_i {h_i}^2} \times V$ … [Eq. 9]

Where, $F_i$ = Design lateral seismic force at level $i$, $W_i$ = Seismic weight at level $i$ (dead load + appropriate portion of imposed load). $h_i$ = Height of level $i$ measured from the base, $\sum h_i^2$ = Square of the height term, indicating a parabolic distribution of seismic forces, $\sum W_i\, h_i^2$ = Summation $W_i\, h_i^2$ over all storeys, $V$ = Total design base shear of the building.

Main assumptions include linear elastic response, equivalent static analysis applicability (T < 0.5 s), rigid diaphragm action, and absence of torsional irregularity. This outline enables consistent comparison of seismic demand estimates and design implications for masonry structures under different international and national seismic codes.

## 3. Results and Discussion

The comparative evaluation demonstrates how variations in seismic hazard representation, response modification factors, and force distribution rules among NBC105:2020, IS 1893:2016, and NZS 1170.5:2004 impact seismic demand in low-rise masonry buildings.

### 3.1 Code provisions and fundamental period

Although soil classification systems differ in nomenclature there exist four classes in NBC, three in IS, and five in NZS for the selected site condition (N = 15) consistently agrees to medium soil across all codes. NZS offers a more tough hierarchy for classification, emphasising shear wave velocity, whereas NBC and IS rest on mainly on standard penetration indices. This difference is methodological rather than numerical for the current case.

The empirical time period relations are mostly consistent, obeying $T_1 = 1.25\ k_t H^{\frac{3}{4}}$ in NBC and NZS, while IS presents base-dimension dependency for masonry through $T_a = 0.09h/\sqrt{d}$. As shown in Figure 6, the computed periods for the two-storey model lies within a narrow band of 0.191 to 0.266 second, signifying negligible sensitivity to code choice for low-rise regular masonry buildings. This verifies that, for short-period structures (T < 0.5 s), differences in seismic demand are not ruled by period estimation but by force minimisation and hazard factors.

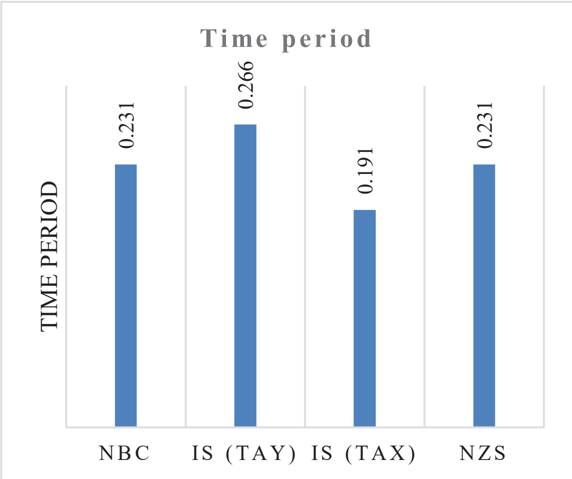


**Figure 6**: Time period of building as per NBC, IS, NZS codes

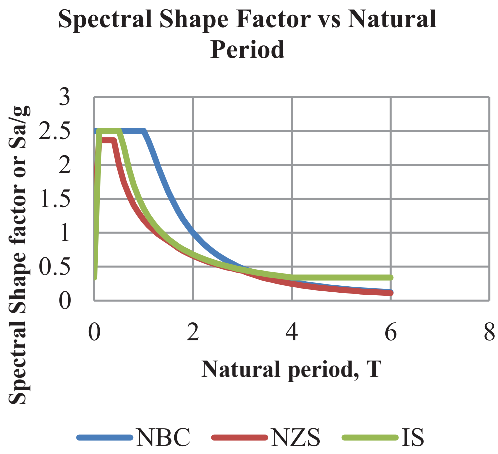


**Figure 7**: Spectral shape factor for equivalent soil type

### 3.2 Spectral shape factor

The comparative graph of spectral shape factors presented in Figure 7 clarifies that the three codes deliver similar amplification for short-period structures. However, differences become more noticeable at longer vibration periods. For short-period structures ($T \leq 4$ s), spectral shape factors among the codes vary by only 5.93%, signifying close agreement in predicted seismic demand. However, at $T = 1$ s, the NBC curve remarkably up-rises than the others, with values 102% higher than NZS and 83% higher than IS almost twice that of NZS and 1.8 times that of IS. This graphical divergence reveals NBC's more traditional long-period amplification, suggesting considerably greater design forces for flexible or mid-rise structures. However, the study deliberates low-rise masonry buildings having less than 8 m height, the real-world difference remains limited to 5.93%, leading to comparable design implications**.**

### 3.3 Horizontal base shear coefficient

The most noticeable discrepancy was observed in horizontal base shear coefficients as shown in Figure 8. The horizontal base shear coefficient is ruled by spectral shape factor, zone (or hazard) factor, over-strength factor, and ductility factor. In IS 1893:2016, over-strength and ductility come together as the response reduction factor, whereas NZS 1170.5 initiates the elastic site hazard spectrum incorporating spectral shape, hazard, return period, and near-fault factors. The ductility factor in NZS is pointedly lower than in NBC

105:2020 and IS, causing significantly higher base shear. Consequently, NZS produces base shear coefficients 161% higher than IS and 51% higher than NBC. This illustrates NZS adopts a more traditional force-based design approach. Besides, both NBC and NZS present serviceability limit state base shear requirements, where remarkable variation is noticed, reflecting different performance prospects at reduced seismic intensity levels.

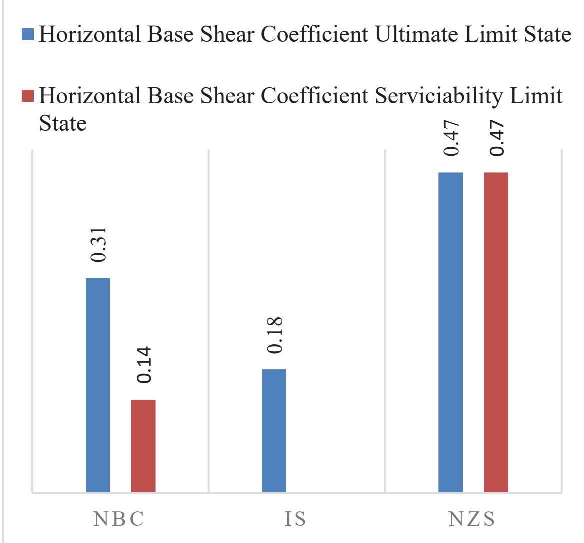


**Figure 8**: Horizontal base shear coefficient

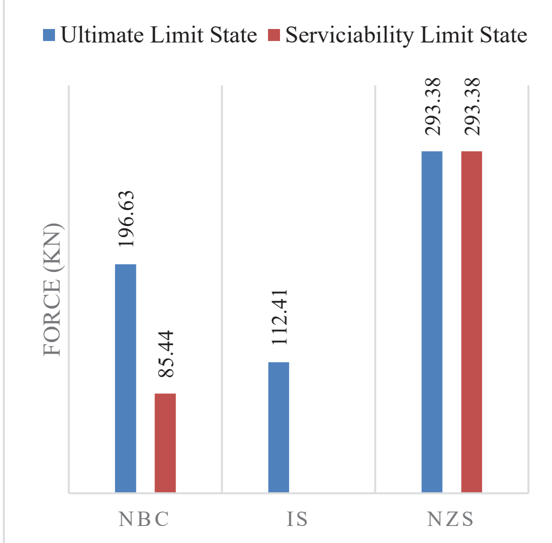


**Figure 9**: Base shear

### 3.4 Base shear and seismic weight

Seismic weight calculations as in Table 6 show marginal variation because imposed load participation factors only slightly differ. So, the base shear variation directly indicates coefficient differences. As shown in Table 5 and Figure 9, NZS yields the largest base shear, followed by NBC and IS. The NZS base shear is about 75% higher than NBC and around 161% higher than IS results. From an engineering perspective, this denotes substantially greater member forces, reinforcement demand, and construction cost under NZS requirements.

**Table 5**: Horizontal base shear (kN)

| Codes | Ultimate Limit State | Serviceability Limit State |
|---|---|---|
| NBC | 196.63 | 85.44 |
| IS | 112.41 | |
| NZS | 293.38 | 293.38 |

The visible variation in base shear coefficients has vital design implications. Masonry structures normally possess inadequate ductility and energy dissipation capacity.

Therefore, high value seismic coefficients translate straight into increased wall stresses instead of being absorbed by way of inelastic deformation. Accordingly, the larger base shear projected by NZS code provisions leads to higher shear demand in masonry walls, which may necessitate thicker walls, enriched mortar quality, or extra reinforcement to maintain adequate safety margins.

**Table 6**: Parameters for computation of base shear for Model 1

| S. N. | Parameters | NBC | IS | NZS |
|---|---|---|---|---|
| 1 | Soil Classification (N Value of 15 within depth of 50m) | Soil Type -B | Soil Type-II | Class C |
| 2 | Zone factor (PGA) | 0.3 | 0.36 | 0.3 |
| 3 | Response Reduction Factor including overstrength factor | $R\mu \times \Omega u$ =2.4 | R=2.5 | $\frac{K_{\mu}}{S_p} = 1.475$ |
| 4 | Importance Factor | 1 | 1 | NA |
| 5 | Near Fault Factor | NA | NA | 1 |
| 6 | Return Period Factor | NA | NA | 0.975 |
| 7 | Time Period | $T_1 = 1.25 k_t H^{\frac{3}{4}} =$ 0.231 | $T_a = \frac{0.09h}{\sqrt{d}}$ ($T_{ax}$)= 0.191sec ($T_{ay}$)= 0.266sec | $T_1 = 1.25 k_t {h_n}^{0.75}$ =0.231 |
| 8 | Spectral Shape Factor | 2.5 | 2.5 | 2.36 |
| 9 | Base Shear Coefficient | $C_d(T_1) = \frac{C(T_1)}{R\mu \times \Omega u} =$ 0.313 | $A_h = \frac{(\frac{Z}{2})(\frac{S_a}{g})}{(\frac{R}{I})}$ =0.18 | $C_d(T_1) = \frac{C(T_1)S_p}{K_{\mu}}$ $= 0.467$ |
| 10 | Seismic Weight | = DL+0.3LL=579.69 kN | = DL+0.25LL =575.07kN | =DL+0.3LL=579.69kN |
| 11 | Base Shear (Ultimate Limit State in kN) | 196.63 | 112.41 | 293.38 |

### 3.5 Storey force distribution

Storey force distribution patterns in Table 7 and Figure 10 expose additional code-dependent variation. IS applies a quadratic height distribution, NBC employs a period-dependent exponent, and NZS uses 8% of base shear at roof level with the remaining 92% linearly distributed. NZS results in greater forces at both storeys, mainly at the top level, escalating overturning demand. This has direct consequences for wall border stresses and anchorage detailing.

**Table 7**: Storey force distribution (kN)

| Storey level | NBC | IS | NZS |
|---|---|---|---|
| 1st Floor | 76.74 | 27.82 | 114.50 |
| 2nd Floor | 104.70 | 75.69 | 156.22 |

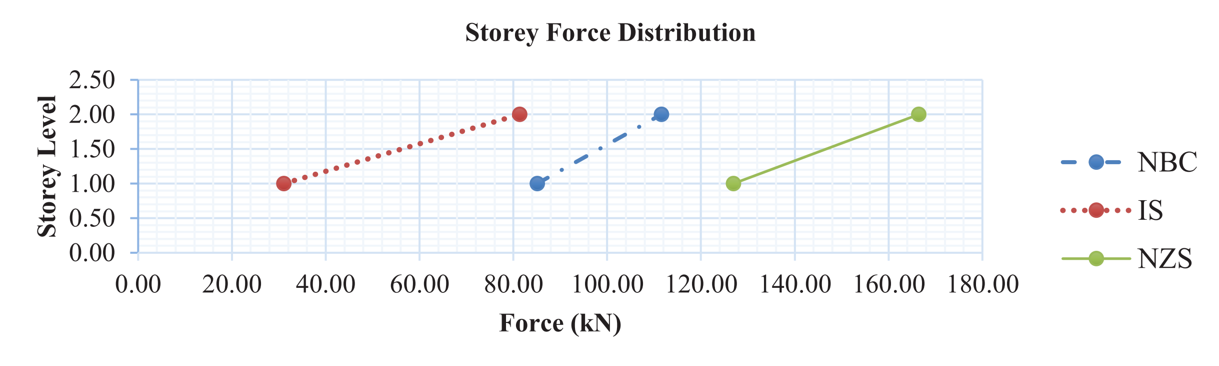


**Figure 10**: Storey force distribution

### 3.6 Stress response from finite element analysis

Finite element analysis in ETABS computed compressive (S22) and shear (S12) stresses for three geometric models as shown in Tables 8. For all models, compressive stresses under NBC and IS remain within alike ranges and approach permissible limits defined by IS 1905:1987. NZS-based loading consistently produces higher compressive and shear stresses because of larger base shear demand.

**Table 8**: Average stress at strip (MPa)

| Model | Stress type | NBC | IS | NZS |
|---|---|---|---|---|
| Model 1 | Compressive stress (S22) | 0.62 | 0.58 | 0.76 |
| | Shear Stress (S12) | 0.13 | 0.10 | 0.21 |
| Model 2 | Compressive stress (S22) | 0.58 | 0.54 | 0.78 |
| | Shear Stress (S12) | 0.18 | 0.14 | 0.25 |
| Model 3 | Compressive stress (S22) | 0.62 | 0.61 | 0.83 |
| | Shear Stress (S12) | 0.15 | 0.13 | 0.23 |

Shear stress values surpass permissible limits in several cases, particularly under NZS loading. This points out that shear capacity governs design for low-rise masonry instead of axial compression. Increasing wall thickness or improving masonry compressive strength would be essential to satisfy code limits. The stress contours presented in Figure

11 to 16 confirm concentration of shear stresses near wall diaphragm interfaces and at critical strips.

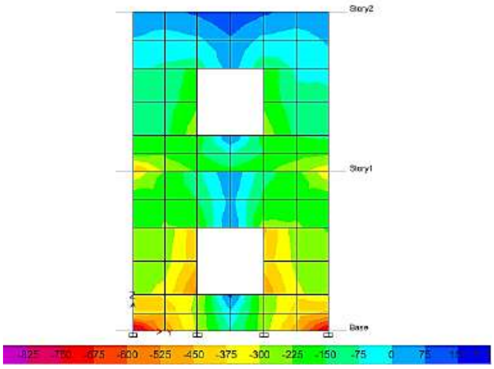


**Figure 11**: Compressive stress (S22) along grid A-A as per IS code (Model 1)

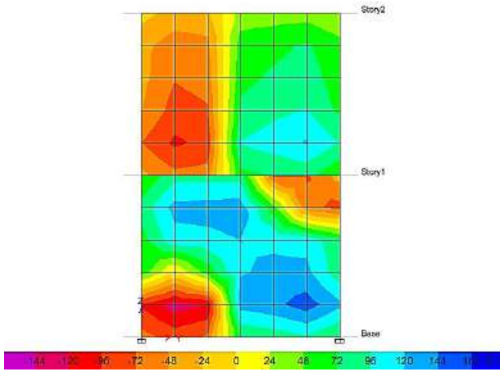


**Figure 12**:Shear stress (S12) at grid B-B as per IS code (Model 1)

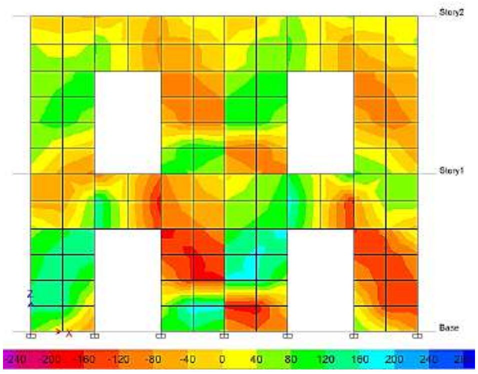


**Figure 13**: Shear stress (S12) along grid 1-1 as per NZS code (Model 1)

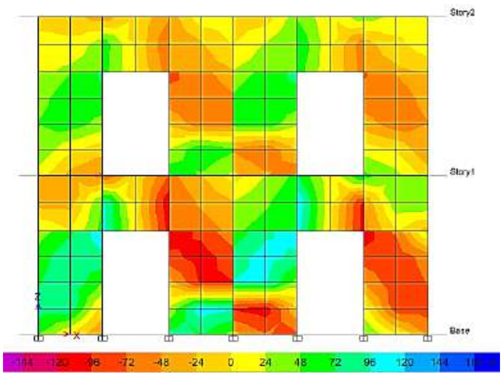


**Figure 14**: Shear stress (S12) along grid A-A as per NBC (Model 1)

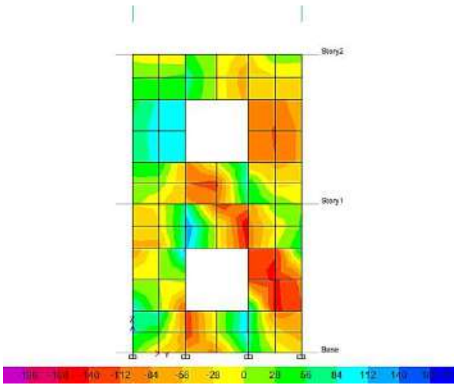


**Figure 15:** Shear stress (S12) along grid C-C as per IS code (Model 2)

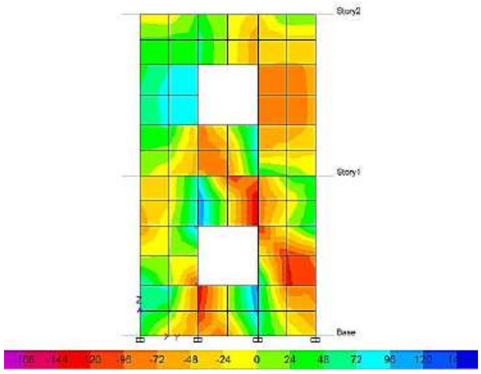


**Figure 16**: Shear stress (S12) along grid C-C as per IS code (Model 3)

The outcomes align with earlier comparative studies as an example (Giri et al.) that identified higher base shear estimates under more conservative or lower-ductility code bases. However, dissimilar to reinforced concrete systems, masonry structures display limited ductility. So, higher force demand directly turns into higher stress ratios without substantial redistribution capacity.

### 3.7 Engineering significance

For representative low-rise masonry buildings of Nepal, estimated natural time period and spectral shape variances have limited effect on seismic design outcomes. In its place, seismic demand is highly controlled by response reduction philosophy and performance factors rooted in each code. NZS provisions primarily focus to considerably higher design forces and stress levels, requiring improved safety margins but increased material demand. IS produces the lowest force demand, reliably resulting in more economical but less conservative designs. NBC dwells in a midway position, exhibiting calibration to national hazard circumstances.

These findings validate that selection of code significantly affects structural demand predictions even for matching geometry and material properties. For masonry practice in Nepal, cautious evaluation of ductility assumptions and shear capacity is important, as shear stresses commonly govern design sufficiency.

### 3.8 Implications for masonry design in seismic regions

For real-world engineering application, the results advise that the selection of seismic design code pointedly influences predicted seismic demand for low-rise masonry buildings. NBC code provisions offer intermediate seismic force levels consistent with national hazard conditions, whereas IS code arrangements may lead to low value design forces and more economically optimised construction. NZS code provisions distinctly result in higher design forces and greater stress levels, which may enhance safety margins but escalate material demand. These outcomes may support engineers and code developers in evaluating the appropriateness of seismic design parameters for masonry construction in regions with alike seismic hazard features.

## 4. Conclusions

The research exhibits that, for typical low-rise masonry buildings of Nepal, the estimated time period across NBC, IS, and NZS codes endorses negligible variation, confirming that empirical relations yield comparable dynamic features. Spectral shape factors for short-period structures

($T \leq 4$ s) differ by only 5.93%, highlighting minimal influence of soil classification on short-period seismic demand. But, base shear coefficients vary significantly, with NZS predicting 161% higher values than IS and 51% higher than NBC, designating the differences in ductility and performance factor provisions. Storey shear distribution also varies by code, with NBC applying a period-dependent exponent, IS using a quadratic distribution, and NZS following a linear distribution with 8% applied at the roof, impacting member force allocation. Finite element analysis exposes that compressive stresses under NBC and IS remain within analogous ranges, whereas NZS generates significantly higher compressive and shear stresses, often impending or beyond permissible limits. These conclusions focus that selection of code substantially affects seismic force demand, stress levels, and design necessities, mainly for masonry walls critical in shear. The results exhibit that while empirical period estimation and spectral shape factors indicate comparatively small variation for short-period masonry structures, the selection of response reduction and performance factors considerably influences seismic force estimation. On the other hand, differences in base shear coefficients directly impact wall stress levels and structural safety limits. These relationships spotlight the significance of careful calibration of ductility and response modification parameters in seismic design codes for masonry structures. Engineering consequences suggest that careful and accountable consideration of ductility, base shear, and storey force distribution is indispensable for safe and economical design of low-rise masonry structures in seismic areas.

## 5. Recommendations for future research

Future research should address limitations perceived in the present study by line up with analytical models with the newest release of NBC 105:2025 (Second Revision) (DUDBC, 2025). Explicitly, revisions to masonry guidelines in NBC 202 (DUDBC, 2015) are needed to ensure wall thickness, rebar placement, and building dimensions satisfactorily limit shear stress within permissible ranges. Comparative studies could discover corrections in IS code load combinations and zoning factors to harmonize elastic site spectra with NBC provisions. Modelling should incorporate multiple seismic zone scenarios (0.25g to 0.4g) to cover up regional variability in Nepal. Furthermore, the dependence on elastic analysis should be expanded using nonlinear dynamic or pushover analysis to evaluate masonry performance under genuine seismic demand, delivering more accurate predictions of structural safety and serviceability.

**Acknowledgements**

The authors would like to acknowledge Prof. Dr. Tek Raj Gyawali, Prof. Dr. Govind Prasad Lamichhane, Assoc. Prof Dr. Hemchandra Chaulagain and Er. Suraj Thapa for their advice and invaluable feedbacks. The authors also express sincere gratitude to colleagues and helping hands for this research. Furthermore, authors gratefully acknowledge Pokhara Engineering College (PEC) for creating platform to publish the research under civil and structural engineering.

**References**

- Adhikari, R. K., Vatteri, A. P., & D'Ayala, D. (2023). Seismic performance assessment of low rise unreinforced and confined brick masonry school buildings using the applied element method. Buildings, 13(1), Article 159. https://doi.org/10.3390/buildings13010159
- Baruwal, R., Chhetri, B., & Chaulagain, H. (2020). Probabilistic seismic hazard analysis and construction of design spectra for Pokhara valley, Nepal. Asian Journal of Civil Engineering, 21(10), 1297–1308.
- Bureau of Indian Standards. (2016). IS 1893 (Part 1): 2016—Criteria for earthquake resistant design of structures, Part 1: General provisions and buildings (Sixth revision). Bureau of Indian Standards.
- Bureau of Indian Standards. (2016). IS 1893 (Part 1): 2016—Criteria for earthquake resistant design of structures, Part 1: General provisions and buildings (Sixth revision). Bureau of Indian Standards.
- Bilham, R. (2015). Raising Kathmandu. Nature Geoscience, 8(8), 582–584.
- Borah, B., Kaushik, H. B., & Singhal, V. (2023). Analysis and design of confined masonry structures: Review and future research directions. Buildings, 13(5), Article 1282. https://doi.org/10.3390/buildings13051282
- Bothara, J., Dizhur, D., & Ingham, J. (2018). Masonry building design for earthquake affected remote areas of Nepal. In 10th Australasian Masonry Conference, Sydney, Australia.
- Chaulagain, H., Rodrigues, H., Jara, J., Spacone, E., & Varum, H. (2013). Seismic response of current RC buildings in Nepal: A comparative analysis of different design/construction. Engineering Structures, 49, 284–294.

- Chi, B., Quan, Y., Wang, F., & Yang, X. (2024). An investigative study for the seismic performance of composite reinforced masonry wall with prestressing technology. Buildings, 14(1), Article 264. https://doi.org/10.3390/buildings14010264
- Department of Urban Development and Building Construction. (1994). NBC 105: 1994-Seismic design of buildings in Nepal. His Majesty's Government of Nepal.
- Department of Urban Development and Building Construction. (2015). NBC 202: 2015-Mandatory rules of thumb: Reinforced cement concrete buildings without masonry infill. Government of Nepal.
- Department of Urban Development and Building Construction. (2020). NBC 105: 2020-Seismic design of buildings in Nepal. Government of Nepal.
- Department of Urban Development and Building Construction. (2025). NBC 105: 2025 – Seismic design of buildings in Nepal (Second revision). Government of Nepal.
- Dixit, A. M., Parajuli, Y. K., & Guragain, R. (2004, August). Indigenous skills and practices of earthquake resistant construction in Nepal. In 13th World Conference on Earthquake Engineering (pp. 1-6).
- Dogangun, R., & Livaoglu, R. (2006). A comparative study of the design spectra defined by Eurocode 8, UBC, IBC and Turkish Earthquake Code on R/C sample buildings. Journal of Seismology, 10, 335–351.
- Gautam, D., & Chaulagain, H. (2016). Structural performance and associated lessons to be learned from world earthquakes in Nepal after 25 April (Mw 7.8) Gorkha earthquake. Engineering Failure Analysis, 68, 222–243.
- Giri, A., Bhatt, D., Gautam, D., & Chaulagain, H. (2018). Comparison between the seismic codes of Nepal, India, Japan, and EU. Asian Journal of Civil Engineering.
- Khatri, A., Chaisir, G. S., Yadav, A. K., Sah, G. K., Chaulagain, K., Khanal, N., & Ojha, B. (2025). Comparison of seismic parameter in RC building using NBC 105:2020, IS 1893:2016 and ASCE 7 22. International Journal on Engineering Technology, 3(1), 279–288. https://doi.org/10.3126/injet.v3i1.87073
- Khose, V. N., Singh, Y., & Lang, D. H. (2012). A comparative study of design base shear for RC buildings in selected seismic design codes. Earthquake Spectra, 28(3), 1047-1070.

- Kunwar, S., Thapa, D., Paudel, A., & Shrestha, A. (2024). A comparative analysis of an RC low rise building with the seismic codes of countries lying in the Himalayas: China, India, Nepal, and Pakistan. Discover Civil Engineering, 1, Article 117. https://doi.org/10.1007/s44290-024-00122-7
- McIntosh, R., & Pezeshk, S. (1997). Comparison of recent U.S. seismic codes. Journal of Structural Engineering, 123(8), 993–1000. https://doi.org/10.1061/(ASCE)0733-9445(1997)123:8(993)
- Mosleh, H., Rodrigues, H., Varum, A., Costa, A., & Arede, A. (2016). Seismic behaviour of RC building structures designed according to current codes. Structures, 7, 1–13.
- New Zealand Standard. (2004). NZS1170.5 Supp1:2004. New Zealand.
- New Zealand Standard. (2013). Concrete masonry buildings not requiring specific engineering design, NZS 4229:2013. New Zealand.
- Niu, S. (2025). Seismic resilience evaluation and improvement of confined masonry structures using finite element analysis and the N2 method. Applied and Computational Engineering. https://doi.org/10.54254/2755-2721/2025.20185
- Parajuli, R. R., Furukawa, A., & Gautam, D. (2020). Experimental characterization of monumental brick masonry in Nepal. Structures, 28, December 2020 Structures 28:1314 1321 DOI:10.1016/j.istruc.2020.09.065
- Shah, P., Karki, S., Magar, R., Pathak, S. K., Sherpa, N., Keshari, N. K., & Dhakal, B. P. (2025). Comparison of seismic analysis and design outputs using IS 1893 (Part 1):2016 and NBC 105:2020 codes using finite element software. Journal of Advanced College of Engineering and Management, 11(1), 193–201.https://doi.org/10.3126/jacem.v11i1.84539
- Waris, M., Al-Jabri, K., & El-Hussain, I. (2017). Comparison of Oman Seismic Code for buildings with international counterparts. In World Conference on Earthquake (16WCEE), Santiago, Chile.
- Zhinan, J., & Zhonghai, Z. (2012). Comparison of base shear force method in the seismic design codes of China, America and Europe. Applied Mechanics and Materials, 166–169, 2345–2352. https://doi.org/10.4028/www.scientific.net/AMM.166-169.2345

# Pokhara Engineering College Journal (PECJ)

*Applied Sciences and Engineering Insights*

ISSN: 3021-9795 (Print) / 3059-9628 (Online)

(Volume-3, Issue- I)


# Seismic Vulnerability Assessment of Plan Irregularity Reinforced Concrete Framed Building


Praju Pasin Thakali[1], Puja Roka Magar[2], Himal Gurung[3], Krisha Khadka[4] Bimal Bhandari[5], Yam Bahadur Thapa[6]

[1, 2, 3,4] Department of Civil Engineering, Pokhara Engineering College, Pokhara, Nepal

[5,6]Assistant Professor, Department of Civil Engineering, Pokhara Engineering College, Pokhara, Nepal

**Corresponding email*: prajuthakali061@gmail.com





*Received: 15- December-2025; Revised 15-February -2026; Accepted: 05-March-2026*

*DOI: : https://doi.org/10.3126/pecj.v3i1.93531*



**Abstract**

The study presents the seismic vulnerability assessment of plan irregular reinforced concrete framed building. At PEC, there are a total of 5 blocks among which Block-B, established in 2000 AD was selected for detailed assessment due to its structural irregularities. The assessment started with visual inspection using FEMA guidelines, which revealed undersized members, poor concrete quality, irregular plan layout, torsional irregularity, and visible deterioration. Non-destructive tests (Ultrasonic Pulse Velocity and Rebound Hammer) confirmed good internal concrete integrity but weak surface strength. To understand the building's seismic performance more clearly, a structural model was developed in ETABS v22.5 following NBC 105:2020. The analysis showed that 130 members failed seismic checks, including torsional irregularities, storey drift, and displacement limits. Based on these findings, a hybrid retrofitting plan was proposed combining concrete jacketing for columns and beams, steel jacketing for selected beams, and the addition of reinforced concrete shear walls. Post-retrofitting analysis showed clear improvements in displacement, drift, and torsional behavior bringing the building's performance closer to national seismic safety standards. From an economic point of view, retrofitting of the building is far more affordable than demolishing and constructing a new one. In other words, retrofitting required only 15.6% of the replacement cost making it the practical choice. Overall hybrid retrofitting stands out as both technically effective and economically practical.

**Keywords:** Seismic Vulnerability, Non-Destructive Test, Hybrid Retrofitting

## 1. Introduction

Nepal, located at the convergence of the Indian and Eurasian tectonic plates, is among the most seismically active regions globally. Nepal ranks as the 11$^{th}$ most vulnerable country globally to earthquakes, as reported by UNICEF(UNICEF Nepal, 2017). Pokhara falls under Seismic Zone V according to NBC 105:2020, indicating very high earthquake risk. Its proximity to the Main Central Thrust Fault and soft layered soil conditions further amplify ground shaking, increasing seismic vulnerability(Baruwal, Chhetri and Chaulagain, 2020).

Educational buildings play a significant role in disaster recovery. In addition to their role as classrooms, they often serve as shelters and emergency hubs. For this reason, NBC 105:2020 grants them an Importance Factor of 1.25 to increase seismic design loads and ensure functionality before and after earthquakes.

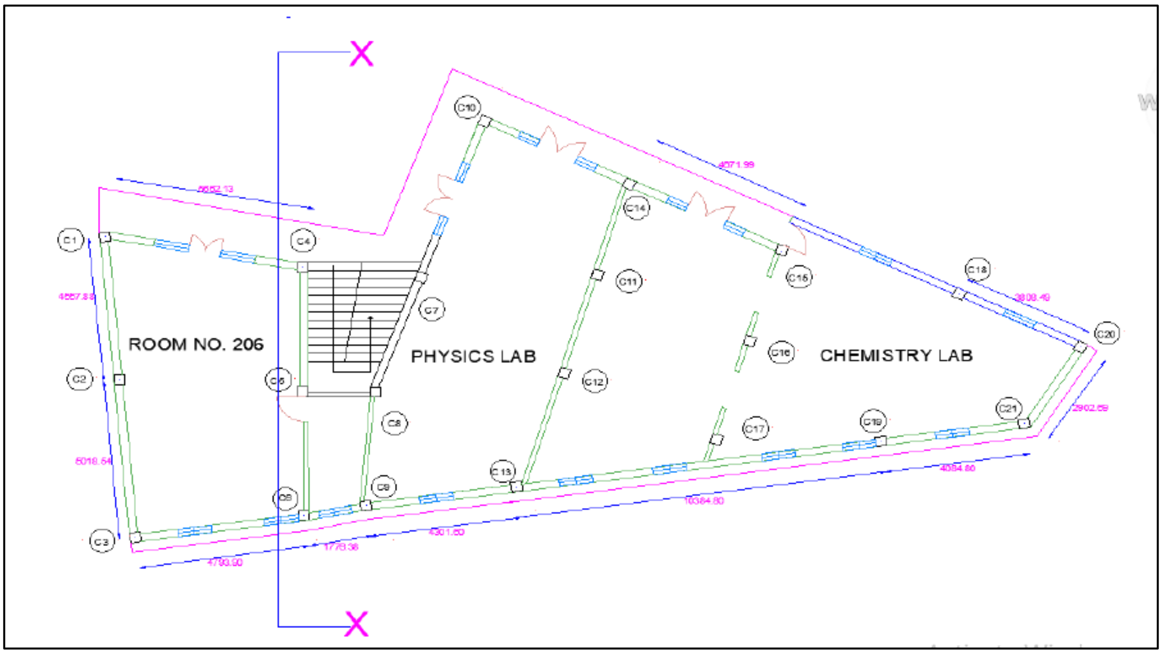


**Figure 1:** Architectural drawing of first floor

The Diploma Building (Block B) of the Pokhara Engineering College (PEC) is a six storey reinforced concrete (RC) frame structure with hollow block infill walls built in 2000 AD. Since the structure was built before the implementation modern seismic codes, it has serious plan irregularities in the form of re-entrant corners and an asymmetric column layout which would induce torsional effects and stress concentrations during earthquakes. Over time, material deterioration reduces the structure's capacity to resist lateral loads, raising the risk of severe damage if an earthquake occurs.

This paper presents the seismic vulnerability assessment of plan-irregular RC framed building in regional centers like Pokhara. Block B was evaluated based on visual inspection, (NDT), and structural modeling in ETABS v22.5. The findings highlight critical structural deficiencies and recommend hybrid retrofitting measures to ensure the building remains safe, stable, and functional during future earthquakes.

## 2. Materials and Methods

### 2.1 Qualitative assessment

Qualitative assessment is performed to determine whether the building in existing condition meets the seismic performance capability(DUDBC, 2011). It was carried out by on-site inspections, reviewing available drawings and interviewing to gather information. The checklist was prepared as per FEMA 310 to identify vulnerabilities factors(FEMA, 1998). This assessment serves as a qualitative measure to identify seismic weaknesses in a building before conducting a detailed evaluation(DUDBC, 2011).

### 2.2 Quantitative assessment

It is the second phase in seismic vulnerability assessment which follows a quantitative approach after the qualitative analysis. It includes a detailed seismic evaluation to identify deficiencies more accurately and identify appropriate retrofitting measures.

#### 2.2.1 Non-Destructive Test

Non-destructive tests were performed to evaluate the in-situ strength and quality of concrete without damaging the structure. The Rebound Hammer test was conducted to determine the surface hardness and compressive strength of concrete. For each test point, six sets of readings were taken and average rebound number was calculated after discarding outliers(Bureau of Indian Standards, 1978). As per IS 516 (Part 5/Sec 4), average rebound number was used to classify concrete quality. The correlation graph was used to determine the corresponding compressive strengths(Bureau of Indian Standards, 2020).

Indirect method was used to test UPV by placing the transducers on opposite faces of the same surface of the concrete member. At each test point, nine readings were taken and the average pulse velocity was calculated. A velocity criteria for concrete quality grading specified in IS 516 (Part 5/Sec 1) was used to interpret the result of the tests(Bureau of Indian Standards, 2018).

2.2.2 Structural modeling and analysis

The building was modeled in ETABS v22.5 to evaluate its seismic performance under earthquake loading. The analysis was carried out using the Equivalent Static Method (ESM) where lateral seismic forces were applied to the structure based on parameters such as the seismic zone factor, importance factor, response reduction factor, and the building's seismic weight and non-parallel load combination was used to realistically capture multi-directional forces which is especially important in case of irregular buildings. Then the building response was checked against the provisions of NBC 105:2020 including torsional irregularity, storey drift, soft storey condition, and overall storey displacements(DUDBC, 2020). These evaluations were carried out to ensure that the building's seismic response meets the requirements of NBC 105:2020.

2.3 Hybrid Retrofitting

To enhance seismic performance of the building and also for compliance with present code requirements, a hybrid retrofitting approach was adopted combining concrete jacketing for columns and beams, steel jacketing for selected beams, and the addition of reinforced concrete shear wall. This combination was selected to address both local member deficiencies and global structural irregularities identified during analysis. These retrofitting measures were modeled in ETABS by updating member properties and by introducing new lateral load-resisting components. The structure was then reanalyzed under the same seismic load combinations to evaluate improvements in its performance.

2.4 Economic Feasibility

The economic feasibility of the proposed retrofitting was evaluated by estimating costs based on present market rates for construction materials and skilled labor. The tentative retrofitting cost was calculated and compared with the plinth area cost of constructing a new building. Retrofitting was considered viable where the estimated expenditure remained below 25% of the replacement cost of the structure(Nateghi and Shahbazian, 1992).

## 3. Result and Discussion

3.1 Qualitative Evaluation

The qualitative evaluation revealed that the existing building does not meet the desired seismic performance capability. A comparison with the requirements of NBC 105:2020 highlighted that columns and beams were undersized and M15 concrete was used.

**Table 1:** Key structural parameters vs NBC 105:2020

| Aspect | Observed | NBC105:2020 Requirement | Compliance |
|---|---|---|---|
| **Column size** | 230×230mm | ≥ 300 × 300 mm | NC |
| **Beam size** | 230×230mm | ≥ 230 × 300 mm | NC |
| **Concrete grade** | M15 | ≥ M20 | NC |

The FEMA 310 checklist further identified seismic vulnerabilities including irregular plan layout, discontinuous load paths, lack of redundancy, torsional irregularity and material deterioration.

**Table 2:** Identification of Vulnerability Factors as per FEMA 310.

| Vulnerability Factor | Compliance | Remarks |
|---|---|---|
| **Plan Regularity** | NC | Irregular layout |
| **Load Path Continuity** | NC | Discontinuity in transfer of seismic force to foundation. |
| **Redundancy** | NC | Lack of proper redundancy. |
| **Weak storey** | C | No weak storey observed. |
| **Short column** | C | No short column was observed. |
| **Adjacent building** | NC | Gap < 4% of shorter building. |
| **Torsion** | NC | The eccentricity of the building isn't within the limit. |
| **Material Deterioration** | NC | Visible deterioration of concrete and rusting of reinforcement observed. |

Note; C= Compliance and NC= Non-Compliance

Also misalignment of parapet walls, looseness of window frames and ceiling fixtures were some of the non-structural hazards that were observed which are prone to falling during seismic events. Quick checks was done to assess seismic capacity of columns under shear and axial loads to supplement the visual observations.

Storey-wise Shear Stress in RC columns

Storey-wise shear stress in column was calculated using IITK-GSDMA Guidelines for Seismic Evaluation and Strengthening of buildings 6.5.1(Indian Institute of Technology Kanpur, 2005).

**Table 3:** Calculation of shear stress in RC column

| **Storey** | **nc** | **$n_{f1}$** | **$n_{f2}$** | **Ac ( m $^2$)** | **Storey Shear** | **Shear Stress (Mpa)** | | **DCR in** | | **Remarks** |
|---|---|---|---|---|---|---|---|---|---|---|
| | | | | | | **τcol1** | **τcol2** | **X-direction** | **Y-direction** | |
| **Roof** | 6 | 2 | 3 | 0.56 | 160.66 | 0.43 | 0.58 | 0.61 | 0.81 | DCR<1; So safe in shear |
| **5** | 19 | 5 | 7 | 1.77 | 1085.47 | 0.83 | 0.97 | 1.18 | 1.37 | DCR>1; So unsafe in shear |
| **4** | 19 | 5 | 7 | 1.77 | 2029.28 | 1.56 | 1.82 | 2.20 | 2.56 | |
| **3** | 19 | 5 | 7 | 1.77 | 2726.46 | 2.10 | 2.45 | 2.95 | 3.44 | |
| **2** | 19 | 5 | 7 | 1.77 | 3195.08 | 2.46 | 2.87 | 3.46 | 4.04 | |
| **1** | 19 | 5 | 7 | 1.77 | 7839.72 | 6.03 | 7.03 | 8.49 | 9.90 | |

Since the DCR in the top storey is less than 1, this storey is safe but the DCR of lower 5 storey is greater than 1. So, these storeys are overstressed and maybe liable to failure during an earthquake.

Axial Stress Check

Axial stresses due to overturning forces were calculated according to FEMA 310, Clause 3.5.3.6(FEMA, 1998).

**Table 4:** Axial stresses due to overturning forces

| **Direction** | **Base shear × Load factor (KN)** | **$F_0$ (KN)** | **σ (MPa)** | **$\sigma_{all}$ (MPa)** | **DCR** | **Status** |
|---|---|---|---|---|---|---|
| **X** | 11759.58 | 1001.35 | 18.93 | 3.75 | 5.05 | Unsafe |
| **Y** | 11759.58 | 1798.25 | 33.99 | 3.75 | 9.07 | Unsafe |

Moreover axial stresses in both X- and Y-directions of the column exceed the permissible limit of 3.75 MPa. Demand Capacity Ratios of 5.05 and 9.07 further confirm severe overstress. Hence, the column is unsafe in axial stress.

Taken them all together, the NBC comparison, FEMA 310 checklist, and quick checks all show that the building does not meet seismic performance capability. When linked to EMS-98, the structure corresponds to Damage Grade 2, which refers to moderate damage characterized by visible cracks and impairment of non-structural elements.

3.2 Quantitative Evaluation

3.2.1 Data Interpretation for Non-Destructive Tests

The Ultrasonic and Rebound Hammer tests were carried out as per the provisions of IS 516. The results have been summarized below.

**Table 5:** Ultrasonic Pulse Velocity (UPV) test result

| Section | PV (km/s) | Quality | CS (MPa) |
|---|---|---|---|
| **Slab** | 5.93 | Excellent | 37.45 |

**Table 6:** Rebound hammer test result

| Section | R-value | Quality | CS (MPa) |
|---|---|---|---|
| **Column** | 31 | Good layer | 22 |
| **Slab** | 24 | Fair | 17 |

The UPV test on the slab revealed a velocity of 5.93 km/s which according to IS 516 (Part 5/ Sec 1), describes excellent concrete quality with a strength of 37.45 MPa. On the other hand, the Rebound Hammer test gave very low rebound numbers for column and slab that is 31 and 24 respectively. These corresponds fair to good layer *quality* concrete with strengths of 22 MPa and 17 MPa respectively according to IS 516 (Part 5/ Sec 4).This difference in results implies good internal integrity but weak surface strength.

3.2.2 Structural modeling and analysis

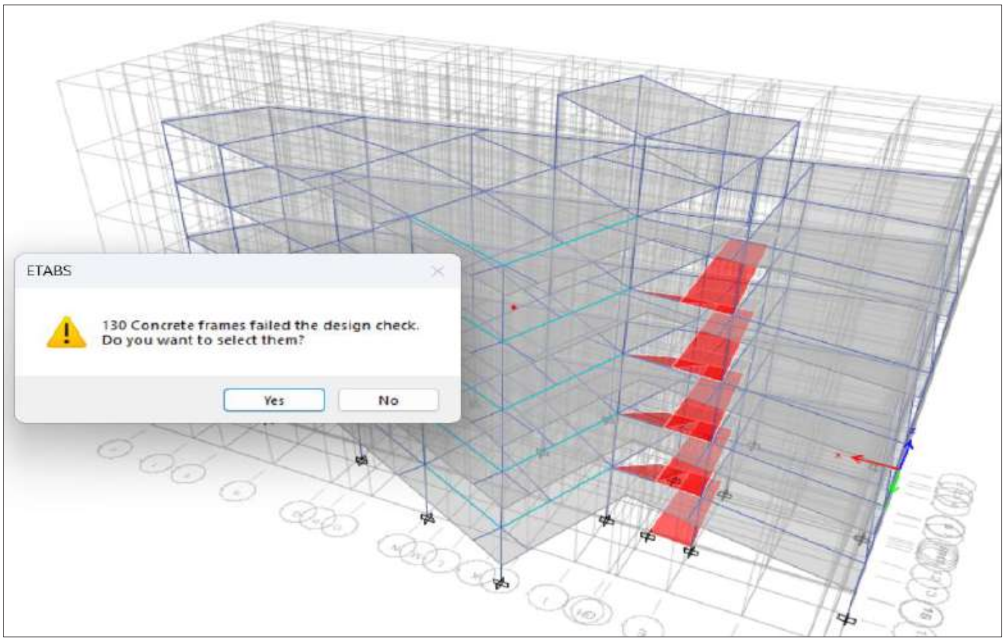


**Figure 2:** Verifying if all members passed the design check

A. Soft storey condition

As shown in Tables 7-8, soft storey checks revealed no critical weakness in either direction. The stiffness ratios remained above the minimum requirement of 0.7 across all storeys, except for minor irregularity observed at the roof level, which is not structurally significant.

**Table 7:** Soft storey check for ULS along X-direction (EQX)

| Storey | ki | 0.7*ki | 0.7*(ki+1) | Check if ki>0.7*(ki+1) |
|---|---|---|---|---|
| **6** | 0 | 0 | 0.7 | FALSE |
| **5** | 18871.93 | 13210.35 | 13211.05 | TRUE |
| **4** | 27144.51 | 19001.16 | 19001.86 | TRUE |
| **3** | 32148.89 | 22504.22 | 22504.92 | TRUE |
| **2** | 37321.56 | 26125.09 | 26125.79 | TRUE |
| **1** | 55440.43 | 38808.3 | 38809 | TRUE |

**Table 8:** Soft storey check for ULS along Y-direction (EQY)

| Storey | ki | 0.7*ki | 0.7*(ki+1) | Check if ki>0.7*(ki+1) |
|---|---|---|---|---|
| **6** | 0 | 0 | 0.7 | FALSE |

| | | | | |
|---|---|---|---|---|
| **5** | 16292.41 | 11404.68 | 11405.38 | TRUE |
| **4** | 18063.78 | 12644.64 | 12645.34 | TRUE |
| **3** | 18665.85 | 13066.1 | 13066.8 | TRUE |
| **2** | 19501.22 | 13650.85 | 13651.55 | TRUE |
| **1** | 27663.47 | 19364.43 | 19365.13 | TRUE |

B. Torsion Irregularity

As shown in the Figure 3, the building exhibits torsion irregularity in the Y-direction with displacement ratios exceeding 1.5 between storey 1 to 5 under both ULS and SLS. While in the X-direction the displacement ratio remain within the permissible limit, indicating no torsion irregularity.

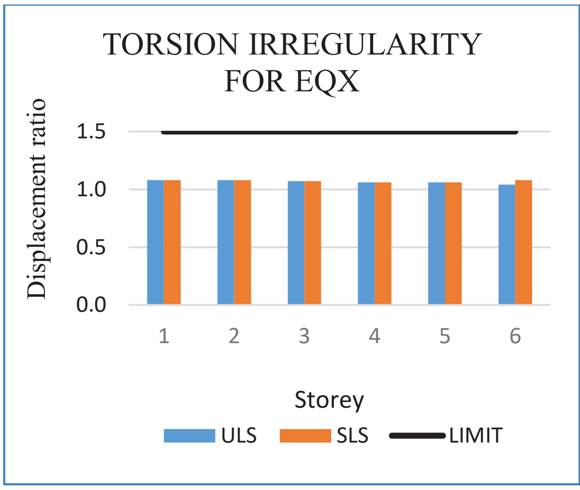


(a)

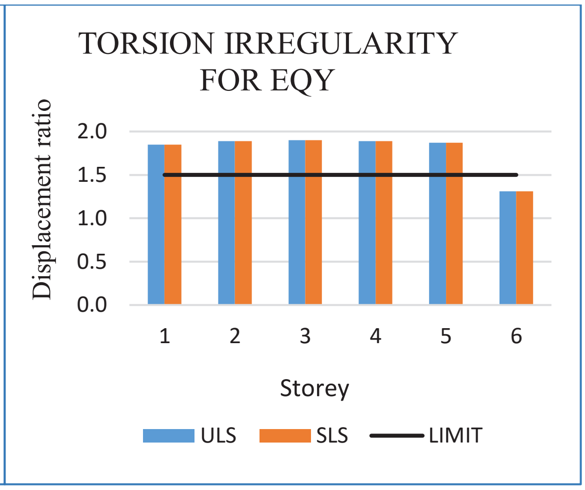


(b)

**Figure 3:** Torsion irregularity for ULS and SLS in: (a) X-direction; (b) Y-direction.

C. Storey Displacement

As show in the Figure 4, the maximum displacement in X-direction was 74.96 mm under ULS and 71.72 mm under SLS which are both within the permissible limits of 112.5 mm and 108 mm. In Y-direction, the maximum displacement was 218.49 mm and 209.06 mm exceeding the permissible limits.

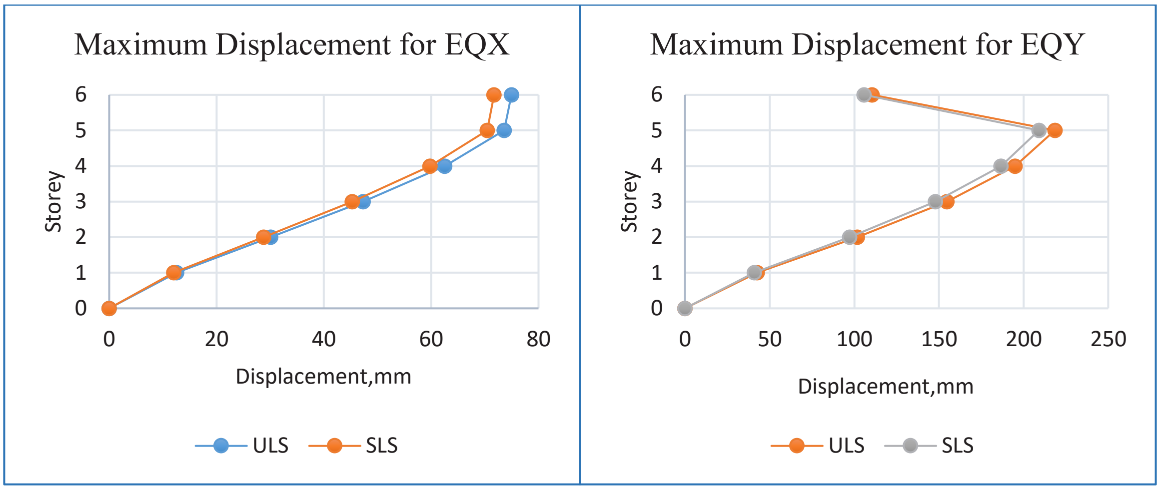


(a) (b)

**Figure 4:** Maximum storey displacement for both ULS and SLS in: (a) X-direction; (b) Y-direction

D. Storey Drift

As shown in the Figure (5-6), the maximum storey drift was 0.00567 under ULS and 0.00549 under SLS in X-direction, both within the permissible limits of 0.00625 and 0.006 respectively. In the Y-direction the maximum drift was 0.0197 under ULS and 0.0188 under SLS both exceeding the permissible limits.

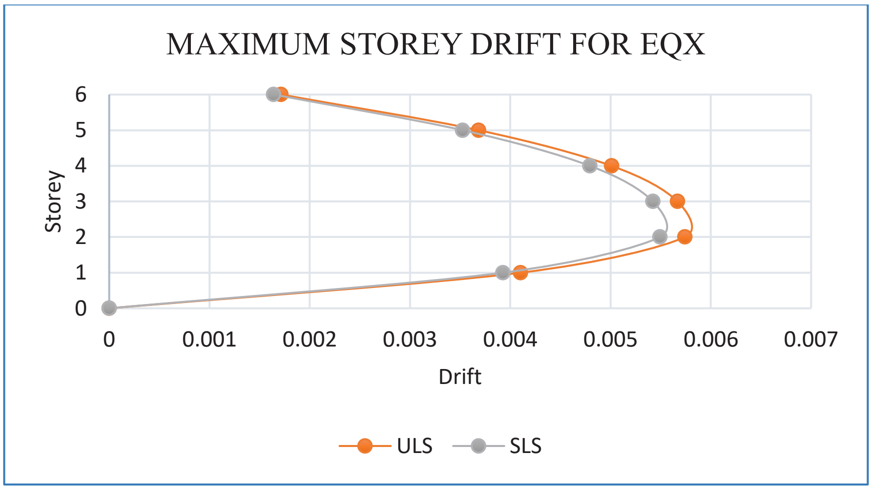


**Figure 5:** Maximum storey drift for both ULS and SLS in X-direction

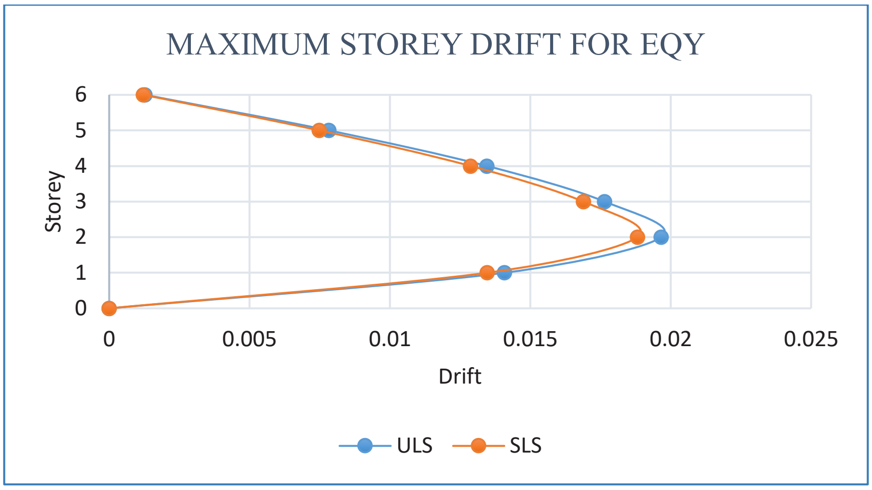


**Figure 6:** Maximum storey drift for both ULS and SLS in Y-direction

Overall analysis confirms that the building fails to meet seismic performance criteria of NBC 105:2020. Structural analysis shows torsional irregularity in the y-direction, excessive storey displacement and drift values exceeding permissible limits. These failures clearly indicate that the building is vulnerable and requires retrofitting measures to enhance safety and ensure code compliance.

3.3 Hybrid Retrofitting

Since the building was facing several seismic deficiencies at the same time like torsion irregularity, excessive storey drift and displacement we adopted a hybrid retrofitting approach combining concrete jacketing of columns and beams, steel jacketing of beams and addition of shear wall. Concrete jacketing of columns was chosen to increase axial load capacity, ductility and to improve confinement as recommended by IS 15988:2013. Beam showed inadequate flexural and shear resistance so both concrete and steel jacketing was chosen. Furthermore to improve the overall lateral stability of the building and control excessive storey drift reinforced concrete shear wall were added at strategic location. This hybrid approach improves both the strength of individual members and enhance the building's overall seismic performance.

Concrete jacketing of columns was carried out in accordance with IS 15988:2013. As per the code, the minimum thickness of the jacket should be 100 mm and the grade of jacket concrete should be at least 5 MPa higher than that of the existing concrete(Bureau of Indian Standard, 2013).

**Table 9:** Column Retrofitting Details as per is 15988:2013

| Stage | Column specification |
| --- | --- |

| | |
|---|---|
| **Before retrofitting** | 230×230 mm (M15) |
| **After retrofitting** | 430×430 mm (M20); 16-12 mm Ø bars |
| | 500×550 mm (M25); 12-16 mm Ø+6-12mm Ø bars |
| | 750×530 mm (M25); 10-20 mm Ø+6-16mm Ø bars |

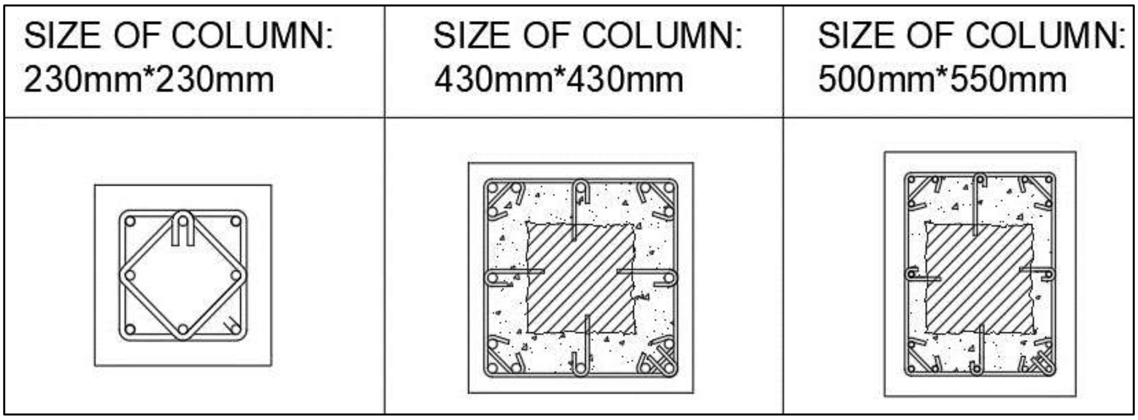


**Figure7:** Column cross-sections before and after retrofitting

Beam jacketing was designed in accordance with IS 15988:2013. After concrete jacketing, the beam section was enlarged to 375 × 375 mm reinforced with 3-16 mm bars and 4-12 mm bars tied with 8mm stirrups at 100 mm spacing using M20 concrete. For steel jacketing, five different sizes of angles (ISA 70×70×10, ISA 65×65×8, ISA 45×45×6, ISA 45×45×5, ISA 45×45×4) were proposed.

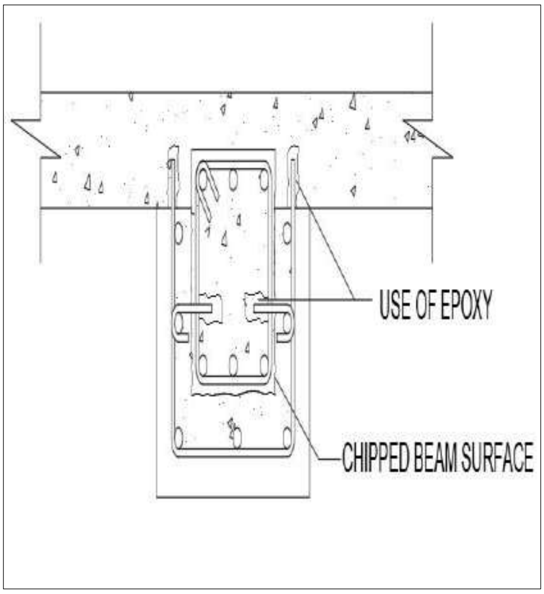


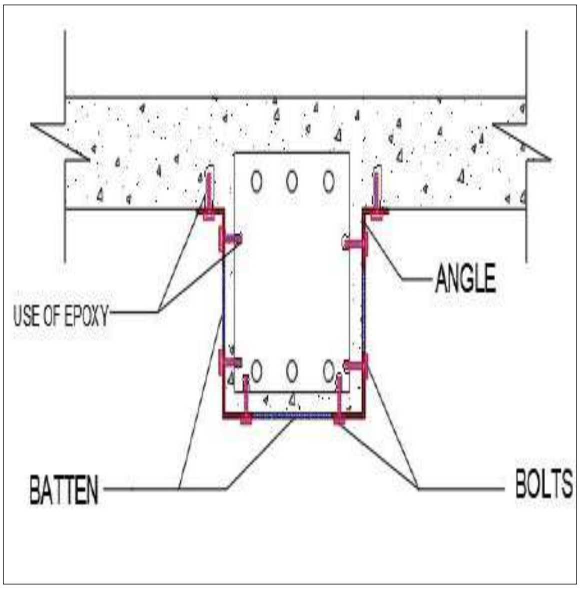


**Figure 8:** Typical cross-section of beam after RC jacketing and Steel jacketing

Shear walls were introduced at three locations, each 300 mm thick and extending up to 15 m in height, with lengths of 1.2021m, 1.0259m using M20 concrete. At the building corners shear walls of 300 mm thickness were arranged along both the x-axis and the y-axis.

Post-retrofitting analysis

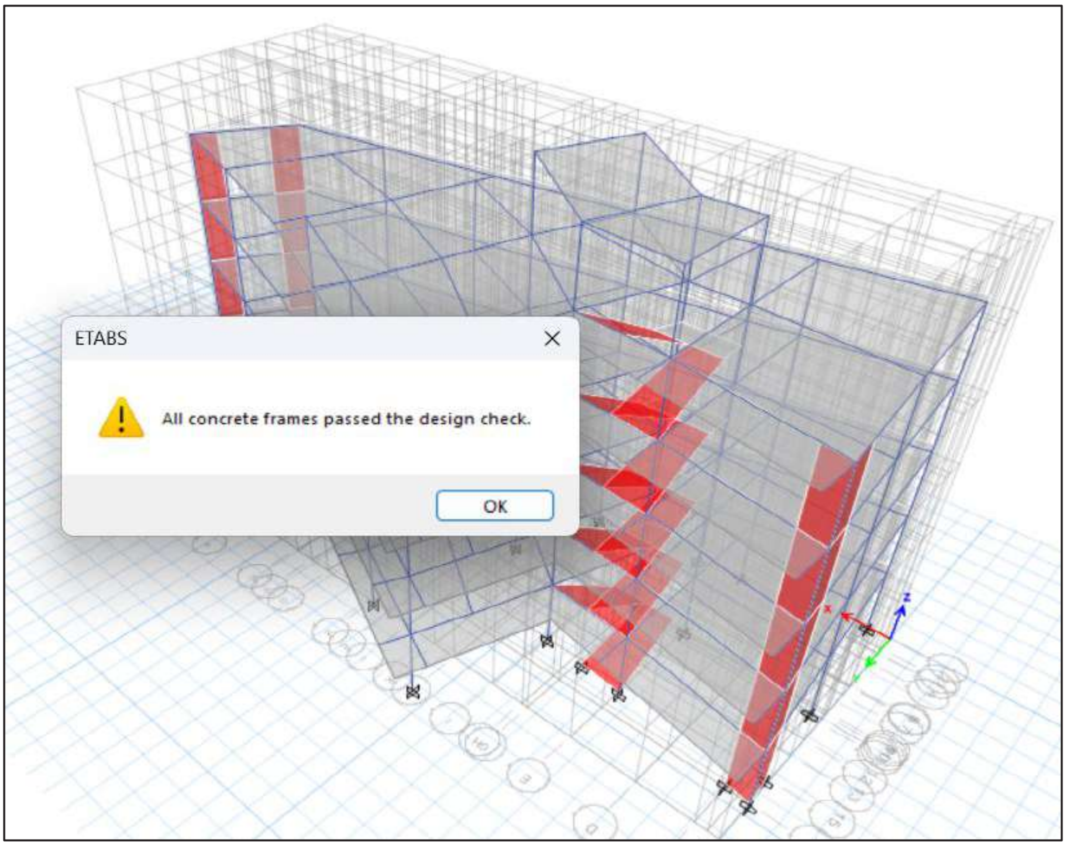


**Figure 9:** Verifying if all members passed the design checks after retrofitting

A. Soft storey condition

As show in the table (10-11) soft storey condition remained similar to pre-retrofitting case.

**Table 10:** Soft storey check for ULS along X-direction (EQX) after retrofitting

| Storey | Stiffness | 0.7*ki | 0.7*(ki+1) | Check if ki>0.7*(ki+1) |
|---|---|---|---|---|
| **6** | 0 | 0 | 0.7 | FALSE |
| **5** | 45792.22 | 32054.55 | 32055.25 | TRUE |
| **4** | 97209.11 | 68046.38 | 68047.08 | TRUE |
| **3** | 131303 | 91912.09 | 91912.79 | TRUE |
| **2** | 165903.4 | 116132.4 | 116133.1 | TRUE |
| **1** | 339327.3 | 237529.1 | 237529.8 | TRUE |

**Table 11:** Soft storey check for ULS along Y-direction (EQY) after retrofitting

| Storey | Stiffness | 0.7*ki | 0.7*(ki+1) | Check if ki>0.7*(ki+1) |
|---|---|---|---|---|
| **6** | 0 | 0 | 0.7 | FALSE |
| **5** | 41225.21 | 28857.65 | 28858.35 | TRUE |
| **4** | 93383.43 | 65368.4 | 65369.1 | TRUE |
| **3** | 135481.4 | 94836.97 | 94837.67 | TRUE |
| **2** | 202069.3 | 141448.5 | 141449.2 | TRUE |
| **1** | 433925.3 | 303747.7 | 303748.4 | TRUE |

B. Torsion irregularity

As shown in the Figure 10, the torsion irregularity in the Y-direction was resolved with ratios below 1.5, while the X-direction remained within the permissible limits.

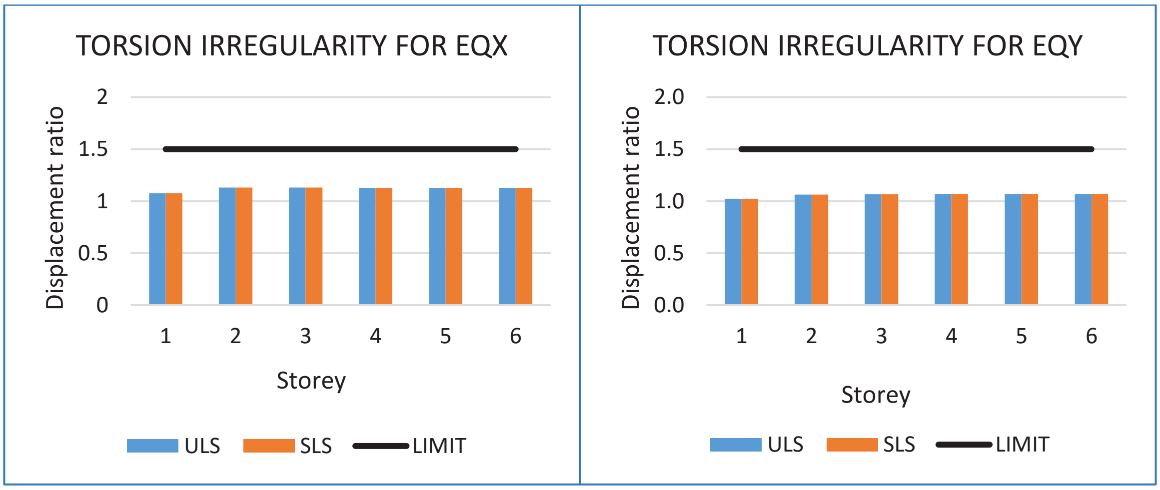


(a) (b)

**Figure 10:** Torsion irregularity for ULS and SLS after retrofitting in: (a) X-direction; (b) Y-direction

C. Storey Displacement

As shown in the Figure 11, the building no longer shows storey displacement in the Y-direction and the X-direction remains within the limits.

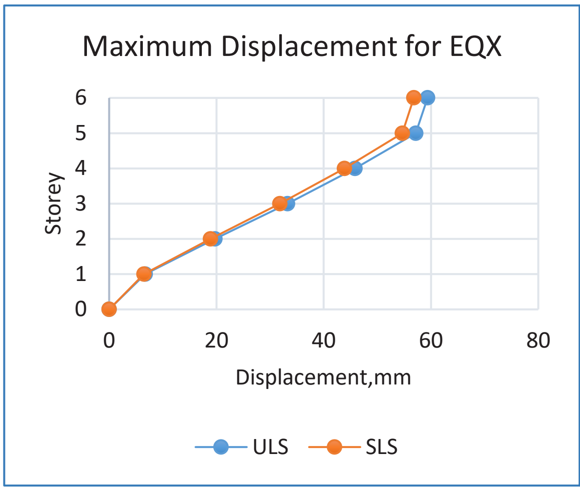


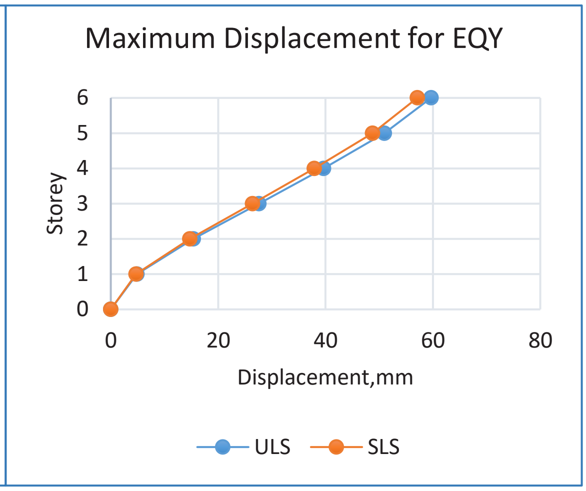


(a) (b)

**Figure 11:** Maximum displacement for ULS and SLS after retrofitting in: (a) X-direction; (b) Y-direction

D. Storey Drift

As shown in the Figure (12-13) the building no longer shows storey drift in Y-direction and storey drift in X-direction has also been improved.

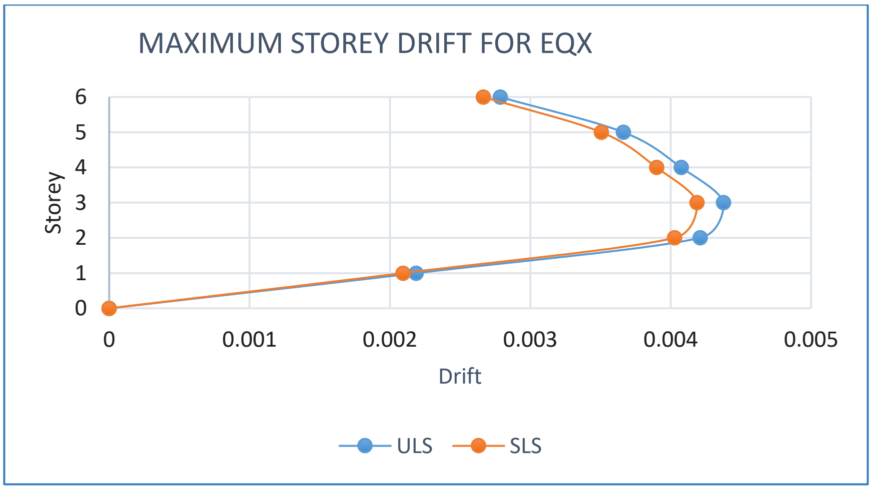


**Figure 12:** Maximum storey drift for ULS and SLS after retrofitting in X-direction

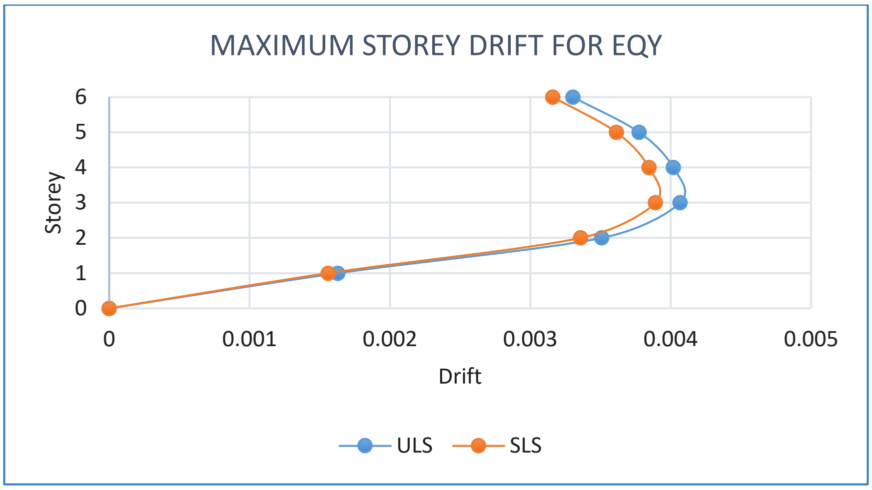


**Figure 13:** Maximum storey drift for ULS and SLS after retrofitting in Y-direction

Post retrofitting analysis confirms that the building meets the seismic performance criteria of NBC 105:2020. These improvements demonstrate that the retrofitting measures effectively enhanced safety and ensured compliance with code requirements.

3.4 Economic Feasibility

From an economic perspective, the tentative total retrofitting cost was estimated at NPR 80,94,000 based on present market rates for materials and skilled labor. In comparison, the plinth area cost of constructing a new building was approximately NPR 5,20,00,000. This indicates that the retrofitting expenditure amounted to nearly 15.6% of the replacement cost, which remains below the 25% threshold suggested by(Nateghi and Shahbazian, 1992).

## 4. Conclusion

The combined evaluation revealed that the existing six-storey RC framed building was highly vulnerable to seismic forces, failing both qualitative and quantitative evaluation. Pre-retrofitting analysis revealed torsion irregularity, excessive displacement and drift, while NDT revealed weak surface strength.

The proposed hybrid retrofitting were effective in addressing those deficiencies. Post-retrofitting analysis showed compliance with NBC 105:2020 eliminating torsion irregularity and controlling excessive displacement and drift.

From an economic point of view, retrofitting of the building is far more affordable than demolishing and constructing a new one. The retrofitting cost came out to be NPR 80.94 lakh while a new building would have cost around NPR 5.2 crore. In other words, retrofitting required only about 15.6% of the replacement cost, making it the practical choice. Hence, hybrid retrofitting stands out as both technically effective and economically practical.

**References**


- Baruwal, R., Chhetri, B. and Chaulagain, H. (2020) "Probabilistic seismic hazard analysis and construction of design spectra for Pokhara valley, Nepal," *Asian Journal of Civil Engineering*, 21(8), pp. 1297–1308. Available at: https://doi.org/10.1007/s42107-020-00278-4.
- Bureau of Indian Standard (2013) "IS 15988 (2013): Seismic Evaluation and Strengthening of Existing Reinforced Concrete Buildings - Guidelines."
- Bureau of Indian Standards (1978) "IS 8900 (1978): Criteria for the rejection of outlying observations."
- Bureau of Indian Standards (2018) "IS 516 : Part 5 : Sec 1 : 2018: Hardened Concrete Methods of Test Part 5 Non-destructive Testing of Concrete Section 1 Ultrasonic Pulse Velocity Testing (First Revision)."
- Bureau of Indian Standards (2020) "IS 516 : Part 5 : Sec 4 : 2020: Hardened Concrete Methods of Test Part 5 Non-Destructive Testing of Concrete Section 4 Rebound Hammer Test (First Revision)."
- DUDBC (2011) *Seismic Vulnerability Evaluation Guideline for Private and Public Buildings (Part 1)*.
- DUDBC (2020) "NBC 105:2020 : Seismic Design of Buildings in Nepal."
- FEMA (1998) "Handbook for the Seismic Evaluation of Buildings – A Prestandard (FEMA 310). Washington, D.C.: Federal Emergency Management Agency."
- Indian Institute of Technology Kanpur (2005) "IITK-GSDMA Guidelines for Seismic Evaluation and Strengthening of Existing Buildings." National Information Centre of Earthquake Engineering (NICEE), IIT Kanpur.

- Nateghi and Shahbazian (1992) "Economic Justification of Retrofitting versus Replacement of Structures," *International Association for Earthquake Engineering (IAEE)*, 10.
- UNICEF Nepal (2017) *Emergency | UNICEF Nepal*. Available at: https://www.unicef.org/nepal/emergency (Accessed: November 17, 2025).

Pokhara Engineering College Journal (PECJ)
*Applied Sciences and Engineering Insights*
ISSN: 3021-9795 (Print) / 3059-9628 (Online)
(Volume-3, Issue -I)

# Design of a Hardware-Integrated OCR System for Devnagari Text in Nepalese Citizenships

Prashant Subedi[1*], Sandesh Bashyal[1], Pragati Basnet[1], Amrit Giri[1], Suraj Basant Tulachan[2], Smita Adhikari[3]

[1] *Department of Electronics and Computer Engineering, Pashchimanchal Campus, IoE, TU*

[2] *Department of Compute, Pokhara Engineering College, PU*

[3] *Department of Electronics and Computer Engineering, IoE, TU*

*Corresponding email: prashantsubedi35@gmail.com



*Received:10- January-2026; Revised: 12- February-2026; Accepted: 27- March-2026*

*DOI: https://doi.org/10.3126/pecj.v3i1.93533*

## Abstract

In today's date banks to government institutions, most forms still require users to fill in details on the paper and then retype them into a database. Essential documents such as citizenship cards, national identification cards, driving licenses, and passports are only available in physical form. To digitize such information, an Optical Character Recognition (OCR) system is required. OCR systems are technologies that convert printed or handwritten text from the images into machine-readable format. A complete hardware-integrated machine learning framework is presented for automatically extracting Devanagari text from citizenship documents and storing it in a database without manual input. A document feeder mechanism equipped with a high-torque planetary gear motor was designed, in which the roller is rotated to replace documents from a stack and capture images sequentially. The captured image is processed using a YOLO-based model to detect the region of interest (ROI) of the document, which is then passed to Tesseract OCR for converting the printed Devanagari details into machine-readable text. Experimental results show that our model achieves a Character Error Rate (CER) of average 13% on previously unseen citizenship documents, showing the feasibility of our approach for large-scale document digitization.

**Keywords:** Character Error Rate (CER), Citizenship Document, Devanagari Script, Document Feeder Mechanism, Optical Character Recognition (OCR), Tesseract, YOLO.

## 1. Introduction

### 1.1 Background

Optical Character Recognition (OCR) is a technology that enables the automatic identification and conversion of printed or handwritten text into machine readable digital data. By analyzing the shapes and patterns of characters in images or scanned documents, OCR systems can extract textual information efficiently, eliminating the need for manual data entry by different bodies.

Previously OCR were used in technology involving telegraphy and creating reading devices for the bind. Later, the OCR was made available online as a service (WebOCR), in a cloud computing environment (Tafti *et al.*, 2016), and in mobile applications like real-time translation of foreign-language signs on a smartphone, with the advancement overtime they are used on the internet connected mobile devices to extract text from the images using the device's camera (Cutter and Manduchi, 2017).

Analyzing the characteristics of Nepalese citizenship documents (12.7*8.9 cm), designing a deep-learning OCR model tailored for Devanagari script, and integrating the model with dedicated hardware for real-time performance is what this paper is all about. The proposed system targets applications in financial institutions, government service centers, and digital archiving platforms where fast, reliable extraction of citizenship data is essential.

The recent advances in artificial intelligence and deep learning have transformed OCR capabilities by enabling models to automatically learn robust representations from large collections of annotated images. Convolutional Neural Networks (CNNs) improve text detection, while Recurrent Neural Networks (RNNs), Transformers (Hasan *et al.*, 2024), and Connectionist Temporal Classification (CTC) mechanisms enhance sequence prediction without the need for explicit character segmentation. Incorporating CNN and LSTM models in a single pipeline enables directly transcription of the text directly and this OCR engine is popularly known as Tesseract (Kumar *et al.*, 2024). These end-to-end learning systems have demonstrated strong performance in multilingual scene text recognition, making them suitable for languages such as Nepali (Mehta and Mehta, 2025) that require understanding of script-specific structural variations.

OCR systems understand contextual description of documents, multimodal and real-time-like processing of text in the video, enhanced adaptability, security and privacy. This impact on the application like automating data entry, invoice processing, financial operation, digitizing textbooks for easier research and study (Mittal and Garg, 2020).

### 1.2 Problem Statement

Nepal's administrative and financial systems still heavily rely on physical documentation. Most institutions require an individual person just to fill in paper forms; later, the employees manually transfer that information into digital databases. This workflow introduces multiple inefficiencies: Manual data entry is slow, Human errors, Large-scale digitization is impractical, Existing OCR solutions lack support for Devanagari.

Given these limitations, there is a need for a system that can automatically feed the physical documents, capture their images, detect relevant textual regions from the obtained image, and convert printed Devanagari text into structured machine-readable data. Such a solution must be accurate, reliable, and capable of operating without human intervention to support nationwide digitization efforts.

### 1.3 Objective

The objective of the research study is:

- To develop an accurate and efficient system that detects the region and extracts Devanagari text from citizenship documents for digitization in banks and government institutions

## 2. Literature Review

A segmentation-free LSTM-based recognition approach has been applied to significantly enhance printed Devanagari OCR performance. The outcomes were reported in the study by Karayil et al. (2015), where LSTM achieved a 9% error rate compared to Tesseract's 11.96%, highlighting the benefits of sequence-learning models for structured Indic scripts (Karayil, Ul-Hasan and Breuel, 2015).

Research conducted by Dessai and Patil in 2019 extended OCR research to handwritten Devanagari text by employing a convolutional neural network model (Dessai and Patil, 2019). Their system achieved an accuracy of approximately 89%, showing the effectiveness of deep-learning-based feature extraction in handling the irregularities and variations present in handwritten scripts.

Comparative studies between traditional OCR engines and artificial neural networks further demonstrate the progression toward the latter. Neural network models have achieved higher training and testing accuracies than Tesseract when applied to Nepali script, demonstrating better adaptability and generalization. This trend was observed in the work of Prajapati et al. (2018), where ANN-based OCR outperformed Tesseract across multiple evaluation premises (Prajapati *et al.*, 2018).

Document-level OCR automation has recently been enhanced through integrated deep-learning-powered text detection pipelines. Such systems combine detection and recognition to handle real-world identification documents with high precision. A notable example is the citizenship-document extractor developed by Dhakal et al. (2024), which achieved mean average precision values of 99.1% on the document front and 96.4% on the back, illustrating the maturity of end-to-end OCR frameworks for official document processing (Dhakal *et al.*, 2024).

In 2020, Luthra team demonstrated a low-cost hardware-assisted OCR workflow by developing an automated document scanning machine using Raspberry Pi for camera control, page turning, and flexible motor–sensor positioning (Luthra, Chauhan and Ahmad Ansari, 2020). Their system incorporated image preprocessing prior to Tesseract OCR, resulting in improved text extraction performance across documents of varying sizes and thicknesses.

A more advanced hardware–software co-design was proposed by Rybalkin et al. (2020) through the iDocChip architecture, a portable and low-power SoC-based accelerator designed for real-time historical document processing (Rybalkin *et al.*, 2018). By integrating segmentation, image enhancement, and neural-network-based OCR directly into a CPU–FPGA hybrid workflow, the system delivered significant improvements in throughput and energy efficiency, establishing one of the most cited hardware-accelerated OCR frameworks in recent literature.

A modular hardware OCR implementation was presented by Parween and Saha, who structured their system around dedicated preprocessing, segmentation, and feature-extraction modules (Parween and Saha, 2021). Character recognition was performed using an artificial neural network implemented in MATLAB, revealing the advantages of classical ANN models for printed-text OCR when paired with structured hardware support.

Assistive hardware applications have similarly benefited from embedded OCR pipelines. Team along with Saint-Vil introduced a headband-mounted document scanner incorporating a microcontroller, high-resolution camera, and wireless transmission module for hands-free text capture (Saint-Vil *et al.*, 2022). The system leveraged Tesseract OCR for recognition alongside a live video stream to a mobile application, providing an accessible solution for users with motor impairments and highlighting the role of lightweight embedded platforms in personalized OCR systems.

## 3. Methodology

### 3.1 Datasets

The dataset consists of images of Nepali citizenship documents containing both printed and handwritten components with text written in Nepali language. Along with these images, there exist ground truth annotations for structured components with a total of six prominent fields. The images were obtained from structured forms filled out by participants who were given a non-disclosure and data-use agreement with mutual consent. The images have been carefully labeled with labels corresponding to these structured components named as Name, Citizenship Number, Issuing Office, Gender, Birthdate, and Address. Various preprocessing operations have been done on these images including denoising and transforming them into grayscale. To make these images more robust under differing imaging conditions, some more operations have also been conducted on these images. The brightness, saturation, and hue of these images were controlled. It should be noted that for consistency within the data set, images were obtained and then resized to 640x640 resolution. The data set itself consists of 85%, 7.5%, and 7.5%, partitioning into train, validate, and testing sets, respectively.

**3.2 System Architecture**

The Nepali citizenship documents were fed one by one into an automatic paper feeder mechanism controlled by a microcontroller and a relay switch. The document is loaded into a dedicated frame, where the top citizenship image is captured using a camera module. After that, the raw image is transmitted to the backend server, which acknowledges the receipt and triggers the feeder to process the next document.

The backend communicates with both the microcontroller and the machine learning model about the readiness of the document to capture and the captured one to process further, respectively. The machine learning model, after receiving the captured images, comes into play. The workflow of the model part is explained in detail in the section below. After receiving the output from the machine learning model, it is sent to Tesseract to generate the characters in the form of a result. All the results obtained out of it are gathered and stored for further usage.

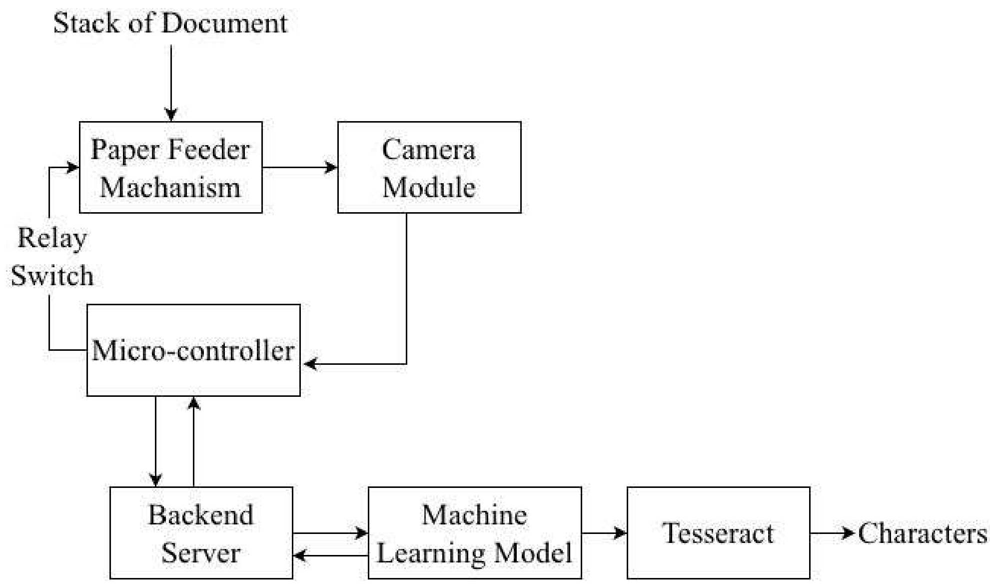


**Figure 1:** System Architecture

### 3.3 Hardware Architecture

The illustrated figure shows the mechanism of the automatic paper feeder and scanner. As shown in (1), the bundle of citizenship documents is placed. The top part of the document is captured using a camera module that is placed at (2). The captured image is then sent to the backend server. The server then passes it to the machine learning framework.

A binary handshaking protocol is implemented between the Arduino and the backend to ensure precise synchronization between document processing and mechanical actuation. The Arduino continuously checks for an acknowledgement from the backend server. The backend triggers the microcontroller to fetch the next paper by switching ON the relay module as soon as it acknowledges reception of the image. The microcontroller sends a high signal to turn on the relay as initially it's in the OFF state. The relay module is responsible for supplying power to a high-torque DC motor. This DC motor drives the primary roller and the roller attached to the primary roller via a rubber belt in a clockwise direction. Similarly, the secondary roller, which is in contact with the primary roller, moves as a reaction to the primary roller in an anticlockwise direction, thereby moving the paper forward as shown in (4). Then the whole process is repeated until all of the paper is passed through the motor.

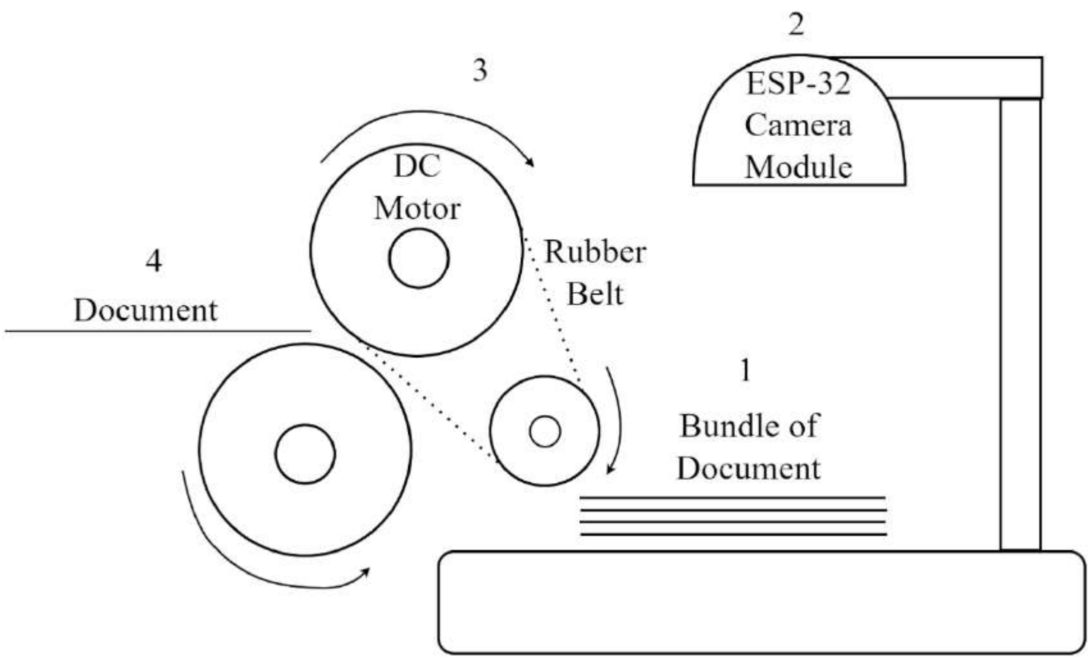


**Figure 2:** Document Feeder Mechanism

**3.4 Machine Learning Workflow**

The machine learning workflow as shown in diagram 3 begins with image acquisition, which is done with the help of the hardware setup described previously. After which, the image is passed to an ML-driven Region of Interest (ROI) detection algorithm. An ROI refers to any specific portion of the input image containing meaningful information that was annotated. The algorithm identifies these regions within scanned documents and isolates them through the cropping of ROIs to remove irrelevant details. After cropping, the cropped segments are passed into the character reader (such as Tesseract), from where characters are extracted from the segments. The raw OCR output then undergoes a cleaning process that removes noise and normalizes characters. Finally, all cleaned outputs are assembled into a structured format, producing a coherent digital representation of the original document.

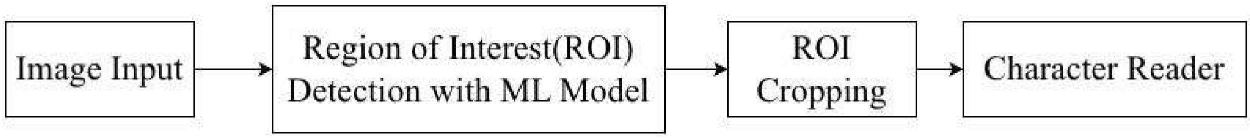


**Figure 3:** Machine Learning Workflow

**3.5 Model Architecture**

There are 2 model architectures used in the research. First one is YOLO and is followed by Tesseract which are explained below.

***3.5.1 YOLO***

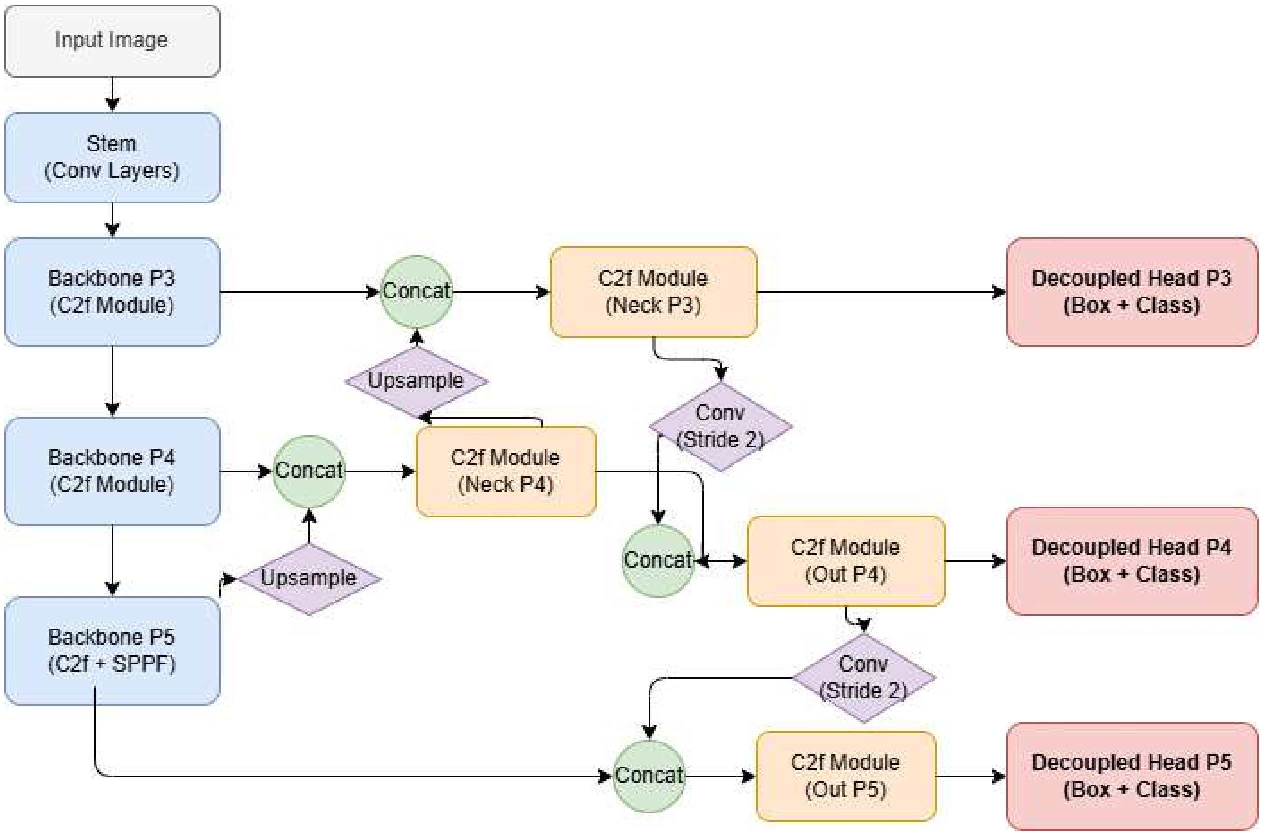


**Figure 4:** YOLO Architecture

YOLO architecture has always been popular on the object detection problem (Liu *et al.*, 2018). The architecture flow of figure 4 depicts a modern YOLO detector made up of a convolutional Stem layer (process images in first layer), a hierarchical (cross- stage partial with 2 fusion paths) C2f-based Backbone, and a multi-scale fusion Neck. Stem manages initial spatial reduction and low-level feature extraction, providing progressively richer representations to Backbone stages P3, P4, and P5. Each stage employs C2f modules to boost gradient flow, efficiency, and feature reuse; the deepest stage incorporates an SPPF block to gather multi-scale contextual information and enhance large-object detection. These components work together to form a hierarchy of semantically rich feature maps, which are then processed at various resolutions.

These features are fused in the Neck through up sampling, stride convolution, and feature concatenation, with additional C2f modules refining each merged representation to produce three output scales (Out P3, Out P4, and Out P5). Each scale is handled by a decoupled detection head that separates bounding-box regression and classification, reducing gradient interference while increasing accuracy. Architecture detects objects of varying sizes in a robust and computationally efficient manner by utilizing efficient feature extraction, cross-scale aggregation, and task-separated prediction.

### *3.5.2 Tesseract*

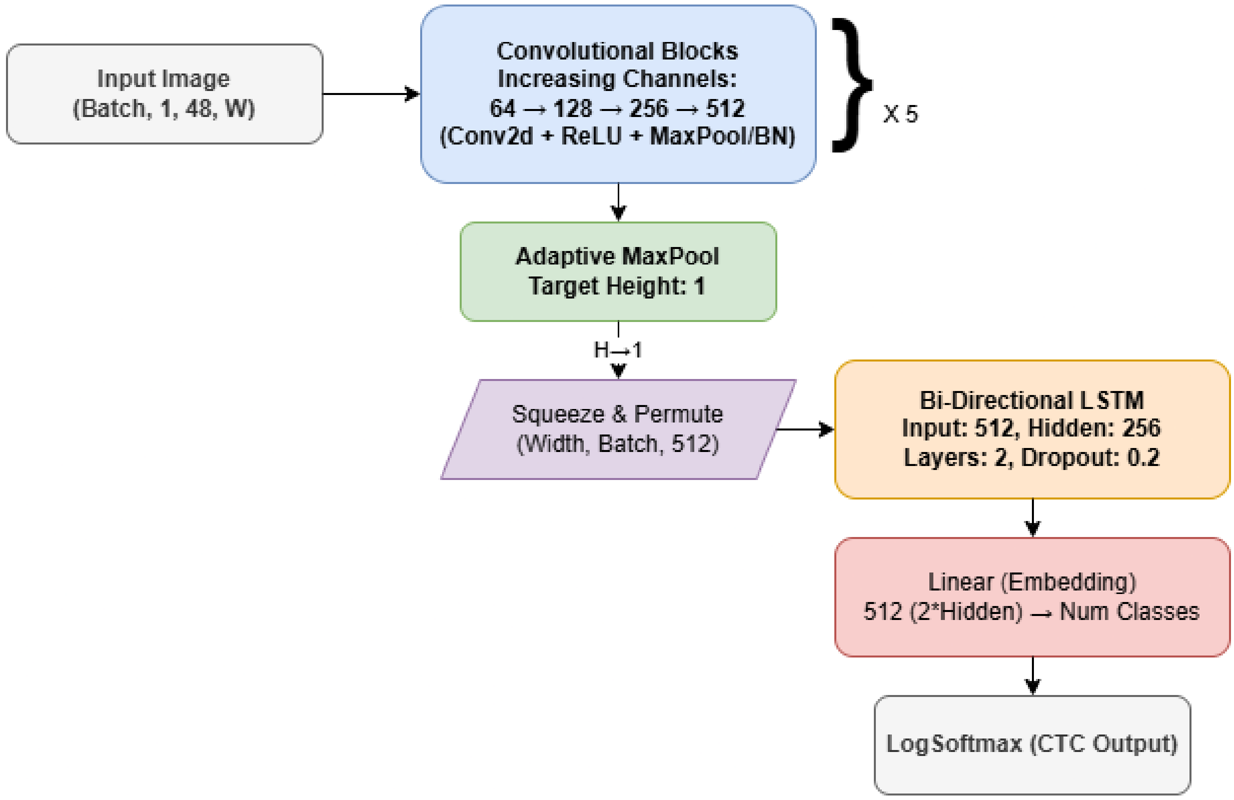


**Figure 5:** Tesseract Architecture

This architecture illustrated in figure 5 represents a deep learning version of the Tesseract OCR recognition system. It uses convolutional feature extraction alongside sequence modeling to ensure precise text retrieval. The input image, normalized to a fixed height and flexible width, passes through five blocks, which boosts channel capacity starting from 64 up, to 512. Every block contains convolution, ReLU activation and either max pooling or batch normalization, enabling the network to capture abstract visual features while minimizing spatial dimensions. This convolutional encoder generates a representation of nearby stroke configurations, letter forms, and text layout.

After extracting features, an adaptive max-pooling step compresses the height dimension to one row, transforming the 2D feature map into a sequence. Each line of text is handled as a sequence during a squeeze-and-permute operation. It changes the tensor into a (Width, Batch, 512) shape. The sequence is then processed by a two-layer bidirectional LSTM containing 256 hidden units in each direction. Doing so enables data from both past and future positions to affect every prediction. Afterwards, a linear embedding layer translates the 512- features into character categories. Finally, the Log SoftMax layer generates probabilities for Connectionist Temporal Classification (CTC). Combining all these allows the precise recognition of variable-length text without the need for any character segmentation.

### 3.6 Training

The citizenship document datasets were prepared with all the preprocessing steps. It was then trained using Roboflow. The preprocessed images were uploaded and annotated manually with bounding boxes for predefined classes representing key textual fields. The annotations were all reviewed manually again to ensure consistency and accuracy in proper localization of the designated fields.

Roboflow preprocessing included image resizing, noise clearance through normalization, and removing low-quality document samples. Data augmentation techniques were applied that include hue, saturation, and brightness adjustments. It was essential to make the model more robust. Before being exported in YOLO format for model training, the datasets were divided into training, validation, and test sets.

The model was trained for 100 epochs with a weight decay of $1\times10^{-3}$ to reduce overfitting and improve generalization. Different hyperparameters were changed and the best ones to produce stable convergence and balanced performance across all classes were selected. Different validation metrics were considered to verify the performance.

### 3.7 Evaluation

The various evaluation metrics used in the study to determine the feasibility and efficiency of the YOLO model are loss curves, precision and mean Average Precision (mAP50-95) graphs, confusion matrix, and that of the extracted text from Tesseract model is Character Error Rate (CER).

1. Loss Graphs:

Loss graphs represent the model's training progress over time. It shows the change in loss values over time. The total loss in YOLO is made up of several components, one of the most important being the bounding box (localization) loss. It determines whether the predicted box aligns with the ground truth ones. The bounding box loss graph is plotted on both training and validation data. The decreasing training loss indicates a better fit to the training data. In validation data, it indicates better generalization on unseen data.

2. Precision:

Precision refers to the proportion of true positive detections to the total positives (true positives and false positives). Mathematically, it is represented as:

$$Precision = \frac{TP}{TP + FP} \qquad 1$$

Where TP = True Positive, FP = False Positive.

The precision graph shows how accuracy in detection changes with training epochs or confidence thresholds.

3. Mean Average Precision 50-95:

Mean Average Precision (mAP50–95) is one of the main metrics which is used to determine the performance of YOLO-based models in object detections. It calculates the mean of Average Precision (AP) values over various Intersection over Union (IoU) thresholds from 0.50 to 0.95 with a step of 0.05. With the step of 0.05, this metric calculates the average of those 10 average precisions. This metric assesses strict localization, accurate classification, and makes it way better than mAP50 in complicated and sensitive tasks that seek the best accuracy. The formula for $mAP_{50-95}$ is given as:

$$mAP_{50-95} = \frac{1}{10}\sum_{t=0.5}^{0.95} AP_t \qquad 2$$

Where t = threshold.

4. Confusion Matrix:

A confusion matrix, always a square matrix, is the performance evaluation tool used for classification models. It helps to compare the true and predicted labels produced by the trained model. Each row represents a predicted class, while each column speaks for actual class and a strong efficient model always has strong principal diagonal values showing how well the model correctly classifies each class.

5. Character Error Rate:

Character Error Rate is an OCR accuracy metric that evaluates the percentage of incorrect characters in the extracted text when compared to the correct ones. Mathematically, it is defined as,

$$CER = \frac{S + D + I}{N} \qquad 3$$

where S = Substitutions, D = Deletions, and I = Insertions are normalized by the total number of ground-truth characters (N).

## 4. Result and Discussion

### 4.1 Results

To evaluate the effectiveness of the model architecture, a series of experiments with different combinations of hyperparameters were conducted. By systematically tuning the learning rates, batch sizes, and image size, we aimed to identify the configuration of architecture that could deliver most contented performance. These hyperparameters helped to get a significant Region of Interest (ROI), resulting in high diagonal values in the confusion matrix.

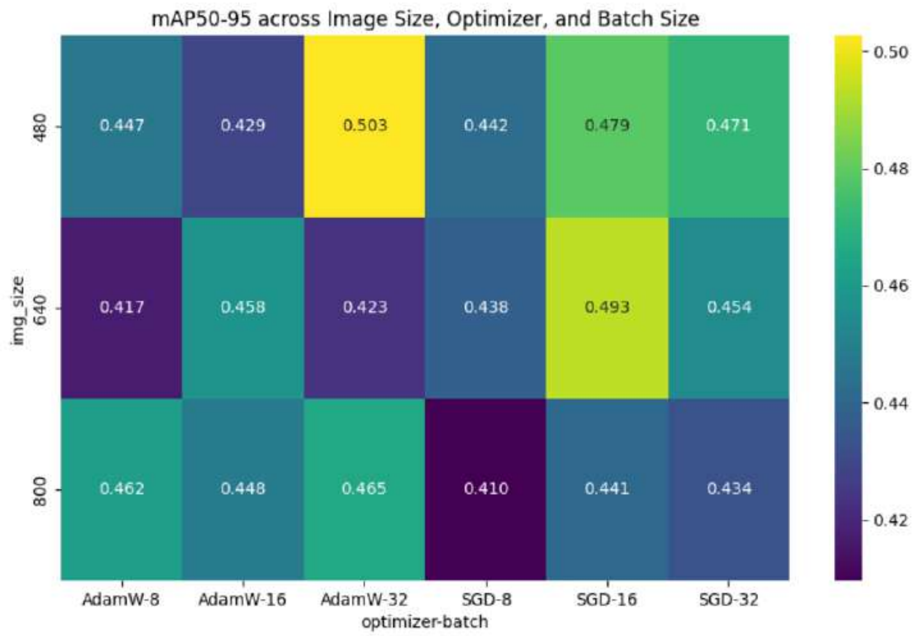


**Figure 6:** Combinations of image size, optimizer and batch size

The object detection model was evaluated on 18 different combinations involving 3 image square shapes of 480, 640, 800, 2 optimizers (AdamW and SGD), and 3 batch sizes of 8, 16, 32. The resulting mAP50-95 values are illustrated in the heatmap figure 6, where darker regions represent low performance and brighter high. From the diagram, AdamW optimizer produced the best results at an image size of 480 and batch size of 32, with a mAP50-95 of 0.503.

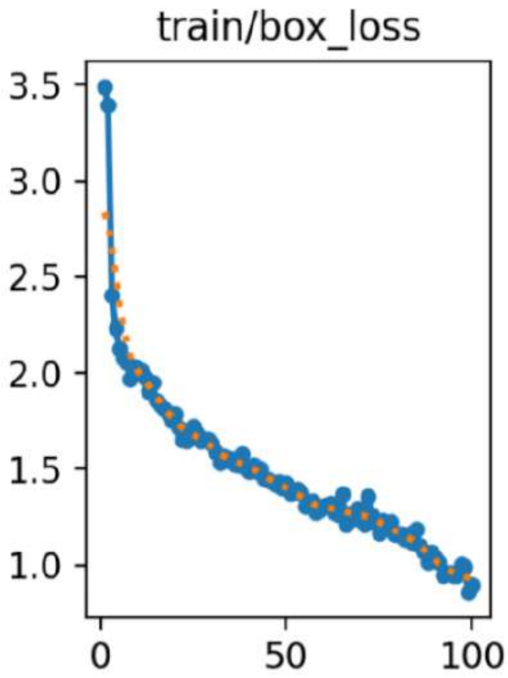


**Figure 7:** Bounding box graph of train loss

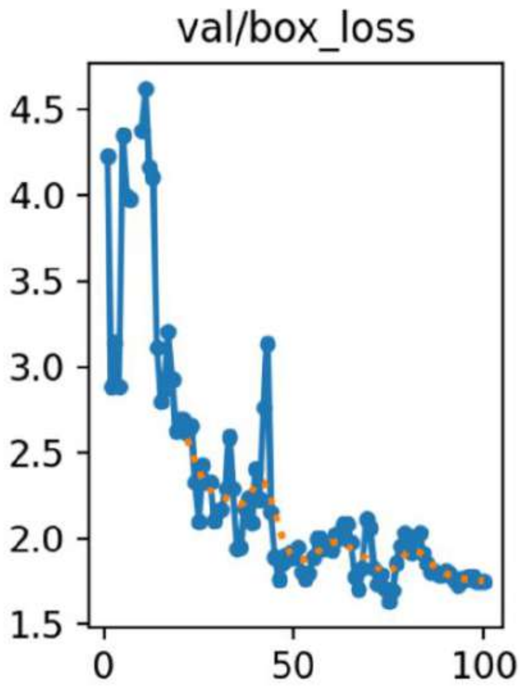


**Figure 8:** Bounding box graph of validation loss

Figures 7 and 8 represent the loss curve of the train dataset and validation dataset respectively. Loss value during training means the discrepancy between predicted and actual values at a certain epoch. The model training loss experienced a very steep decline from 3.5 to 1.5 in the first 25 epochs. Then there is gradual decrease to 100 epochs which is less than. On the other hand, validation loss fluctuates until the first 50 epochs while it tries to be in a steady state for the next 50 training periods.

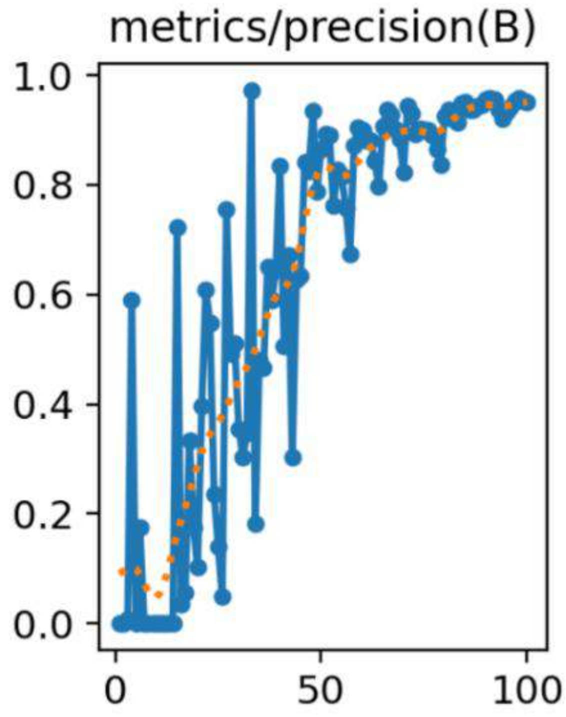


**Figure 9:** Precision graph

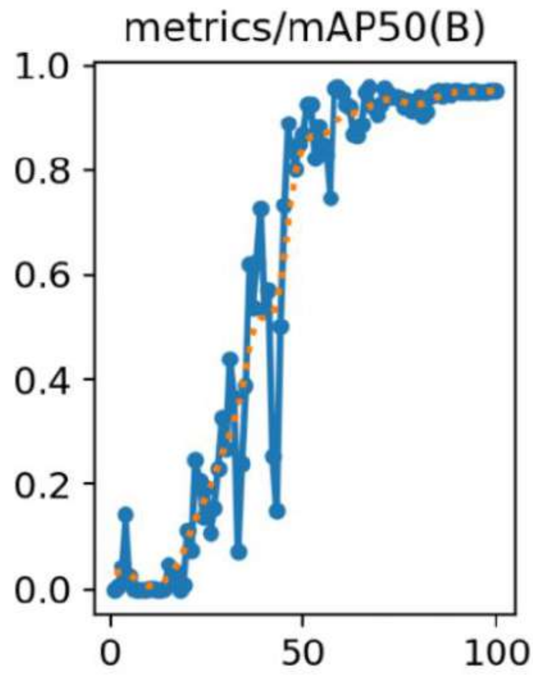


**Figure 10:** Mean average precision 50 graph

Likewise, figures 9 and 10 represent the precision and mAP50 evaluation metrics during the model training respectively. There is fluctuation in both precision and mAP50 till 50 epochs in the range of 0.1 to 0.75 and remains in stable state for next epoch. These metrics define how models are optimized from each data sample.

Figure 11 depicts the confusion matrix of dimension 7×7 incorporating Region of Interest (ROI) of the targets. However, there are 6 labels and 7 in dimension with consideration of background because predicting the regions, the model may label unnecessary regions as the specific target. The labels named 'DOB', 'address', 'karyalaya' (Issuing Office), and 'sex' correctly predict the region with 100% accuracy. In contrast, predicting 'Citizenship number' and 'name' regions, YOLO over captures these regions with the accuracy of 86% making it error prone. These fields from each test sample are cropped and sent to the Tesseract to evaluate CER Value.

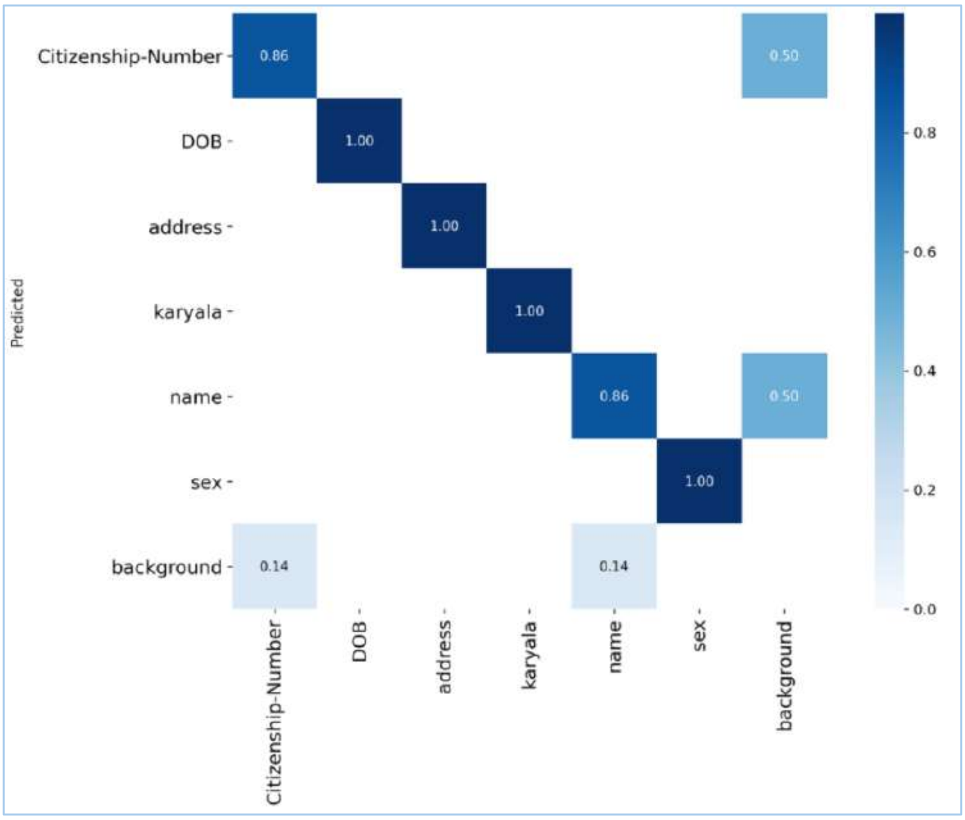


**Figure 11:** Confusion matrix of test dataset

Above experimental results are deliverable from Yolo model architecture.

**Table 1:** CER values in test sample

| Test Files | CER Value |
|---|---|
| f1 | 0.156 |
| f2 | 0.119 |
| f3 | 0.130 |
| f4 | 0.159 |
| f5 | 0.069 |
| f6 | 0.119 |
| f7 | 0.168 |
| **Total: 7 files** | **Average CER Value: 0.1315** |

Table 1 presents 7 unseen files with their respective CER value after ROI fields being cropped from YOLO and assessed from Tesseract. Each of the tested file CER is below 20%, with highest and lowest value in 7th and 5th file with values 16.8% and approx. 7% respectively.

### 4.3 Limitations

The trained model still struggles with handwritten text and old format of the Nepalese citizenship. This is due to the overlapping of the target regions. As intended, it supports only the Devnagari script of the document while failing to extract findings from the back of the paper. Likewise, it also fails for other linguistic variant countries, and multi-script documents. The system's metrics quality lessens as the quality of the image record degrades. The hardware is adjusted as per the height and record size. For different shapes, the hardware system needs to be modified to make documents fit.

## 5. Conclusion

This research presented a hardware-integrated OCR system designed for the digitization of Nepali citizenship documents, addressing the challenges associated with the intensive manual data entry and document handling. By combining a custom relay-controlled paper feeder mechanism, synchronization of hardware, backend and machine learning model with Tesseract, the system demonstrates an effective pipeline for automated extraction of required information from citizenship records.

The YOLO-based object detection model showed promising results by detecting the ROI of to-extracted labels like Name, Citizenship Number, Gender, etc., where Tesseract extracts Devnagari text from those regions with good character error rate supporting automated digitization. The result showed an average CER value with approximately 0.13 across test samples reflecting the model's capability to perform on structured printed fields. Nonetheless, the study validates that the end-to-end system with hardware is a faster and more convenient alternative for different banks, government institutions and agencies to handle the information of the Nepalese documents improving digitization workflows in Nepal.

## 6. Recommendation for future Research

Even though the proposed system provides an efficient foundation for automated Nepali citizenship digitization, there is still room for improvements and advancements. The first extension would be the support of a multilingual pipeline including English scripts as many government documents support English language. Next would be incorporating deep learning-based attention models like Transformer for the character recognition. Testing on these models would significantly improve character error rate.

From the hardware perspective, the paper feeder mechanism should be adjusted making it compatible with any type of government records based on document sizes, thickness and color. Encrypting it with security keys will further enhance the usability of the system in real-world cases. Additionally, real-time mechanisms can enable centralized storage, faster verification. Ultimately, all above future work can significantly strengthen digital governance initiatives in Nepal.

**References**


- Cutter, M. and Manduchi, R. (2017) Improving the Accessibility of Mobile OCR Apps Via Interactive Modalities | ACM Transactions on Accessible Computing. Available at: https://dl.acm.org/doi/abs/10.1145/3075300 (Accessed: December 13, 2025).

- Dessai, B. and Patil, A. (2019) "A Deep Learning Approach for Optical Character Recognition of Handwritten Devanagari Script," in 2019 2nd International Conference on Intelligent Computing, Instrumentation and Control Technologies (ICICICT). 2019 2nd International Conference on Intelligent Computing, Instrumentation and Control Technologies (ICICICT), pp. 1160–1165. Available at: https://doi.org/10.1109/ICICICT46008.2019.8993342.

- Dhakal, S. et al. (2024) "Mero Nagarikta: Advanced Nepali Citizenship Data Extractor with Deep Learning-Powered Text Detection and OCR." arXiv. Available at: https://doi.org/10.48550/arXiv.2410.05721.

- Hasan, S.M.R. et al. (2024) "Optical Text Recognition in Nepali and Bengali: A Transformer-based Approach." arXiv. Available at: https://doi.org/10.48550/arXiv.2404.02375.

- Karayil, T., Ul-Hasan, A. and Breuel, T.M. (2015) "A segmentation-free approach for printed Devanagari script recognition," in 2015 13th International Conference on Document Analysis and Recognition (ICDAR). 2015 13th International Conference on Document Analysis and Recognition (ICDAR), pp. 946–950. Available at: https://doi.org/10.1109/ICDAR.2015.7333901.

- Kumar, S. et al. (2024) "Text Extraction from Images Using Tesseract," in Deep Learning Techniques for Automation and Industrial Applications. John Wiley & Sons, Ltd, pp. 1–18. Available at: https://doi.org/10.1002/9781394234271.ch1.

- Liu, C. et al. (2018) "Object Detection Based on YOLO Network," in 2018 IEEE 4th Information Technology and Mechatronics Engineering Conference (ITOEC). 2018 IEEE 4th Information Technology and Mechatronics Engineering Conference (ITOEC), pp. 799–803. Available at: https://doi.org/10.1109/ITOEC.2018.8740604.

- Luthra, P., Chauhan, P. and Ahmad Ansari, I. (2020) "Low Cost Automatic Document Scan Machine Using Raspberry Pi and Tesseract Ocr." Rochester, NY: Social Science Research Network. Available at: https://doi.org/10.2139/ssrn.3575389.

- Matveev, I.V., Khalyasmaa, A.I. and Matrenin, P.V. (2025) "Analysis of Modern Models Capabilities and Software for Automatic Annotation of Graphical Data in the Power Industry," in 2025 IEEE 26th International Conference of Young Professionals in Electron Devices and Materials (EDM). 2025 IEEE 26th International Conference of Young Professionals in Electron Devices and Materials (EDM), pp. 990–994. Available at: https://doi.org/10.1109/EDM65517.2025.11096708.

- Mehta, D. and Mehta, P. (2025) "Devanagari Handwritten Character Recognition using Convolutional Neural Network." arXiv. Available at: https://doi.org/10.48550/arXiv.2507.10398.

- Mittal, R. and Garg, A. (2020) "Text extraction using OCR: A Systematic Review," in 2020 Second International Conference on Inventive Research in Computing Applications (ICIRCA). 2020 Second International Conference on Inventive Research in Computing Applications (ICIRCA), pp. 357–362. Available at: https://doi.org/10.1109/ICIRCA48905.2020.9183326.

- Parween, G. and Saha, S. (2021) "Design of an OCR System and its Hardware Implementation," International Journal for Research in Applied Science and Engineering Technology, 9(12), pp. 159–174. Available at: https://doi.org/10.22214/ijraset.2021.39217.

- Prajapati, S. et al. (2018) "Evaluating Performance of Nepali Script OCR using Tesseract and Artificial Neural Network," in 2018 IEEE 3rd International Conference on Computing, Communication and Security (ICCCS). 2018 IEEE 3rd International Conference on Computing, Communication and Security (ICCCS), pp. 104–107. Available at: https://doi.org/10.1109/CCCS.2018.8586808.

- Rybalkin, V. et al. (2018) "iDocChip: A Configurable Hardware Architecture for Historical Document Image Processing: Percentile Based Binarization," in Proceedings of the ACM Symposium on Document Engineering 2018. New York, NY, USA: Association for Computing Machinery (DocEng '18), pp. 1–8. Available at: https://doi.org/10.1145/3209280.3209538.

- Saint-Vil, A. et al. (2022) "High Resolution Headband Document Scanner and Transmitter for the Disabled People," in 2022 IEEE International Conference on Imaging Systems and Techniques (IST). 2022 IEEE International Conference on Imaging Systems and Techniques (IST), pp. 1–2. Available at: https://doi.org/10.1109/IST55454.2022.9827664.

- Tafti, A.P. et al. (2016) "OCR as a Service: An Experimental Evaluation of Google Docs OCR, Tesseract, ABBYY FineReader, and Transym," in G. Bebis et al. (eds.) Advances in Visual Computing. Cham: Springer International Publishing, pp. 735–746. Available at: https://doi.org/10.1007/978-3-319-50835-1_66.

# Pokhara Engineering College Journal (PECJ)

*Applied Sciences and Engineering Insights*

ISSN: 3021-9795 (Print) / 3059-9628 (Online)
(Volume-3, Issue I)

# Analyzing the gap between its curriculum and industry demand in Nepal using NLP

Hari Prasad Baral[1], Bhoj Raj Ghimire [2*]
[1] Faculty of Science Health & Technology, Nepal Open University Katmandu Nepal
*Corresponding email: haripbaral@wrc.edu.np



*Received:20- January-2026; Revised: 17- February-2026; Accepted: 21- March-2026*
*DOI: https://doi.org/10.3126/pecj.v3i1.93534*

**Abstract**

Bridging the gap between academic IT curricula and industry requirements remains a pressing challenge in Nepal, given the rapid evolution of technology. This study presents a systematic, data-driven approach to evaluate the alignment between IT programs and industry needs using Natural Language Processing (NLP) techniques. Course descriptions from leading universities were analyzed alongside IT job postings using BERT-based embeddings to calculate semantic similarity, enabling the classification of courses into high, medium, or low alignment categories. Concurrently, KeyBERT was employed to extract key skills, tools, and technologies from both datasets, allowing for an assessment of keyword coverage. By integrating semantic similarity scores with keyword overlap, a comprehensive alignment metric was developed, capturing knowledge domains, technical skills, and professional competencies.

The analysis identified measurable gaps, including a knowledge Gap of 0.40, a Technical Skills Gap of 0.25, and a Competency Gap of 0.40, yielding an Overall Gap of 0.34 and an Alignment Index of 0.66. These findings indicate moderate alignment while highlighting deficiencies in emerging technologies and employability skills. The methodology offers a reproducible and quantitative framework for curriculum evaluation, providing actionable insights for educators, curriculum developers, and policymakers to enhance program relevance and better prepare graduates for the evolving demands of the IT industry.

***Keywords:*** IT curriculum, industry demand, NLP, BERT, KeyBERT, curriculum industry alignment, Nepal

## 1. Introduction

In recent years, Nepal's Information Technology (IT) sector has experienced substantial growth, driven by digital transformation initiatives and the expanding adoption of technology-based services (Zhao and Li, 2020). This expansion has increased the need for graduates who possess not just theoretical knowledge but also practical skills and technical proficiency aligned with the dynamic demands of the labor market. Despite multiple curriculum reforms, a significant disparity remains between the education provided by higher education institutions and the expectations of the IT industry (Bista, 2018).

This mismatch presents considerable challenges. It affects the employability of graduates and constrains Nepal's potential to leverage its human capital for long-term technological development. Previous research indicates that many IT graduates in Nepal have limited exposure to emerging technologies, insufficient practical learning opportunities, and lack essential soft skills such as communication, teamwork, and problem-solving which are highly sought after by employers (Li and Zhang, 2019). Bridging the gap between academic instruction and professional expectations has therefore become a critical priority in Nepal's fast-evolving digital economy.

To tackle this issue, the current study proposes a data-driven approach to assess the alignment between IT curricula and industry requirements using Natural Language Processing (NLP). The methodology involves analyzing university course outlines alongside IT sector job postings. By employing BERT-based embeddings, semantic similarity is measured to classify courses as highly, moderately, or poorly aligned. Additionally, KeyBERT is utilized to extract relevant skills, tools, and technologies from both datasets, enabling the evaluation of keyword coverage. By integrating these two metrics, a composite alignment score is calculated, providing a comprehensive assessment across three key dimensions: knowledge areas, technical skills, and professional competencies.

The results indicate measurable gaps in these domains knowledge Gap of 0.40, a Technical Skills Gap of 0.25, and a Competency Gap of 0.40. Collectively, these lead to an Overall Gap of 0.34 and an Alignment Index of 0.66. This suggests that while the curriculum shows moderate alignment with industry needs, deficiencies remain, particularly in incorporating emerging technologies and cultivating employability-related skills.

Unlike conventional curriculum review approaches in Nepal, which predominantly rely on expert opinion and manual evaluation methods often criticized for being subjective, slow, and unable to keep pace with technological advancements (Shrestha and Acharya, 2019). This study illustrates how NLP-based methods offer a systematic and scalable alternative. The proposed framework provides evidence-based insights to guide educators, curriculum designers, and policymakers in reforming IT programs to enhance industry relevance, boost graduate employability, and promote sustainable growth within Nepal's IT sector.

## 2.Related work

### 2.1. The Gap Between IT Curriculum and Industry Needs

A notable discrepancy continues to exist between the content delivered by academic institutions and the skills demanded by the IT industry, particularly in developing countries like Nepal. This gap has been widely reported in previous studies. Despite efforts to modernize IT curricula, reforms in Nepal lag behind the rapid evolution of technology, leaving graduates insufficiently prepared with practical expertise (Yadav and Shrestha, 2022). Research also indicates that many universities still prioritize theoretical instruction over hands-on learning, resulting in graduates with limited exposure to areas such as cloud computing, artificial intelligence, and mobile application development (Bista, 2018;Joshi, 2020). Employers have further expressed concerns regarding graduates underdeveloped soft skills, including teamwork and communication (Dahal and Thapa, 2021). Studies recommend stronger collaboration between academia and industry, regular curriculum reviews, and the inclusion of internships to enhance graduate employability (Shrestha and Acharya, 2019; Rajbhandari and Koirala, 2021).

### 2.2. Role of Natural Language Processing (NLP) in Curriculum Evaluation

NLP has emerged as a powerful tool for assessing curriculum relevance. Unlike traditional methods, which are manual, slow, and subjective, NLP enables large-scale, automated, and objective analysis of course content, job postings, and employer requirements (Wang and Chen, 2021). Techniques such as Latent Dirichlet Allocation (LDA) and Non-negative Matrix Factorization (NMF) have been employed to uncover hidden skill clusters and identify curriculum industry misalignments (Brown and Wilson, 2021). More sophisticated approaches, including BERTopic and KeyBERT, facilitate contextual keyword extraction for deeper insights (Gupta and Jain, 2019). These methods support skill mapping, track labor market trends, and highlight emerging needs in areas like machine learning, cybersecurity, and UI/UX design (Ahmed and Rahman, n.d.; Wang and Chen, 2021).

**2.3. Nepal's IT Education and Reform Needs**

Although IT education in Nepal has expanded over the past two decades, curricula remain largely misaligned with industry requirements. Research shows that practical training components such as capstone projects, coding bootcamps, and real-world industry case studies are still limited (Bista, 2018). Employers report deficiencies in skills related to DevOps, cloud computing, and data visualization. Furthermore, the prevailing exam-focused teaching approach constrains the development of creativity and soft skills (Dahal and Thapa, 2021; Joshi, 2020).

**2.4. Research Gap**

While NLP-based curriculum analysis has demonstrated significant potential globally, its application in Nepal remains minimal. Despite policy emphasis on digital transformation, there is little systematic use of NLP for curriculum evaluation in the country. This presents a clear research gap and an opportunity to implement evidence-driven approaches that better align academic programs with the evolving needs of the labor market (Chen and Huang, 2018; Yadav and Shrestha, 2022).

**3.Methodology**

This research employs a mixed-method, data-driven approach, emphasizing the use of Natural Language Processing (NLP) techniques to analyze and address the gap between Nepal's academic IT curricula and the demands of the IT industry. The methodology is organized into five key phases: data collection, data preprocessing, application of NLP methods, gap analysis, and validation with actionable recommendations

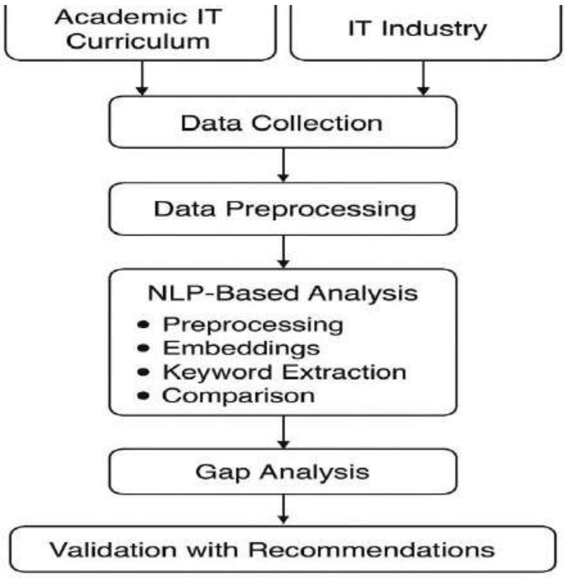


**Figure 1:** System Architecture

The NLP-based analysis follows four major steps:

- To Preparation of Academic and Industry Datasets
- To Preprocessing Cleaning, tokenization, and normalization of textual data.
- To Applying BERT-based embeddings to capture semantic meaning.
- Using KeyBERT to extract skills, tools, and knowledge areas.
- To Computing similarity scores and coverage metrics between curriculum and industry datasets.

### 3.1 Data Collection

To assess how well IT education in Nepal aligns with industry needs, curriculum information was collected from prominent universities offering undergraduate IT programs, including Tribhuvan University, Kathmandu University, Pokhara University, and Purbanchal University. Updated and official syllabi, course outlines, and curriculum frameworks were sourced from university websites, academic handbooks, and prospectuses.

Alongside academic data, IT industry job requirements were compiled from various platforms to capture real-world employer expectations. This included job postings from leading Nepali websites such as merojob.com, jobsnepal.com, and LinkedIn, which provided information on necessary technical skills, qualifications, and essential soft skills.

**3.2Calculating Cosine Similarity**

Cosine similarity is a method for assessing how closely academic courses align with industry requirements by converting both into vectors of skills, topics, or tools. Rather than focusing on the magnitude of these vectors, it measures the angle between them, which allows for a reliable comparison even if the size or scope of the course content differs. The resulting similarity score ranges from 0 to 1, where values closer to 1 indicate strong correspondence with industry needs, and lower values reveal areas where the curriculum may be lacking. This approach enables educational institutions to identify skill gaps and make informed adjustments to their programs, ensuring graduates are better prepared for the workforce. In natural language processing applications, cosine similarity is particularly effective when course descriptions or job requirements are represented as embeddings, such as those generated by BERT, because it captures semantic and contextual relationships rather than just exact word matches.

**3.2.1. Cosine Similarity Formula**

For two vectors A and B (for example, representing course content and industry skills), cosine similarity is calculated as:

$$\cos\theta = \frac{(A \cdot B)}{[A][B]}] \qquad [1]$$

Where:

A.B is the dot product of vectors A and B

[A] is the magnitude of vector A, computed as [A]= $=\Sigma_i A^2$

[B] is the magnitude of vector B, computed as [B]= $=\Sigma_i B^2$

**3.2.2. Gap Score**

The Gap Score measures the difference between the emphasis placed on a particular skill in the academic curriculum and its demand in industry job postings. It is defined as:

Gap Score(x)=Industry Weight(x)−Curriculum Weight(x) [2]

A positive Gap Score highlights a skill deficit where industry demand exceeds curriculum emphasis, while a negative score indicates potential over-emphasis in the curriculum. A score near zero reflects strong alignment between academic training and industry needs

**4.Results and Discussion**

The bar chart labeled "Course–Industry Alignment (Cosine Similarity)" depicts how closely academic IT courses correspond to industry requirements. Courses like Design & Analysis of Algorithms, Cloud Computing, and Mobile App Development exhibit the strongest alignment, whereas subjects such as Introduction to IT and C Programming show comparatively lower relevance. In general, most core technical courses align well with industry needs, though certain areas still reveal significant gaps.

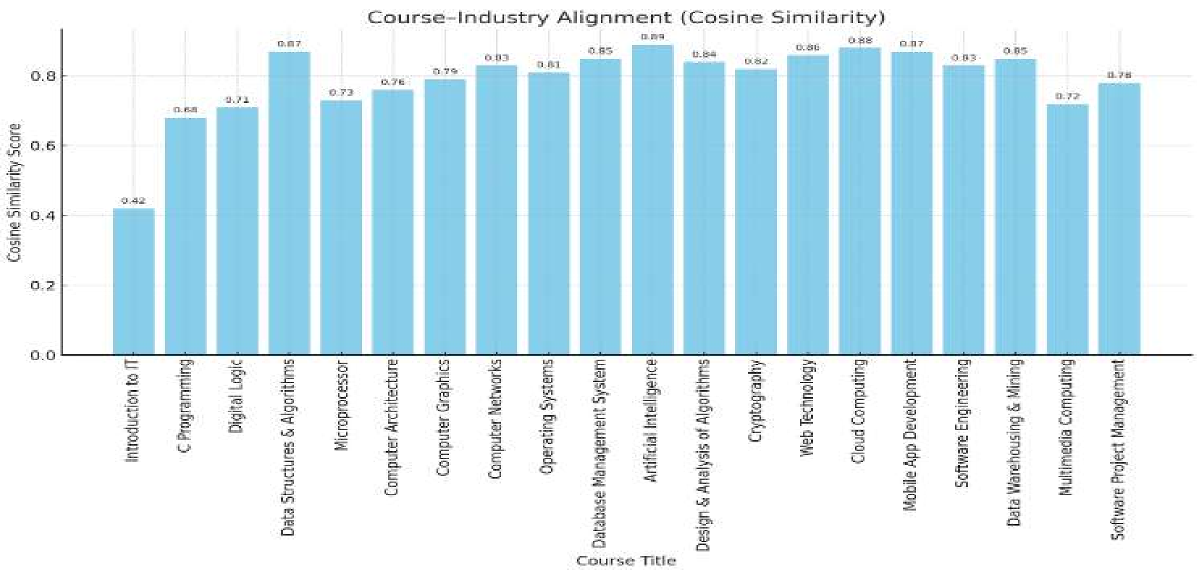


**Figure 2:** cosine similarity industry and IT curriculums

The degree of alignment between IT courses and industry requirements varies across the curriculum. Courses such as Design & Analysis of Algorithms (0.89), Cloud Computing (0.88), Mobile App Development (0.87), and Data Structures & Algorithms (0.87) exhibit high alignment. Core subjects including Database Management Systems (0.85), Artificial Intelligence (0.84), Computer Networks (0.83), and Operating Systems (0.81) demonstrate moderate to strong relevance. Meanwhile, courses like Computer Graphics (0.79), Software Project Management (0.78), and Digital Logic (0.71) require partial updates to remain current. Low alignment is noted in Introduction to IT (0.42) and C Programming (0.68), reflecting content that is either outdated or less aligned with industry demands

### 4.1. Course–Skill Alignment Comparison

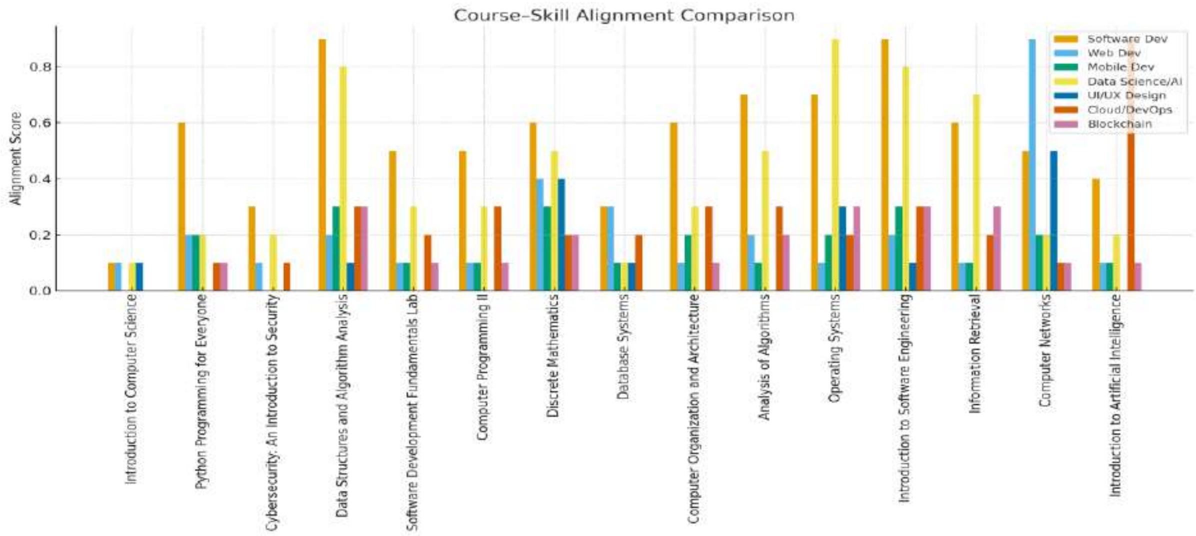


**Figure 3:** Course–Skill Alignment Comparison

The bar chart titled "Course–Skill Alignment Comparison" presents the degree to which various IT courses correspond to key industry skill areas, including Software Development, Web Development, Mobile Development, Data Science/AI, UI/UX Design, Cloud/DevOps, and Blockchain. Courses such as Data Structures and Algorithm Analysis, Analysis of Algorithms, and Introduction to Software Engineering demonstrate strong alignment with Software Development and Data Science/AI skills. Core subjects like Database Systems, Operating Systems, and Computer Networks show moderate alignment across multiple skill areas. In contrast, foundational courses such as Introduction to Computer Science, Python Programming for Everyone, and Cybersecurity: An Introduction to Security exhibit lower alignment scores across most industry skill categories, indicating gaps between the curriculum and current industry expectations. Overall, the chart identifies areas of high relevance as well as courses that may need revision to better match contemporary skill demands.

The alignment analysis reveals that courses like Data Structures & Algorithms and Introduction to Software Engineering are highly relevant to Software Development and Data Science/AI, with alignment scores ranging from 0.8 to 0.9. Likewise, Computer Networks shows strong correspondence with Web Development (0.9), Artificial Intelligence aligns closely with Cloud and DevOps roles (0.9), and Operating Systems is particularly relevant to Data Science/AI (0.9). Conversely, courses such as Introduction to Computer Science and Blockchain have very low alignment (≤ 0.3), while Database Systems and Cybersecurity show only limited to moderate relevance to industry needs. Notable gaps are evident in areas such as Mobile

Development and Blockchain, which have minimal aligned coursework (≤ 0.3), and UI/UX Design, which is insufficiently covered, mainly through Computer Networks (0.5).

**Recommendation**

To prepare graduates for Nepal's rapidly evolving IT industry, universities should update curricula with a strong emphasis on practical, hands-on skills and actively incorporate emerging technologies such as Blockchain, Cloud Computing, and Mobile Development. Core courses should integrate project-based learning, real-world applications in Data Science, and deliberate development of soft skills, including communication, teamwork, and problem-solving. Strengthening collaboration with industry through internships, continuous feedback, and joint initiatives can further ensure that academic training aligns with workplace demands.

This strategy equips students with a solid theoretical foundation alongside practical experience with relevant tools and technologies, cultivating versatile and well-rounded professionals. Continuous engagement with industry partners allows curricula to stay responsive to technological advancements and evolving professional requirements, preparing graduates for both local and global IT markets. By implementing these measures, universities can enhance employability, stimulate innovation, and effectively bridge the gap between academic programs and industry needs, promoting sustainable growth within Nepal's IT sector.

**Conclusion**

In summary, this study finds that Nepal's IT curriculum exhibits moderate alignment with industry requirements, with an overall alignment index of 0.66. While core courses such as Data Structures, Algorithms, and Software Engineering show strong relevance, significant gaps remain in emerging areas like Blockchain, Cloud Computing, and Mobile Development. Additionally, practical skill development and the incorporation of critical soft skills—such as communication, teamwork, and problem-solving are still limited, which affects graduate employability and constrains potential for innovation.

By utilizing Natural Language Processing tools like KeyBERT, BERTopic, and semantic similarity analysis, this research presents a systematic, data-driven approach for assessing curriculum–industry alignment. These methods allow for objective identification of curricular strengths and weaknesses, offering actionable insights to guide evidence-based improvements. This approach enhances the rigor and transparency of curriculum evaluation while providing universities with clear directions to better match academic programs with evolving industry demands.

To bridge the identified gaps, Nepalese universities should modernize IT curricula by emphasizing project-based learning, hands-on engagement with emerging technologies, and structured development of soft skills. Strengthening partnerships with the industry through internships, continuous feedback, and collaborative projects can further ensure graduates are well-equipped for practical challenges. Beyond Nepal, this framework can serve as a valuable model for other developing countries aiming to align academic programs with workforce requirements. Ultimately, aligning IT curricula with industry needs will enhance graduate readiness, stimulate innovation, and support sustainable economic growth by preparing professionals for both local and international IT markets.

**Acknowledgment**

The authors would like to express their sincere gratitude to the faculty and administrative staff of Nepal Open University for their guidance and support throughout this study. Special thanks are extended to my supervisor, Dr. Bhoj Raj Ghimire, for his invaluable guidance, mentorship, and insightful feedback. Appreciation is also extended to the IT departments of Tribhuvan University, Kathmandu University, Pokhara University, and Purbanchal University for providing access to course curricula and academic resources. The authors further acknowledge the contributions of industry professionals and job portal platforms, whose input on IT job requirements was essential for analyzing curriculum–industry alignment. Constructive feedback from peers and colleagues also helped refine the methodology and analysis.

**References**

- Bista, P., 2018. IT education in Nepal: Challenges and prospects. Nepal Journal of Science and Technology, 19(1), pp.77–86.
- Brown, T. and Wilson, A., 2021. Natural language processing for curriculum analysis: A review. Computers & Education, 168, p.104195.
- Chen, Y. and Huang, Z., 2018. Application of BERTopic in curriculum gap analysis. Journal of Educational Data Mining, 10(1), pp.23–40.
- Dahal, K. and Thapa, P., 2021. Integration of industry feedback in IT curriculum development: A case study in Nepal. Nepalese Journal of Educational Development, 5(1), pp.52–63.
- Gupta, N. and Jain, S., 2019. Using topic modeling for educational needs analysis in computer science. IEEE Transactions on Learning Technologies, 12(3), pp.348–359.

- Joshi, R., 2020. Skills gap analysis of IT graduates in Nepal: Employers' perspective. Nepalese Journal of Management, 10(2), pp.89–99.
- Li, M. and Zhang, Y., 2019. An NLP-based approach to evaluate skills demand in IT job postings. IEEE Access, 7, pp.14202–14213.
- Ministry of Education, Nepal, 2022. National curriculum framework for IT education. Kathmandu: Government of Nepal.
- Poudel, S., 2019. Employability skills of IT graduates in Nepal: A study on industry requirements. Nepalese Journal of IT and Software Engineering, 6(1), pp.30–44.
- Rajbhandari, B. and Koirala, S., 2021. Industry-academia collaboration for enhancing IT education in Nepal. International Journal of IT Management, 10(3), pp.47–58.
- Shrestha, S. and Acharya, D., 2019. Curriculum reform in Nepalese IT education: A stakeholder perspective. Education Journal of Nepal, 7(1), pp.12–24.
- Singh, A. and Verma, R., 2021. Aligning IT curriculum with market needs: A data-driven approach using NLP. International Journal of Computer Applications, 182(3), pp.25–31.
- Wang, X. and Chen, L., 2021. Using NLP techniques to analyze curriculum-industry alignment in computer science education. International Journal of Educational Technology, 18(4), pp.223–235.
- Yadav, S. and Shrestha, R., 2022. Challenges and opportunities in Nepalese higher education: An IT perspective. Journal of Educational Technology, 15(1), pp.45–62.
- Zhao, X. and Li, Q., 2020. Analyzing industry requirements through job advertisements using NLP. Journal of Vocational Education & Training, 72(1), pp.61–79.

Pokhara Engineering College Journal (PECJ)
*Applied Sciences and Engineering Insights*

ISSN: 3021-9795 (Print) / 3059-9628 (Online)
(Volume-3, Issue- I)

# Abstractive Summarization of News Articles Using BART

Mohan Bikram KC[1]*, Ayush Sharma Kaundinya[2], Pramish Adhikari[3], Smita Adhikari[4]

[1,2,3] *Department of Computer Engineering, Gandaki College of Engineering and Science,Nepal*

[4] *Department of Electronics and Computer Engineering, Pashchimanchal Campus, Pokhara, Nepal*

*Corresponding email: kcmohan64@gmail.com



*Received:22- January-2026; Revised: 15- February-2026; Accepted: 20- March-2026*
*DOI: https://doi.org/10.3126/pecj.v3i1.93538*

**Abstract**

Abstractive text summarization generates concise summaries that preserve key concepts through newly constructed sentences rather than extraction from the source. As online news content grows rapidly, effective summarization systems are essential for efficient information consumption. This study investigates abstractive summarization using BART-Large, a transformer-based encoder-decoder model, with a novel training approach: fine-tuning on a combined dataset merging XSum and CNN/DailyMail. While XSum emphasizes highly abstractive single-sentence summaries and CNN/DailyMail targets longer multi-sentence outputs, combining these datasets during training aims to produce a more versatile model capable of handling diverse summarization demands. Performance is evaluated using ROUGE metrics, which measure n-gram overlap between generated and reference summaries. The fine-tuned model achieves a ROUGE-2 score of 22.86, demonstrating competitive performance against existing approaches. Qualitative analysis reveals that the model produces fluent, coherent summaries while maintaining factual consistency with source documents. These results indicate that exposing models to varied summarization demands during fine-tuning can improve flexibility without sacrificing quality. This work offers a practical direction for building more generalizable summarization systems and highlights the potential of multi-dataset training strategies for domain adaptation in natural language generation tasks.

**Keywords:** Abstractive Text Summarization, BART-Large, News Articles, ROUGE Evaluation, Natural Language Processing

## 1. Introduction

With expansion of online media, individuals are exposed to an excessive volume of news content. Every moment, numerous articles appear across digital platforms which makes it challenging for readers to remain informed on factual information efficiently. This flooding of data has created a need for automated methods that can produce concise and informative summaries of lengthy news articles. In the field of natural language processing, text summarization has emerged as a practical approach to address this challenge by enabling readers to learn the core ideas of a text in a shorter time.

Text summarization uses two methods i.e., extractive and abstractive. The extractive method identifies the most relevant sentences or phrases in the source and arranges them to form a summary. An abstractive method models the meaning of the source and produces new sentences that deliver the same information with clarity. Abstractive summarization is more complex because it depends on deeper knowledge of linguistic structure, grammar and context. In recent years advances in deep learning and progress of models based on transformers have led to substantial gains in the quality of abstractive summarization.

This study implements the Large variant of the Bidirectional and Auto-Regressive Transformer for the abstractive summarization of news articles. The model is fine-tuned with two widely recognized datasets, XSum, which contains short single sentence summaries, and CNN/DailyMail, which includes longer multiple sentence summaries. These datasets enable evaluation of the ability of the model to adapt to different lengths for summary and writing styles. Performance is evaluated using the Recall Oriented Understudy for Gisting Evaluation (ROUGE) metrics, which quantify the degree of similarity between generated summaries and human summaries.

### 1.1 Problem Statement

The rapid growth of online news has reduced the ability of readers to keep pace with the continuous production of information. A very large number of articles are published continuously across many platforms, which overwhelms readers and makes it difficult to determine what is most important. Although automatic summarization systems are available, many continue to rely on extractive methods that select segments of the source text. These summaries can be produced quickly, but they often read as unnatural and do not accurately represent the meaning or intent of the article.

### 1.2 Objective

The main objective of the study is to fine-tune the BART-Large model on two benchmark datasets: XSum and CNN/DailyMail for producing both short and long summaries while maintaining factual accuracy.

## 2. Literature Review

Lewis et al. (2019) introduced BART, a denoising autoencoder for sequence pretraining that uses a bidirectional encoder similar to BERT and a left-to-right decoder similar to GPT. The model is trained by corrupting input text, for example by shuffling sentences and using a span-masking scheme that replaces continuous segments with a single mask token, and then learning to reconstruct the original sequence. BART performs well on both text generation and text understanding tasks: it reaches performance comparable to RoBERTa on GLUE and SQuAD, and improves results for abstractive dialogue, summarization, and question answering by as much as 6 ROUGE points. In machine translation, target-side pretraining with BART yields a BLEU gain of 1.1. Ablation studies show which pretraining objectives and design choices matter most for downstream performance, and indicate that BART can be applied effectively to a wide range of natural language processing tasks.

Zhang et al. (2019) created PEGASUS, a Transformer-based model. It's designed specifically for abstractive summarization. Instead of randomly masking words like most models, it skips entire unimportant sentences. Then it learns to turn the best parts of the text into coherent summaries. They tested it on 12 different dataset news, research papers, stories, even law documents. PEGASUS achieved strong results across all datasets. Even when there's little data, it outperforms older models, and its summaries often read as natural as a human wrote them.

Raffel et al. (2019) introduced T5, a Transformer model that treats every natural language processing task as a text-to-text problem. They ran a large set of experiments comparing different transfer learning methods, pretraining objectives, model architectures, and training datasets across many language tasks. Using large-scale pretraining on the Colossal Clean Crawled Corpus (C4), T5 reached state-of-the-art results in tasks such as summarization, question answering, and text classification. The authors also released pretrained models and the C4 dataset, making it easier to study and apply transfer learning in natural language processing.

Text summarization reduces long texts to concise summaries, and large language models use context to produce human-like summaries. Basyal and Sanghvi (2023) compared MPT-7B-Instruct, Falcon-7B-Instruct, and OpenAI text-davinci-003 on CNN/DailyMail and Extreme Summarization datasets. Text-davinci-003 gave the most accurate summaries by Bilingual Evaluation Understudy, Recall Oriented Understudy for Gisting Evaluation, and Bidirectional Encoder Representations from Transformers score. The study shows that large language models can improve automatic summarization and guide future natural language processing.

Shakil et al. (2024) present a comprehensive survey on abstractive text summarization, categorizing state-of-the-art techniques into five groups: traditional sequence-to-sequence models, pre-trained large language models, reinforcement learning approaches, hierarchical methods, and multi-modal summarization. The authors provide comparative analysis tables offering insights into model complexity, scalability, and appropriate applications. The paper highlights key challenges including inadequate meaning representation, factual consistency, controllable summarization, cross-lingual summarization, and evaluation metrics, while proposing solutions leveraging knowledge incorporation and other innovative strategies. The survey also explores emerging research directions such as domain-specific summarization, long-document summarization, and handling noisy data, providing researchers with a structured overview to advance abstractive summarization research.

Venkataramana, Srividya, and Cristin (2022) proposed using Bidirectional and Auto Regressive Transformers, a deep learning encoder decoder model, for efficient abstractive summarization. The model uses attention to identify key features and predict missing tokens, improving summary quality. Compared with Bidirectional Encoder Representations from Transformers, Text To Text Transfer Transformer, and Robustly Optimized Bidirectional Encoder Representations from Transformers Pretraining Approach, the model performed well on large scale text summarization. This approach shows that deep learning can automate and speed processing of extensive datasets.

Chari et al. (2024) proposed a system using pretrained Bidirectional and Auto Regressive Transformers fine-tuned on CNN/DailyMail to generate abstractive summaries from text files and Uniform Resource Locators. It incorporates the encoder from BERT into Generative Pre-trained Transformer. This model enhances coherence and factual consistency. The repetition, faithfulness and control of length are considered as challenges in this study. In this way, it indicates how a deep learning model can summarize large-scale and diverse documents efficiently.

Automatic text summarization condenses long sentences into brief summaries. Adhik, Lakshmi, and Muralidharan (2024) developed a high-quality summarizer based on a bidirectional encoder and autoregressive decoder model. Their proposed system received a quality score of about 78%, as ROUGE metrics were adopted for assessing the accuracy of generated summaries. It removes unnecessary information and emphasizes only the important ones, which proves that transformer-based models work well in text summarization.

Deep learning models are normally used to summarize large volumes of text data efficiently. Dharrao et al. (2024) compared BART, T5, and PEGASUS on the BBC business article dataset. Model performance was evaluated using ROUGE and METEOR scores. T5 attained the highest accuracy of ROUGE-1: 0.354 and METEOR: 0.35. The results showed that a transformer-based model can effectively get relevant information from business news.

Abstractive summarization produces concise summaries for both brief and lengthy texts. Wilman, Atara, and Suhartono (2024) proposed a method that uses a pre-trained Bidirectional and Auto-Regressive Transformers model with chunking to process long English documents. The text is split into chunks; each chunk is encoded and summarized with the model, and then the summaries are combined into a final version. The results obtained by the CNN/DailyMail pre-trained model were better than those of the Extreme Summarization version. This approach improves summary quality for lengthy texts such as news and research articles.

Ghanem et al. (2025) proposed a hybrid deep learning system that combines Bidirectional Encoder Representations from Transformers, known as BERT, a Transformer encoder and decoder, and long short term memory networks to produce concise summaries that fit the context. The system uses attention to focus on key information and limit repetition. On the Hagupit, SHShoot, and Hyderabad Blast datasets it achieved higher ROUGE scores than earlier methods. The results show practical ways to automate short text summarization on social media.

To find an effective model for summarizing news, Krishna et al. (2025) compared several deep learning approaches. They tested Text-to-Text Transfer Transformer-base, Text-to-Text Transfer Transformer-large, Bidirectional and Auto-Regressive Transformers Cable News

Network, and Pre-training with Extracted Gap-sentences for Abstractive Summarization. The researchers initially prepared the data and conducted exploratory analysis, before assessing the models using Recall-Oriented Understudy for Gisting Evaluation and Bilingual Evaluation Understudy scores. All the results indicate very clear differences in summary quality. This work demonstrates both the promise and the difficulty of using deep learning to generate accurate summaries from long documents.

Nnadi and Bertini (2024) present a survey on abstractive text summarization focusing on datasets, models, and evaluation metrics. The survey covers transformer-based models for summarization including BART, PEGASUS, Longformer, and LongT5 for single documents, and PRIMERA, CENTRUM, and REFLECT for multi-document tasks. A key challenge the authors highlight is that standard transformers struggle with longer sequences (beyond 512-1024 tokens) because self-attention gets computationally expensive as length increases. They evaluate models using ROUGE, METEOR, BertScore, and factual consistency checks, finding that training across multiple datasets and domains improves performance. Interestingly, factual inconsistency rates have dropped compared to the roughly 30% reported in earlier work, though generating reliably accurate summaries remains a hurdle for practical use.

Chen and Song (2021) proposed a hybrid text summarization method combining TextRank with BART to address topic deviation problems in abstractive summarization. Their approach first uses TextRank for extractive summarization and BART for abstractive summarization separately, then splices the results to create a new text that increases the weight of key sentences. This combined text is then fed into the BART model again to generate the final summary. Experimental results demonstrate improvements over a single BART model, with average recall scores increasing by 1.5%, 0.5%, and 1.3% for ROUGE-1, ROUGE-2, and ROUGE-L respectively.

Dhanda and Gupta (2024) compared extractive and abstractive summarization techniques. Algorithms discussed included TextRank, Sequence to Sequence, and Bidirectional and Auto-Regressive Transformers. Results indicated that though TextRank works well with short texts, and Sequence to Sequence models generate summaries of high quality, the Bidirectional and Auto-Regressive Transformers model beats them when applied to benchmark datasets. Hence, based on Recall-Oriented Understudy for Gisting Evaluation scores, transformer-based models generate summaries that are more accurate as well as coherent. This study is an eye-opener regarding the strengths and shortcomings of various summarization algorithms.

## 3. Methodology

### 3.1 Datasets

Two popular benchmark datasets were used for the purpose of model training and evaluation with regards to the abstractive summarization task, the XSum dataset, along with the CNN/DailyMail dataset version 3.0.0. The XSum dataset consists of 204,045 train samples, 11,332 validation samples, and 11,334 test samples, which feature a collection of BBC articles summarized in a single sentence with a highly abstractive nature. The CNN/DailyMail dataset consists of 287,113 train samples, 13,368 validation samples, and 11,490 test samples, with a feature set that provides more extractive two-sentence abstracts. These two datasets were merged together in order to provide a well-rounded corpus consisting of a combined dataset of 491,158 train samples, 24,700 validation samples, and 22,824 test samples.

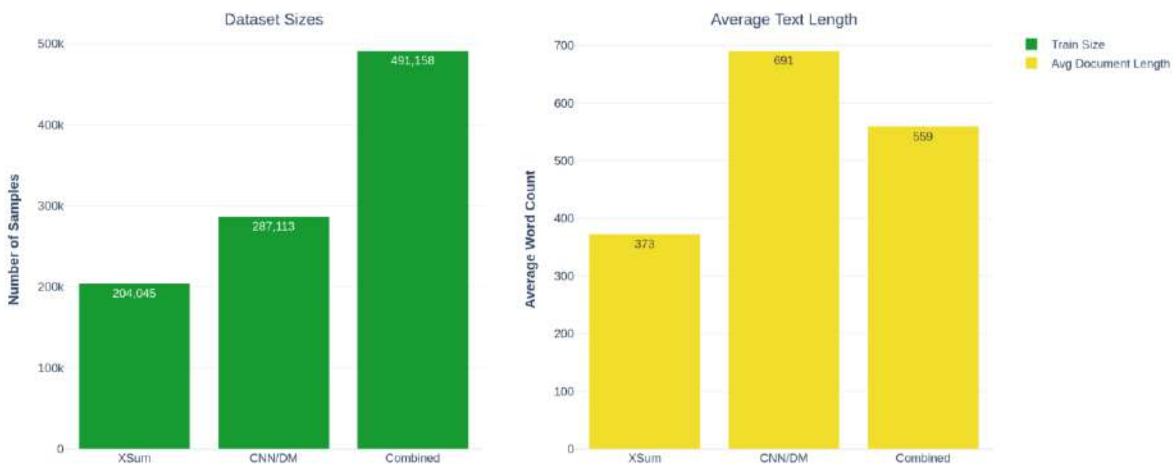


**Figure 1**: Sample Distribution and Average Document Length Across XSum, CNN/DailyMail, and Combined Datasets

### 3.2 Data Preprocessing

During the text processing stage, the BART tokenizer with a vocabulary size of 50,265 tokens was used to convert text into model-compatible representations. The input documents were tokenized and truncated to a maximum length of 1,024 tokens to preserve essential content while maintaining computational efficiency. Target summaries were similarly processed with a maximum length of 128 tokens. Dynamic padding was implemented at the batch level, with sequences padded to the longest sequence within each batch. DataCollatorForSeq2Seq was used for the conversion of summary tokens into label format, with padding tokens replaced with -100 to exclude them from loss computation during training.

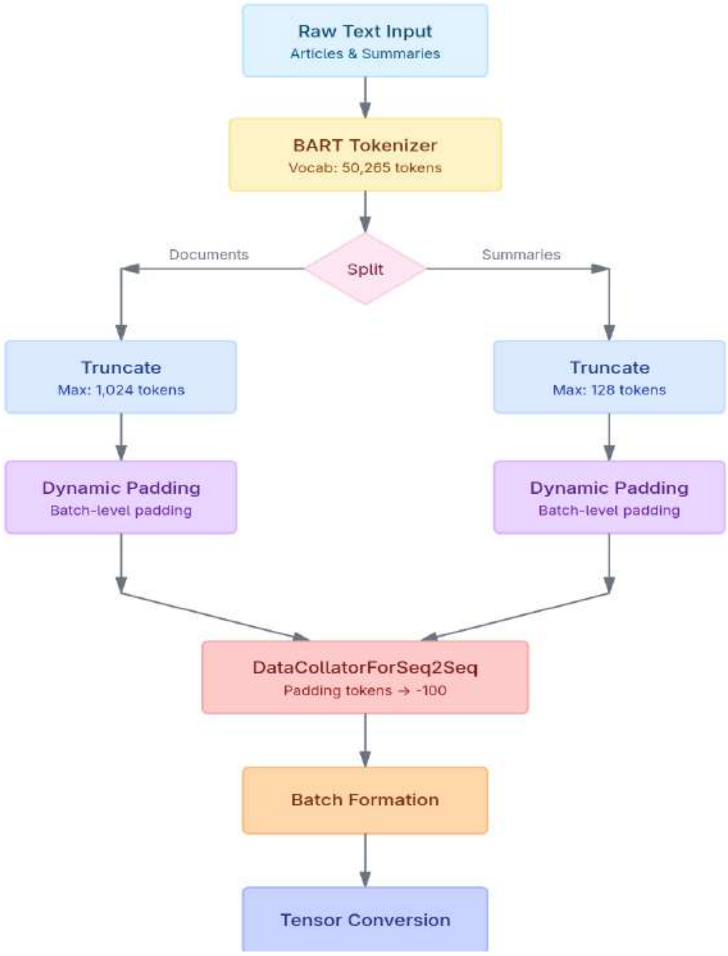


**Figure 2:** Data Preprocessing Pipeline for BART-Large Training

### 3.3 Model Architecture

BART-Large with the pre-trained checkpoint 'facebook/bart-large-xsum' was employed as the foundation for abstractive summarization. The model consists of a transformer-based encoder-decoder architecture with 12 encoder layers and 12 decoder layers. Each layer consists of 16 attention heads, with a hidden dimension of 1,024. This is a model that consists of roughly 406 million parameters, with a bidirectional encoder that encodes the entire input text document, and an autoregressive decoder that generates its output sequentially, on a token basis. This model takes advantage of the self-attention mechanism through cross-attention layers in both its encoder and decoder modules. This feed forward network utilizes a dimension of 4,096, along with GELU activation functions that facilitate complex transformations. In efforts to reduce memory usage during the training process, the application of gradient-checkpointing was considered.

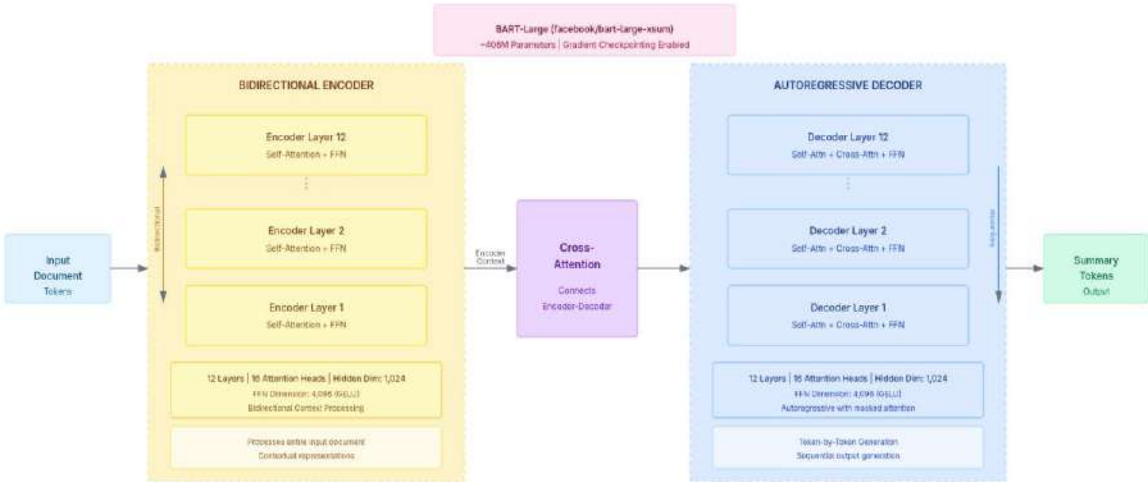


**Figure 3:** BART-Large Encoder-Decoder Architecture for Abstractive News Summarization

### 3.4 Training and Inference Configuration

Fine-tuning was performed using the AdamW optimizer, with hyperparameters being tuned through a two-stage procedure. In the first stage, hyperparameters that relate to training optimization were considered, such as learning rates of ($1\times10^{-5}$, $2\times10^{-5}$, $3\times10^{-5}$), the number of training epochs of (3, 4), and the warmup ratios of (0, 0.05, 0.1) with respect to the total number of training steps. In this case, the most effective configuration consisted of a learning rate of $1\times10^{-5}$ with weight decay of 0.01, along with 3 training epochs with a batch size of 8. This effective batch size was achieved through the use of a per-device batch size of 2 along with gradient accumulation over 4 steps. Mixed precision training with FP16 was employed to accelerate computation and reduce memory usage while maintaining numerical stability. During this, the learning rate was set to linearly decay after the completion of the warmup period. Also, this procedure saves a model checkpoint every epoch, with the best model being selected based on validation loss.

In the second stage of hyperparameter tuning, the generation quality hyperparameters were further tuned during inference. Beam search settings were evaluated with beam sizes of (2, 4, 6), length penalty coefficients of (1.5, 2.0, 2.5), and maximum output sequence lengths of (96, 128) tokens. Although other hyperparameter combinations may work well, the best hyperparameter configuration involved beam search decoding with a beam size of 4 and a length penalty of 1.5. Max length was fixed as 96, with min length fixed as 20 tokens, thus allowing for the generation of summaries that were single sentence, as in the case of the news summary task in XSum, and multiple sentence summaries, as seen in CNN/DailyMail. In addition, n-gram blocking was applied to prevent the repetition of 3-grams within generated summaries for improved coherence. Finally, the early stopping hyperparameter was enabled, such that the beam search decoding would terminate once all beams produced the end-of-sequence token.

### 3.5 Evaluation Metrics

Model performance was evaluated with the ROUGE metrics, computing ROUGE-1, ROUGE-2, ROUGE-L, and ROUGE-Lsum metrics. These metrics calculate n-gram overlap between generated summaries and human-written references. ROUGE-1 captures unigram overlap to account for content selection, while ROUGE-2 looks at bigram overlap to evaluate fluency, and finally, ROUGE-L calculates with the use of the longest common subsequence. During hyperparameter search, the focus was on maximizing the value of ROUGE-2 and that of ROUGE-L.

## 4. Results and Discussion

### 4.1 Hyperparameter Optimization

The hyperparameter optimization was conducted in two stages to identify the optimal configuration for our BART-based news summarization model on 30% of the total dataset. Stage 1 focused on training parameters while Stage 2 optimized generation quality metrics.

4.1.1 Training Parameter Optimization

**Table 1:** Training Hyperparameter Optimization Results-Top 5 Configurations by ROUGE-2 Score

| Learning Rate | Epochs | Warmup Ratio | ROUGE-1 | ROUGE-2 | ROUGE-L |
|---|---|---|---|---|---|
| $1\times10^{-5}$ | 3 | 0.05 | 46.52 | 23.21 | 38.74 |
| $1\times10^{-5}$ | 3 | 0.00 | 46.34 | 23.10 | 38.61 |
| $1\times10^{-5}$ | 3 | 0.10 | 46.35 | 23.16 | 38.43 |
| $1\times10^{-5}$ | 4 | 0.05 | 45.85 | 22.92 | 38.27 |
| $3\times10^{-5}$ | 3 | 0.05 | 45.90 | 22.63 | 38.11 |

From the optimization of the training process, the ideal value of the learning rate was determined to be $1\times10^{-5}$, together with a number of training epochs set to 3, along with a warmup ratio of 0.05, thus providing the best results, as shown by the highest ROUGE-2 score of 23.21. Lower learning rates, such as $1\times10^{-5}$, performed better compared to higher rates like $2\times10^{-5}$ and $3\times10^{-5}$, showing reduced ROUGE-2 scores with increased rates. These results confirm that slower updates of the parameters play a crucial role in the fine-tuning process on the aggregated heterogeneous dataset. Integration of a 5% warmup period led to minor but consistent improvements across all learning rates, stabilizing the training process during the initial adaptation phase.

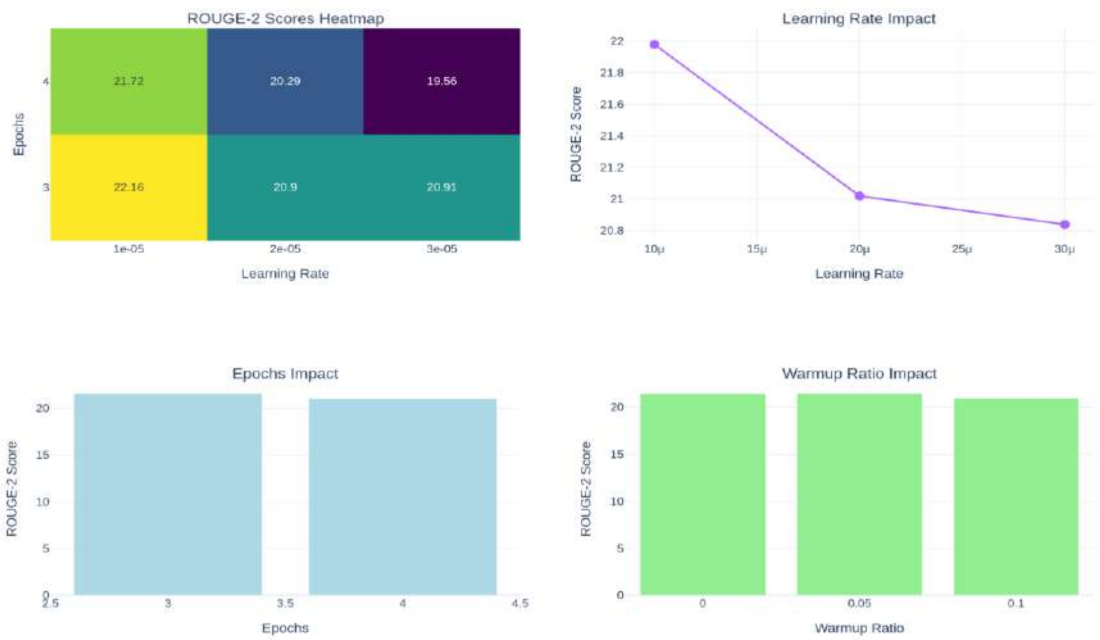


**Figure 4:** ROUGE-2 Scores Across Learning Rate, Epochs, and Warmup Ratio Variations

4.1.2 Generation Quality Optimization

**Table 2**: Inference Generation Parameter Optimization Results: Top 5 Configurations by ROUGE-2

| Beam Width | Length Penalty | Max Length | ROUGE-1 | ROUGE-2 | ROUGE-L |
|---|---|---|---|---|---|
| 4 | 1.5 | 96 | 47.56 | 24.06 | 39.64 |
| 4 | 2.0 | 96 | 47.45 | 23.94 | 39.60 |
| 4 | 2.5 | 96 | 47.39 | 23.86 | 39.49 |
| 6 | 1.5 | 96 | 47.19 | 23.77 | 39.45 |

| | | | | | |
|---|---|---|---|---|---|
| 2 | 1.5 | 96 | 47.17 | 23.62 | 39.38 |

Experiments on generation quality show that beam search with the beam size set to 4 and the length penalty set to 1.5 produced the best-quality summaries, with a ROUGE-2 score of 24.06. It is important to note that varying the maximum length parameter between 96 or 128 tokens did not impact the result, as the same scores were generated in both cases. It is presumed that 96 tokens is sufficient to capture the essential information in both single-sentence as well as multi-sentence summaries. Also, further increase in the beam size beyond 4 resulted in diminishing returns, with slight performance degradation at a beam size of 6, indicating that excessive exploration during decoding may introduce noise rather than improve summary quality.


**Figure 5:** Generation Parameter Impact Analysis: ROUGE Scores Across Beam Width, Length Penalty, and Maximum Length Variations

### 4.2 Model Performance

Following hyperparameter optimization, the model was trained on the complete combined dataset using the identified optimal configuration.

**Table 3:** Final Model Performance: ROUGE Scores on Validation and Test Sets

| Metric | Validation Set | Test Set |
|---|---|---|
| ROUGE-1 | 46.82 | 46.43 |
| ROUGE-2 | 22.91 | 22.86 |

| | | |
|---|---|---|
| ROUGE-L | 38.86 | 38.67 |
| ROUGE-Lsum | 39.13 | 38.93 |

The final model achieved a ROUGE-2 score of 22.86 on the test set, demonstrating strong generalization capability with minimal overfitting (validation-test gap of only 0.09 points). The average generated summary length of 29.6 tokens indicates the model learned to produce concise summaries appropriate for news articles.

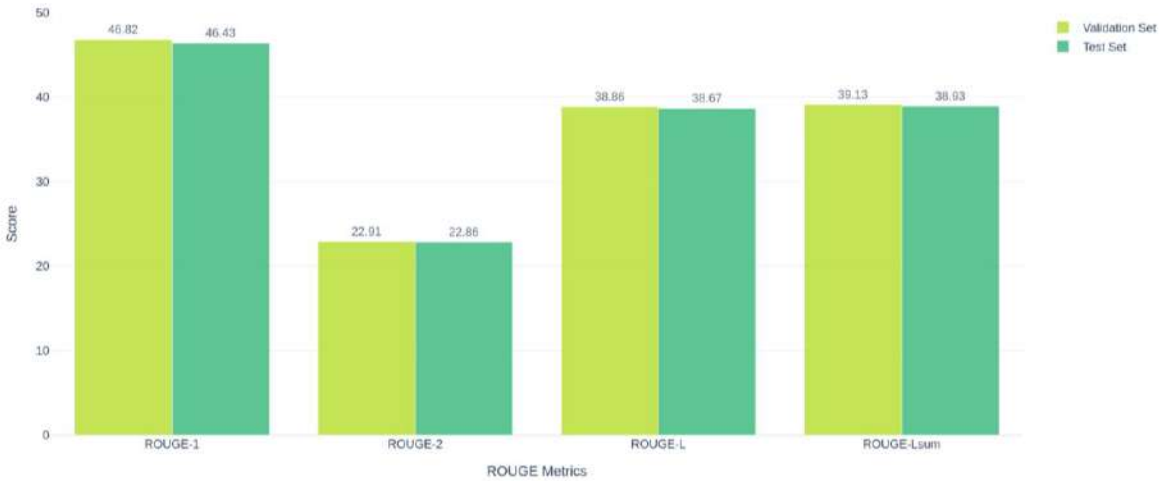


**Figure 6:** Comparison of ROUGE Metrics Between Validation and Test Sets

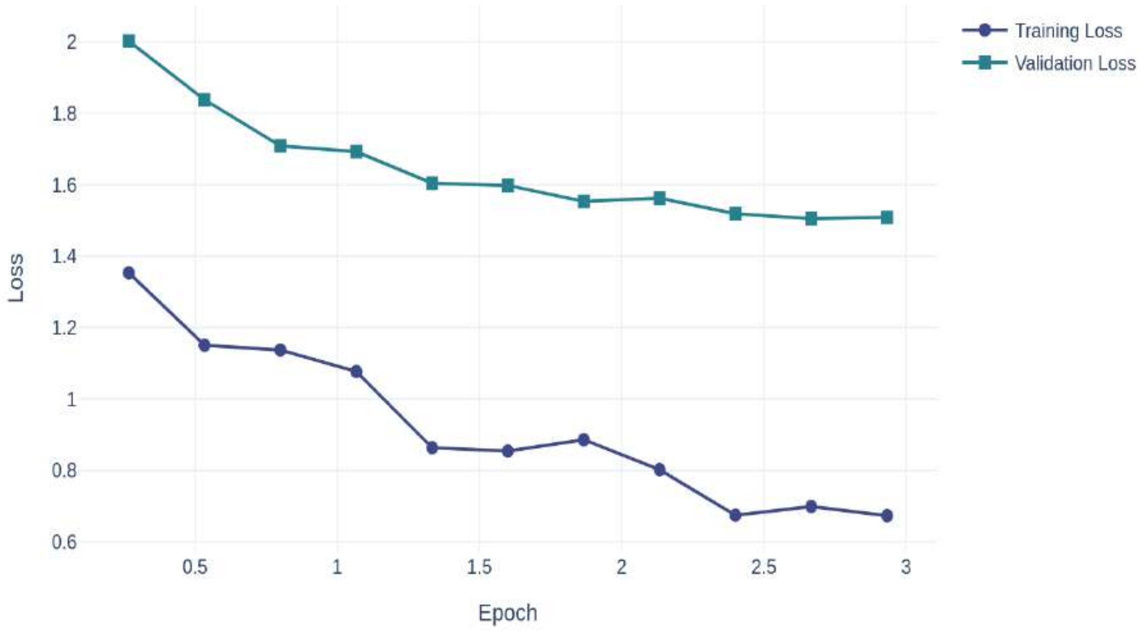


**Figure 7:** Cross-Entropy Loss Progression Across Training Epochs for Training and Validation Sets

### 4.3 Discussion

Our hyperparameter tuning produced several findings for training Transformer models on heterogeneous summarization datasets. The optimal learning rate of $1 \times 10^{-5}$ accords with best practices in the fine-tuning of pretrained models. Conservative learning rates reduce catastrophic forgetting while allowing effective adaptation. Given the diversity of the combined dataset, the positive effect of warmup set to five percent of training steps was notable. It enables gradual adaptation to the distinct summarization styles in the Extreme Summarization dataset which uses highly abstractive single sentences and in the CNN/DailyMail dataset which contains more extractive multiple sentence summaries.

Generation parameters showed consistent patterns. A beam width of four provided a balance between exploration and exploitation during decoding. A length penalty of 1.5 achieved a balance between brevity and completeness and prevented both short summaries that omit key information and verbose outputs that lack focus. The model was relatively insensitive to maximum length settings of 96 and 128 tokens and this indicates that it learned appropriate length control from the training data itself rather than from hard constraints.

Training dynamics showed efficient convergence. Training loss decreased by 45 percent from 1.353 to 0.6731 over three epochs while maintaining a gap between training and validation losses that indicates good generalization without overfitting.

#### 4.3.1 Comparison with Existing Approaches

**Table 4:** Performance Comparison of fine-tuned BART-Large with other Summarization Models

| Model | Dataset | ROUGE-1 | ROUGE-2 | ROUGE-L | Parameters |
|---|---|---|---|---|---|
| Our Model | XSum + CNN/DailyMail | 46.43 | 22.86 | 38.67 | 406M |
| BART-Large (Lewis et al., 2019) | XSum only | 45.14 | 22.27 | 37.25 | 406M |
| BART-Large (Lewis et al., 2019) | CNN/DailyMail only | 44.16 | 21.28 | 40.90 | 406M |

| | | | | | |
|---|---|---|---|---|---|
| PEGASUS (Zhang et al., 2019) | XSum | 47.21 | 24.56 | 39.25 | 568M |
| PEGASUS (Zhang et al., 2019) | CNN/DailyMail only | 44.17 | 21.47 | 41.1 | 568M |
| T5-Large (Raffel et al., 2019) | CNN/DailyMail | 43.52 | 21.55 | 40.69 | 770M |
| ProphetNet (Qi et al., 2020) | CNN/DailyMail | 44.20 | 21.17 | 41.30 | 393M |

## 5. Conclusion

This study demonstrates the effectiveness of fine-tuning the Large Bidirectional and Autoregressive Transformer for abstractive news summarization across datasets with diverse characteristics. A systematic two stage hyperparameter optimization yielded coherent and concise summaries that balance the highly abstractive style of the Extreme Summarization dataset with the more extractive style of the CNN/DailyMail articles. The results confirm that Transformer based encoder decoder architectures adapt well to varied summarization requirements when configured appropriately. These findings advance automated news summarization systems by enabling summaries that allow readers to process large volumes of online content efficiently.

## 6. Recommendation for future research

This work provides an initial basis for abstractive summarization across multiple domains and several directions remain for further research. Future research should develop resource efficient fine-tuning methods to increase reproducibility across computing environments. Adaptive sampling can address dataset imbalance and reduce the observed bias toward extractive styles. Expanding the training corpus with scientific legal and medical documents will improve generalization beyond news. Evaluation protocols need to extend beyond the ROUGE metrics. Semantic similarity metrics such as the Bidirectional Encoder Representations from Transformers score known as BERTScore and factuality checking software such as the Fact Consistency Classifier known as FactCC together with systematic human reviews will provide a more comprehensive measure of summary quality and factuality. There are two principal technical limitations in this approach. The first is factual inconsistency in which the model generates information that is not present in the source text and this may be mitigated with factual verification modules, retrieval augmented generation, or reinforcement learning with human feedback. The second is a fixed input limit of 1024 tokens which prevents processing of long or multiple topic documents. Transformer architectures that support long context, sliding window encoding, or hierarchical chunking can address this constraint.

**References**


- Lewis, M. et al. (2019) BART: Denoising Sequence-to-Sequence Pre-training for natural language generation, Translation, and Comprehension. https://arxiv.org/abs/1910.13461v1.
- Zhang, J. et al. (2019) PEGASUS: Pre-training with Extracted Gap-sentences for Abstractive Summarization. https://arxiv.org/abs/1912.08777.
- Raffel, C. et al. (2019) Exploring the Limits of Transfer Learning with a Unified Text-to-Text Transformer. https://arxiv.org/abs/1910.10683.
- Basyal, L. and Sanghvi, M. (2023) Text summarization using large language models: a comparative study of MPT-7B-Instruct, Falcon-7b-Instruct, and OpenAI Chat-GPT models. https://arxiv.org/abs/2310.10449.
- Shakil, H., Farooq, A. and Kalita, J. (2024) 'Abstractive text summarization: State of the art, challenges, and improvements,' Neurocomputing, 603, p. 128255. https://doi.org/10.1016/j.neucom.2024.128255.
- Venkataramana, A., Srividya, K. and Cristin, R. (2022) 'Abstractive text summarization using BART,' 2022 IEEE 2nd Mysore Sub Section International Conference (MysuruCon), pp. 1–6. https://doi.org/10.1109/mysurucon55714.2022.9972639.
- Parabrahma Chari, S. et al. (2024) AUTOMATIC TEXT SUMMARIZATION USING BART, International Journal of Creative Research Thoughts (IJCRT). journal-article, pp. c411–c413. https://www.ijcrt.org/papers/IJCRT2402277.pdf.
- Adhik, C., Lakshmi, S.S. and Muralidharan, C. (2024) 'Text summarization using BART,' AIP Conference Proceedings, 3075, p. 020038. https://doi.org/10.1063/5.0217004.
- Dharrao, D. et al. (2024) 'Summarizing business news: Evaluating BART, T5, and PEGASUS for effective information extraction,' Revue D Intelligence Artificielle, 38(3), pp. 847–855. https://doi.org/10.18280/ria.380311.

- Wilman, P., Atara, T. and Suhartono, D. (2024) 'Abstractive English Document Summarization Using BART Model with Chunk Method,' Procedia Computer Science, 245, pp. 1010–1019. https://doi.org/10.1016/j.procs.2024.10.329.
- Ghanem, F.A. et al. (2025) 'Deep Learning-Based Short Text Summarization: an integrated BERT and transformer Encoder–Decoder approach,' Computation, 13(4), p. 96. https://doi.org/10.3390/computation13040096.
- Krishna, K.M.R. et al. (2025) 'Deep learning for text summarization using NLP for automated news digest,' Scientific Reports, 15(1), p. 36343. https://doi.org/10.1038/s41598-025-20224-1.
- Nnadi, G.O. and Bertini, F. (2024) 'Survey on Abstractive Text Summarization: Dataset, models, and Metrics,' arXiv (Cornell University) [Preprint]. https://doi.org/10.48550/arxiv.2412.17165.
- Chen, Y. and Song, Q. (2021) News Text Summarization Method based on BART-TextRank Model, 2021 IEEE 5th Advanced Information Technology, Electronic and Automation Control Conference (IAEAC). https://doi.org/10.1109/iaeac50856.2021.9390683.
- Dhanda, N. and Gupta, K.K. (2024) 'A novel approach to text summarization using machine learning,' Asian Journal of Research in Computer Science, 17(4), pp. 95–104. https://doi.org/10.9734/ajrcos/2024/v17i4432.
- Narayan, S., Cohen, S.B. and Lapata, M. (2018) 'Don't give me the details, just the summary! Topic-Aware convolutional neural networks for extreme summarization,' arXiv (Cornell University) [Preprint]. https://doi.org/10.5281/zenodo.2399761.
- Hermann, K.M. et al. (2015) 'Teaching machines to read and comprehend,' arXiv (Cornell University) [Preprint]. https://doi.org/10.48550/arxiv.1506.03340.
- Qi, W. et al. (2020) 'ProphetNET: Predicting future N-Gram for Sequence-to-Sequence pre-training,' arXiv (Cornell University) [Preprint]. https://doi.org/10.48550/arxiv.2001.04063.

# Pokhara Engineering College Journal (PECJ)

*Applied Sciences and Engineering Insights*

ISSN: 3021-9795 (Print) / 3059-9628 (Online)
(Volume-3, Issue- I)


## Synthetic Inertia Emulation And Frequency Control In Distributed PV Grid Using Battery Energy Storage System


Anisha Tiwari[1*], Ajita Acharya[1], Ananta Adhikari[1]

[1]School of Engineering, Faculty of Science and Technology, Pokhara University Kaski, Nepal

*Corresponding email: tiwarianisha83@gmail.com





*Received:01- February-2026; Revised: 28- February-2026; Accepted: 25- March-2026*

*DOI: : https://doi.org/10.3126/pecj.v3i1.93539*



**Abstract**

The rapid integration of distributed photovoltaic (PV) systems provides a promising solution to environmental concerns and climate obligations, yet it introduces significant challenges to power system stability. As PV penetration increases, system inertia decreases, making the grid more vulnerable to frequency deviations during contingencies such as sudden load changes, generator outages, or high PV output. Battery Energy Storage Systems (BESS) offer a viable solution by emulating synthetic inertia and providing fast frequency regulation. This study investigates the dynamic behaviour of BESS under low-inertia conditions and evaluates strategies for inertia emulation, droop-based frequency response, primary frequency response, and primary frequency regulation. An innovative approach is presented in which BESS dynamically injects or absorbs active power to mimic the inertial response of conventional synchronous generators, thereby stabilizing frequency fluctuations. The effects of BESS sizing, placement, and parameters on system performance and power losses are analyzed mathematically and through simulations. The IEEE 9-bus test system is employed to model varying PV penetration levels of 20%, 40% and 60%, along with generator outages and load scenarios. Results indicate that increasing PV penetration leads to higher Rate of Change of Frequency, deeper frequency nadir, and slower recovery. With the implementation of a 35 MVA BESS, frequency response, and steady-state frequency deviations were maintained within Nepal's operational limits of $\pm$5% of nominal frequency. These findings demonstrate the effectiveness of BESS-based synthetic inertia in enhancing frequency stability and improving grid resilience in low-inertia, high-renewable power systems.



**Keywords**: Battery Energy Storage System, Synthetic Inertia, Frequency Stability, Photovoltaic Integration, Low-Inertia Power Systems, Rate-Of-Change-Of-Frequency.


## 1. Introduction

The worldwide energy sector is experiencing a significant shift as growing environmental concerns and climate targets are pushing the transition towards more sustainable alternatives. Clean power surpassed 40% of global electricity generation in 2024, driven by record growth in renewables (Wiatros-Motyka *et al.*, 2024). Global electricity generation grew by over 1200 TWh in 2024. Mirroring the rise in electricity demand, this annual increase of 4% represents a significant acceleration from average growth rate of 2.6% seen between 2010 and 2030. In

2024, renewables alone made up almost three-quarters of the overall increase in power generation. Solar led the way, increasing by about 480 TWh - the highest source of any and far exceeding the previous year. With this growth, installed solar PV capacity worldwide reached an estimated 2.2 TW (International Energy Agency, 2025).

Among renewable energy technologies, Photovoltaic generation is one of the fastest-growing energy sources. However, PV systems interfaced with the grid lack rotational inertia. The absence of inertial energy increases the Rate of Change of Frequency immediately following a disturbance. High RoCoF can trigger UFLS or even system collapse if not addressed. In low-inertia systems with high PV penetration, the absence of significant rotating masses results in steeper frequency drops, deeper frequency nadirs, and delayed post-disturbance recovery.

Beyond large-scale utility PV plants, distributed photovoltaic systems are increasingly contributing to total generation, particularly in urban and semi-urban areas. While DPV provides benefits such as reduced transmission losses and improved local energy autonomy, its decentralized nature further aggravates the low-inertia conditions in high PV penetration systems. Most DPV systems are interfaced through grid-following inverters, which rely on external voltage and frequency references and do not provide inherent inertial responses. As a result, widespread DPV deployment amplifies the frequency stability challenges, reducing effective system inertia and weakening the grid's natural frequency response.

To address these low-inertia challenges, Energy Storage Systems have become a vital asset for frequency regulation and grid support. Although technologies such as Pumped Hydro Storage, Flywheels, and Compressed Air Energy Storage exist as viable solutions to the grid instability issue. Battery Energy Storage Systems have emerged as one of the most effective options. Energy Storage System (ESS) have been widely proposed to compensate for the reduction in system inertia and damping caused by the displacement of conventional synchronous generators as they can emulate the dynamic behaviour of synchronous machines and provide fast acting support through function such as Inertial Response (IR) and Primary Frequency Reserve (PFR). ESS also helps reduce peak power demand by storing energy during low-demand periods and supplying it during peak hours thereby improving overall system efficiency and reliability (Amin *et al.*, 2021).

Battery Energy Storage Systems store electrical energy electrochemically in cells which are arranged in series and/or parallel to meet power and voltage requirements. Among various chemical battery such as Lead-Acid, Sodium-Sulphur, Nickel-Cadmium, and Vanadium Redox Flow, Lithium-ion stands out for its high energy density, rapid response capabilities, and comparatively longer lifespan as (Assery, Zhang and Chen, 2024).

Battery energy storage systems also offer a wide range of applications in power systems, including frequency control, voltage support, power balancing, and energy shifting. Among these, frequency control is one of the most attractive applications for grid-connected BESS, as it enables rapid restoration of system frequency following disturbances through the controlled injection or absorption of frequency-dependent power. The nature of rechargeable batteries, charging for down-regulation and discharging for up-regulation with immediate response and adjustable power scale is an inherent advantage compared with other components in the power system. The frequency response without the deadband and enhanced frequency response without the deadband and enhanced frequency response and the service stacking cases, which promote the BESS to operate at high usage frequency since it exploits the full utilization potential of the BESS (Chunyang *et al.*, 2023).

## 2. Methodology

### 2.1 Research Framework

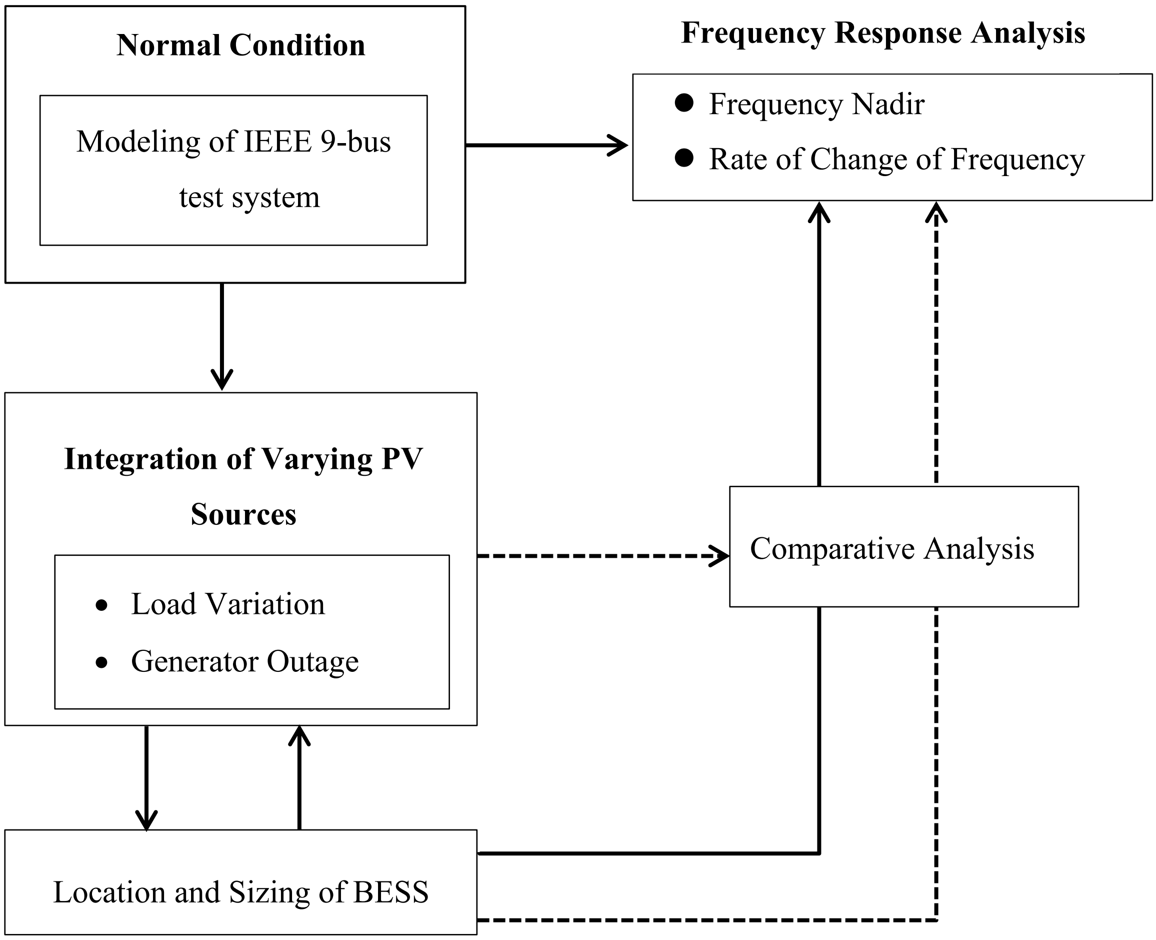


**Figure 1**: Block diagram of research framework

Figure 1 illustrates the research framework adopted for evaluating frequency stability in a Photovoltaic (PV)-integrated power system. Initially, the IEEE 9-bus test system is modeled under normal operating conditions. Varying levels of photovoltaic (PV) penetration are then integrated, and system disturbances such as load variations and generator outages are introduced. The frequency response is assessed using key performance indicators, including frequency nadir and Rate of Change of Frequency (RoCoF). Based on the observed dynamics, the optimal location and sizing of the battery energy Storage System (BESS) are determined. Finally, a comparative analysis is conducted to quantify the effectiveness of BESS in enhancing system frequency stability.

### 2.2 Power Grid Test Network

The IEEE 9-bus test system is employed as a benchmark to evaluate frequency dynamics under varying PV penetration and contingency scenarios. The network configuration and parameters are adopted from the standard IEEE 9-bus test system as detailed by P.M. Anderson (Anderson and Fouad, 2003). The system initially includes three synchronous generators, which provide the primary source of system inertia. The transmission network is modelled using detailed line parameters, including series resistance, reactance, and line susceptance.

Each synchronous generator is equipped with detailed governor and automatic voltage regulator (AVR) models. The governor regulates turbine speed by adjusting water flow. It provides inertial support by sensing frequency deviation and modulating active power output of the synchronous generator. This rapid adjustment helps restore power balance and maintain stable system frequency (Department of Hydropower and IIT Roorkee, n.d.). An AVR maintains the generator terminal voltage at a desired level by continuously monitoring output voltage. It automatically adjusts the generator excitation current to compensate for load changes and varying operating conditions (IEEE Power System Dynamic Performance Committee, 1992).

A steady-state load flow analysis is first performed to ensure system convergence before conducting dynamic simulations. The generator, transformer and load data of the IEEE 9-bus test system is shown on Tables 1-3. The system configuration is shown in Figure 2.

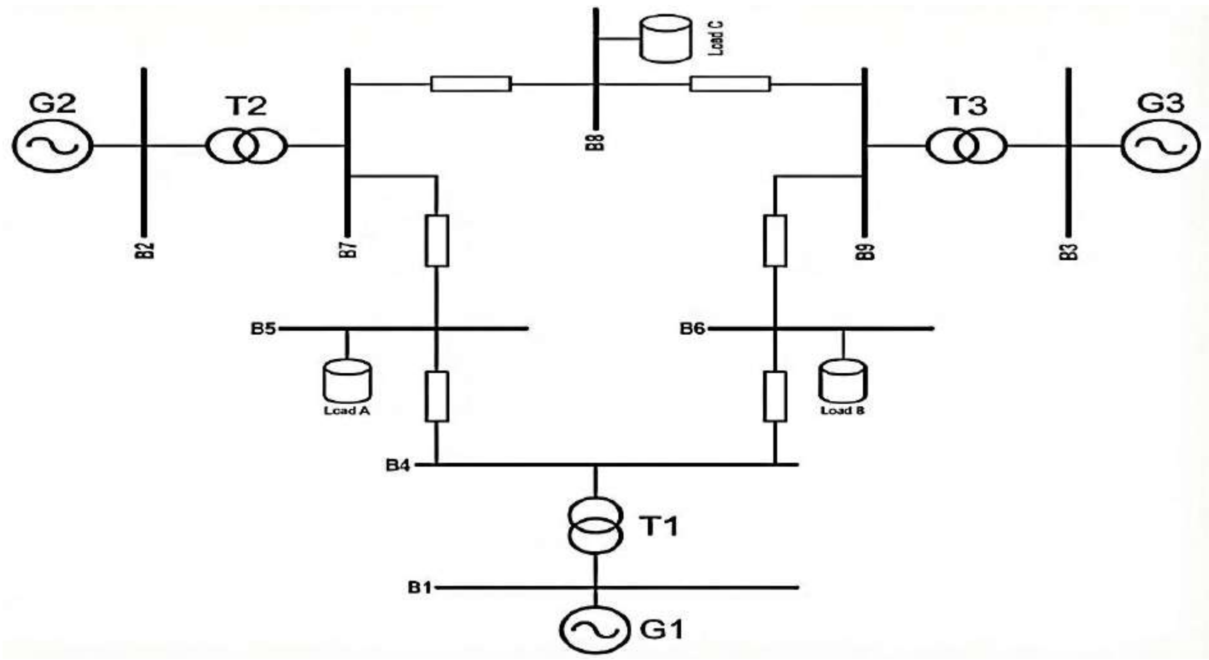


**Figure 2:** 9-bus test system

**Table 1:** Generator data of 9-bus test system

| | Nominal Apparent Power[MVA] | Active power [MW] | Reactive Power [MVAr] | Load controller | Power Factor |
|---|---|---|---|---|---|
| Gen 1 | 247.5 | 71.6 | 27 | Reference | 0.85 |
| Gen 2 | 192 | 163 | 6.7 | Constant V | 0.85 |
| Gen 3 | 128 | 85 | -10.9 | Constant V | 0.85 |

**Table 2:** Transformer data of 9-bus test system

| Transformer | Rated Power (MVA) | Short Ckt Voltage uk(%) |
|---|---|---|
| T1 | 250 | 14.4 |
| T2 | 200 | 12.5 |
| T3 | 150 | 8.79 |

**Table 3:** Load data of 9-bus test system

| Load | MW | MVAr |
|---|---|---|
| Load A | 125 | 50 |
| Load B | 90 | 30 |
| Load C | 100 | 35 |

### 2.3 Integration of PV Sources

PV sources are integrated using the standard inverter-based PV model available in DIgSILENT PowerFactory. All PV units are operated in grid-following mode with active power control implemented through PQ control. In this study, three distributed PV units are connected at the load buses. PV penetration levels of 20%, 40%, and 60% are considered to represent lightly stressed, moderately stressed, and extremely low-inertia operating conditions, respectively. Equal distribution of PV generation among the load buses ensures a balanced representation of spatially distributed inverter-based resources. For each penetration level, the total PV contribution is adjusted accordingly, while the active power output of the synchronous generators is proportionally reduced to maintain system power balance.

Photovoltaic system does not consist of any rotating parts unlike conventional generator, with no rotating parts present, the PV system does not possess inherent inertia which is necessary to maintain the grid frequency stability during disturbances. Furthermore, Solar power is intermittent and most often non-dispatchable, as the Sun does not shine for all hours of the day in each location. As a result, high PV penetration reduces overall system inertia, leading to higher RoCoF and deeper frequency nadirs under contingencies. The PV penetration scenarios considered in this study are summarized in Table 4.

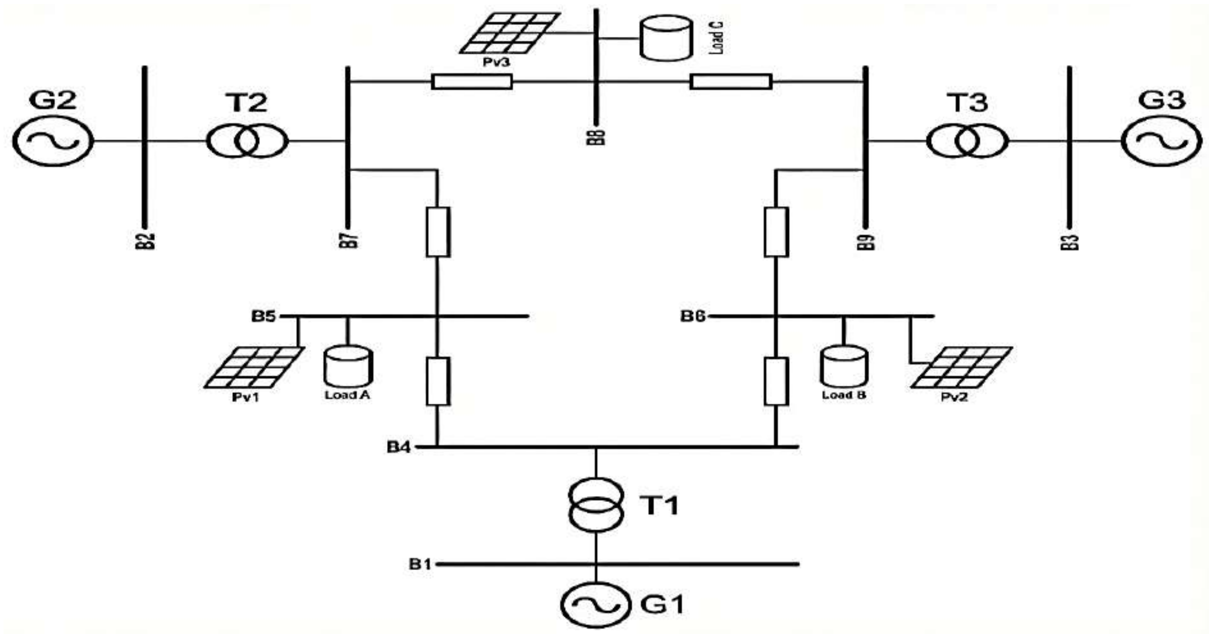


**Figure 3:** 9-bus test system with PV

**Table 4:** Distributed PV sources data

| PV Penetration Level | PV on Load bus A (MW) | PV on Load bus B (MW) | PV on Load bus C (MW) | Total PV Power (MW) |
|---|---|---|---|---|
| 20% | 21.3 | 21.3 | 21.3 | 63.92 |

| | | | | |
|---|---|---|---|---|
| 40% | 42.61 | 42.61 | 42.61 | 127.84 |
| 60% | 63.92 | 63.92 | 63.92 | 191.76 |

### 2.4 Contingencies

Contingencies are modelled as disturbances that cause sudden imbalances between generation and load, leading to frequency deviations. To evaluate the system's frequency response under realistic operating conditions, the following contingencies are considered.

Sudden Generator Outage: A generator outage represents the sudden disconnection of a synchronous generator, resulting in an instantaneous loss of generation. This creates a power imbalance that causes a rapid decline in system frequency.

Load variation in the grid: Load variation is introduced to analyze the impact of demand fluctuations on system frequency. In this study, the load of the selected buses is increased and decreased by ±10%.

### 2.5 Energy Storage Systems

Energy Storage System (ESS) have been widely proposed to compensate for the reduction in system inertia and damping caused by the displacement of conventional synchronous generators as they can emulate the dynamic behaviour of synchronous machines and provide fast acting support through function such as Inertial Response (IR) and Primary Frequency Reserve (PFR). ESS also helps reduce peak power demand by storing energy during low-demand periods and supplying it during peak hours thereby improving overall system efficiency and reliability (Amin *et al.*, 2021).

ESS that are potentially fast responding and have superior characteristics include super-capacitor, flywheels, Super Magnetic Energy Storage (SMES), CAES, BESS, and Pumped hydro energy storage. Battery Energy Storage System (BESS) are widely recognized as an effective technology for supporting frequency stability and are increasingly deployed in modern power systems (Amin *et al.*, 2021). The ESS is expressed as

$$P_{ESS} = S_{ESS}\,(P_{IR} + P_{PFR}) \tag{1}$$

#### 2.5.1 ESS for Inertial Response

ESS can provide IR by acting as a source of virtual or synthetic inertia, where active power is rapidly injected into or absorbed from the grid in proportion to the RoCoF. This control mimics the kinetic energy release of synchronous generator, which helps to reduce the initial frequency drop after a disturbance. This fast response is especially important in low-inertia power systems with high renewable energy penetration, where conventional generator inertia is not sufficient to control RoCoF (Knap *et al.*, 2016). The inertial response of ESS is commonly expressed as

$$\mathrm{P_{IR}} = \mathrm{K_{IR}}\frac{\mathrm{df}}{\mathrm{dt}} \tag{2}$$

Where, $\mathrm{P_{IR}}$ represents the active power injected or absorbed by the ESS, $\mathrm{K_{IR}}$ is the inertial response gain that determines the magnitude of the power response, and $\frac{\mathrm{df}}{\mathrm{dt}}$ denotes the measured RoCoF.

The swing equation can be reformulated to define inertia constant ($\mathrm{H_{ESS}}$) as follows (Knap *et al.*, 2016):

$$H_{ESS} = \frac{P_{IR} f_o}{2} . (\frac{df}{dt})^{-1}$$
(3)

From the above two equations, the inertial constant $H_{ESS}$ can be determined as,

$$H_{ESS} = \begin{cases} \frac{f_0}{2} . K_{IR,} & \text{if } |P_{IR}| \leq 1 \\ \frac{f_0}{2} . (\frac{df}{dt})^{-1} & \text{if } |P_{IR}| \geq 1 \end{cases}$$
(4)

**a) Sizing of IR:**

The sizing of ESS for IR is determined by ensuring that the combined physical and synthetic inertia of the system is sufficient to limit RoCoF under a worst-case generation loss. This requirement can be represented by (Assery, Zhang and Chen, 2024).

$$\sum_{i=1}^{n} H_{ESSi} S_{ESSi} \geq \frac{\triangle P_{max} f_\circ}{2 \frac{df_{max}}{dt}} - \sum_{i=1}^{n} H_i S_i$$
(5)

Where, $\triangle P_{max}$ is the maximum power imbalance, $f_\circ$ is the nominal frequency, and $H_{sys}$ and $S_{sys}$ denote the inertia and ratings of existing generators. This condition ensures that the ESS can effectively support frequency stability during the initial moments of disturbance.

### 2.5.2 ESS for Primary Frequency Response

PFR restores system frequency to a steady state level after the inertial response. ESS provide PFR by adjusting their active power output proportionally to the frequency deviation using a droop-based control, sharing the power imbalance with synchronous generators, and helping to prevent further frequency decline (Knap *et al.*, 2016). The primary frequency reserve of ESS is commonly expressed as

$$P_{PFR} \approx - \frac{f - f_\circ}{f_\circ R_{ESS}}$$
(6)

Where, f is the measured frequency, $f_\circ$ is the nominal frequency, and $R_{ESS}$ is the droop setting.

**a) Sizing of PFR:**

The sizing of ESS for PFR ensures adequate power and energy to keep frequency within limits during disturbances. For a maximum power imbalance $\Delta P_{max}$, the target power–frequency characteristic $\lambda_{target}$ is defined as (Assery, Zhang and Chen, 2024):

$$\lambda_{target} = -\frac{\Delta P_{max}}{f_0 - f_{min}}$$
(7)

The actual system power–frequency characteristic under the largest contingency, $\lambda_{CO}$, is obtained from the combined droop response of the synchronous generators:

$$\lambda_{CO} = \sum_{1}^{N} \frac{1}{R_i S_i f_0}$$
(8)

To meet the required frequency performance, the ESS must provide the additional power–frequency characteristic $(\lambda_{target} - \lambda_{CO})$. Therefore, the ESS contribution for PFR can be expressed as:

$$\sum_{i=1}^{m} \frac{1}{R_{ESS,i} S_{ESS,i} f_0} \geq \lambda_{target} - \lambda_{CO}$$
(9)

Where, $m$ is the number of ESS units and $N$ is the number of synchronous generators. $R_{ESS,i}$ and $S_{ESS,i}$ are the droop coefficient and rated power of the $i^{th}$ ESS unit, respectively, and $f_0$ is the nominal system frequency.

For a single ESS unit with droop coefficient $R_{ESS}$, the required ESS size for PFR reduces to:

$$S_{ESS} = (R_{ESS} f_0)(\lambda_{target} - \lambda_{CO})$$
(10)

### 2.6 Battery Energy Storage System Modelling

Battery Energy Storage Systems introduced in the grid model at strategic buses provides frequency support under low-inertia conditions after PV generation (Sun *et al.*, 2024). The BESS is modelled in DIgSILENT PowerFactory using the standard BESS control template.

The model includes AC voltage, frequency, and PQ measurement blocks, which provides real-time system information to the control system. Frequency control generates a power reference based on grid frequency deviations, while the PQ controller determines the corresponding current reference. A battery model supplies voltage, current, and SoC information to the charge control unit, which ensures safe charging and discharging within operational limits. The converter block executes the current reference to enable controlled bidirectional power

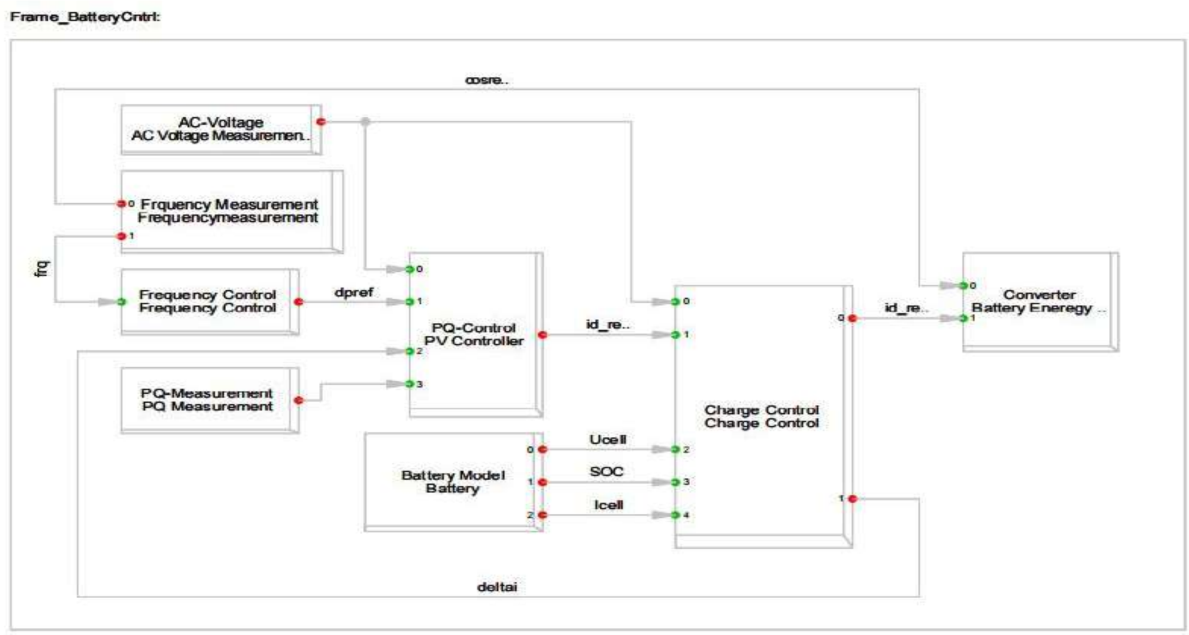


**Figure 4:** BESS Controller Frame available in DIgSILENT Power Factory

exchange between the battery and the grid. This coordinated control structure enables rapid active power injection or absorption to stabilize system frequency during disturbances. The BESS controller framework available in the DIgSILENT PowerFactory is shown in Figure 4.

**2.6.1 Location of BESS**

The effectiveness of BESS in providing synthetic inertia and frequency support strongly depends on its placement within the network. In this study, the BESS location is determined using a sensitivity analysis approach. Time-domain simulations are conducted under different PV penetration levels and contingency scenarios. Key performance indicators, including voltage magnitude, Rate of Change of Frequency, and frequency deviations are monitored to all buses. Buses exhibiting larger deviations during disturbances are identified as highly sensitive locations.

The bus with the lowest voltage magnitude and highest frequency sensitivity is selected as the most suitable location for BESS installation. Placing the BESS at this enhances voltage support and improves frequency stability through rapid active power injection or absorption.

**2.6.2 Sizing of BESS**

For a power system, the BESS is sized to ensure that frequency deviation, RoCoF, frequency nadir and steady-state frequency within acceptable operational limits under the largest contingency event.

For the IEEE 9-bus test system with 60% PV, the largest contingency is the loss of 10% of the total connected generation, corresponding to a generator outage of 31.96 MVA. This event is treated as the worst-case scenario for BESS sizing. Based on this disturbance magnitude and the system frequency response requirements, the BESS is sized to provide adequate IR and PFR. Knowing the system inertia, allowable RoCoF, frequency deviation limits and disturbance magnitude, the required BESS capacity for inertial response and primary frequency response is calculated.

**3. Results and Discussion**

The IEEE 9-bus system was modelled and integrated with PV generation to study its impact on system dynamics. Simulations are conducted in DIgSILENT PowerFactory version 15.1 on different computing platforms, including a Lenovo Ideapad and a Dell Insprion 16, to ensure computational consistency and validate results across hardware configuration.

**3.1 Frequency Response of the 9-Bus Test System**

The base system, consisting of all synchronous generators, was first simulated to establish the baseline frequency response. As shown in Figure 5, the system frequency dropped to a minimum value of 49.976 Hz at t = 3.460s and subsequently stabilized near 49.996 Hz. The high inertia contribution by the synchronous generators ensured a low RoCoF, keeping the overall frequency deviation within the acceptable operating limits.

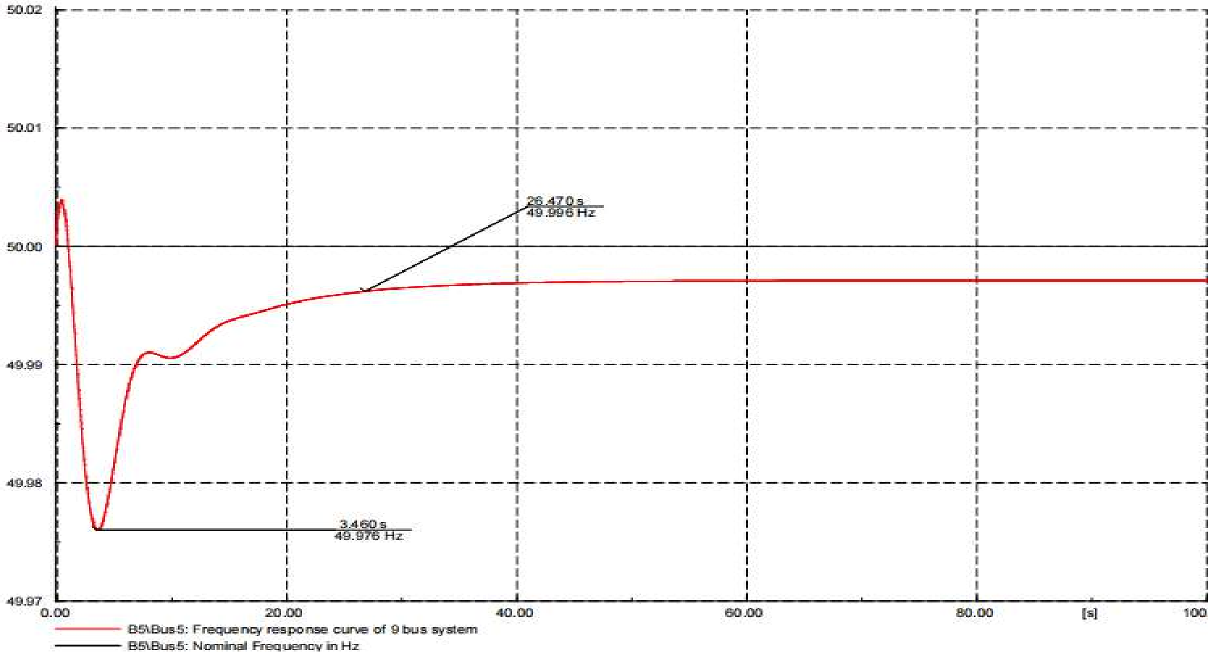


**Figure 5:** Frequency response curve of 9-bus test system

### 3.2 Frequency Response of the 9-Bus Test System with Varying PV Penetration

The system was simulated under PV penetration levels of 20%, 40%, and 60% to evaluate the impact of reduced inertia on frequency stability. As illustrated in Figure 6, the frequency response progressively deteriorated as PV penetration increases.

At 20% PV penetration, the frequency nadir decreased to 44.906 Hz, indicating a moderate loss of inertia. At 40% PV penetration, the nadir further declines to 42.962 Hz, while at 60% PV penetration, the frequency drops sharply to 40.434 Hz, accompanied by a significantly

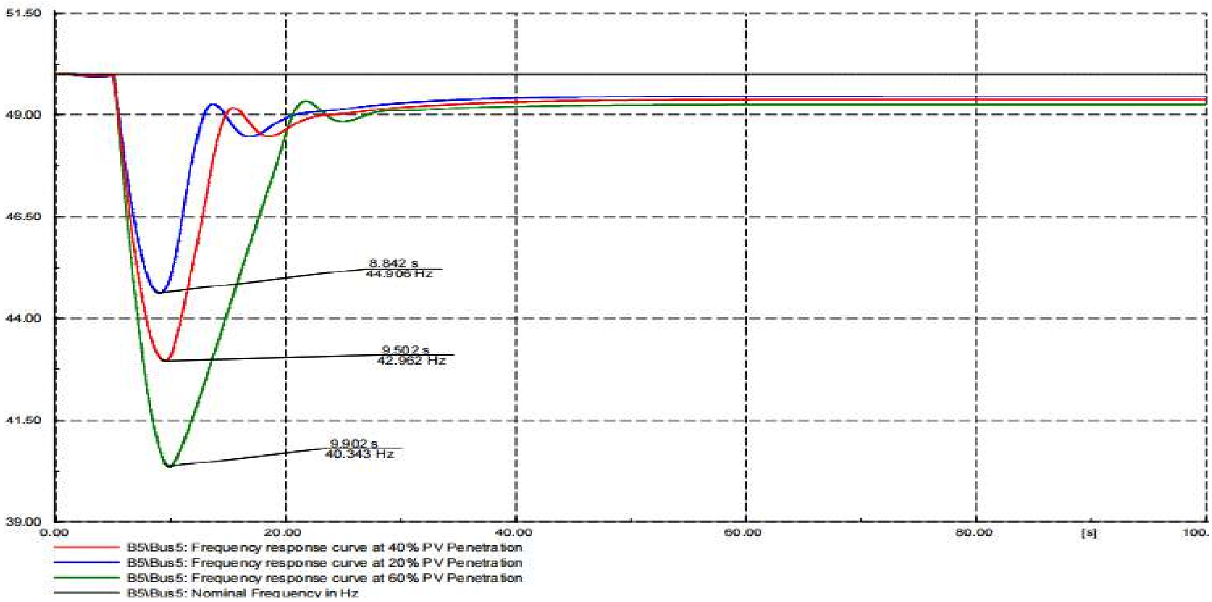


**Figure 6:** Frequency response curve with varying PV penetration

higher RoCoF. These results clearly demonstrated that high PV penetration severely weakens system frequency stability due to reduced inertial support. The increasing severity of frequency deviation highlights the growing vulnerability of low-inertia grids to disturbances.

**Table 5:** Frequency response of 9-bus test system with varying PV penetration

| PV penetration | 20% | 40% | 60% |
|---|---|---|---|
| Frequency nadir | 44.906 Hz | 42.962 Hz | 40.343 Hz |

### 3.3 Determination of the location of the BESS

The location of the Battery Energy Storage System was determined by evaluating the system operating conditions under high PV penetration and contingency events. Since the primary objective of the BESS in this study is to improve frequency stability through active power support, the system voltage profile was first examined to assess the need for reactive power support and to identify any weak buses.

Load flow analysis was performed for the low-inertia system with varying PV penetration levels using the Newton-Raphson method. The bus voltage magnitudes obtained under different contingency conditions at 60% PV penetration are summarized in Table 6.

**Table 6:** Bus voltage under different contingency cases at 60% PV penetration

| **Bus voltage in pu under different contingency cases at 60% PV penetration level** | | | |
|---|---|---|---|
| **Bus** | **-10%** | **+10%** | **10% outage** |
| Bus 1 | 1.04 | 1.04 | 1.04 |
| Bus 2 | 1.025 | 1.025 | 1.025 |
| Bus 3 | 1.025 | 1.025 | 1.025 |
| Bus 4 | 1.036 | 1.034 | 1.010 |
| Bus 5 | 1.013 | 1.011 | 0.959 |
| Bus 6 | 1.028 | 1.026 | 0.994 |
| Bus 7 | 1.030 | 1.030 | 1.022 |
| Bus 8 | 1.023 | 1.022 | 1.013 |
| Bus 9 | 1.037 | 1.036 | 1.021 |

According to the grid code, a $\pm$5% variation in the bus voltage is acceptable so, a bus with voltage level less than 0.95 pu is called a weak bus (Krishan and Suhag, 2019). From the load flow results, all bus voltages remained within the permissible range for all contingency cases. Therefore, reactive power support from the BESS is not required and the BESS is operated solely in active power control mode to provide synthetic inertia and primary frequency response.

Among all buses, Bus 5 consistently exhibited the lowest voltage magnitude, particularly under the outage condition, where the voltage drops to 0.959 pu. Bus 5 is also a load bus carrying the largest demand 125 MW and 50 MVAr in the system. Due to this high concentration, Bus 5 experiences the most significant impact during generation-load imbalance and contingency events. Placing the BESS at this bus allowed active power support to be delivered directly at the point of maximum load, which is highly effective for mitigating frequency deviations during disturbances. During sudden loss of generation or rapid PV output variation, the BESS can inject power at Bus 5, thereby reducing the effective power deficit seen by the system and improving the frequency nadir and RoCoF.

Considering its high load concentration, relatively low voltage under contingencies and suitability for high-voltage interconnection, Bus 5 at 230 kV is identified as the suitable location for integrating a large-scale BESS. Connecting the BESS at this bus ensures rapid and effective active power injection or absorption during power imbalance events, thereby significantly enhancing the system frequency response. Based on these considerations, Bus 5 was selected as the suitable location for BESS integration into the IEEE 9-bus test system.

### 3.4 Calculation and Integration of Optimal BESS Sizes

For the power system under study, the BESS was sized such that it limits key frequency response parameters, RoCoF, frequency nadir, and steady-state frequency deviation, within prescribed limits following the largest contingency event. In this project, a 10% generator outage at 60% PV penetration, corresponding to a power loss of 31.96 MW, was considered as the largest disturbance for calculating the BESS size.

According to ENTSO-E guidelines, the allowable RoCoF limit is less than 0.5 Hz/s, i.e. RoCoF<0.5 Hz and the steady-state frequency deviation should be limited to $\pm 0.2$ Hz, i.e. $\Delta f_{ss} \leq 0.2$ Hz (Abuagreb, Abuhussein and Alzahir, 2021). The nominal frequency of the system is 50 Hz. The droop constant of the BESS is selected as 0.004. These limits formed the basis for determining the BESS size required to provide inertial response and primary frequency response.

Using these parameters, the BESS size required to provide IR and PFR is calculated. The BESS size was calculated considering the worst-case operating condition, as the maximum RoCoF and the lowest nadir occur at high PV penetration levels. In this study, the highest PV penetration corresponds to 191.96 MW, and the BESS size is calculated for this condition.

*BESS Sizing for Inertial Response*

Initial Response is required to limit the rate of change of frequency immediately after a disturbance, before primary frequency control becomes effective. The minimum inertia required to restrict RoCoF within acceptable limits was determined using the inertia balance condition given by the inertial response sizing criterion in equation 5.

For the IEEE 9-bus test system, the total inertia contributed from the synchronous generator is calculated as 2957. At higher PV penetration levels, only 40% of the synchronous generator inertia remains available, resulting in an effective system inertia is 1182.8. The remaining inertia requirements must therefore be supplied by the BESS. Using the BESS inertia constant obtained from inertial response model in equation 3-4, the minimum BESS rating required to satisfy the RoCoF constraint is calculated Based on the worst-case disturbance and the allowable RoCoF limit, the required BESS rating required for inertial response is found to be 33.89 MVA.

*BESS Sizing for Primary Frequency Response*

Primary Frequency Response is responsible for arresting the steady-state frequency deviation following a disturbance by adjusting active power output in proportion to frequency deviation. In this study, the BESS provides PFR through a droop-based control mechanism as described in equation 6.

The sizing of the BESS for PFR was carried out using the target power-frequency characteristics defined in equation 7. Based on the maximum power imbalance of 31.96 MW and the allowable steady-state frequency deviation of 0.2 Hz, the required system power-frequency slope is determined.

The power-frequency characteristic contributed by the synchronous generators under the largest contingency is evaluated using equation 8. The additional power-frequency support required from the BESS is then obtained using the sizing condition in equation 9. For a single BESS unit with a droop coefficient of 0.004, the required BESS rating is calculated using equation 10. Accordingly, the minimum BESS power rating required to provide adequate PFR is 31.96 MVA.

*Integration of BESS*

The BESS size requirements for inertial response and primary frequency response are 33.89 MVA and 31.96 MVA, respectively. Since these services may partially overlap, the largest power requirement was selected to ensure adequate frequency support under all operating conditions.

To account for converter losses, line losses, and practical implementation considerations, a 35 MVA BESS is selected. The BESS is integrated into the IEEE 9-bus test system at the 230kV Bus-5 through an 18/230kV step-up transformer to enhance frequency stability. During periods of excess generation, the BESS absorbs power to limit frequency rise, while during generation deficit, it injects power to arrest frequency decline. This coordinated operation enhances the overall frequency stability of the power system. Additionally, the selected placement at Bus-5 increases the effectiveness of frequency support by providing strong electrical coupling to both generation and load centers.

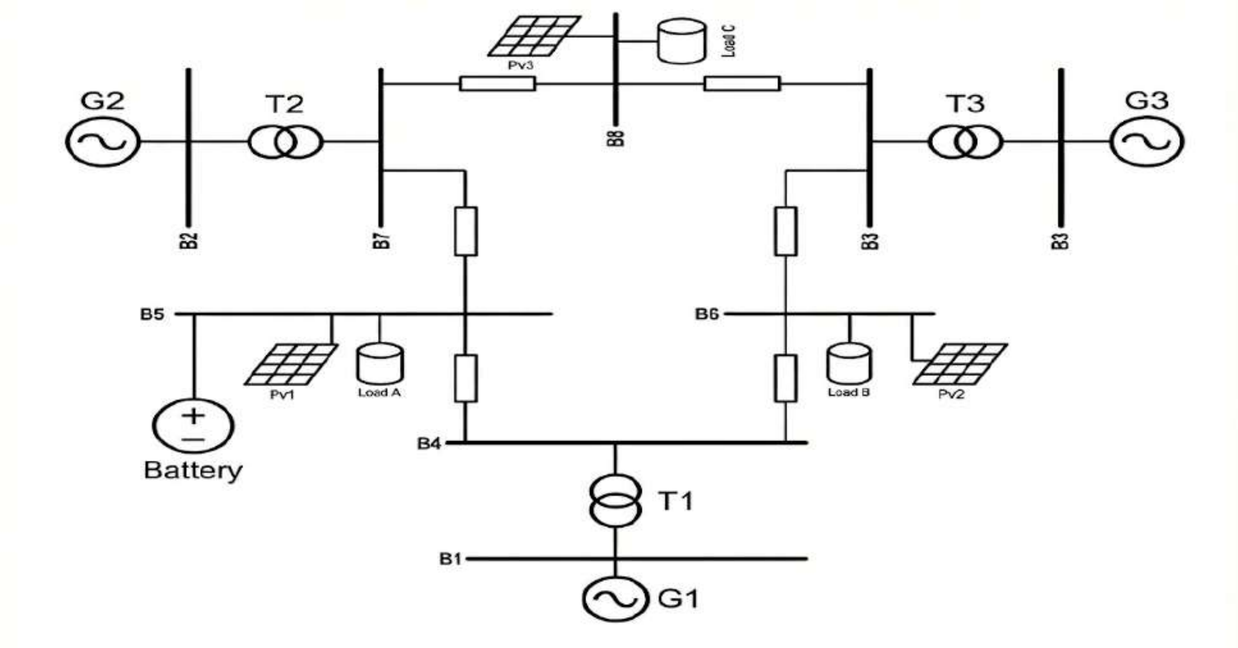


**Figure 7:** 9-bus test system with BESS

### 3.5 Varying level of PV Penetration

#### 3.5.1 Frequency Response with 20% PV penetration

The frequency response of the system with 20% PV penetration was analyzed with and without integration of BESS, as shown in Figure 8. Without BESS, the frequency dropped to a nadir of 44.906 Hz at t = 9.212s, indicating a significant deviation from the nominal value. With BESS integration, the frequency nadir improved to 49.624 Hz, demonstrating a substantial reduction in frequency deviation. This improvement confirms that BESS effectively limits the frequency drop and enhances overall dynamic stability.

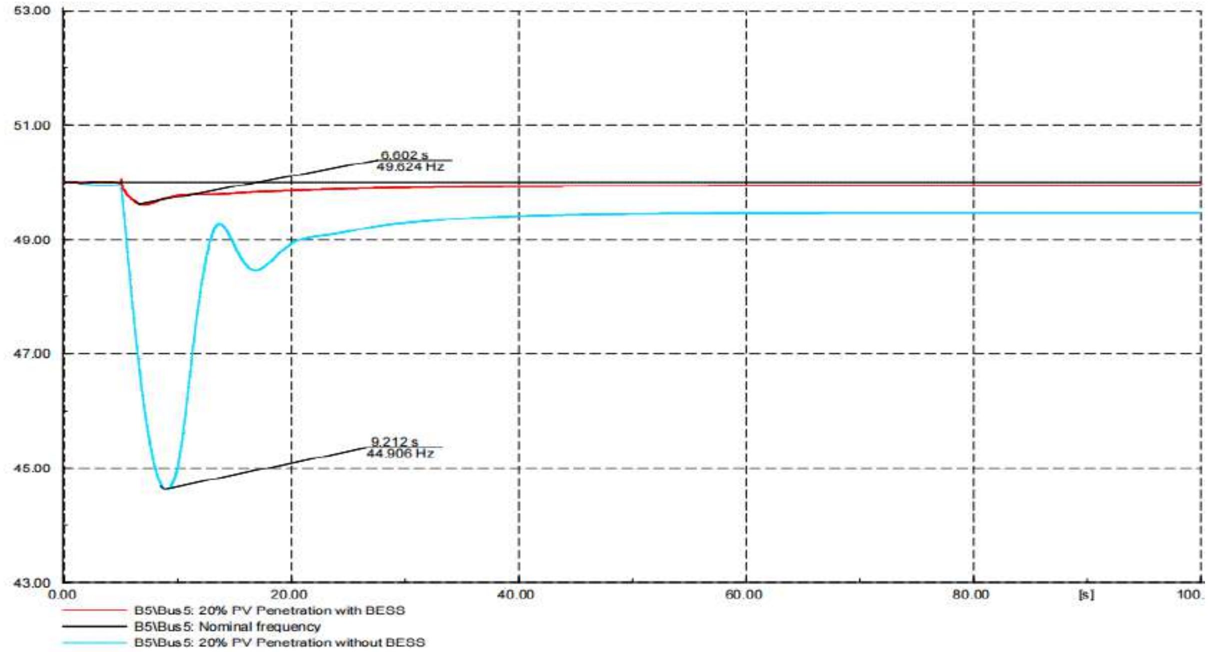


**Figure 8:** Frequency response curve with 20% PV penetration

*Frequency Response of Generator Outage with 20% PV Penetration*

Generator outage events of 10% and 20% were simulated to assess the effectiveness of BESS. For 10% generator outage, the frequency without BESS is dropped to 43.263 Hz at t = 9.152s, whereas with BESS the frequency nadir improved to 49.292 Hz at t =7.023s, with faster stabilization. Under 20% generator outage, the system without BESS experienced a critical frequency drop to 42.983 Hz at t =9.302s. With BESS, the frequency nadir increases to 48.981 Hz at t = 7.312s, keeping the system within acceptable operating limits.

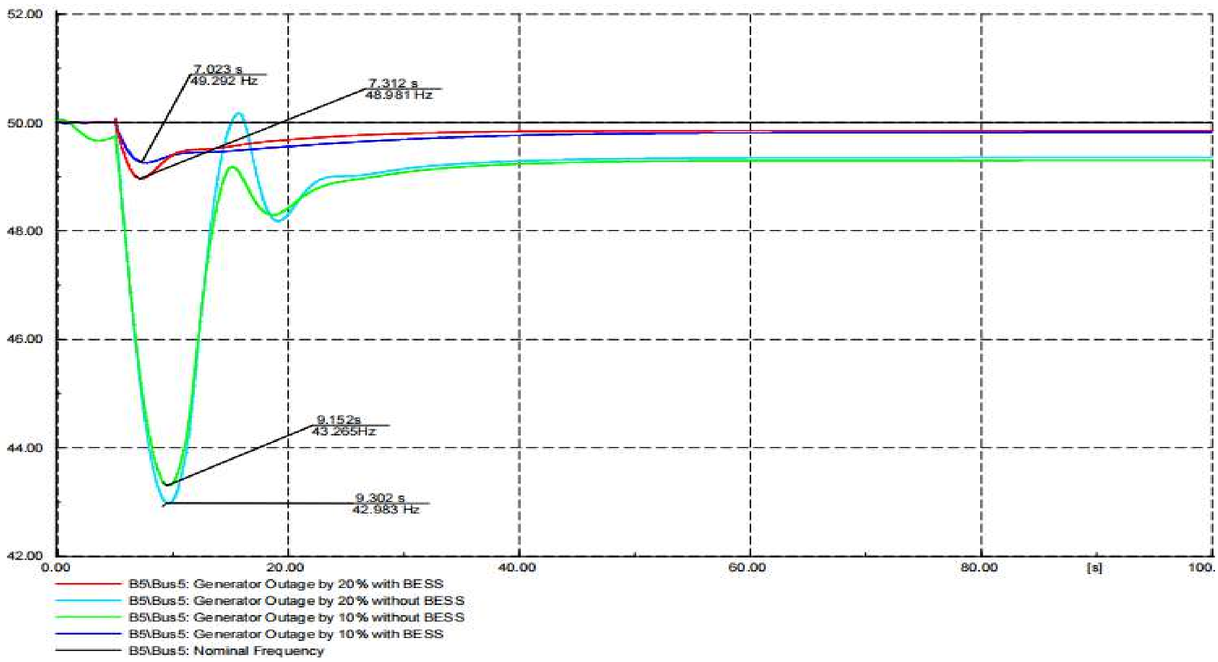


**Figure 9:** Frequency response curve of generator outage with 20% PV

*Frequency Response of Load Variation with 20% PV Penetration*

During a +10% load increase, the frequency nadir without BESS was 43.462 Hz at t = 9.112s, while BESS integration raised it to 49.301 Hz at t = 7.022s. Similarly, for -10% load variation, the frequency nadir improved from 45.611 at t = 8.382s to 49.892 Hz at t = 6.182s with BESS.

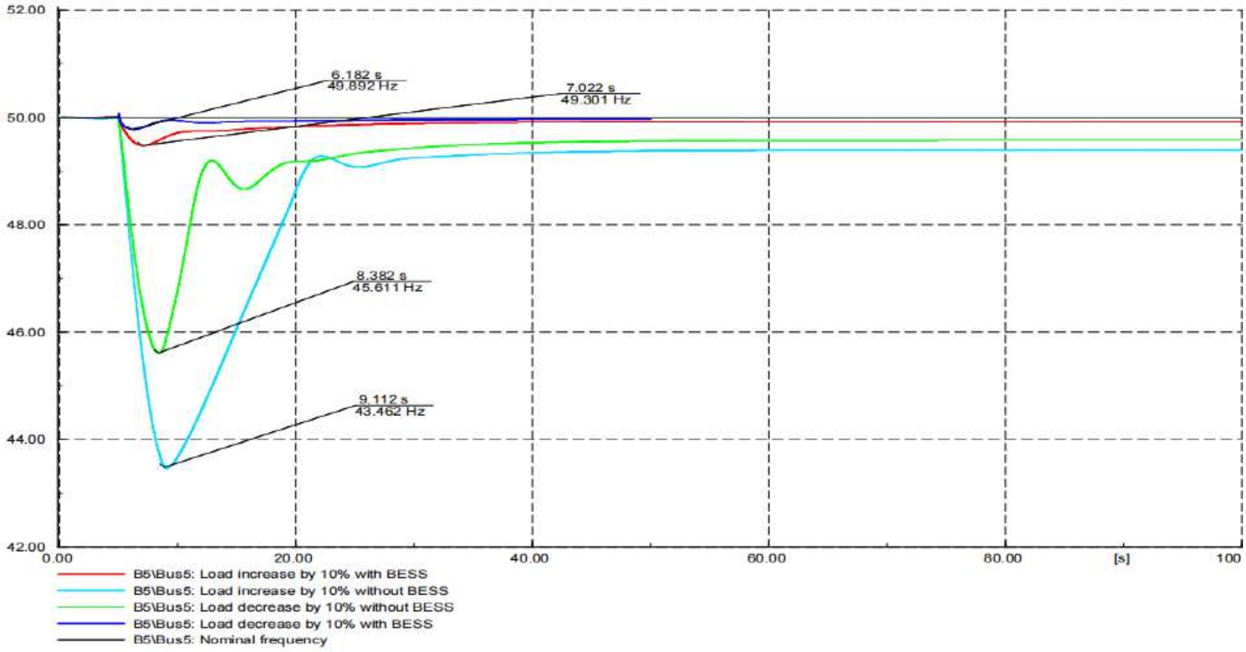


**Figure 10:** Frequency response curve of load variation with 20% PV

### 3.5.2 Frequency Response with 40% PV penetration

At 40% PV penetration, the system without BESS experienced a sharp frequency drop to 42.962 Hz at t = 9.372s, as shown in Figure 11. With BESS integration, the frequency nadir improved to 48.825 Hz at t = 7 .22s, demonstrating effective mitigation of low-inertia effects.

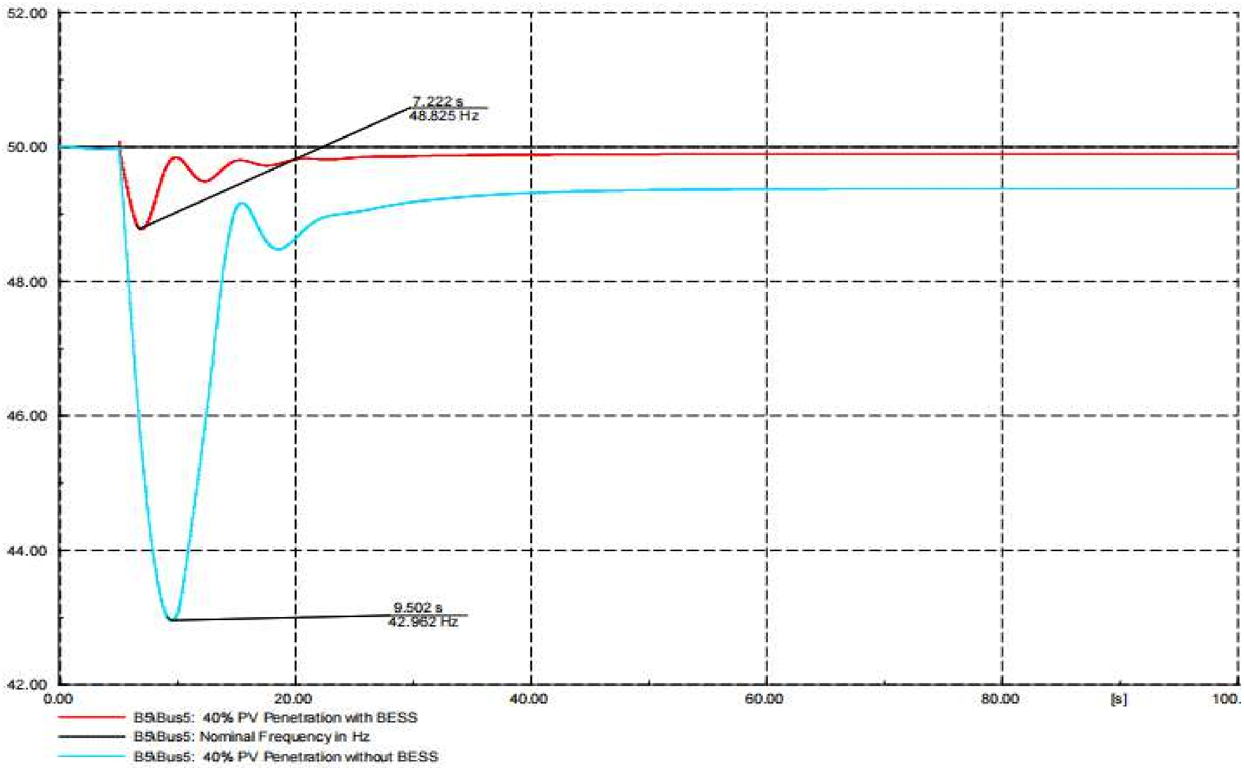


**Figure 11:** Frequency response curve with 40% PV penetration

*Frequency Response of Generator Outage with 40% PV Penetration*

For 10% generator outage, the frequency nadir without BESS was 40.677 Hz at t = 9.922s while with BESS it improved to 48.497 Hz at t = 7.472s. Under 20% generator outage, the frequency without BESS fell critically to 39.979 Hz at t = 10.472 s, whereas BESS raised the nadir to 48.361 Hz at t = 7.032 s, stabilizing the system within permissible limits.

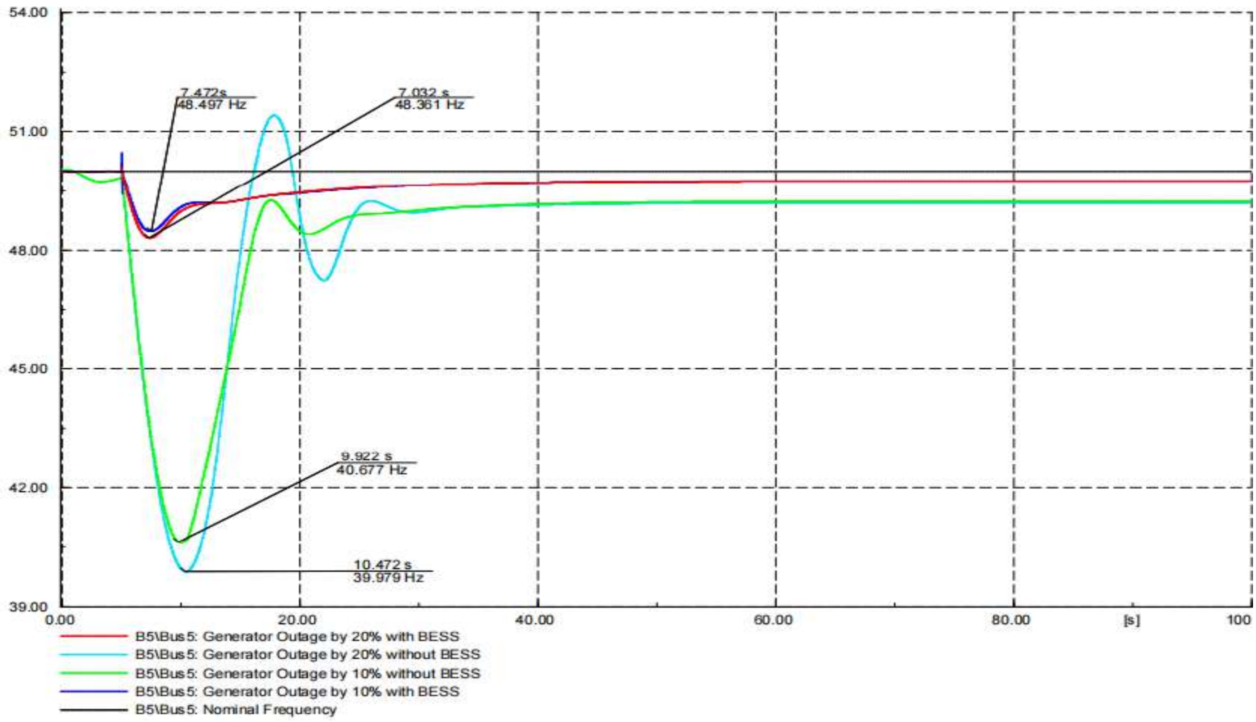


**Figure 12:** Frequency response curve of generator outage with 40% PV

*Frequency Response of Load Variation with 40% PV Penetration*

With +10% load increase, the frequency nadir improved from 41.997 Hz at t = 9.612s to 48.642 Hz at t = 6.682s with BESS. Similarly, during -10% load decrease, the frequency nadir increased from 44.669 Hz at t = 8.322s to 49.391 Hz at t = 6.872s, indicating enhanced damping and faster frequency recovery.

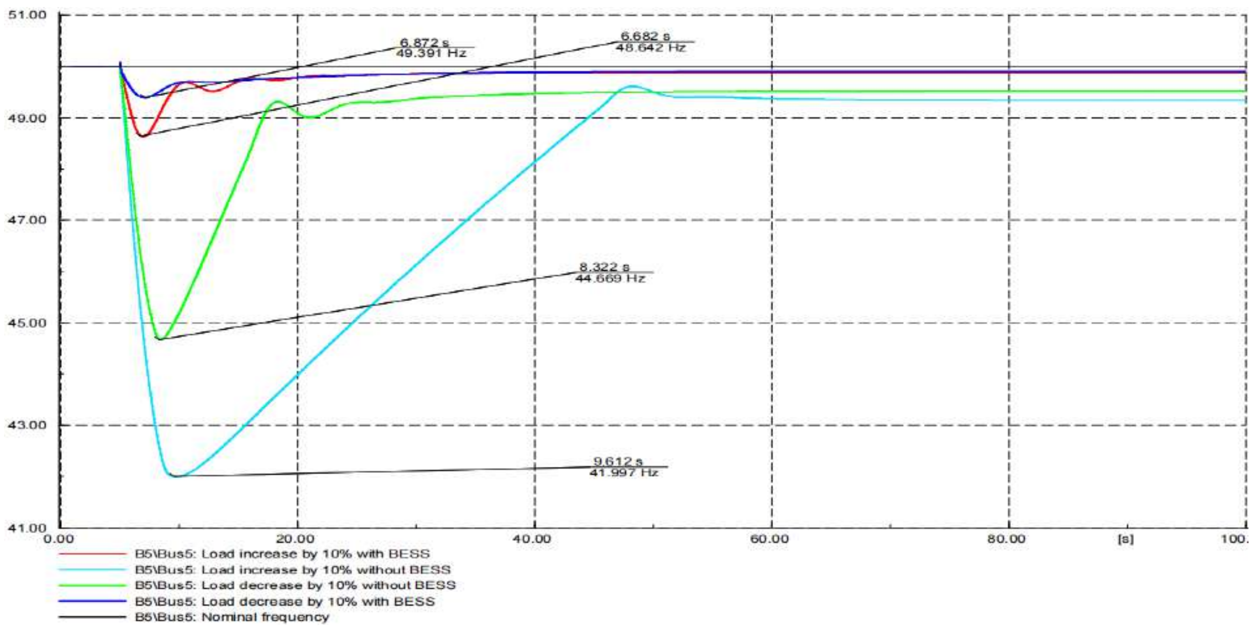

**Figure 13:** Frequency response curve of load variation with 40% PV

### 3.5.3 Frequency Response with 60% PV penetration

The system frequency response with 60% PV penetration represents extremely low-inertia conditions as illustrated in Figure 14. Without BESS, the frequency dropped sharply to 40.343 Hz at t = 9.892s, indicating severe instability. With BESS, the frequency nadir improved to 48.384 Hz at t = 7.222s, significantly enhancing system stability.

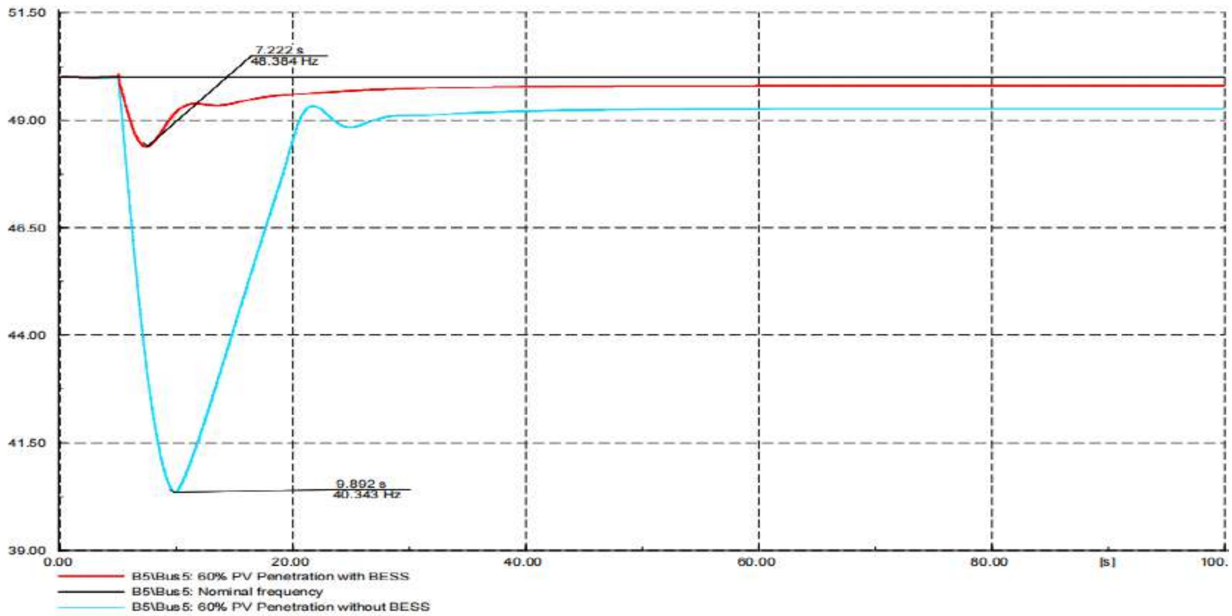


**Figure 14:** Frequency response curve with 60% PV penetration

*Frequency Response of Generator Outage with 60% PV Penetration*

For 10% generator outage, the system without BESS experienced a severe frequency drop to 39.770 Hz at t = 10.062s. With BESS, the frequency nadir improved to 48.207 Hz at t = 7.062s, demonstrating effective frequency support. A 20% generator outage led to excessive system instability, with the frequency falling below acceptable operational limits and therefore was excluded from further analysis.

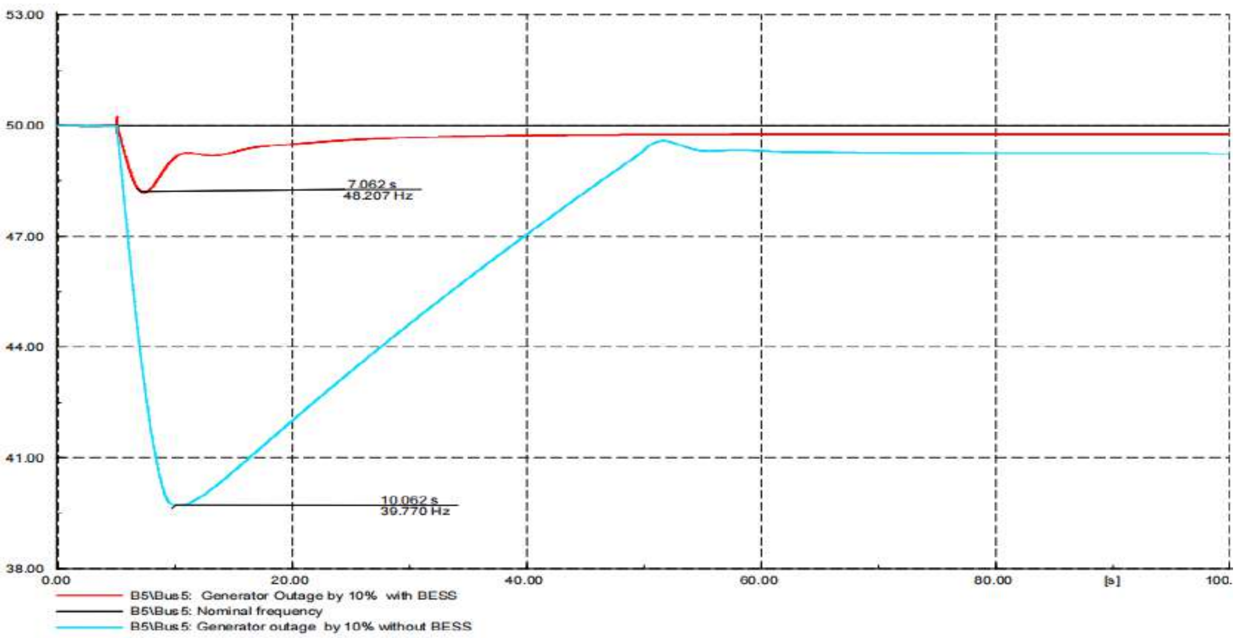


**Figure 15:** Frequency response curve of generator outage with 60% PV

*Frequency Response of Load Variation with 60% PV Penetration*

During +10% load increase, the frequency nadir improved from 39.936 Hz at t =1 0.882s to 48.291 Hz at t = 6.772s with BESS. Similarly, for -10% load decrease, the frequency nadir increased from 42.867 Hz at t = 8.442s to 48.780 Hz at t = 6.772s, accompanied by improved damping and faster recovery.

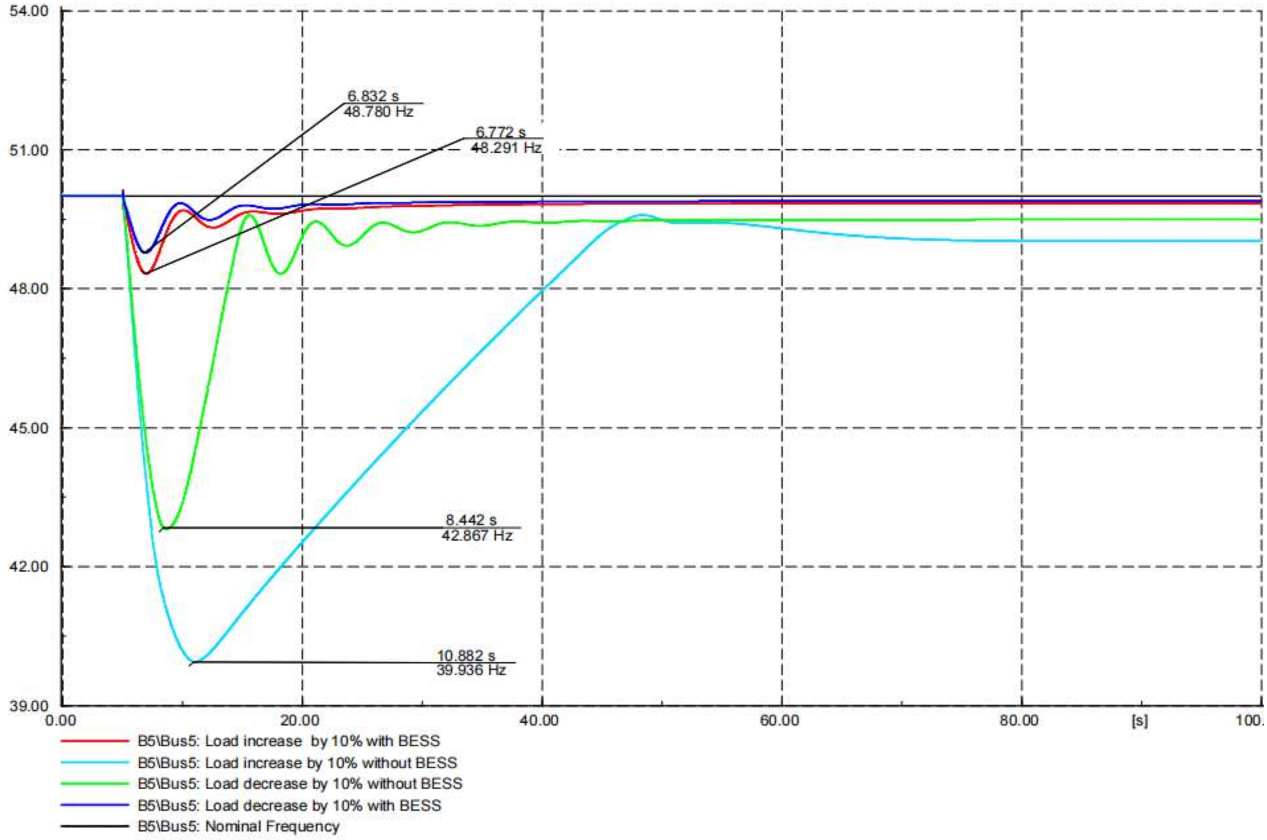


**Figure 16:** Frequency response curve of -10% load variation with 60% PV

### 3.6 Summary Table of Frequency Nadir of All Conditions

**Table 7:** Frequency nadir of all conditions

| Scenario | | Without BESS | With BESS |
|---|---|---|---|
| Varying 20% of PV Penetration | | 44.906 Hz | 49.624 Hz |
| Contingency Event | Generator Outage (10%) | 43.265 Hz | 49.292 Hz |
| | Generator Outage (20%) | 42.983 Hz | 48.981 Hz |
| | Load Increases (+10%) | 43.462 Hz | 49.301 Hz |
| | Load Decreases (-10%) | 45.611 Hz | 49.892 Hz |
| Varying 40% of PV Penetration | | 42.962 Hz | 48.825 Hz |
| Contingency Event | Generator Outage (10%) | 40.677 Hz | 48.497 Hz |
| | Generator Outage (20%) | 39.979 Hz | 48.361 Hz |
| | Load Increases (+10%) | 41.997 Hz | 48.642 Hz |
| | Load Decreases (-10%) | 44.669 Hz | 49.391 Hz |
| Varying 60% of PV Penetration | | 40.343 Hz | 48.384 Hz |
| Contingency Event | Generator Outage (10%) | 39.770 Hz | 48.207 Hz |
| | Load Increases (+10%) | 39.936 Hz | 48.291 Hz |
| | Load Decreases (-10%) | 42.867 Hz | 48.780 Hz |

## 4 Conclusion

The global energy sector is undergoing a rapid transition as climate goals and environmental concerns drive the large-scale integration of renewable energy sources, particularly solar PV generation. While this transition supports sustainability objectives, it also introduces significant challenges to power system frequency stability due to the reduction of system inertia resulting from the displacement of synchronous generators.

This project analyzed the impact of high PV penetration on frequency stability using a modified IEEE 9-bus test system modelled in DIgSILENT PowerFactory. Time-domain simulations were conducted for PV penetration levels of 20%, 40%, and 60%, considering various contingency scenarios such as generator outages and load variations. The results demonstrated that increasing PV penetration reduces system inertia, leading to higher RoCoF, deeper frequency nadirs, and slower post-disturbance recovery. At higher penetration levels, frequency deviations became critically unstable, highlighting that PV generation alone is insufficient to maintain frequency stability during sudden disturbances.

To address these low-inertia challenges, a 35 MVA BESS was implemented for the IEEE 9-bus system. Using the swing equation and related analytical formulas, the BESS size was determined to ensure adequate frequency support. After BESS implementation, the frequency response parameters including RoCoF, frequency nadir and steady-state frequency deviation improved significantly, remaining within Nepal's operational limits of ±5% of the nominal frequency under all scenarios (Electricity Regulatory Commission, 2024).

These results confirm that BESS with synthetic inertia emulation and droop-based frequency control provides a technically robust, flexible and fast-acting solution to enhance frequency stability in PV-dominated power systems. The study demonstrates that systematic assessment of PV penetration levels, contingencies analysis, and appropriate BESS sizing can effectively maintain frequency stability, accelerate post-disturbance recovery and improve dynamic system performance.

The methodology and findings of this study can be applied to the planning and operation of low-inertia power systems with high penetration of renewable generation. The proposed BESS sizing and frequency control approach can assist system operators and planners in determining minimum storage requirements for fast frequency response, contingency management and grid code development. This framework is particularly relevant for power systems such as Nepal's grid, where large-scale solar integration is planned alongside conventional hydropower generation.

Future enhancements of this work may include extending the analysis to larger and more realistic network models, incorporating advanced control techniques such as adaptive droop control and grid-forming inverter operation, and evaluating coordinated frequency control between hydropower plants and BESS. Additional research could also focus on optimal BESS placement, economic feasibility, and real-time or hardware in the loop simulations to further assess system performance under practical operating conditions.

**References**


- Wiatros-Motyka, M., Fulghum, N., Jones, D., et al. (2024) Global Electricity Review 2024. London: Ember Energy.
- International Energy Agency (2025) Electricity – Global Energy Review 2025. Paris: International Energy Agency.
- Amin, M.R., Negnevitsky, M., Franklin, E., Alam, K.S. and Naderi, S.B. (2021) 'Application of battery energy storage system for primary frequency control in power systems with high renewable energy penetration', Energies, 14(5), Article 1379.
- Assery, S.A., Zhang, X.-P. and Chen, N. (2024) 'Large-scale BESS for damping frequency oscillations of power systems with high wind power penetration', Inventions, 9(1), Article 3.
- Chunyang, Z., Andersen, P.B., Træholt, C. and Hashemi, S. (2023) 'Grid-connected battery energy storage system: A review on application and integration', Renewable and Sustainable Energy Reviews, 182, Article 113400. doi:10.1016/j.rser.2023.113400.
- Anderson, P.M. and Fouad, A.A. (2003) Power System Control and Stability. 2nd edn. Piscataway, NJ: IEEE Press.
- Department of Hydropower and Indian Institute of Technology Roorkee (n.d.) 'Hydro generator characteristics and performance', in Modern Hydroelectric Engineering, Vol.
- IEEE Power System Dynamic Performance Committee (1992) 'Hydraulic turbine and turbine control models for system dynamic studies', IEEE Transactions on Power Systems, 7(1), pp. 167–179.
- Energy Education (n.d.) 'Solar power'. Available at: https://energyeducation.ca/encyclopedia/Solar_power (Accessed: 25 November 2025).
- Knap, V., Chaudhary, S.K., Stroe, D.-I., Swierczynski, M., Craciun, B.-I. and Teodorescu, R. (2016) 'Sizing of an energy storage system for grid inertial response and primary frequency reserve', IEEE Transactions on Power Systems, 31(5), pp. 3447–3456.

- Sun, Y., et al. (2024) 'The frequency regulation control method of large-scale distributed energy storage systems in the smart grid', Elektronika ir Elektrotechnika, 30(5), pp. 14–21. doi:10.5755/j02.eie.38186.
- Krishan, O. and Suhag, S. (2019) 'An updated review of energy storage systems: Classification and applications in distributed generation power systems incorporating renewable energy resources', International Journal of Energy Research, 43(12), pp. 6171–6210.
- Abuagreb, M., Abuhussein, A. and Alzahir, S. (2021) 'Sizing of energy storage systems for virtual inertia emulation', Energies, 14(13), Article 4002.
- Electricity Regulatory Commission (2024) Annual Report 2080/81. Kathmandu: Electricity Regulatory Commission. Available at: https://api.erc.gov.np/media/documents/ERC-Annual-Report-2080-81.pdf (Accessed: 22 February 2026).

**Pokhara Engineering College Journal (PECJ)**

*Applied Sciences and Engineering Insights*

ISSN: 3021-9795 (Print) / 3059-9628 (Online)
(Volume-3, Issue- I)

# Comparative Influence of Cohesion and Friction Angle on the Stability of Dry Slopes: A Parametric Sensitivity Study of Ramche Landslide

*Sanjay Baral*[1*]

[1]*School of Engineering, Faculty of Science and Technology, Pokhara University, Nepal*

**Corresponding email: sanjaybaral@pu.edu.np https://orcid.org/0009-0009-8742-5821*



*Received:02- February-2026; Revised: 24- February-2026; Accepted: 08- March-2026*

*DOI: https://doi.org/10.3126/pecj.v3i1.93540*

## Abstract

The reliability and safety of slope designs largely depend on accurately understanding and measuring the soil properties of slope, because small errors in estimating this parameter can significantly affect stability predictions. This study investigates the sensitivity of slope stability to variations in cohesion (c) and internal friction angle (ϕ) with respect to the Factor of Safety (FoS). The research focuses on the Ramche landslide in Rasuwa District, Nepal, representing a typical Himalayan slope condition. Six disturbed and undisturbed soil samples were collected from different locations along the slope profile during a detailed field investigation. Laboratory testing was conducted to determine key engineering properties, including cohesion, friction angle, and unit weight. Based on field measurements, slope geometry was prepared using AutoCAD and SW DTM software, and a numerical model was developed in Slide2. The soil behavior was simulated using the Mohr–Coulomb failure criterion. Slope stability was evaluated using four limit equilibrium methods: Bishop Simplified method, Janbu Simplified method, Spencer method, and Morgenstern–Price method. Sensitivity analyses, including tornado and spider plots, indicate that ϕ is the most influential parameter, producing significantly greater variation in FoS compared to cohesion. The results consistently show that slope stability is more sensitive to uncertainties in the friction angle, highlighting the importance of accurate shear strength characterization for reliable slope design and risk assessment.

**Keywords:** Sensitivity analysis of slope, Slide2 numerical modeling, Cohesion and friction angle, Factor of Safety

## 1. Introduction

Landslides represent one of the most persistent and destructive natural hazards affecting mountainous regions worldwide (Osman, 2018). In countries characterized by steep terrain, intense rainfall, and fragile geological formations, slope failures frequently disrupt communities, damage infrastructure, and hinder sustainable development. Nepal, situated in the central Himalaya, exemplifies this vulnerability. The country's dramatic topographic relief from the low-lying Terai plains to the towering peaks of the Mountain region creates sharp elevation gradients within a relatively short north south distance (Chhetri and Easterling, 2010). Such geomorphological conditions, combined with active tectonics and seasonal monsoon precipitation (Shrestha et al., 2000, Sharma et al., 2020), make slope instability a recurring and critical national concern. In this context, understanding the mechanical behavior of slopes and the parameters that govern their stability is not only an academic pursuit but also a practical necessity for engineering design and disaster risk reduction.

To appreciate the complexity of slope failures in Nepal, it is important to define several key concepts. A landslide is the downslope movement of soil, rock, and debris under the influence of gravity, often triggered by external factors such as rainfall, earthquakes, or human activity (Skilodimou et al., 2018, Ahmed, 2021, Highland and Bobrowsky, 2008). The stability of a slope is commonly evaluated using the FoS, defined as the ratio of resisting forces to driving forces. When the FoS is greater than one, the slope is considered stable; when it approaches or falls below one, failure becomes likely. The shear strength of soil, a fundamental property governing slope stability, is primarily described by two parameters derived from the Mohr Coulomb failure criterion: cohesion (c), representing the bonding between particles, and friction angle (ϕ), representing the internal resistance due to particle interlocking and friction. Variations in these parameters whether due to changes in moisture content, weathering, or stress conditions can significantly influence the FoS and, consequently, slope performance (Iverson, 2000, Medina et al., 2021, Malla and Dahal, 2021).

In Nepal, more than seventy-five percent of the annual rainfall occurs during the monsoon season, typically from June to September (Shrestha et al., 2000, Sharma et al., 2020). This intense and prolonged precipitation increases soil moisture, raises groundwater levels, and reduces effective stress within slopes (Findell and Eltahir, 1997). As pore water pressure rises, the apparent cohesion and effective friction angle may decrease, thereby reducing shear strength (Iverson, 2000, Medina et al., 2021, Malla and Dahal, 2021, Baral et al., 2025, Baral and Tiwari, 2025). Numerous studies have identified monsoon rainfall as the primary triggering mechanism for slope failures in the Himalayan region (Dahal, 2012, Gnyawali et al., 2023, Kincey et al., 2024). Furthermore, rapid infrastructure expansion such as road construction, hydropower development, and urban growth has altered natural slope geometries and drainage conditions, exacerbating instability in many areas (McAdoo et al., 2018, Paudyal et al., 2023). Although extensive research has been conducted on landslide occurrence, mapping, and rainfall thresholds in Nepal (Dahal and Hasegawa, 2008, Basnet and Acharya, 2019), a critical gap remains in site-specific geotechnical investigations that quantitatively evaluate how variations in shear strength parameters influence slope stability. Many existing studies provide regional-scale hazard assessments or focus on identifying triggering factors, yet fewer studies systematically examine the sensitivity of the FoS to changes in cohesion and friction angle at the local scale. In practice, soil parameters are inherently uncertain due to spatial variability, limited sampling, and laboratory testing constraints (Stark et al., 2008). Designers often rely on representative or conservative values without fully understanding how small deviations in these parameters may affect stability outcomes. Neglecting to analyze parameter sensitivity may produce either excessively conservative designs that drive up costs or overly optimistic assumptions that could endanger safety.

Previous analytical approaches to slope stability have predominantly employed the Limit Equilibrium Method (LEM), including Bishop's simplified method, Fellenius' method, and Janbu's method (Li et al., 2019, Zhu et al., 2003). These techniques divide the slope into slices and satisfy force and moment equilibrium to compute the FoS (Zolkepli et al., 2019). LEM remains widely used due to its conceptual simplicity and computational efficiency (Aryal, 2006, Liu et al., 2015). More recently, numerical methods such as the Finite Element Method (FEM) have gained prominence relationships (Matthews et al., 2014, Hammouri et al., 2008, Salih, 2021, Griffiths and Lane, 1999). FEM-based approaches, particularly those employing the Shear Strength Reduction (SSR) technique, enable simulation of stress–strain behavior and progressive failure mechanisms (Ramadhani and Ihzan, 2023, VandenBerge and McGuire, 2019). Despite these advancements, many applications in Nepal have focused on obtaining a single FoS value under assumed parameter sets, rather than conducting comprehensive sensitivity analyses that explore the relative influence of cohesion and friction angle on slope stability.

The rationale for this study arises from the recognition that cohesion and friction angle are not fixed constants but variable properties influenced by geological conditions, weathering, saturation, and sampling uncertainty (Abramson et al., 2001). A rigorous sensitivity analysis provides insight into which parameter exerts the greatest control on the FoS and how variations within realistic ranges affect slope safety. Such understanding is essential for prioritizing field investigations, optimizing laboratory testing programs, and improving the reliability of geotechnical designs. Moreover, in data-scarce mountainous environments, identifying the most influential parameters can guide resource allocation and risk mitigation strategies.

Accordingly, the primary objective of this paper is to investigate the sensitivity of slope stability to variations in cohesion and friction angle with respect to the FoS. The study focuses on a representative Himalayan slope in Nepal, where six soil samples were collected from different locations along the Ramche slope profile. The soil mass is modeled as a single homogeneous layer to isolate the effects of shear strength parameters. The FoS is computed using Bishop Simplified method, Janbu Simplified method, Spencer method, and Morgenstern–Price method implemented in Slide 2D software. External influences such as building loads and seismic forces are not considered in order to concentrate specifically on the intrinsic material parameters. By systematically varying cohesion and friction angle within plausible ranges, the research quantifies their relative impact on FoS and identifies the parameter to which the slope is most sensitive.

## 2. Materials and Methods

### 2.1. Study area

The study area is located at the Ramche landslide in Rasuwa District, Nepal (Figure 1), along the 36-km section of the Trishuli–Dhunche road at 28.026072 N, 85.223361 E above the Trisuli River. Geologically, the site lies within the Kuncha Formation of the Lower Nawakot Group in central Nepal (Jharendra et al., 2018). These rocks are highly weathered and fractured, making the slope weak and vulnerable to failure. The Ramche landslide is classified as a debris flow type movement (Jharendra et al., 2018). It extends for more than 3 km downslope and regularly damages the road section. According to local residents, the landslide was first activated in 1983 and reactivated on 14 August 2003, causing significant loss of life and property (Ghimire et al., 2007). Since then, it has remained active, especially during the monsoon season.

High rainfall increases pore water pressure in the slope materials, reducing soil strength and triggering debris movement over the bedrock. In addition, heavy traffic vibrations along the highway further destabilize the slope (Ghimire et al., 2007, Jharendra et al., 2018). Human activities such as haphazard road cutting, unplanned settlements, and unscientific agricultural practices have increased the size and intensity of the landslide. The absence of proper geotechnical mitigation measures has further increased the vulnerability of the area. The surrounding area is densely populated and widely used for cultivation, placing local communities at high risk. The settlement near the landslide remains in serious danger due to the continued activity of the slope and the potential for further expansion during intense rainfall events.

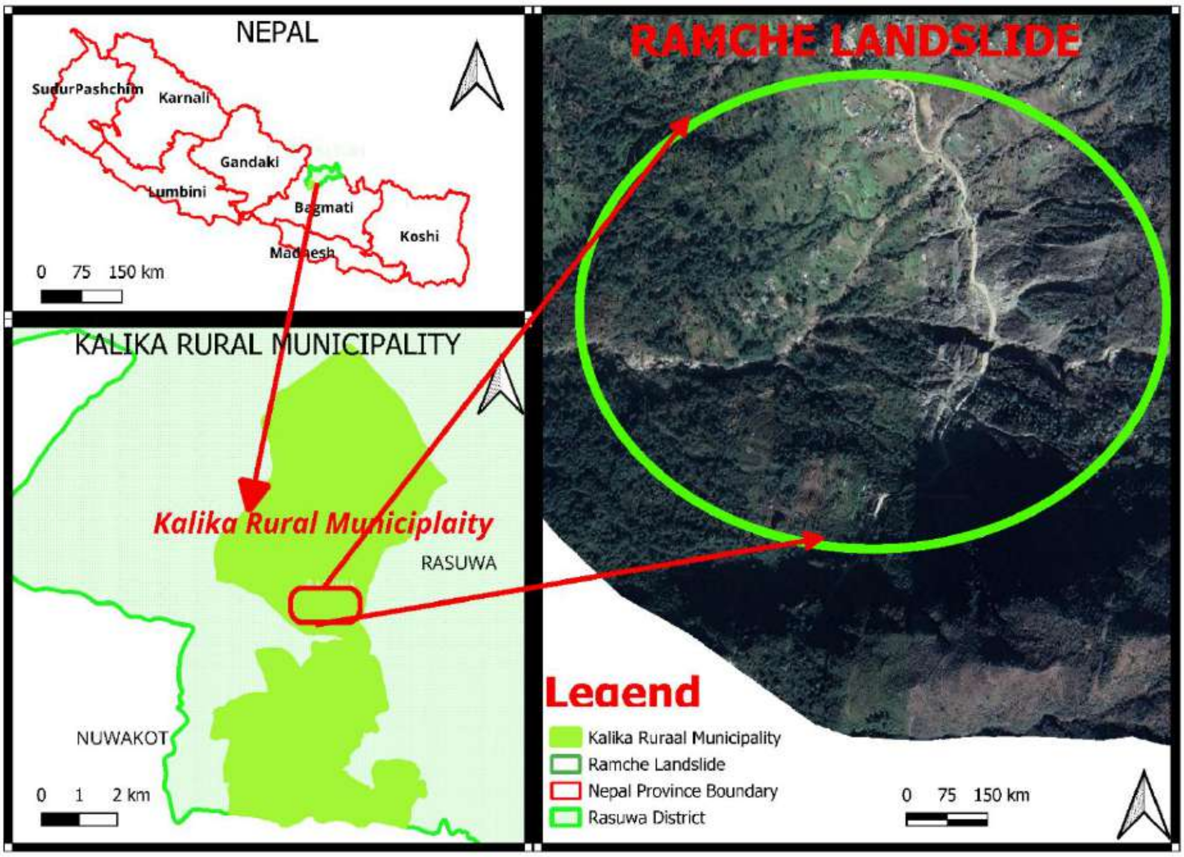


**Figure 1**: Study area map of Ramche Landslide, Rasuwa, Bagmati Province, Nepal

The detailed site visit was conducted to collect necessary field information. During the visit, topographic data, available reports, and soil samples were gathered. Both disturbed and undisturbed soil samples were collected from six different locations along the slope. These samples were tested in the laboratory to determine the required engineering properties, particularly cohesion (c), internal friction angle ($\phi$), and unit weight.

After obtaining the laboratory results, a numerical model of the slope was developed using AutoCAD, SW DTM - Software and Slide2. The slope geometry was first defined based on field measurements in AutoCAD with the help of SW DTM - Software. Then only the model is prepared in Slide2 (Figure 2). After that, material properties obtained from laboratory testing were assigned to the model. The soil behavior was simulated using the Mohr–Coulomb failure criterion, which relates shear strength to cohesion and friction angle.

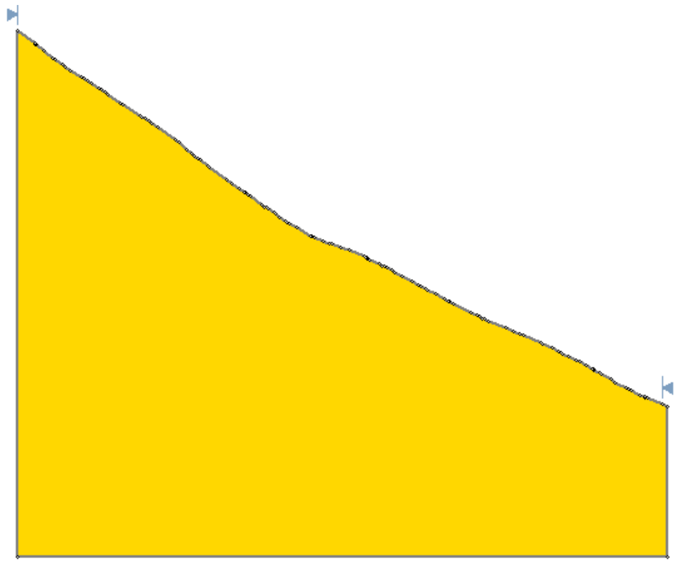

**Figure 2:** Model for Ramche Slope with material assignment (Slide2 model)

To ensure uniformity and reliability in the analysis, identical slope geometry was maintained for all simulation cases. Consequently, any observed variation in the FoS can be attributed solely to changes in the shear strength parameters, eliminating the influence of other modeling factors.

Slope stability was evaluated using four different limit equilibrium methods: The Bishop Simplified method, Janbu Simplified method, Spencer method, and Morgenstern–Price method. These methods were adopted to evaluate how variations in the assumptions regarding inter-slice force interactions affect the computed FoS. All analyses were performed under dry conditions. Groundwater effects, pore water pressure, surcharge loads, and seismic forces were not included. The earthquake coefficient was set to zero so that the results reflected only the effect of soil shear strength.

Finally, a parametric sensitivity analysis was conducted. Cohesion (c) and friction angle ($\phi$) were varied systematically within selected ranges, while all other parameters remained constant. For each variation, the model was reanalyzed using all four methods, and the minimum global FoS was recorded. The relationship between FoS and the shear strength parameters was then established to identify which parameter had greater influence on slope stability and to compare the consistency of results among the different methods. Detail work flow is shown in Figure 3.

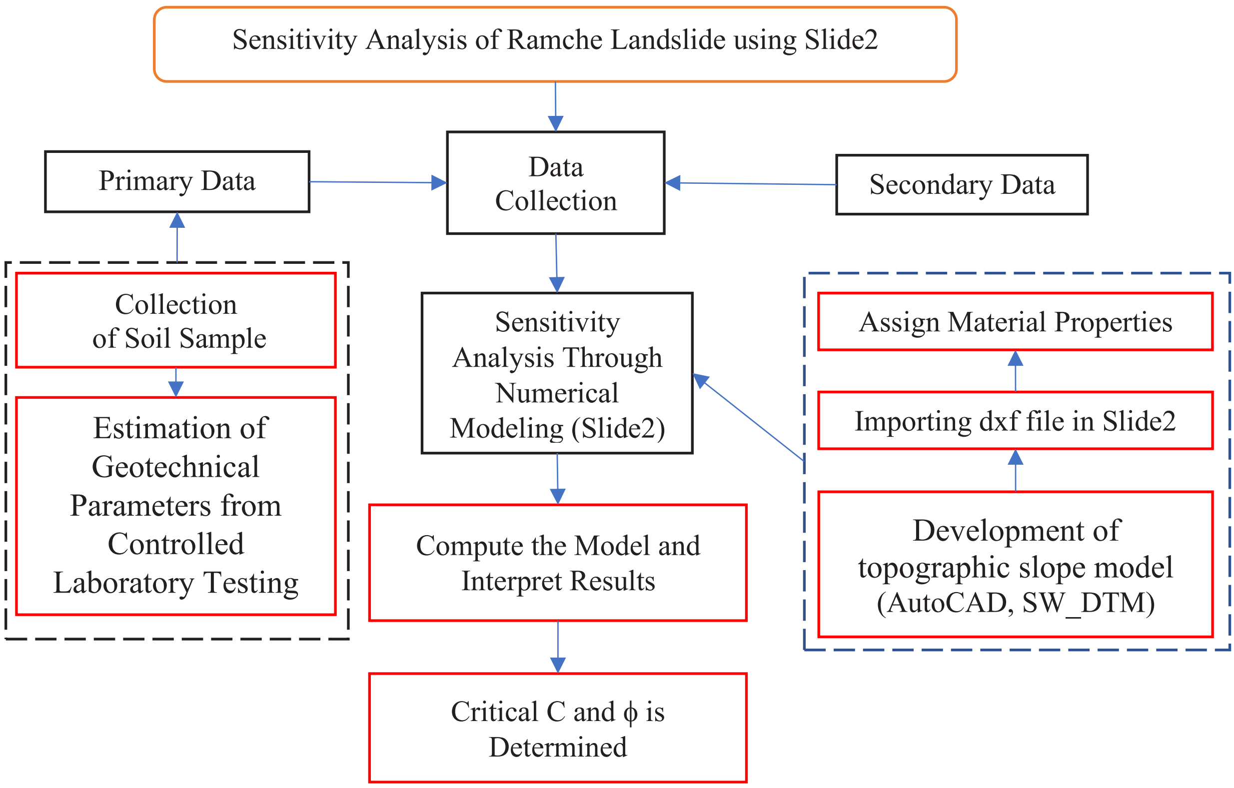


**Figure 3:** Presents the workflow for the numerical and computational analysis.

### 3. Results and Discussion

The case study focuses on a landslide located along the Trishuli Highway at Ramche in Rasuwa District (28.026072° N, 85.223361° E), situated above the Trishuli River. The fundamental soil parameters required for the development of the numerical model were determined through laboratory testing of collected soil samples. These soil parameters were subsequently used to evaluate the sensitivity analysis of the Ramche slope.

The results of the direct shear tests demonstrate that the shear strength characteristics of the soil conform to the Mohr–Coulomb failure criterion. This is evidenced by the linear relationship observed between shear stress (y-axis) and normal stress (x-axis), as presented in Figure 4. The shear stress and normal stress relationships derived from the six representative soil samples were used as key input parameters for the sensitivity analysis of the slope. These relationships help to understand how variations in soil strength properties influence the overall stability of the slope and identify which parameters have the most significant impact on potential failure. The dispersion of the plotted data reflects inherent variability in the soil properties, indicating that the slope materials are not perfectly uniform across the site. This natural heterogeneity plays an important role in sensitivity analysis, as even small variations in strength parameters can produce significant changes in the predicted stability condition of the slope.

The tested samples show relatively low cohesion values (2.95–7.93 kN/m²) and internal friction angles (16.12°–21.19°), which correspond to limited shear strength. Since cohesion (c) and friction angle (ϕ) directly govern the shear resistance of soil, minor reductions in these parameters can considerably lower the FoS. This highlights the sensitivity of the slope to variations in shear strength properties and explains its vulnerability to instability under unfavorable conditions. For the sensitivity analysis, the average values of cohesion (4.326 kN/m²) and friction angle (19.14°) were adopted as representative baseline parameters. Using the mean values provides a rational and balanced estimate of the overall shear strength of the slope material, minimizing the influence of extreme test results while still reflecting site specific conditions (Duncan et al., 2014, Chowdhury et al., 2023). These average parameters were then systematically varied to evaluate how changes in c and ϕ affect slope stability, thereby offering a clearer understanding of the slope's response to uncertainty in soil strength characteristics.

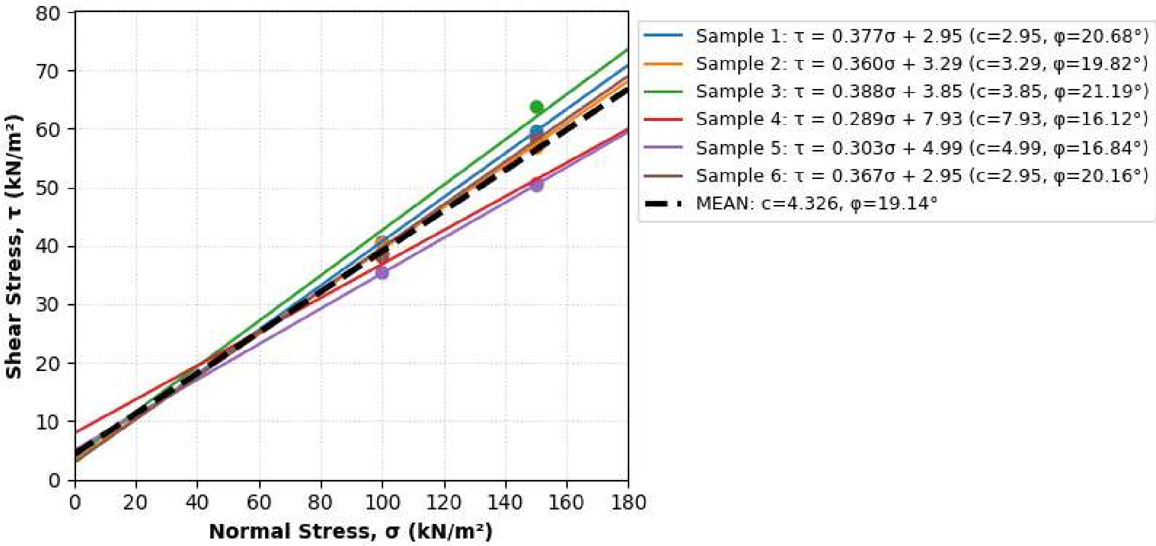


**Figure 4:** Experimental Determination of Shear Strength Parameters Using Direct Shear Test

The Figure 5 presents the contour distribution of the FoS for the analyzed slope under fully dry and unloaded conditions for the four different methods. The color scale illustrates the variation in stability within the slope mass, where warmer colors such as yellow to red indicate lower FoS values and relatively less stable zones. Most of the slope appears in yellow to light orange shades, suggesting that the FoS is close to 1.0 across a significant portion of the slope. However, the highlighted area identifies a critical zone with a minimum FoS less than one.

Because a FoS value less than 1.0 indicates that the available shear strength is insufficient to resist the driving forces, this result confirms an unstable condition along the identified slip surface. The contour pattern further reveals a curved failure surface extending from the crest toward the toe of the slope, which is characteristic of rotational failure in homogeneous soil. Since groundwater pressure, external surcharge loads, and seismic effects were not considered in the analysis, the observed instability is attributed solely to inadequate shear strength parameters, namely cohesion and internal friction angle. These findings demonstrate the high sensitivity of slope stability to variations in shear strength (Di Matteo et al., 2013, Khan and Wang, 2021) and indicate that the selected parameter combination is insufficient to maintain equilibrium under dry conditions.

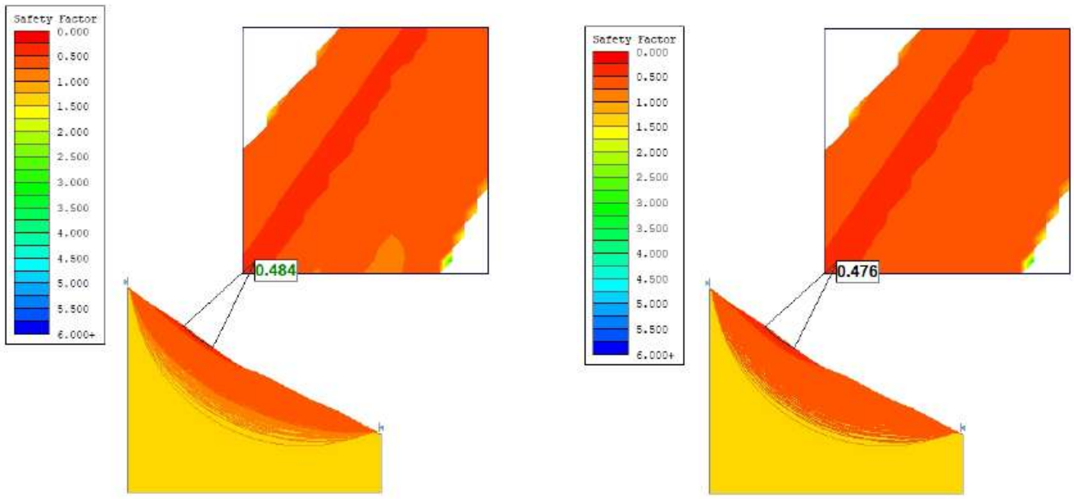


(a) Bishop Simplified Method (b) Janbu Method Simplified

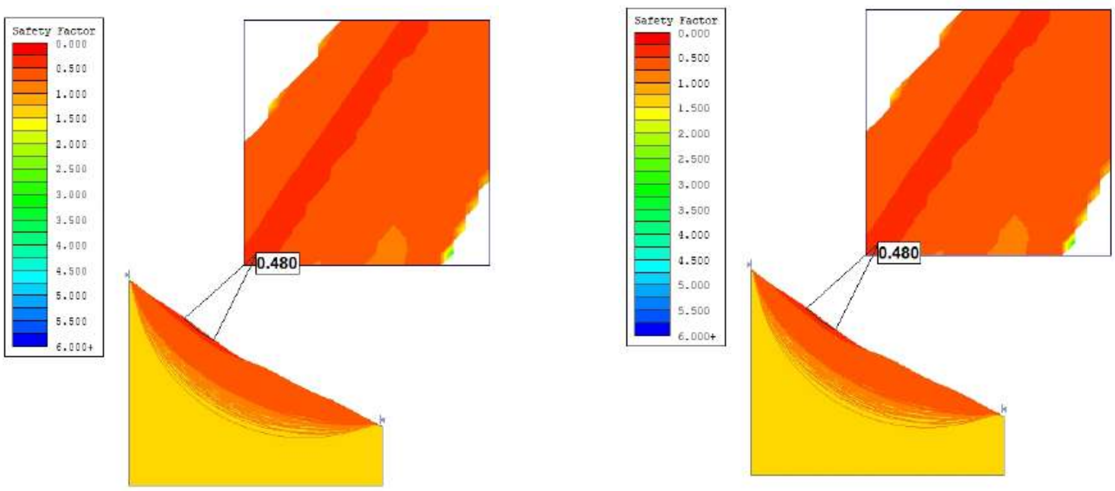


(c) Spencer Method (d) GLE / Morgenstern-Price Method

**Figure 5:** Sensitivity analysis of Ramche slope for average base value of Cohesion and friction angle for obtaining FoS for soil sample

The Figure 6 (a and b) illustrates how the FoS varies with changes in clay friction angle and cohesion using four limit equilibrium methods: Bishop, Janbu, Spencer, and Morgenstern–Price (GLE). The horizontal axis represents the clay friction angle (Figure 6 a) and cohesion (Figure 6 b), while the vertical axis shows the corresponding FoS values. A red dashed line marks the critical stability threshold at FoS = 1.0. Across all methods, FoS increases almost linearly as the friction angle and cohesion increases, clearly demonstrating that slope stability is strongly controlled by the shear strength contribution from friction angle and cohesion (Khan and Wang, 2021).

At low friction angles, all methods predict FoS values well below 1.0, indicating unstable conditions. As ϕ increases, FoS gradually improves and crosses the stability threshold at different points depending on the method. Janbu consistently predicts the highest FoS values, followed by Morgenstern–Price and Bishop, while Spencer provides slightly lower estimates. Although there are small differences in magnitude among the methods, the overall trend remains consistent, confirming that increasing the friction angle significantly enhances slope stability.

From a practical standpoint, the results highlight the dominant influence of the internal friction angle on slope performance. Even modest increases in ϕ produce noticeable improvements in FoS, while low ϕ values quickly lead to unsafe conditions. This emphasizes the need for accurate laboratory and field determination of friction angle in clayey soils, as uncertainty in this parameter can substantially affect design reliability and safety assessments (Khan and Wang, 2021, Phoon and Tang, 2019).

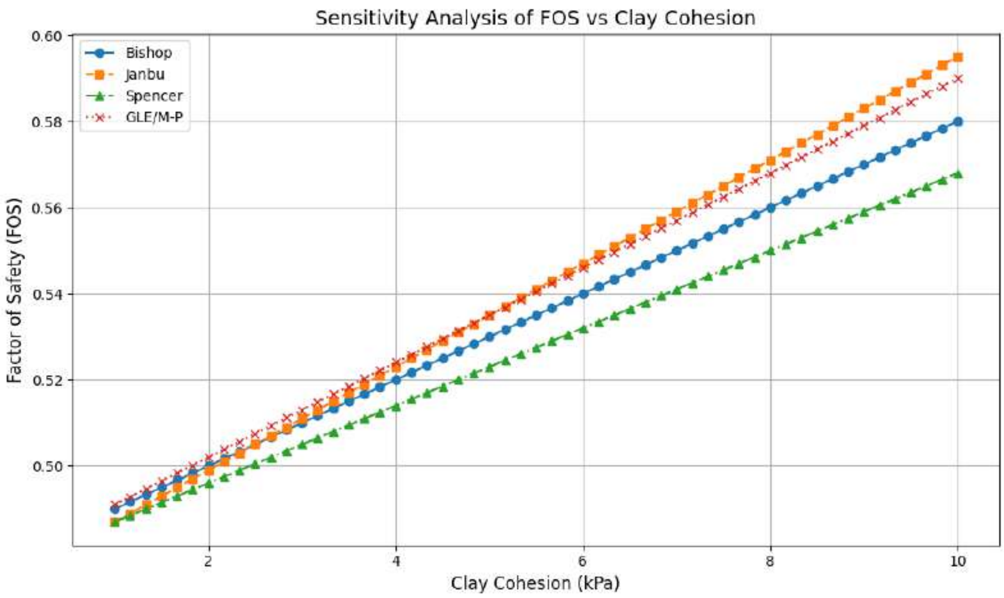


(a)

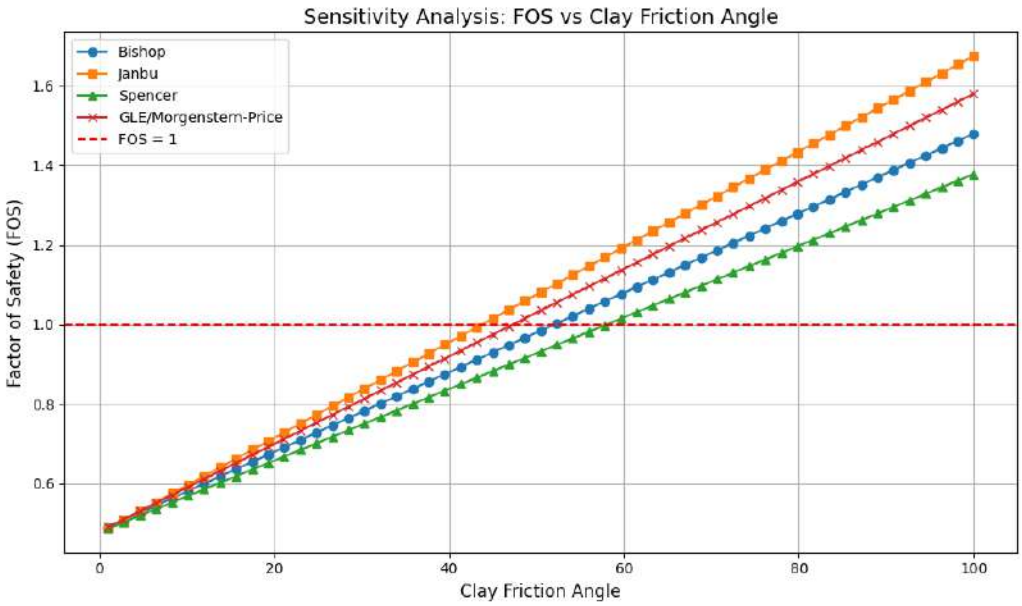


(b)

**Figure 6:** Sensitivity analysis of slope for (a) Clay cohesion Vs FoS (b) Friction Angle Vs FoS for Ramche slope

The Figure 7 presents a sensitivity spider plot illustrating the impact of percentage changes in cohesion and internal friction angle on the FoS, evaluated using four limit equilibrium methods: Bishop, Janbu, Spencer, and Morgenstern–Price (GLE/MP). The horizontal axis represents percentage variation from baseline soil parameters (−80% to +80%), while the vertical axis shows the corresponding FoS values. A red horizontal line marks the failure threshold at FoS = 1.0.

The results indicate that FoS is highly sensitive to variations in the internal friction angle across all methods. As ϕ increases, FoS rises nonlinearly and significantly, crossing the failure threshold at approximately +35% to +40% variation. Conversely, reductions in ϕ cause a sharp decline in FoS, indicating critical instability. In contrast, cohesion (c) shows minimal influence on FoS within the same variation range. The cohesion curves remain nearly horizontal, with only slight increases in FoS as c increases, demonstrating a comparatively weak sensitivity response. This consistent pattern across Bishop, Janbu, Spencer, and Morgenstern–Price methods confirms that frictional resistance governs slope stability behavior in the analyzed model.

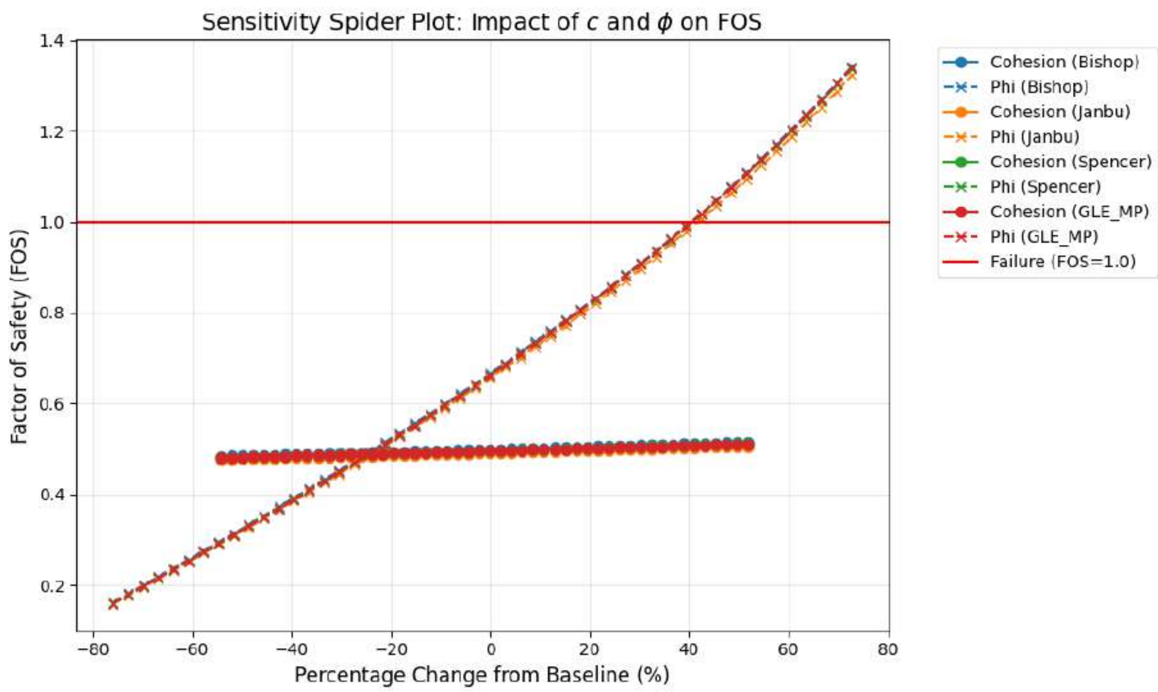


**Figure 7:** Sensitivity analysis of slope and Comparison of the influence of friction angle and cohesion, on slope stability across Ramche slope (Spider plot)

The relative influence of shear strength parameters cohesion (c) and internal friction angle (ϕ), on the FoS was also evaluated using a Tornado diagram based on the Spencer Method as shown in Figure 8. The results indicate that ϕ is the most sensitive parameter, producing a total FoS variation of approximately 1.177, compared to 0.032 for cohesion. This confirms that slope stability is more susceptible to uncertainties in the friction angle, suggesting that the frictional component contributes more significantly to shear resistance for the studied configuration (Deng et al., 2017).

Also cohesion shows very low influence, its relative impact is very lower than that of ϕ (Deng et al., 2017). The sensitivity ranking (ϕ >> c) highlights the importance of accurate determination of ϕ through laboratory testing such as triaxial or direct shear tests. Given that both parameters generate FoS variations, the slope may be classified as highly sensitive to shear strength fluctuations. Consequently, environmental factors that reduce shear strength such as elevated pore water pressure or weathering may significantly decrease stability.

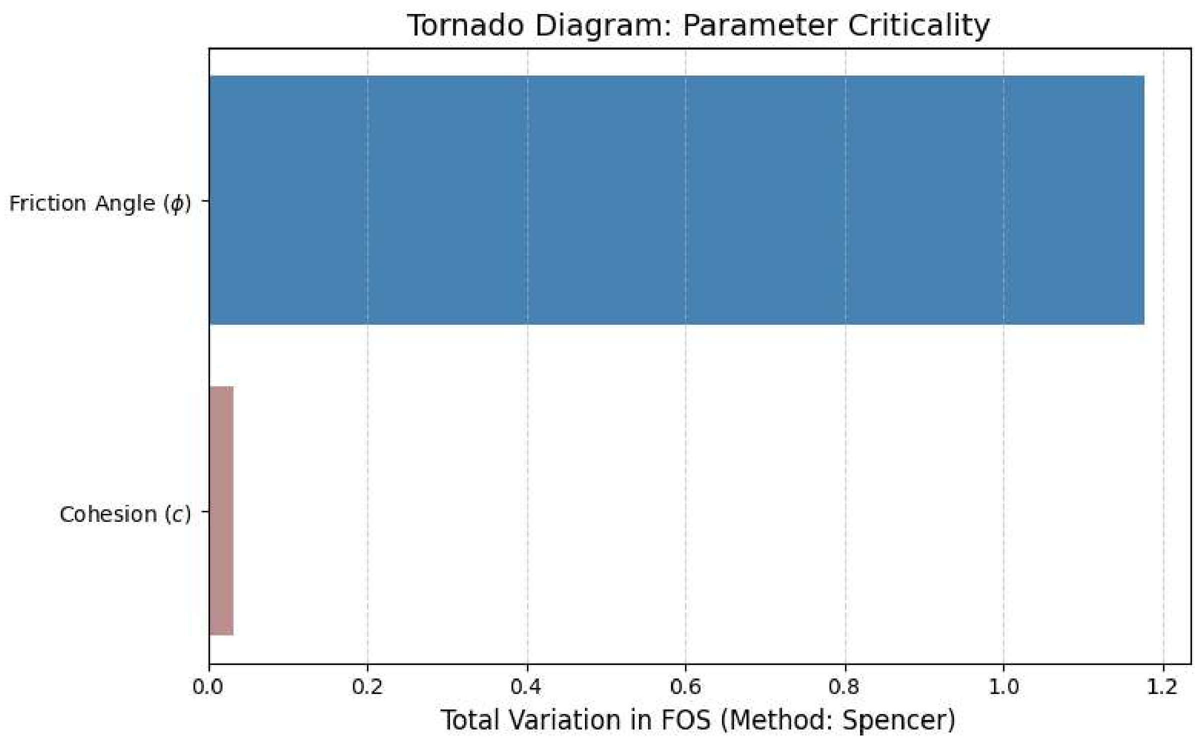


**Figure 8:** Sensitivity analysis of the Ramche slope to evaluate and compare the effects of cohesion and internal friction angle on overall slope stability

The Figure 9 presents FoS stability contours obtained using limit equilibrium method, illustrating the combined influence of cohesion (c) and internal friction angle (ϕ) on slope stability. Cohesion varies along the horizontal axis (approximately 5–14 kN/m²), while the internal friction angle ranges from about 7° to 43° on the vertical axis. The color gradient transitions from red (low FoS, unstable) to green (high FoS, stable), with a distinct contour marking FoS = 1.0, which represents the critical boundary between stable and unstable conditions.

The contour pattern shows that FoS is significantly more sensitive to changes in the internal friction angle than to cohesion. The predominantly horizontal contour bands indicate that small increases in ϕ produce substantial improvements in stability, whereas similar proportional changes in cohesion result in comparatively minor changes in FoS. The FoS = 1.0 line occurs at higher friction angles (around 41.75°) for low cohesion values, and slightly lower friction angles as cohesion increases, demonstrating the compensatory relationship between the two shear strength parameters.

The results suggest that slope stability in this analysis is primarily governed by the frictional component of shear strength rather than cohesion. Instability is concentrated in regions with low ϕ values, even when moderate cohesion is present. These findings emphasize the importance of accurate determination of the internal friction angle in design and reliability assessments, as uncertainties in ϕ are likely to have a greater impact on stability predictions than comparable uncertainties in cohesion.

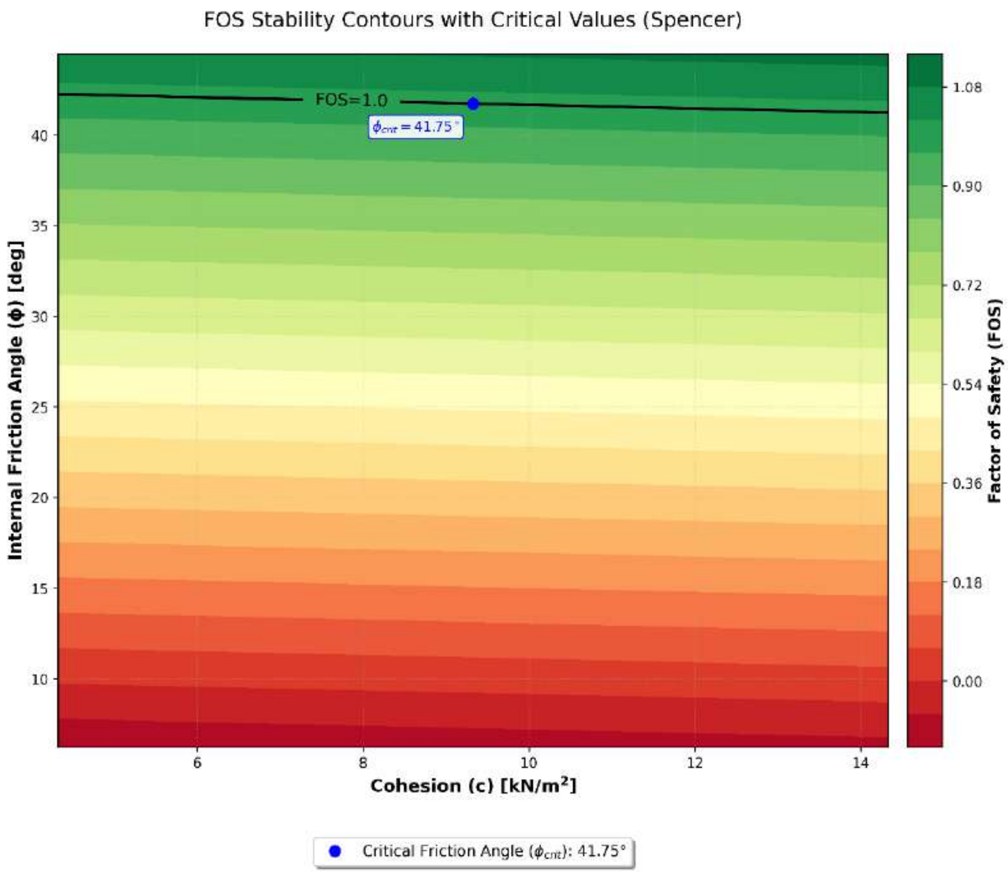


**Figure 9:** Sensitivity analysis of slope and Comparison of the influence of friction angle and cohesion, on slope stability across Ramche slope (FoS stability contours).

## 4. Conclusions

This study evaluated the sensitivity of slope stability to variations in cohesion (c) and internal friction angle (ϕ) of clay using four limit equilibrium approaches, Bishop Simplified Method, Janbu Method, Spencer Method, and Morgenstern–Price Method. The results consistently demonstrate that the internal friction angle is the dominant parameter governing the FoS for the analyzed clay slope.

Across all methods, FoS increased almost linearly with increasing ϕ, and reductions in ϕ led to rapid decreases in stability, frequently driving FoS below the critical threshold of 1.0. In contrast, cohesion exhibited a comparatively moderate influence. Although increases in c improved FoS, the magnitude of change was smaller than that associated with equivalent variations in ϕ. Sensitivity spider plots and stability contours further confirmed that slope response is strongly controlled by the frictional component of shear strength, while cohesion plays a secondary but still meaningful role.

The tornado diagram analysis quantified this hierarchy, showing a greater total FoS variation attributable to ϕ than to c. This indicates that uncertainties in friction angle have a more pronounced impact on predicted stability than comparable uncertainties in cohesion. Importantly, the similarity of trends obtained from all four limit equilibrium methods suggests that the sensitivity ranking (ϕ > c) is methodologically robust, even though slight differences exist in absolute FoS values.

From an engineering perspective, these findings underscore the critical importance of accurately determining the internal friction angle in clayey soils. Given the high sensitivity of FoS to ϕ, even modest errors in its estimation may significantly alter design outcomes and safety margins. While cohesion should not be neglected particularly under short-term or undrained conditions the frictional component ultimately governs long-term stability behavior for the slope configuration analyzed.

Overall, the study confirms that reliable slope design and risk assessment in clay soils require careful characterization of shear strength parameters, with particular emphasis on minimizing uncertainty in the internal friction angle to ensure dependable and safe stability predictions.

**References**


- ABRAMSON, L. W., LEE, T. S., SHARMA, S. & BOYCE, G. M. 2001. Slope stability and stabilization methods, John Wiley & Sons.
- AHMED, B. 2021. The root causes of landslide vulnerability in Bangladesh. Landslides, 18**,** 1707-1720.
- ARYAL, K. P. 2006. Slope stability evaluations by limit equilibrium and finite element methods.
- BARAL, S., JOSHI, N. & TIWARI, R. C. 2025. Stability Assessment of Landslide in Himalayan Terrain: A Spectral Element Method and Back Analysis-Based Approach. Engineering Reports, 7**,** e70541.
- BARAL, S. & TIWARI, R. C. 2025. Slope Stability Analysis of Landslide in the Nepalese Himalaya: A Case Study of Kuiyadaha Landslide, Gokuleshor, Baitadi. Himalayan Journal of Applied Science and Engineering, 5**,** 23-44.
- BASNET, K. & ACHARYA, D. 2019. Flood Analysis at Ramghat, Pokhara, Nepal Using HEC-RAS. Technical Journal, 1**,** 41-53.

- CHHETRI, N. B. & EASTERLING, W. E. 2010. Adapting to climate change: Retrospective analysis of climate technology interaction in the rice-based farming system of Nepal. Annals of the Association of American Geographers, 100**,** 1156-1176.
- CHOWDHURY, R., BHATTACHARYA, G. & METYA, S. 2023. Geotechnical slope analysis, Crc Press.
- DAHAL, R. K. 2012. Rainfall-induced landslides in Nepal. International Journal of Erosion Control Engineering, 5**,** 1-8.
- DAHAL, R. K. & HASEGAWA, S. 2008. Representative rainfall thresholds for landslides in the Nepal Himalaya. Geomorphology, 100**,** 429-443.
- DENG, Z.-P., LI, D.-Q., QI, X.-H., CAO, Z.-J. & PHOON, K.-K. 2017. Reliability evaluation of slope considering geological uncertainty and inherent variability of soil parameters. Computers and Geotechnics, 92**,** 121-131.
- DI MATTEO, L., VALIGI, D. & RICCO, R. 2013. Laboratory shear strength parameters of cohesive soils: variability and potential effects on slope stability. Bulletin of Engineering Geology and the Environment, 72**,** 101-106.
- DUNCAN, J. M., WRIGHT, S. G. & BRANDON, T. L. 2014. Soil strength and slope stability, John Wiley & Sons.
- FINDELL, K. L. & ELTAHIR, E. A. 1997. An analysis of the soil moisture-rainfall feedback, based on direct observations from Illinois. Water Resources Research, 33**,** 725-735.
- GHIMIRE, T., PAUDEL, L. & PANT, B. 2007. The devastating Ramche Landslide (Rasuwa) and the future of Polchet residents. Journal of Nepal Geological Society, 36**,** 27-27.
- GNYAWALI, K., DAHAL, K., TALCHABHADEL, R. & NIRANDJAN, S. 2023. Framework for rainfall-triggered landslide-prone critical infrastructure zonation. Science of the Total Environment, 872**,** 162242.
- GRIFFITHS, D. & LANE, P. 1999. Slope stability analysis by finite elements. Geotechnique, 49**,** 387-403.
- HAMMOURI, N. A., MALKAWI, A. I. H. & YAMIN, M. M. 2008. Stability analysis of slopes using the finite element method and limiting equilibrium approach. Bulletin of Engineering Geology and the Environment, 67**,** 471-478.
- HIGHLAND, L. M. & BOBROWSKY, P. 2008. The landslide handbook-A guide to understanding landslides, US Geological Survey.

- IVERSON, R. M. 2000. Landslide triggering by rain infiltration. Water resources research, 36, 1897-1910.
- JHARENDRA, K., GAUTAM, D., NEUPANE, P. & PAUDYAL, K. R. 2018. Landslide inventory mapping and assessment along the Ramche-Jharlang area in Dhading, Rasuwa and Nuwakot districts, Lesser Himalaya Central Nepal. Journal of Nepal Geological Society, 55, 103-108.
- KHAN, M. I. & WANG, S. 2021. Slope stability analysis to correlate shear strength with slope angle and shear stress by considering saturated and unsaturated seismic conditions. Applied Sciences, 11, 4568.
- KINCEY, M., ROSSER, N., SWIRAD, Z., ROBINSON, T., SHRESTHA, R., PUJARA, D., BASYAL, G., DENSMORE, A., ARRELL, K. & OVEN, K. 2024. National-scale rainfall-triggered landslide susceptibility and exposure in Nepal. Earth's Future, 12, e2023EF004102.
- LI, L., WANG, Y., ZHANG, L., CHOI, C. & NG, C. W. 2019. Evaluation of critical slip surface in limit equilibrium analysis of slope stability by smoothed particle hydrodynamics. International Journal of Geomechanics, 19, 04019032.
- LIU, S., SHAO, L. & LI, H. 2015. Slope stability analysis using the limit equilibrium method and two finite element methods. Computers and Geotechnics, 63, 291-298.
- MALLA, B. & DAHAL, B. K. Effect of Rainfall on Stability of Soil Slope. Proceedings of 10th IOE Graduate Conference Peer Reviewed ISSN, 2021. 2350-8914.
- MATTHEWS, C., FAROOK, Z. & HELM, P. 2014. Slope stability analysis–limit equilibrium or the finite element method. Ground Engineering, 48, 22-28.
- MCADOO, B. G., QUAK, M., GNYAWALI, K. R., ADHIKARI, B. R., DEVKOTA, S., RAJBHANDARI, P. L. & SUDMEIER-RIEUX, K. 2018. Roads and landslides in Nepal: how development affects environmental risk. Natural Hazards and Earth System Sciences, 18, 3203-3210.
- MEDINA, V., HÜRLIMANN, M., GUO, Z., LLORET, A. & VAUNAT, J. 2021. Fast physically-based model for rainfall-induced landslide susceptibility assessment at regional scale. Catena, 201, 105213.
- OSMAN, K. T. 2018. Soils on steep slopes. Management of soil problems. Springer.
- PAUDYAL, P., DAHAL, P., BHANDARI, P. & DAHAL, B. K. 2023. Sustainable rural infrastructure: guidelines for roadside slope excavation. Geoenvironmental Disasters, 10, 11.

- PHOON, K.-K. & TANG, C. 2019. Characterisation of geotechnical model uncertainty. Georisk: Assessment and Management of Risk for Engineered Systems and Geohazards, 13**,** 101-130.
- RAMADHANI, S. & IHZAN, M. The Slope Instability Potential in the Balaroa area based on the Finite Element Method using Shear Strength Reduction. IOP Conference Series: Earth and Environmental Science, 2023. IOP Publishing, 012020.
- SALIH, A. G. Stability Analysis of Residual Soil Slope Model by Numerical Modeling Using FEM Against LEM. IOP Conference Series: Earth and Environmental Science, 2021. IOP Publishing, 012046.
- SHARMA, S., HAMAL, K., KHADKA, N. & JOSHI, B. B. 2020. Dominant pattern of year-to-year variability of summer precipitation in Nepal during 1987–2015. Theoretical and applied climatology, 142**,** 1071-1084.
- SHRESTHA, A. B., WAKE, C. P., DIBB, J. E. & MAYEWSKI, P. A. 2000. Precipitation fluctuations in the Nepal Himalaya and its vicinity and relationship with some large scale climatological parameters. International Journal of Climatology: A Journal of the Royal Meteorological Society, 20**,** 317-327.
- SKILODIMOU, H. D., BATHRELLOS, G. D., KOSKERIDOU, E., SOUKIS, K. & ROZOS, D. 2018. Physical and anthropogenic factors related to landslide activity in the Northern Peloponnese, Greece. Land, 7**,** 85.
- STARK, T., NEWMAN, E. J. & AUST, R. 2008. Back-analysis of a PVC geomembrane-lined pond failure. Geosynthetics International, 15**,** 258-268.
- VANDENBERGE, D. R. & MCGUIRE, M. P. 2019. Practical use of modified Hoek–Brown criterion for soil slope stability analysis. Geotechnical and Geological Engineering, 37**,** 5441-5455.
- ZHU, D., LEE, C. & JIANG, H. 2003. Generalised framework of limit equilibrium methods for slope stability analysis. Geotechnique, 53**,** 377-395.
- ZOLKEPLI, M., ISHAK, M. & ZAINI, M. Slope stability analysis using modified Fellenius's and Bishop's method. IOP Conference Series: Materials Science and Engineering, 2019. IOP Publishing, 012004.

**Pokhara Engineering College (PEC)**
Phirke, Pokhara-8, Kaski, Nepal
PO Box: 540, Tel: 977-61-581209/578530
E-mail: info@pec.edu.np.
www.pec.edu.np